THE MODELLING OF MULTIPLE BEAM X-RAY SYSTEMS USING VISIBLE LIGHT

Hock-Woon Hon B.Eng.

A thesis submitted in partial fulfilment of the requirements of
The Nottingham Trent University for the degree of
Doctor of Philosophy

Department of Electrical and Electronic Engineering,
The Nottingham Trent University,
Burton Street,
Nottingham.

November 2000

Collaborating Establishment:

Home Office Science and Technology Group,
Police Scientific Development Branch (P.S.D.B.),
Sandridge, Hertfordshire,
United Kingdom.

THE MODELLING OF MULTIPLE BEAM X-RAY SYSTEMS USING VISIBLE LIGHT

Hock-Woon Hon

Abstract

In general, x-ray shadowgraph images are very difficult to interpret for human observers due to the lack of visual depth cues in an image which has been produced by transmitted radiation. The psychological cues to depth associated with 'normal' two-dimensional images such as a photograph are not available in a standard x-ray image. Further, these cues can be incorrectly interpreted as being present in an x-ray image and can lead to serious ambiguity in the subsequent visual interpretation of that image. In an attempt to solve this problem previous research has utilized the powerful physiological depth cue of binocular parallax by the production of binocular stereoscopic image pairs.

The solution put forward in this research is to introduce another powerful physiological depth cue of motion parallax into the resultant shadowgraph x-ray images. This is achieved by collecting a number of different views (i.e. from 6 to 16) of the object under inspection and displaying the resultant 'raw' perspective images in a specific sequence on a standard video monitor. This produces the effect of the object appearing to undergo a partial rotation in the display. Further work combined the geometric and temporal design theory developed for the production of motion parallax with that required for the production of binocular stereoscopic images. Therefore, the resultant image information can be viewed in a number of different modes. These include a sequence of perspective images exhibiting motion parallax or a sequence of perspective images exhibiting motion parallax and binocular parallax.

In order to test the premise on which the theoretical analysis of the multiple view imaging techniques is based would require the development of sophisticated x-ray imaging apparatus. However, a visible light analogy of transmission x-ray imaging was identified as the theoretical basis for developing a visible light experimental system utilising a standard charge coupled device (CCD) area array camera. The camera is used to obtain perspective images during a single linear translation of the object under inspection. Thus the camera in conjunction with an appropriate image capture mechanism is used to obtain multiple perspective images in its standard mode of operation (i.e. area array 'snapshot') or a novel multiple line-scan mode. Therefore, both a theoretical and an empirical analysis of the imaging properties of these techniques has been conducted.

The results from this work produced sufficient interest by the Police Scientific Development Branch (P.S.D.B.) part of Home Office Science and Technology Group to provide funding to conduct definitive experiments with shadowgraph images. This was successfully achieved by implementing a real time image intensified x-ray set to validate the findings of the earlier visible light work. Thus the high degree of correlation between the x-ray and visible light techniques in terms of the spatial and temporal content of the resultant images has been empirically demonstrated and evaluated. The operational and scientific constraints adhered to throughout this programme of work enhance the general applicability of the imaging techniques developed for on-line applications encountered in security screening and industrial inspection.

Acknowledgements

I would like to extend my sincere thanks to the following people for their help during this work.

My supervisors, Dr. Paul Evans and Professor Max Robinson for their guidance, technical input and advice regarding this thesis.

Image Scan Holdings, especially Dr. Simon Godber, for providing equipment for the experimental work.

Mr. Philip Chester-Nash and Mr. Jien-Hau Ng for the useful discussion regarding this thesis.

Wee Yee, my family and friends for their irreplaceable support.

I would like to thank Dr. Paul Evans again for his continuous encouragement throughout this research programme.

Table of contents

List of figures

List of tables

List of graphs

1 INTRODUCTION

After the discovery of x-rays by Roentgen [1] in 1895, x-ray imaging has undergone constant development, particularly in the fields of medicine, industrial inspection and security screening [2, 3, 4, 5, 6, 7, 8, 9, 10]. However, the interpretation of standard shadowgraph x-ray images by a human observer is very difficult due to a lack of visual depth cues. The problem associated with the interpretation of a shadowgraph of a complex three-dimensional structure arises as a direct consequence of using transmitted radiation to produce an image. This is because the psychological cues [11, 12] to depth associated with 'normal' two-dimensional images such as a photograph are not available in the 'standard' x-ray image.

A binocular stereoscopic x-ray image pair of an object under inspection can greatly enhance a human observer's spatial interpretation of that object. However, binocular stereoscopic imaging techniques can suffer from localized occlusion which results in the destruction of spatial information contained in the resultant stereoscopic images. Occlusion in x-ray imaging occurs as the result of the x-ray beam undergoing a total attenuation as it propagates through the object under inspection. Thus occlusion can be produced by the effect of many different structures appearing to be superimposed in the resultant image. Therefore changing the viewing position/angle of the imaging system with respect to the object under inspection can effect a relative repositioning of these structures in the resultant image. Thus enabling a translucent view of these object features to be obtained. Further, if these perspective views are collected from a continuous relative repositioning of an object under inspection, then the changing interposition of these structures in the 'live' display will impart additional three-dimensional information to the human observer by the powerful physiological depth cue of motion parallax. It is therefore concluded that the ability to choose more appropriate viewpoints over a wider arc would be highly advantageous for the human observer in terms of structural interpretation of the resultant x-ray images. For instance, a live binocular stereoscopic view of a rotating object could be presented to the human observer by utilizing an area type x-ray detector such as an image intensifier illuminated by a cone x-ray beam source. Thus the display of the rotating object could impart depth information to the observer by combining the powerful physiological cues of motion parallax [13, 14] and binocular parallax [15, 16] if suitable display mechanisms were incorporated. However, the research presented in this thesis is constrained to investigate techniques that are suitable for on-line applications encountered in security screening and industrial inspection applications. Thus, the rotation of the object under inspection is not a viable solution as this off-line procedure could introduce unconstrained motion to object structures that would destroy the integrity of the resultant images.

The solution put forward in this research is the introduction of motion parallax produced by the relative linear translation of the object under inspection with respect to camera system. This is

achieved by collecting a number of different views of the object under inspection and displaying the resultant 'raw' perspective images in a specific sequence on a 'standard' video monitor. This produces a similar effect to the object undergoing a partial rotation in the display [17]. Further work combined the geometric and temporal design theory developed for the production of motion parallax with that required for the production of binocular stereoscopic images. Therefore, the resultant image information can be viewed in a number of different modes. These include:

- a sequence of perspective images exhibiting motion parallax;
- the choice of multiple 'static' binocular stereoscopic images;
- a sequence of binocular stereoscopic images exhibiting motion parallax.

Previous research has stated that motion has a super additive effect [18] on binocular parallax and the combination of motion and binocular parallax information allows the object under inspection to be viewed over a relatively wider arc compared to conventional binocular stereoscopic techniques [19]. In order to produce a number of perspective images during a single object pass a multiple view x-ray imaging system is required. The development of a prototype re-configurable multiple view x-ray system is inhibited by high development costs. However, a cost-effective proof of principle can be effected by implementing a visible light analogy to transmission x-ray imaging [20,21]. In other words, the analogous ray geometry produced by the nodal point in a lens and a point source of x-ray illumination is exploited in order to produce geometrically equivalent images from each modality [22]. Thus, the imaging properties of an x-ray system can be simulated by using a visible light camera in conjunction with an appropriate image capture mechanism. The camera is used to obtain multiple perspective images in its standard mode of operation (i.e. area array 'snapshot') or a novel multiple line-scan mode [23]. Therefore, a visible light experimental system was constructed and utilized to conduct experiments in order to compare the two-dimensional and three-dimensional imaging characteristics of the multiple view techniques investigated.

The successful implementation of a visible light system influenced the design of an experimental multiple view x-ray system based on a commercially available cone-beam x-ray system [24] incorporating an image intensifier. The two-dimensional and three-dimensional imaging characteristics of the x-ray techniques are examined and found equivalent to those techniques achieved by the visible light experimental configuration. The results indicate that the line-scan imaging technique has inherent advantages over the area array technique in a number of aspects. The operational and scientific constraints adhered to throughout this programme of work enhance the general applicability of the imaging technique for on-line applications encountered in security and industrial inspection.

1.1 Previous related work

An on-going programme of work is being conducted by the 3-D Imaging Group at The Nottingham Trent University into three-dimensional security x-ray screening. Initially this research was conducted for HM Custom and Excise and currently for the Police Scientific Development Branch, part of the Home Office Science and Technology Group [25, 26, 27, 28, 29, 30].

In an attempt to interpret the three-dimensional information contained in the shadowgraph images produced by transmitted x-radiation two major research themes have been investigated. First, the development of a binocular stereoscopic line-scan x-ray imaging technique that has been successfully applied to both 'standard' [31] x-ray sensors and folded array dual-energy [32] x-ray sensors. Second, the automatic interrogation of the three-dimensional data inherent in the stereoscopic image pairs in order to produce 2 ½-D visualisations of the data [33, 34, 35]. Each of these research areas are closely interrelated and are being investigated and developed in parallel.

1.2 Research objectives

A fundamental aim of this research is to investigate multiple view x-ray imaging techniques in order to introduce motion parallax, or motion parallax in combination with binocular parallax into the resultant x-ray images. The objectives of the research are summarised below in the context of the three phases in which the work was undertaken.

Phase 1

I. The selection of a suitable x-ray imaging source/sensor arrangement which could be configured to produce:
   - a sequence of perspective images exhibiting motion parallax;
   - a sequence of binocular stereoscopic images exhibiting motion parallax.

II. To establish the geometric relationship between a visible light camera utilizing reflected radiation and an x-ray imaging system utilizing transmitted radiation.

III. The development of a design theory which takes into account the geometry of the proposed configurations and provides the human observer with three-dimensional information which is comfortable to view.

Phase 2

I. To construct an experimental visible light system based on the design theory above in order to simulate a sequence of perspective images produced by a multiple view x-ray imaging system.

II. Empirical evaluation of the experimental visible light system in two modes of operation. These are:
    - a novel multiple view line-scan technique;
    - a multiple view area array 'snapshot' technique.

Phase 3

I. To construct an experimental x-ray system in order to test the validity of utilizing only motion parallax or motion parallax in combination with binocular parallax using transmitted x-ray images.
II. Empirical evaluation of the experimental x-ray system in two modes of operation. These are:
    - a novel multiple view line-scan technique;
    - a multiple view area array 'snapshot' technique.

1.3 Structure of the thesis

The arrangement of this thesis is summarised in the following paragraphs.

Chapter two outlines the enabling technologies that have been utilized in this programme of work. The three areas of interest are: the shadowgraph image; factors governing the display of image sequences and, the simulation of multiple view x-ray imaging techniques using visible light.

Chapter three discusses the design philosophy and the decisions taken in order to select imaging techniques that satisfy the operational and scientific criteria developed.

Chapter four presents the theoretical appraisal of the selected multiple view techniques in terms of their temporal and geometric imaging properties.

Chapter five presents the experimental multiple view visible light configurations and the relevant empirical analysis.

Chapter six presents the experimental multiple view x-ray arrangements and the relevant empirical analysis.

Chapter seven discusses the three-dimensional display methods investigated.

Chapter eight presents a discussion of the results, conclusions and the direction of the further work.

2 BACKGROUND INFORMATION

2.1 Introduction

The fundamental aim of this research is the investigation of multiple view x-ray systems for on-line inspection applications. The resultant image sequences produced by the imaging techniques under consideration in this research utilize motion parallax, binocular parallax or a combination of both motion and binocular parallax to enable the three-dimensional structure of an object under inspection to be better understood by a human observer. The discussion presented is split into three broad areas:

I. The shadowgraph image; this discusses the nature of a shadowgraph image in terms of visual depth cues and the problems encountered in their interpretation by a human observer.

II. Factors governing the display of image sequences; this discusses the criteria governing the human observer's perception of three-dimensional information in a sequential display of perspective images.

III. The simulation of multiple view x-ray imaging techniques using visible light; this presents the geometric equivalence between reflected visible light imaging and transmission x-ray imaging and, proposes a number of multiple view configurations.

2.2 The shadowgraph image

A shadowgraph is a shadow picture produced by a point source illuminating an object. In the case of x-rays the information content in a shadowgraph is contained in the pattern of varying intensity of the modulated x-ray beam produced by the differential attenuation of x-rays due mainly to the structure and material type of the object under inspection. The density of the shadowgraph is controlled by the exposure time and the amount of electrical current flowing in the x-ray tube whereas image contrast is controlled by the voltage across the tube [21]; details of the factors governing the intensity of the x-ray beam can be found in *Pope* [36]. To present the shadowgraph information to the human observer, a 'visible light version' of the pattern of x-radiation intensity is required. This conversion can be achieved by using a florescent screen, x-ray converter tubes or fibre scintillators [37]. The visible light version of the shadowgraph is generally known as an *x-ray image*. The research presented here is limited to the geometric considerations of x-ray image production and does not purport to investigate or optimise aspects of the production of the x-rays and their characteristics in the generation of images. For instance the x-ray images discussed in this work are assumed to be produced by a perfect point source and thus the blurring effects on the resultant image [36], due to the finite size of the focal spot, are not considered further.

When a three-dimensional structure in object space is imaged it is 'flattened' into a two-dimensional planar image. For such an optical two-dimensional image (i.e. photograph), depth information is generally provided by psychological cues [11, 38, 39, 40]. The psychological cues arise

from the planar retinal image in the eye, being assisted by the experience and imagination of the observer. However, these psychological cues provide little or no value in interpreting a shadowgraph x-ray image. In theory, relative object size, linear perspective and texture gradient may be of some limited use but usually only when the observer has a prior knowledge of the structure under inspection. Also, occlusion can exist in an x-ray image, although this may be interpreted incorrectly as a dense occluding object can be in front of or behind the structure which it is occluding in a transmitted image. Additionally occlusion can be created by the superposition of many individually translucent features occurring in the same x-ray beam path. Thus, in practice, there is virtually no indication of the three-dimensional structure of an object under inspection produced by a single two-dimensional x-ray image. However, depth information can be imparted to the human observer by introducing the physiological cue of binocular parallax into the resultant x-ray images. The stereoscopic image can be perceived to be at the viewing screen surface, or extend in front or behind the viewing screen. The ability to judge the position in space of objects or features in an image can dramatically enhance an observer's understanding of the true nature of the three-dimensional scene under observation. However a static binocular stereoscopic view produces information from a very limited arc about the object and can exhibit occlusion. It would be highly advantageous for the human observer in terms of spatial interpretation of the resultant images if many different views of the object under examination can be made available. The solution proposed in this research is to impart three-dimensional information using another powerful physiological cue of motion parallax. Thus motion parallax as a visual cue to depth perception and its relationship with binocular parallax is discussed in the following section.

2.3 Factors governing the display of image sequences

Movement or rotation of an object relative to the observer produces a very vivid effect of spatial perception. This is due to the parallax differences in the images formed in succession on the retina in both eyes; the configuration of the image on the retina varies continuously. Therefore, the effect of the variation of an object image on the retina can be reproduced by showing perspective images [41] that have been obtained from different viewpoints relative to the object of interest. In order to explain this effect in more detail the following discussion concerning the physiological aspects of viewing a sequence of images is divided into the following related areas:

a) apparent motion;
b) motion parallax;
c) combining motion parallax and binocular parallax.

a) Apparent Motion

Real motion is specified as the continuous displacement of an object from one location to another at a particular velocity and acceleration in the real world [42, 43, 44]. Apparent motion is the illusory impression created by the rapid alteration of images of the object at different spatial locations that

the object has moved smoothly from one location to another location [45, 46]. This apparent motion used routinely in cinematic and televisual displays is known as phi motion [47]. When the successive images depicting motion are presented to the human observer, the human's visual system fills in the temporal gaps between successive perspective images [48] to produce the perception of continuous motion [42]. In fact phi phenomenon is the visual basis for a flipbook, cinema, television, cartoon and computer animation [49, 50, 51, 52, 53]. The effect of phi phenomenon is strengthened by the persistence of vision [54, 55, 56] that encourages the fusion of successive images, and also by the human tendency to group similar form and location into meaningful whole stimuli [57]. In order to produce this effect in an image display requires that the perspective images be refreshed at a minimum rate of 16 Hz [58]. However, this display rate produces objectional flicker [59]. Therefore a minimum threshold frequency termed the critical fusion frequency [60], has to be exceeded to produce a flicker-free display. For instance, the flicker in the cinema (i.e. 24 pictures/second) is eliminated by using a 3-bladed shutter in order to optically 'chop' each individual picture or frame. Hence, the display frequency is artificially increased to 72 flashes/second [47].

b) Motion parallax

The information provided by the relative movement of the projection of objects onto the retina as an observer moves laterally is called motion parallax [13]. It provides small displacements and continuous movement in a visual display in a way that permits the viewer to extract depth information. Interestingly, *Valyus* [19] reported that the depth effect obtained in motion can exceed that produced by the binocular stereoscopic effect:

"*..... the base between the view points of the successive images may increase indefinitely, so that the depth effect from motion may be greater than that obtained by the binocular effect.*"

Valyus also pointed out that:

"*The nature of the motion effect resembles that of the binocular stereoscopic effect, because both depend upon the parallax of corresponding points in the images, i.e. the parallax difference in the retinal images, occurring in the former in a time sequence and in the latter by virtue of the spatial arrangement.*"

In relation to this, *Rock* [61] also reported that the motion parallax cue is dependent upon the same geometry as that which produces stereopsis [62]. The difference being that the comparison of different viewpoints occurs *sequentially* in the case of motion parallax rather than *synchronously* in the case of binocular parallax. It is also reported that motion parallax is primarily a relative depth cue [63], although it may also provide some absolute distance information [64]. It has also been identified that binocular parallax, motion parallax and rotation all provide similar three-dimensional information when a small angle of rotation [7] (i.e. ~15°) is used.

A special case of motion parallax termed the kinetic depth effect [65, 66] was first systematically investigated by *Wallach* and *O'Connell* [67] in 1953 and is an adaptation from the previous work reported by *Miles* [68] and *Metzger* [69]. This effect involves the recovery of three-dimensional information from a sequence of two-dimensional silhouettes. This effect involves the motion of objects, rather than observers; a figure looks flat when it is stationary and appears to have depth once it moves. Figure 2-1 illustrates an experiment conducted by *Wallach* and *O'Connell* and this experiment is briefly described below:

"*An object is placed between a punctiform light source and a translucent screen and is rotated or turned back and forth. Its shadow is observed from the other side of the screen. .... the shadows of some forms will look three-dimensional only in such a moving presentation.*"

and

"*... the shadows cast by the wireframe must display contours or lines which change their length and their direction simultaneously.*"

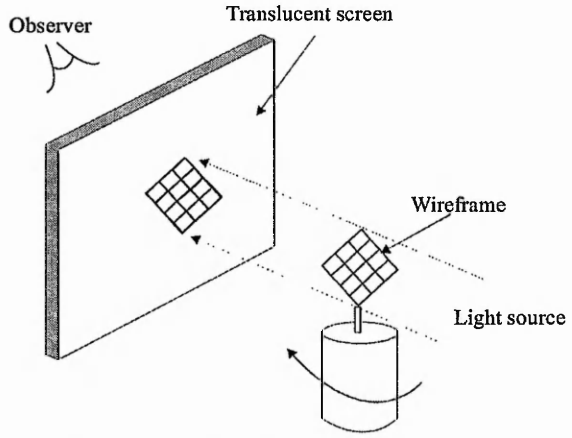

Figure 2-1 *Depiction of the kinetic depth effect experiment conducted by Wallach and O'Connell*

It has also been reported that the shape of the object under inspection (wire-frame object) can be worked out by the observer with remarkable accuracy from the shadows during a full or a partial rotation [70]. The kinetic depth effect provides only relative depth information, that is, the three-dimensional shape of the object in space is conveyed, but not its absolute distance from the human observer [63]. Thus, when a sequence of perspective images are displayed, a corresponding object point in the successive views undergoes a transition in coordinate position and hence this dynamic change of parallax information (motion parallax) provides depth information to the human observer. The perspective images can be presented, back and forth, in a continuous loop to induce a positive and a negative change in the coordinate positions that in turn produce an oscillatory motion in the display.

c) Combining motion parallax and binocular parallax

Recent research [71] has reported that there is a degree of interaction between binocular parallax and motion parallax in providing depth information and that the combination of these depth cues can improve the sensitivity of observation of three-dimensional structures. *Tuittle* and *Brausntein* [18] examined a subject's ability to recover the perceived structure of an object (i.e. a rotating cylinder) from its motion with binocular stereoscopic viewing. They concluded that motion had a super-additive effect, that is, the effects of binocular stereoscopic viewing were enhanced with the addition of motion [17, 72, 73, 74]. The combination of binocular parallax and motion parallax effectively allow the object under inspection to be viewed over a relatively wider arc such that aspects which are hidden or occluded from a fixed viewpoint are revealed [19]. In this way the dynamic stereoscopic display ensures a continuous sequence of viewpoints that overcomes the 'cardboarding' effect which can be present in a static binocular stereoscopic display with its two fixed viewpoints.

2.4 The simulation of multiple view x-ray imaging techniques using visible light

The ray geometry of an x-ray imaging system is directly analogous to that of a visible light imaging system [20, 21]; this analogy is based on the principle of the pinhole model [22]. The perspective centres in the visible light and the x-ray arrangement are the nodal point in a camera lens and focal spot of the x-ray source respectively. The fundamental characteristics of a two-dimensional image, obtained from either reflected or transmitted radiation is that each point in the image represents a corresponding point in object space [75]. Therefore, ideally, the resultant image obtained from a visible light system is geometrically equivalent to that produced by an x-ray system. Figure 2-2 illustrates the geometric equivalence of the sensor field of view in the visible light and x-ray arrangements. The principal distances are different in both arrangements; focal length f in the visible light arrangement and the source-to-sensor separation S_h in the x-ray arrangement. The magnification in both imaging axes is identical and therefore only the y-axis magnification is discussed.

With reference to Figure 2-2, the geometrically equivalent parameters in the visible light and x-ray scenarios are summarised in Table 2-1. However, it is identified that there are a number of fundamental differences in terms of imaging properties [76] of the visible light and x-ray techniques. The resultant images produced by each modality are produced by quite different physical processes. When using x-ray technology, images are obtained by transmitting an x-ray beam through the object under inspection. The degree of x-ray penetration of an object is dependent upon the density and structure of the object. Hence, the internal structure may be seen provided it is not 'shielded'. On the other hand, visible light systems are obtained by focusing the reflected light from the object under inspection onto the photosensitive surface of an imager. Thus, only the

surface of the object can be inspected. Therefore, the grey level quantisation of an x-ray image and a visible light image for an identical scene has no relationship.

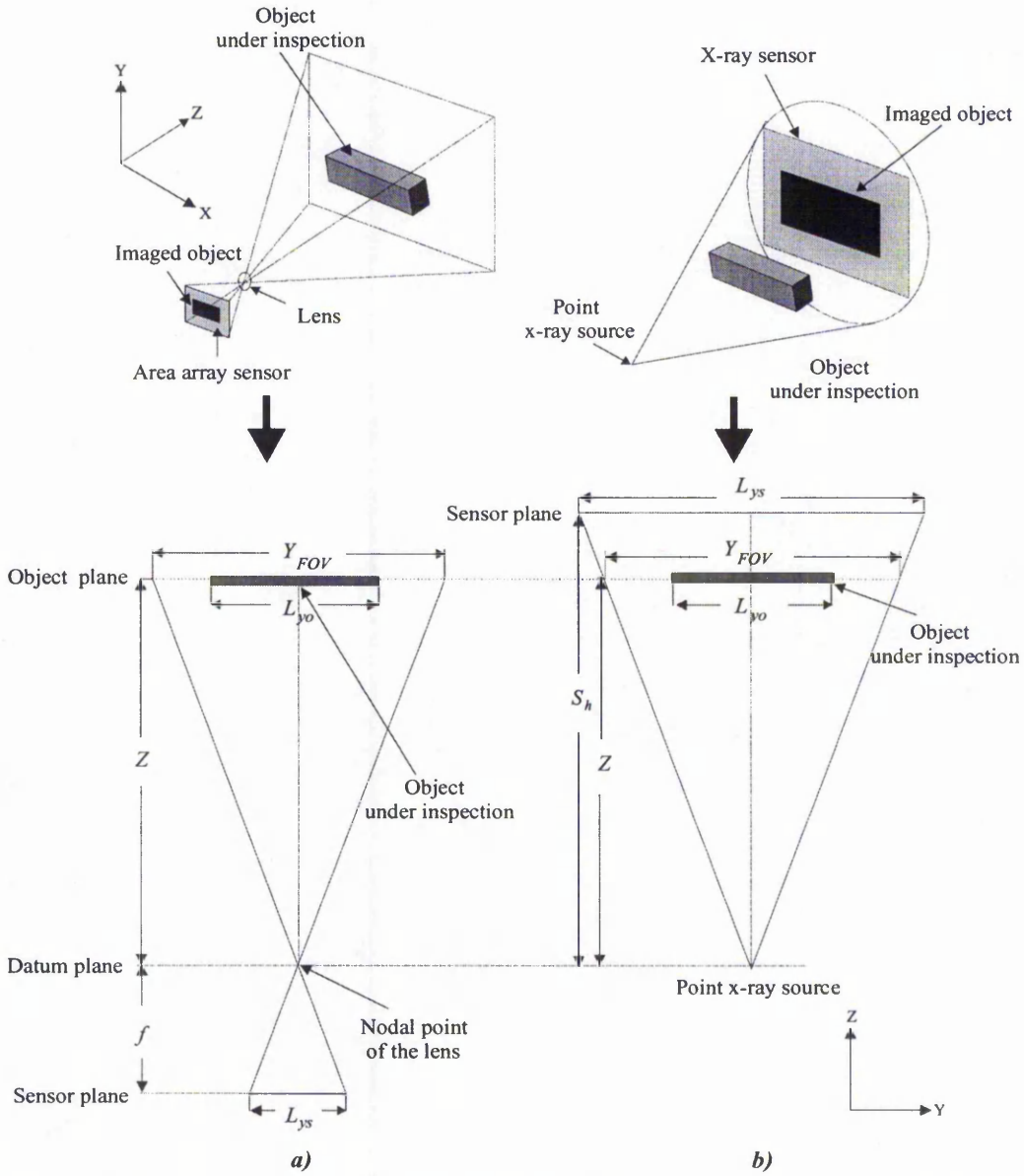

Figure 2-2 *Illustration of the geometric equivalence that exists between a) visible light area array camera and b) x-ray' camera'*

	Visible light arrangement	X-ray arrangement
Perspective centre	Nodal point of the lens	Point x-ray source
Principal distance	Focal length (f)	Source-to-sensor separation (S_h)
Sensor dimensions	Dimensions of the area array sensor (L_{xs}, L_{ys})	Dimensions of the x-ray sensor (L_{xs}, L_{ys})
Object range from the perspective centre	Camera-to-object range (Z)	Source-to-object range (Z)

Table 2-1 *Geometrical parameters for the visible light camera and the x-ray camera*

Three multiple view x-ray imaging techniques are presented in the following sections together with their visible light analogies. Each of these techniques may be used to produce motion parallax and binocular parallax information by implementing an appropriate video image capture and display mechanism. A technique employing rotational motion is also included in this discussion for comparative purposes. Although it is not utilized in this work for the reasons presented in Chapter 3.

2.4.1 Rotational technique

The term rotational technique is used in this thesis to describe an imaging system which views a rotating object in order to obtain a sequence of perspective images. *Drugin et al* [17] stated that:

"*When an object is rotated about an axis other than the line of sight, the relative motions of features on the object can specify the three-dimensional structure ... a similar recovery of structure can be obtained if the object and the viewer undergo an angular displacement with respect to one another.*"

The relative rotation required by this technique can be produced by either rotating the object under inspection or rotating the imaging system about a stationary object. This is illustrated in Figure 2-3 where P_1 to P_3 depict the three relative positions of the x-ray source/sensor and the object under inspection.

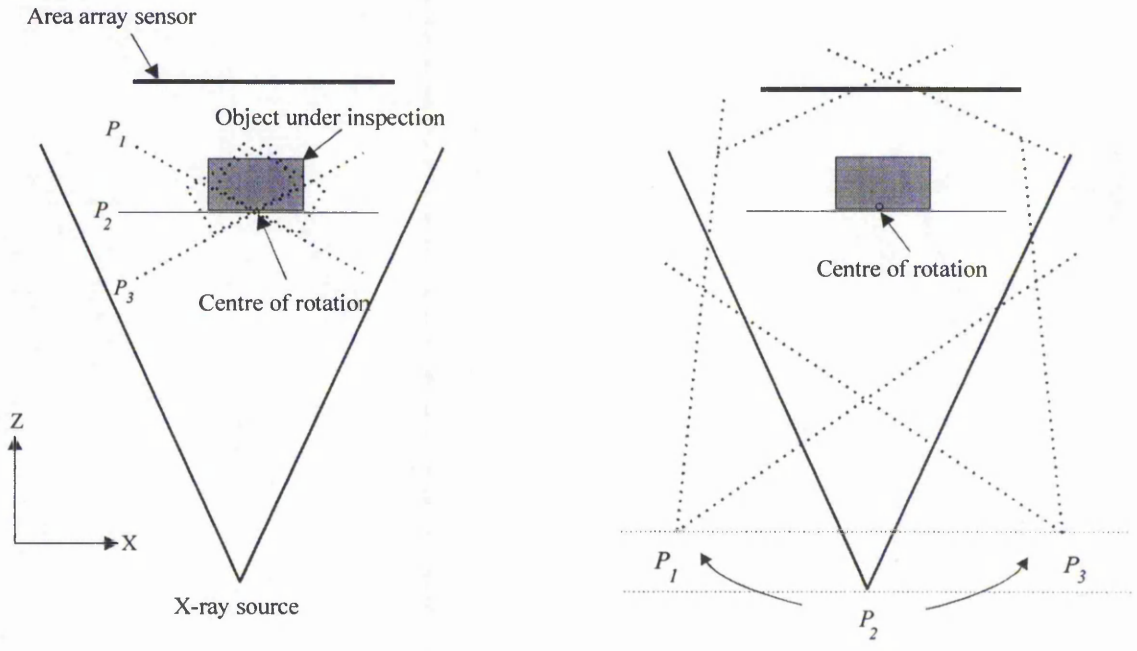

Figure 2-3 *The rotational technique utilizing a) object rotation or b) x-ray source/sensor rotation*

Each of these techniques produces identical image information. However, the following discussion is based on the x-ray source/sensor motion as it lends itself more readily to the diagrammatic representation of the technique. When the resultant perspective images produced by this imaging

technique are displayed in a correct sequence, the object image is perceived to be rotating about a fixation point. The fixation point in the display corresponds to the centre of rotation. This rotational x-ray technique can be modelled in the visible domain by using a visible light camera arrangement. The rotational technique utilizes a similar imaging geometry to a convergent visible light stereoscopic camera [77] depicted in Figure 2-4.

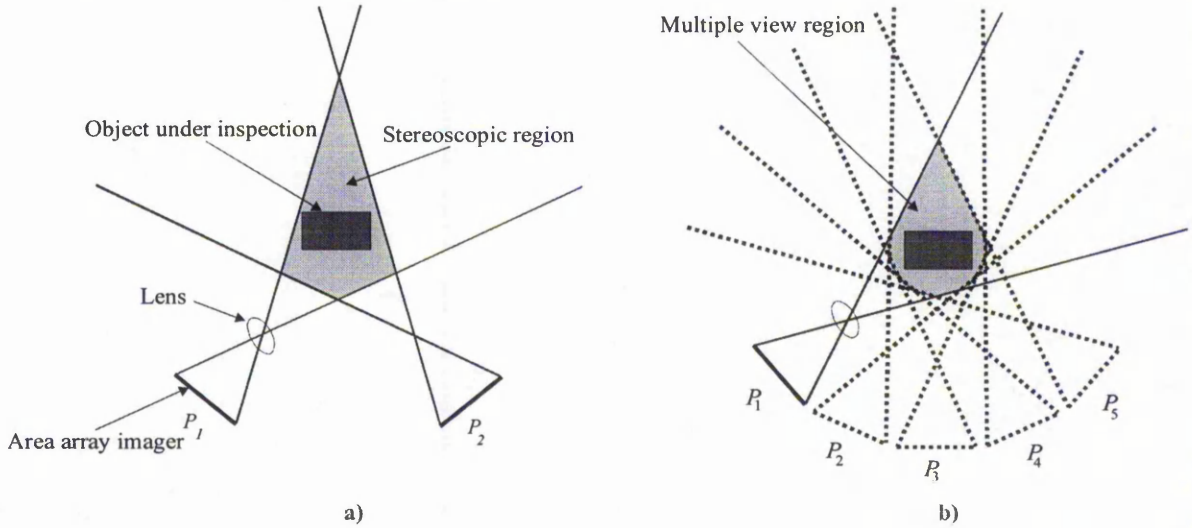

Figure 2-4 *Comparison of a) static convergent stereoscopic arrangement and b) a multiple view rotational arrangement*

Stereoscopic arrangements [78] require two views, P_1 and P_2, such that an overlapping field of view or a *stereoscopic region* is produced. Whereas for the multiple view arrangement, a number of views (i.e. more than two views), P_1 to P_5 in the case of Figure 2-4b, are used to obtain continuous perspective information. The region of overlap in object space is termed the *multiple view region.* It should be noted that the geometric alignment of the imaging sensors is critical in the stereoscopic arrangement as well as in the multiple view arrangement. This is because the integrity of the parallax information in the resultant images is dependent upon the integrity of the geometric alignment of the system configuration.

2.4.2 Lateral shift technique

An alternative method for producing perspective images from an object under inspection is to translate the object through the field of view of the imaging sensor as shown in Figure 2-5. The parallax information obtained from displacing the object under inspection in an orthogonal manner with respect to the imaging sensor is similar to that obtained from relative rotation (Section 2.4.1) under certain conditions. These are, the angular displacement is small and a fixation point is set in the resultant display for the lateral shift technique.

The similarity between the image sequences produced by the lateral shift technique and the rotation technique is in agreement with *Drugin et al* [17] who states:

"*Although the geometry of displacement is different from that of rotation, in both cases, the object is observed from more than one angle. If the observer maintains fixation on the object during angular displacement the two cases are practically identical for small rotation and displacement.*"

Two approaches can be used. These are *a) object movement* and *b) source/sensor movement* as depicted in Figure 2-5 where P_1 to P_3 depict three relative positions between the source/sensor and object under inspection. These two approaches produce identical image information. The relative displacement (i.e. base separation) of the object with respect to the x-ray source/sensor arrangement is denoted by d_o in Figure 2-5.

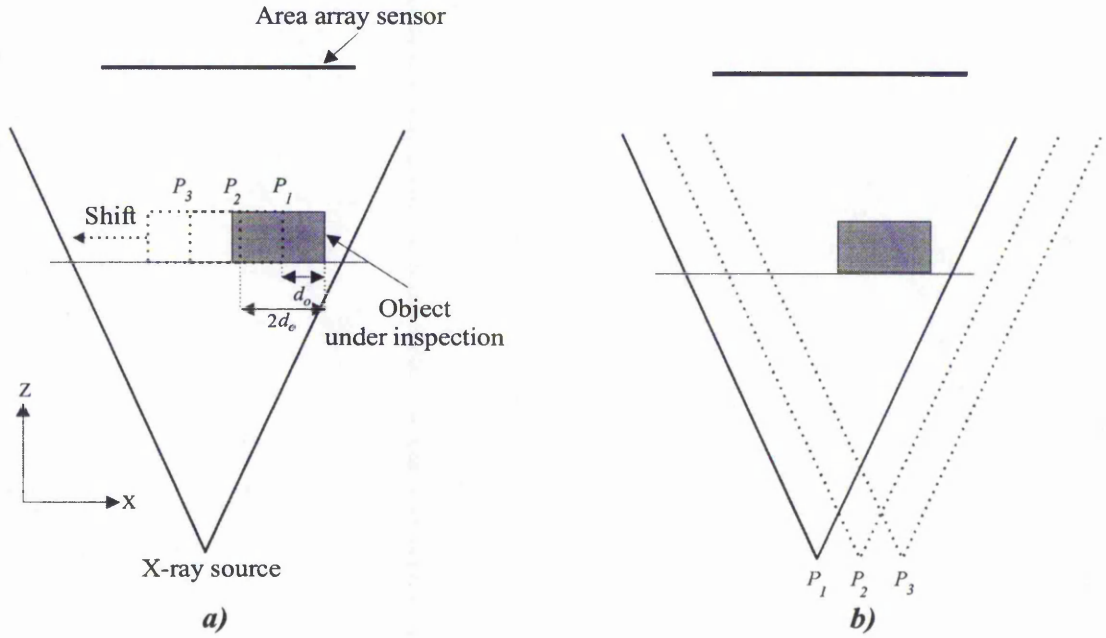

Figure 2-5 *The lateral shift technique a) object movement and b) x-ray source/sensor movement*

The base separation between each successive view is assumed to have the same value. It can be appreciated that this technique is not geometrically equivalent to the rotational technique because the 'sensor planes' for each perspective image are co-planar. The lateral shift technique utilizes similar imaging geometry to the parallel stereoscopic arrangement [79, 80] as depicted in Figure 2-6. Thus, the multiple view region in the lateral shift arrangement is equivalent to the stereoscopic region in the parallel stereoscopic arrangement.

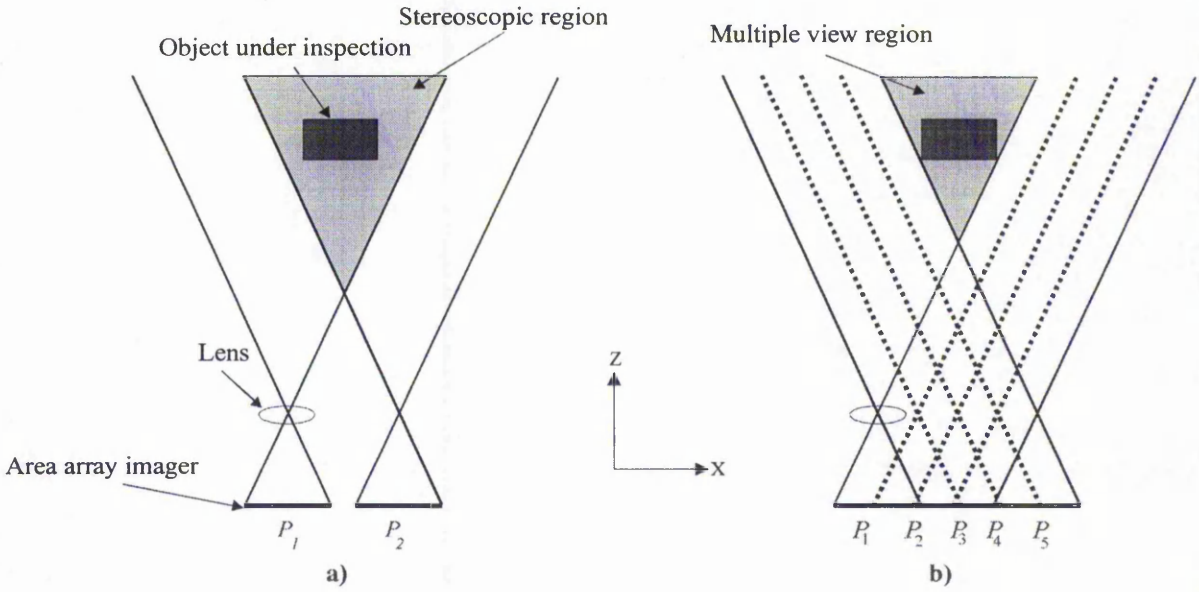

Figure 2-6 *Comparison of a) parallel stereoscopic arrangement and b) multiple view lateral shift arrangement*

2.4.3 Line-scan technique

A multiple view line-scan technique is illustrated in Figure 2-7. In this example, three slit collimated x-ray beams are incident upon three linear x-ray detector arrays. Thus three different line-scan images can be produced.

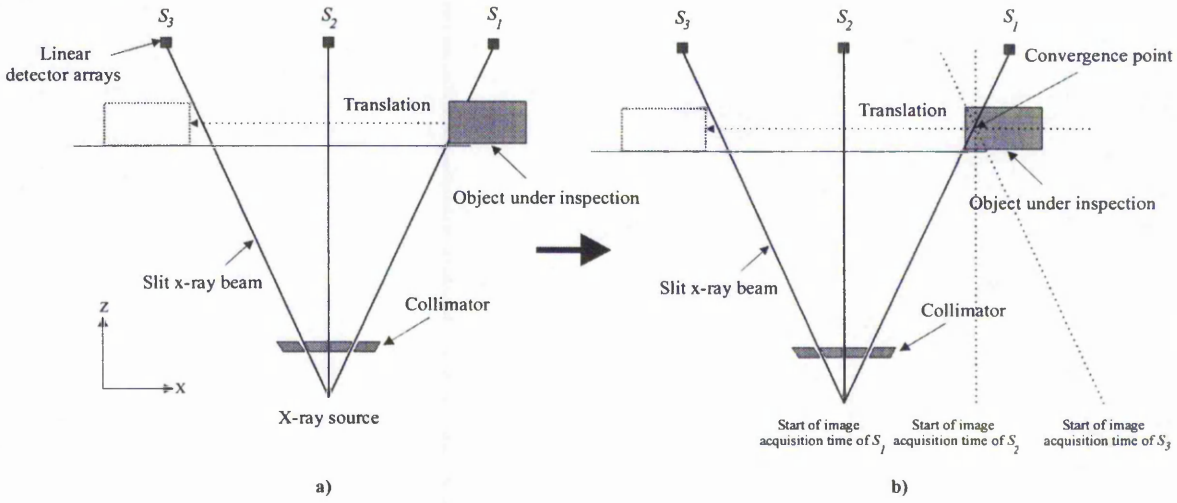

Figure 2-7 *Geometric layout of the multiple view line-scan technique using a single x-ray source a) divergent distribution and b) effective convergent distribution after image acquisition*

The object under inspection is linearly translated through the collimated x-ray beams. Thus, by cyclically storing the image information from the linear detector arrays, a line-scan image can be produced by each of the linear detector arrays. This configuration is a multiple view version of the divergent beam, single x-ray source, twin linear detector screening technique developed by

Evans [32]. It should be noted that the 'divergent' x-ray beams implemented in the physical arrangement illustrated in Figure 2-7a may be used to produce an effective 'convergent' configuration as illustrated in Figure 2-7b by introducing carefully evaluated time delays [32] between the start of image acquisition for each linear x-ray detector.

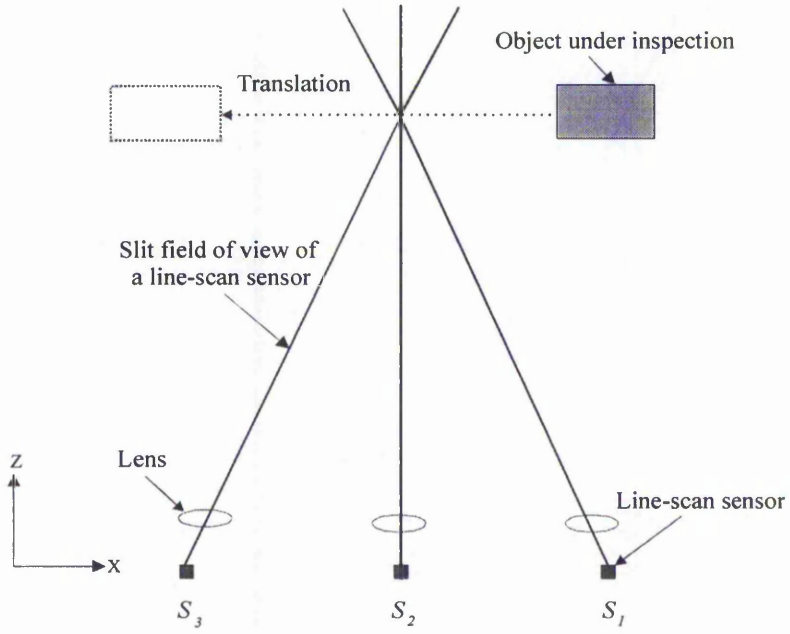

Figure 2-8 *Multiple view line-scan technique using three visible light line-scan sensors*

Therefore, the geometric properties of the perspective images produced by this multiple view x-ray imaging technique can be simulated by the convergent visible light configuration illustrated in Figure 2-8. The image collection and storage is similar to the x-ray version of the technique.

3 DESIGN PHILOSOPHY AND DECISIONS

3.1 Operational and scientific constraints

In order to increase the potential areas of application for the multiple view imaging techniques investigated in this research a number of operational and scientific constraints have been formulated. These are each discussed in detail in the following text.

a) Operational constraints:

The operational constraints have been developed in order to minimize the hardware complexity and also, to maximize the operational simplicity for on-line visual inspection applications.

i. *Single x-ray source* - A single x-ray source is highly desirable for the development of a multiple view technique for the following reasons:
    a. to facilitate the process of alignment/collimation and matching of the x-ray source and x-ray detectors;
    b. reducing the overall mechanical/electrical complexity, size, weight and cost of the imaging system.

ii. *No physical rotation* - The imaging technique must incorporate lateral movement of the object under inspection rather than a physical rotation. This is because the internal structure/arrangement of the object under inspection might be disturbed when physical rotation is introduced; thereby destroying the visual integrity of the resultant images. Additionally conveyored systems are commonly used in industrial scenarios.

iii. *Single pass* - The object under inspection is required to pass through the field of view of the x-ray sensor only once. In addition it is highly desirable to obtain many views of the object under inspection in the same time interval as that required for a single view using a given x-ray source/sensor technology.

b) Scientific constraints:

The scientific constraints have been developed in order to minimize effects which may cause visual discomfort to the human observer.

i. *High visual quality* - The perspective images must exhibit high visual quality in terms of equal contrast and brightness in order to minimize intensity flicker [81] and to enhance motion parallax and binocular stereoscopic fusion.

ii. *No geometric distortion* - There must be no geometric distortion of parallax information as this would destroy the visual integrity of the resultant images.

iii. *Smooth 'object motion' in the display* - The parallax produced in the resultant image display must exist in a format which can be directly appreciated by a human observer from a

sequence of 'raw' perspective images (i.e. no image reconstruction required). Thus apparent movement in the display must be smooth and comfortable to view.

The operational and scientific constraints presented in the preceding text are used to evaluate the suitability of the imaging techniques discussed in Section 2.4. From the results of the preliminary evaluation. The rotational technique is suitable for off-line real-time inspection, e.g. electronic assemblies inspection [6], where live images can be displayed on a monitor screen by utilizing an image intensifier together with a cone x-ray beam source. However, the rotation of an object under inspection could induce unconstrained motion to internal object structures. This would destroy the visual integrity of the resultant images. The alternative solution of rotating x-ray source/sensor arrangement is mechanically complex and not cost-effective. Also, large area sensors (e.g. planar or image intensifier) are limited in size and can be extremely expensive in comparison to linear x-ray detector arrays. Thus, the rotational technique is not a viable option for the on-line inspection applications under consideration in this work. However, the lateral shift and the line-scan techniques fulfil all the operational constraints considered. Further, the line-scan technique exhibits inherent advantages over the lateral shift technique. These include:

- the radiation dose per inspection can be reduced as a slit collimated x-ray beam is used rather than a cone beam, in turn reducing the extent and cost of radiological shielding necessary;
- image contrast is increased due to the reduction in radiation scatter; this is achieved as only a thin section of the object is irradiated at a given time in the image production process;
- linear x-ray detector arrays are generally far more versatile (i.e. they are available in modular form enabling a large field of view to be realized) and lower in cost in comparison to the area type sensors.

It should be pointed out that the line-scan techniques are not suitable for capturing live events. Thus, the object under inspection is required to have no component of movement during the image acquisition process, other than the induced relative motion. However, this is not an issue in the work discussed in this thesis. The following section examines the use of a visible light camera to simulate the multiple view x-ray imaging techniques.

3.2 Choice of the camera system for simulating an x-ray arrangement

The lateral shift technique can be implemented by using a standard area array camera as discussed in Section 2.4.2. However, a number of practical limitations arise when dedicated visible light line-scan sensors are configured in order to simulate a multiple linear x-ray detector array as described in Section 2.4.3. Figure 3-1 illustrates a configuration of three visible light line-scan sensors. The three-dimensional geometric alignment of these sensors with respect to each other and the object under inspection is critical and very difficult to achieve in practice.

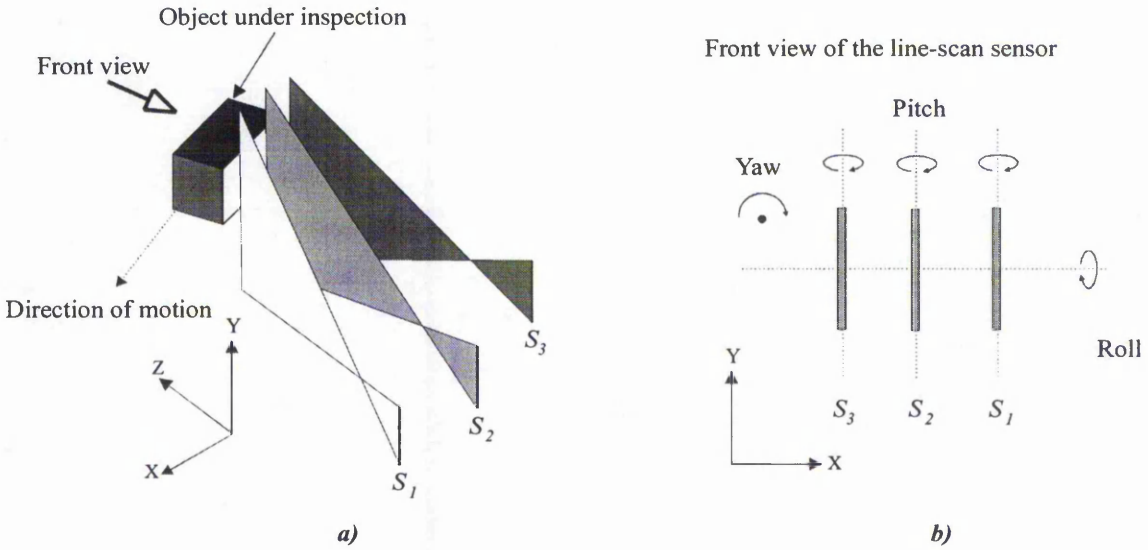

Figure 3-1 *a) Three dedicated line-scan sensors and b) relative orientation of the line-scan sensors*

The relative rotational attitude (i.e. roll, pitch and yaw) and the relative position in the x, y and z axes of each line-scan sensor requires precise setting. The system becomes particularly inflexible when the angular distribution of the line-scan sensors is required to be changed for experimental purposes. Also, the lighting conditions are difficult to set up due to the line-scan sensor being a one-dimensional device. Thus, adjustment for the brightness and contrast of the resultant image is not straightforward; a two-dimensional image has to be produced. In addition, the use of multiple sensors increases the size and the complexity of the experimental arrangement.

3.2.1 The area array line-scan concept

In this research, a Charge-Coupled Device [82, 83, 84] area array camera [85] is utilized in a novel line-scan mode, where single photosite columns are used as individual sensors, in order to produce two-dimensional line-scan images. The use of an area array camera to simulate a line-scan sensor is illustrated in Figure 3-2. This technique in itself represents new research in the field of visible light imaging and to the author's knowledge has not been reported elsewhere in the literature. The instantaneous field of view [86] produced by a photosite column on the sensor's area array is equivalent to that produced by a dedicated line-scan sensor [87, 88, 89, 90, 91, 92]. Thus the 'area array' line-scan sensor can be considered as being geometrically equivalent to a dedicated line-scan system [93]. The term dedicated line-scan sensor is used in this context to highlight the difference between a purpose built line-scan sensor and an 'area array' line-scan sensor.

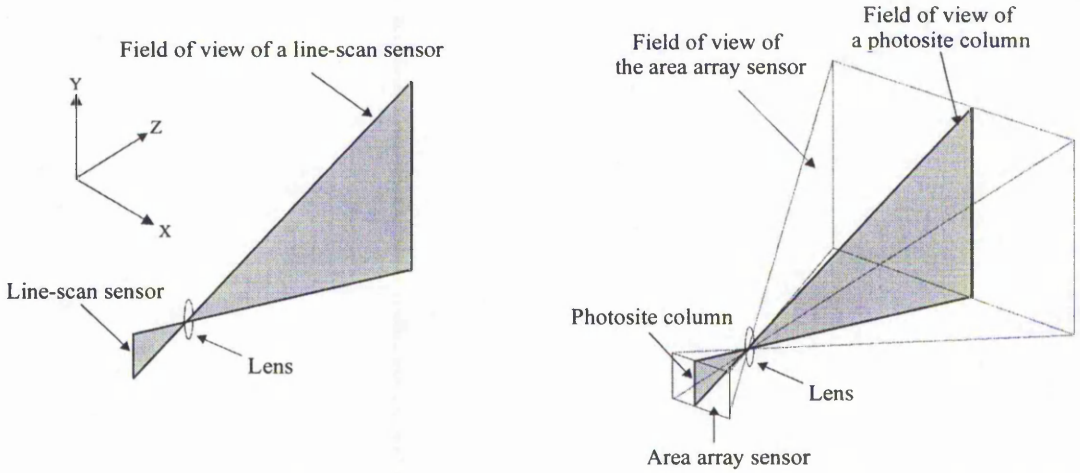

a) Dedicated line-scan camera *b) Area array camera*

Figure 3-2 *The slit field of view of a) a dedicated line-scan sensor and b) a photosite column*

In order to maximize the angular distribution of the slits fields of view, the area array imager implemented in this research is used in its normal orientation because the length of the sensor in the x-axis is longer than the length in the y-axis (i.e. 4:3 aspect ratio imager). The motion axis is defined as the x-axis with the y-axis being defined as coincident with the main axis of the photosite column.

In order to produce a two-dimensional image, the object under inspection is linearly translated through the slit field of view of the 'selected' photosite column. As the object moves, image information is built up by collecting data from the sensor (Figure 3-3).

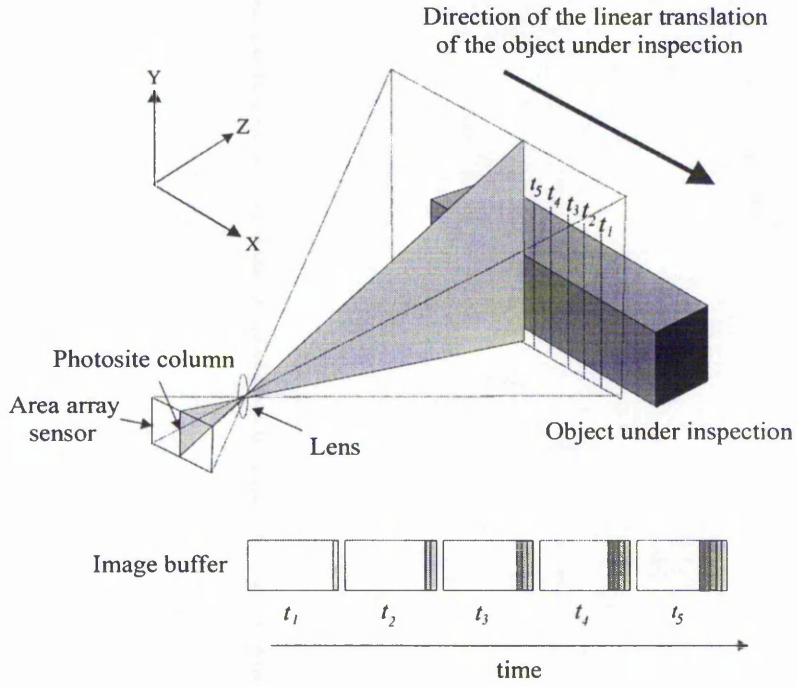

Figure 3-3 *Image capture process in a line-scan system*

Cyclic storage of this 'live' data produces a two-dimensional line-scan image. It should be noted that the same imaging mechanism can be applied to any selected column on the sensor's surface. The growth of picture information in the image buffer is also shown as a function of the line acquisition time t_1 to t_5 in the diagram of Figure 3-3. By treating an area array sensor as a contiguous set of line-scan devices, a number of photosite columns can be used, as individual sensors, to produce a large number of perspective views during a single object translation as illustrated in Figure 3-4.

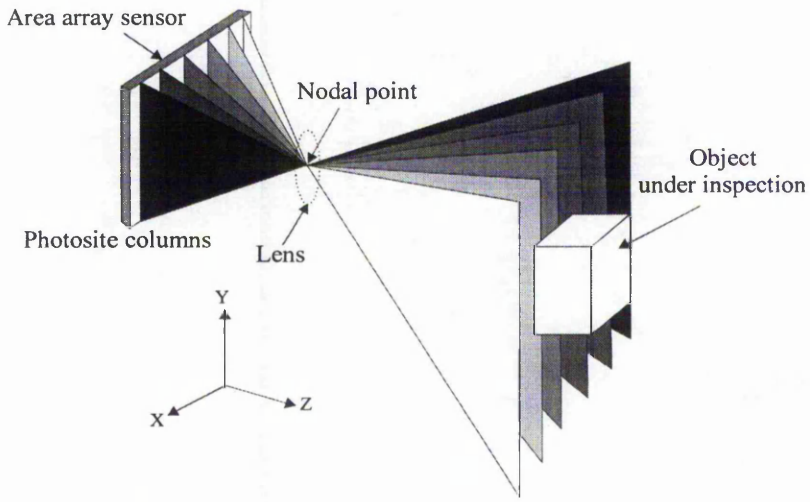

Figure 3-4 *Multiple slit fields of view produced by photosite columns on a single area array sensor*

The geometric equivalence of the visible light and x-ray techniques is illustrated in Figure 3-5. Each slit field of view produced by the area array camera, S_1 to S_6, corresponds to a collimated x-ray beam in the x-ray arrangement.

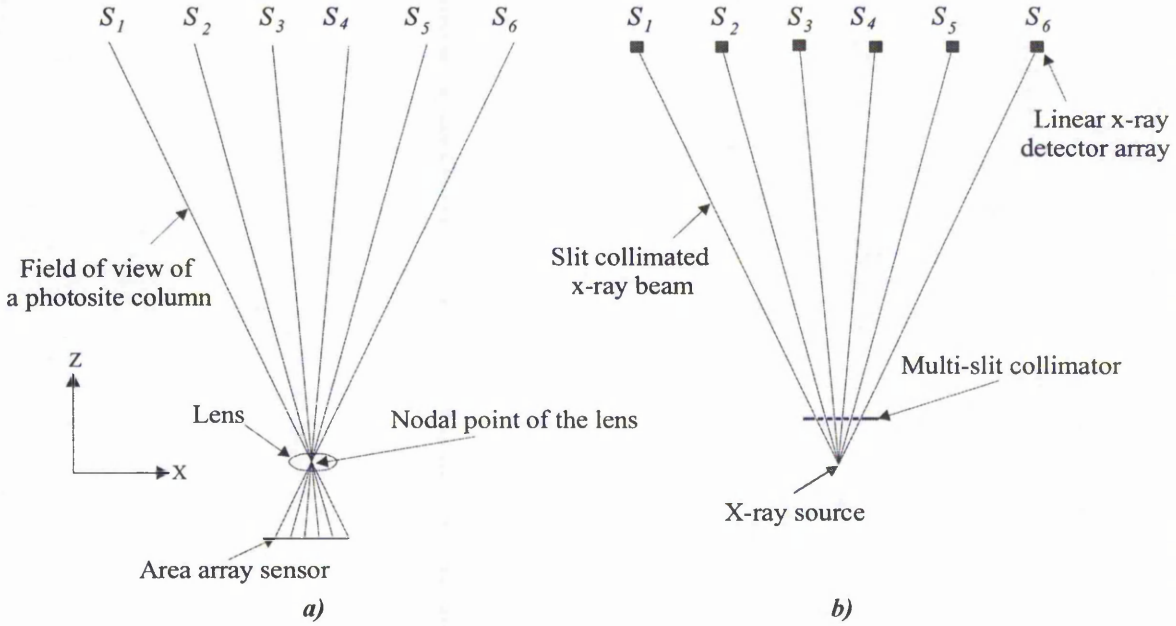

Figure 3-5 *The geometric layout of a six view line-scan arrangement for a) visible light and b) x-ray*

Thus to summarise, the advantages of this novel area array line-scan technique are:

i. The geometric alignment of the individual photosite columns is determined by the construction tolerances of the photosensitive area of the camera's imager. Thus the relative three-dimensional alignment of the sensors is extremely accurate in comparison with dedicated line-scan devices; misalignment in terms of roll, pitch and yaw of each line-scan sensor may be considered non existent as far as this work is concerned.
ii. The angular distribution of the perspective views can be electronically controlled (via software) by the simple expedient of selecting different video lines/photosite columns for the image production process. Thus, *no* mechanical reconfiguration is required.
iii. A live two-dimensional image is available for initial system configuration and set up of the lighting conditions and lens functions.

Having identified the benefits of using an area array camera, it is important to consider the potential limitations. These can be summarised as follows:

i. When a standard video format camera is used, the maximum line acquisition rate is limited by the frame rate (i.e. 25 Hz). Thus the production of a two-dimensional image in the line-scan arrangement, in general, requires a longer duration than that required by a dedicated line-scan system. However, the speed of the system can be greatly increased by using a high-frame rate camera [94, 95]. Although these considerations are not a limiting factor in the work presented here.
ii. The potential angular distribution of the slit fields of view using an area array sensor in a 'line-scan' mode is limited by the focal length of the camera lens. Thus much greater angular separation between successive views can be produced by dedicated line-scan sensors although this is not a limiting factor in this work.
iii. The total number of photosite columns that comprise the array sensor being utilized limits the potential number of views available (typical number is 512). However, this is not a limiting factor in this work. Indeed, a maximum of sixteen views/photosite columns are used in this research.

The following section discusses the geometrical properties of modelling the multiple view x-ray system using an area array camera employing the line-scan principle.

3.2.2 X-axis evaluation

This section discusses the geometrical aspects and image formation using an area array line-scan sensor format. It should be emphasized that the derivations of the formulae developed are based on *perfect* ray geometry. Factors such as the finite width of the photosite columns and lens distortions [96, 97, 98] are not analysed. In the following discussion, the term line-scan sensor refers to

the 'selected' photosite column. The motion axis field of view (X_{FOV}) in this context is defined as the accumulated slit fields of view obtained during a relative translation with respect to the object under inspection. It should be noted that the motion axis field of view has the same magnitude as the inspection length in object space (I_x). The motion axis field of view is determined by the translation speed, line acquisition time and the number of scan lines chosen to produce a two-dimensional image; theoretically, the number of scan lines can tend to infinity, however in practice this is limited by the amount of digital memory available to store the information. Also, it should be noted that the term line acquisition time is used for the time required to acquire information for each scan line. The x-axis magnification from object space to image space exhibited by each perspective image to first order is constant in the motion axis and independent of the object range (z-axis). In other words, the x-axis field of view is nominally parallel or orthographic. This is due to the parallel nature of the field of view of the photosite column or the line-scan sensor. The operational details are discussed in Section 5.5.1. The geometric analysis of x-ray line-scan system and an 'area array' line-scan arrangement in the x-axis is depicted in Figure 3-6.

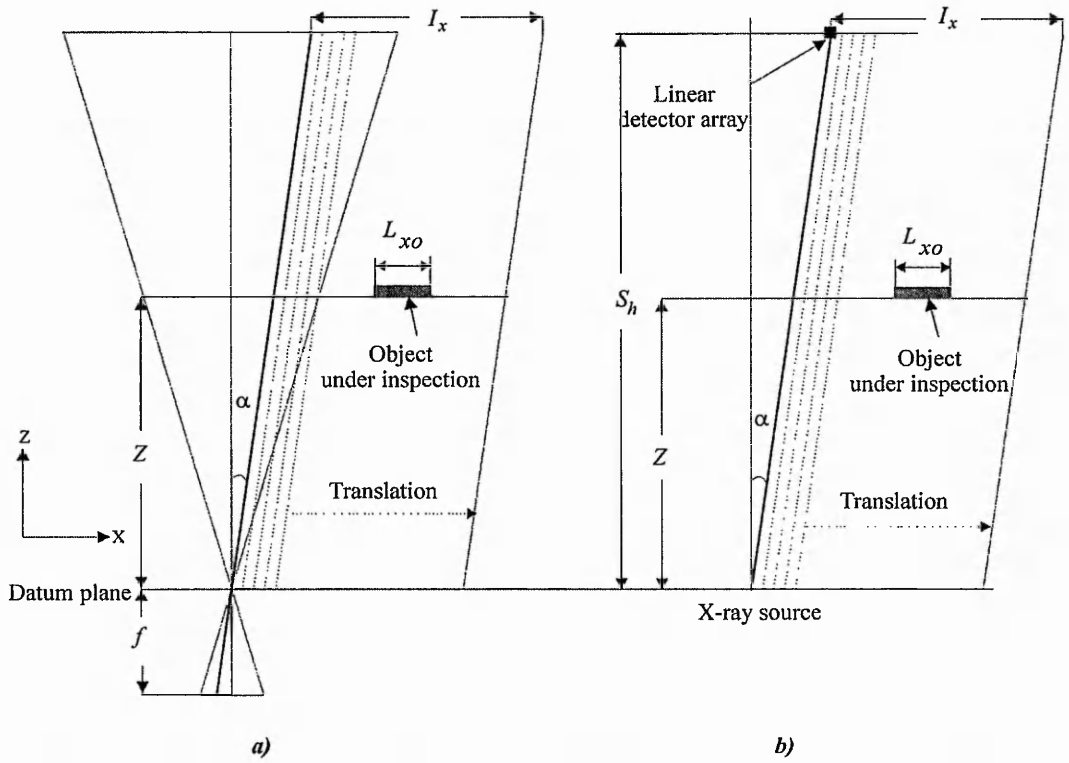

Figure 3-6 *Geometric layout of the x-axis field of view for a) visible light arrangement and b) x-ray arrangement*

The motion axis field of view in the line-scan arrangement for the visible light and the x-ray arrangements can be expressed as:

$$X_{FOV} = S\,t\,N_x \qquad \ldots(3\text{-}1)$$

where,

S = translation speed;

t = line acquisition time;

N_x = number of pixel columns required for a single perspective view.

The perspective angle α for a slit field of view is illustrated in Figure 3-6. It should be noted that in this work the perspective angle is the angle inclined by the field of view of a 'selected' photosite column with respect to the main optical axis of the area array sensor. For the x-ray arrangement, the perspective angle is the angle subtended by the linear detector arrays with respect to the normal of the image sensor plane. The magnification factor M_{ls} from object space to the display in the motion axis can be expressed as a ratio of the display length in the x-axis to the inspection length in object space. The line-scan magnification and the object size in the x-axis in image space L_{xi} are expressed by:

$$M_{ls} = \frac{D_x}{S\,t\,\mathrm{N}_x} \qquad \ldots(3\text{-}2) \qquad\qquad L_{xi} = \frac{D_x\,L_{xo}}{S\,t\,\mathrm{N}_x} \qquad \ldots(3\text{-}3)$$

The potential spatial resolution [99] in the motion axis is dependent upon the translation speed and the line acquisition time. Assuming that the relative translation speed between the sensor and the object remains constant and the image consists of a predetermined number of lines, decreasing the line acquisition time results in less time required for the production of a two-dimensional image. This reduces the inspection length in object space during which the sensor produces image information thus reducing the motion axis field of view. A similar effect is produced when the line acquisition time is kept constant but the translation speed is decreased. Thus the reduced inspection length results in a reduction in the motion axis field of view and an increase in the potential spatial resolution accordingly.

3.2.3 Y-axis evaluation

The field of view in the y-axis is identical to that encountered by utilizing 'standard' area array imaging techniques, that is, image information from a single column of photosites is registered as a vertical column of pixel data in the video display. Thus the slit field of view produced by a photosite column is identical to that produced by 'normal' operation of the area array sensor. The analogy between visible light and x-ray arrangements is illustrated in Figure 2-2 on page 10. The field of view in the y-axis for the visible light and x-ray arrangements are expressed as:

Visible light: $Y_{FOV} = \frac{Z\,L_{ys}}{f}$ ...(3-4) X-ray: Y_{FOV} $\frac{Z\,L_{ys}}{S_h}$

i) magnification from the object space to the sensor plane, M_{os};

Visible light: $M_{os} = \frac{f}{Z}$ ...(3-6) X-ray: $M_{os} = \frac{S_h}{Z}$ ...(3-7)

ii) magnification from the sensor plane to the display, M_{sd}, this magnification is the same for both axes and a common formula is as follows:

$$M_{sd} = \frac{D_y}{L_{ys}} = \frac{D_x}{L_{xs}} \quad ...(3\text{-}8)$$

where D_x and D_y are the dimensions of the display in the x and y axes respectively.

Hence, the object's size in the y-axis L_{yo} in object space is represented by L_{yi} in the display and can be expressed as:

Visible light: $L_{yi} = \frac{L_{yo}\, f\, D_y}{Z\, L_{ys}}$ ...(3-9) X-ray: $L_{yi} = \frac{L_{yo}\, S_h\, D_y}{Z\, L_{ys}}$ ...(3-10)

Therefore, the magnification from object space to image space in each imaging axis is independent of each other and produces an *affine* resultant image. Thus to achieve a 1:1 image aspect ratio at a given range Z the following conditions must be satisfied:

Visible light: $\frac{D_x}{S\, t\, \mathrm{N}_x} = \frac{f\, D_y}{Z\, L_{ys}}$ ...(3-11) X-ray: $\frac{D_x}{S\, t\, \mathrm{N}_x} = \frac{S_h\, D_y}{Z\, L_{ys}}$ ...(3-12)

In order to design the x-ray source/sensor geometry requires that an evaluation of the visual aspects of the proposed technique be theoretically determined. This is addressed in the following chapter.

4 THEORETICAL ANALYSIS OF MULTIPLE VIEW IMAGING

4.1 Introduction

This chapter presents a theoretical analysis of the line-scan multiple view imaging technique and the lateral shift multiple view imaging technique. The analysis is divided into the following areas:

I. Registration of the perspective views in the z-axis in object space; this determines the position of the multiple view region in object space.
II. The production of parallax; this evaluates parallax as a function of the successive perspective views which form the multiple view region.
III. The multiple view region and the binocular stereoscopic depth of field; this determines the geometric relationship between the multiple view region in object space and the binocular stereoscopic depth of field.
IV. The minimum detectable range increment in object space; this discusses the minimum range increment in the z-axis and the stereoscopic zoom in the z-axis.
V. Motion parallax as a function of the spatial sampling pattern in the z-axis; this evaluates the spatial sampling patterns produced by the overlapping perspective views. Also, the effect of the repositioning of the fixation plane in the display on the sampling pattern in object space is examined.

Discussions with respect to the multiple view line-scan technique and the multiple view lateral shift technique are presented in the following sections.

4.2 Line-scan technique

4.2.1 Registration of the perspective views

Figure 4-1 depicts a multiple view arrangement where six photosite columns on the sensor's surface are used as individual line-scan sensors; the slit fields of view produced by these line-scan sensors are denoted by S_1 *to* S_6. The region in object space formed by the overlapping accumulated slit fields of view for each photosite column is termed the multiple view region. If the start of image acquisition for each line-scan sensor in the multiple view arrangement is simultaneous then the position of the convergence plane in object space is fixed by the nodal point of the camera lens. Therefore, only half of the potential multiple view region can be used as illustrated in Figure 4-1a. It should be noted that the distance travelled between the first and last scan lines, e.g. S_6 *to* S_6', for each line-scan sensor is equal. In a divergent arrangement, the convergence plane can be repositioned in object space by the simple expedient of introducing an offset distance, $\Delta d_{1\leftrightarrow 2}$ to $\Delta d_{1\leftrightarrow 6}$, for the start of image acquisition for each of the line-scan sensors (adopting the notation of Δd to signify an offset distance and the symbol $\leftrightarrow$ to indicate 'between' views, for example $1\leftrightarrow n$

= view *1* and view *n*). These offset distances are defined with respect to the reference line-scan sensor, in this case S_1, as depicted in Figure 4-1b. The offset distance can be achieved by introducing a set of time delays, $\Delta t_{1\leftrightarrow 2}$ to $\Delta t_{1\leftrightarrow 6}$, into the start of image acquisition for each sensor. The extent of the multiple view region in the x and z axes is independent of the range of this region. To produce a convergence plane at a specific range in object space, an equation which describes the time delay is required.

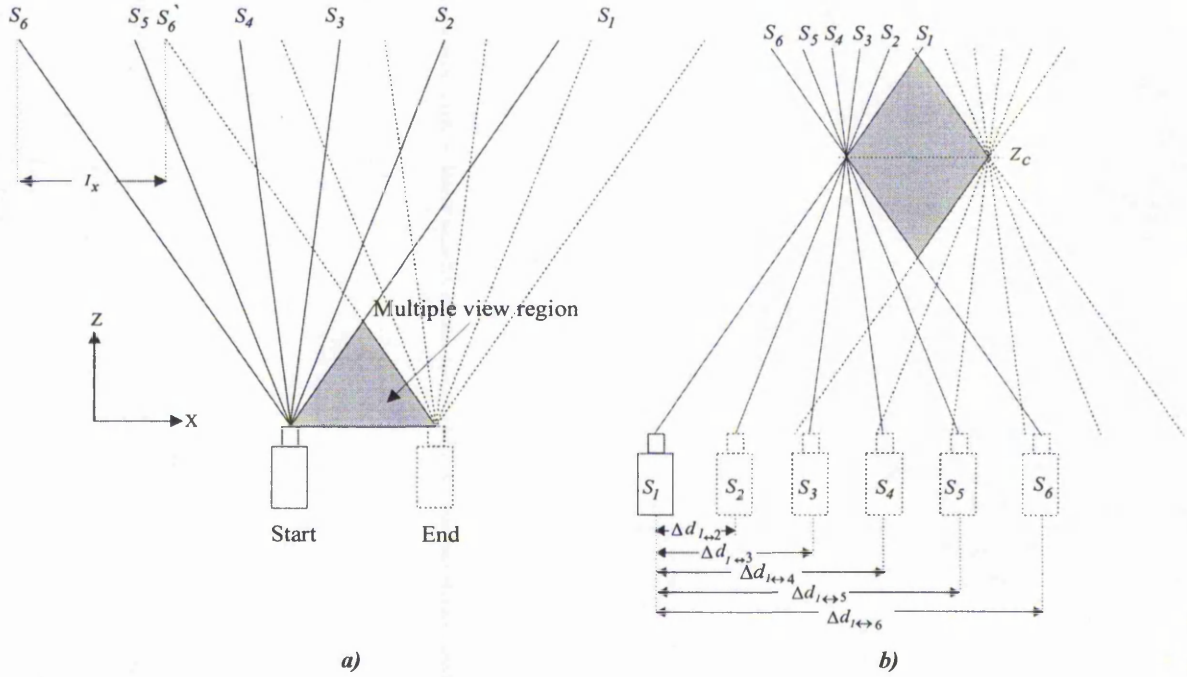

Figure 4-1 *The production of a multiple view region in object space by a single area array camera a) without time delay introduction and b) with time delay introduction*

Figure 4-2 illustrates the geometric layout of the visible light and the x-ray arrangement for time delay analysis. In order to effect an apparent intersection point between the reference view S_1 and the perspective view S_n at a range Z_c an offset distance $\Delta d_{1\leftrightarrow n}$ *is* introduced to view S_n with respect to view S_1. The position of view S_n after introducing an offset distance is denoted by S_n'.

The offset distance required for perspective view S_n to effect a convergence at a range of Z_c is determined by the general equation below:

$$\Delta d_{1\leftrightarrow n} = Z_c \left|\tan\beta - \tan(\pm\alpha_n)\right| \qquad ...(4\text{-}1)$$

where,

α = angle inclined by the perspective view *n* with reference to the main optical axis of the camera lens;

β = angle inclined by the reference view with respect to the main optical axis of the camera lens;

$\Delta d_{1\leftrightarrow n}$ = offset distance between the reference view and the perspective view *n*.

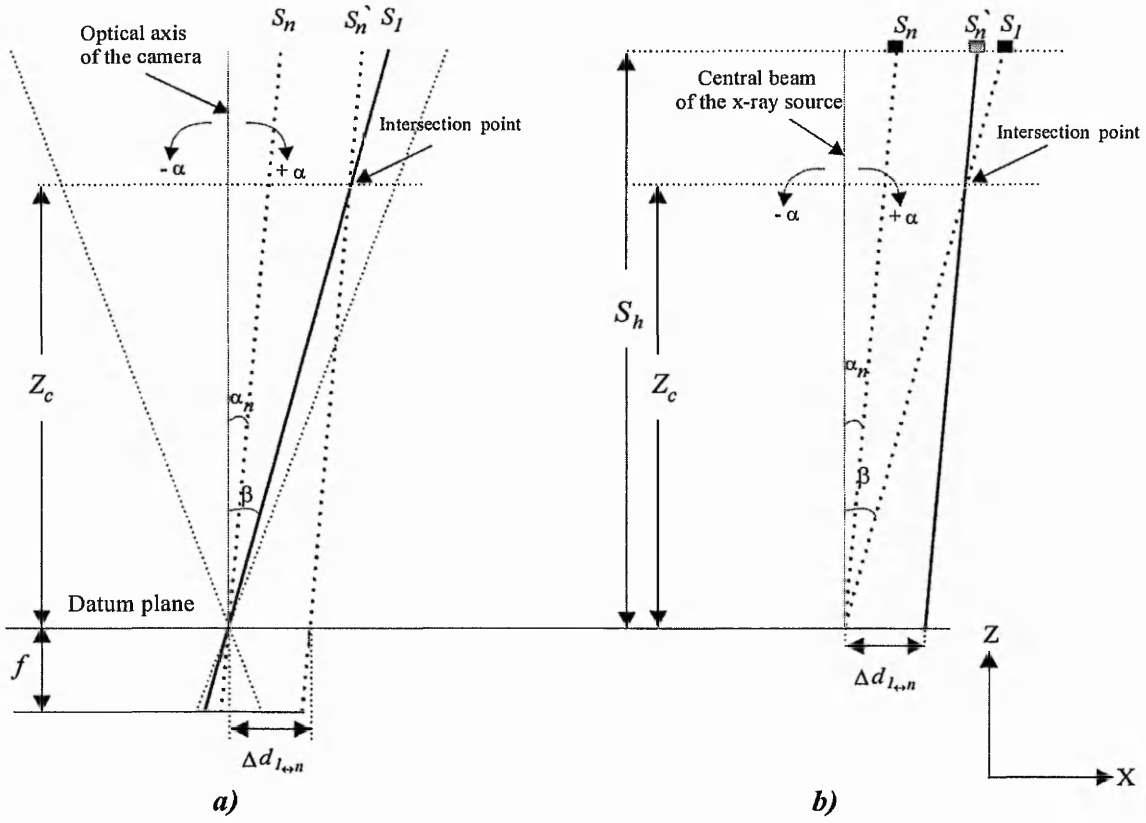

Figure 4-2 *Time delay determination for a) visible light arrangement and b) x-ray arrangement*

The time delay required to produce the offset distance in order to effect a convergence plane at range Z_c is given by:

$$\Delta t_{1\leftrightarrow n} = \frac{Z_c \left|\tan\beta - \tan(\pm\alpha_n)\right|}{S} \qquad \ldots(4\text{-}2)$$

where S is the translation speed and $\Delta t_{1\leftrightarrow n}$ is the offset time delay for view n with respect to the start of image acquisition of the reference view.

The offset distance $\Delta d_{1\leftrightarrow n}$ can be produced by introducing a time delay $\Delta t_{1\leftrightarrow n}$ into the start of image acquisition for the perspective view S_n. As the visible light and x-ray arrangement are geometrically equivalent, from this point onwards, the geometric diagrams are drawn with respect to the datum plane and are common to both visible light and x-ray arrangements. The timing diagrams in Figure 4-3 illustrate the phase relationship between the time delays. For perspective views S_2 to S_6, the time delays required to effect a convergence at a range Z_c are depicted by $\Delta t_{1\leftrightarrow 2}$ to $\Delta t_{1\leftrightarrow 6}$ respectively. It should be noted that the total scan time for each line-scan sensor is equal and the start of image acquisition of the perspective view S_1 is used as a reference for the time delay determination.

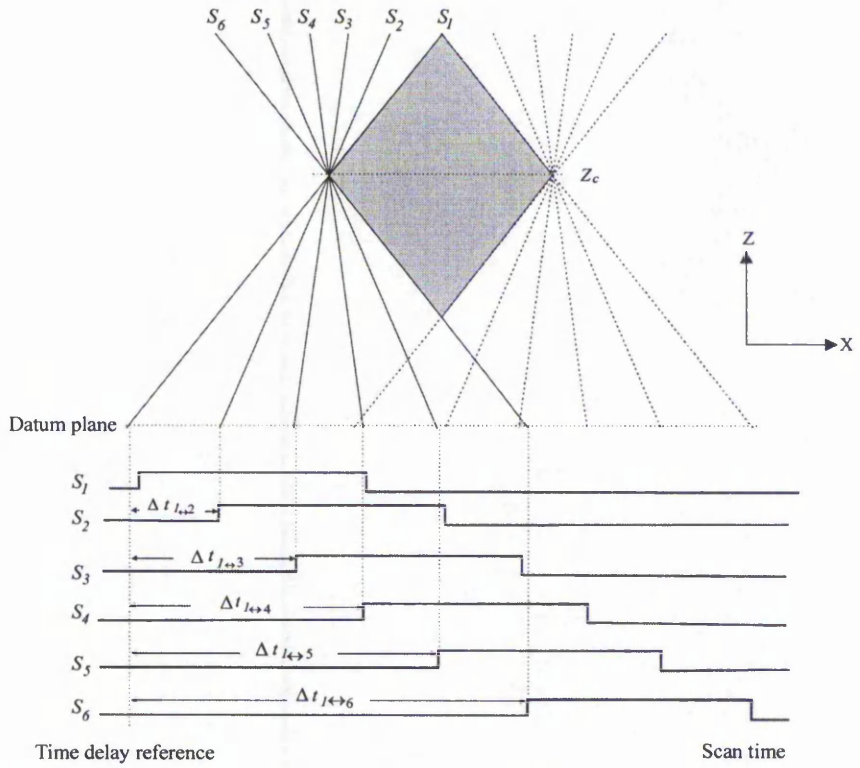

Figure 4-3 *Timing diagrams illustrating the time delays and the total scanning time*

4.2.2 The production of parallax

Figure 4-4 depicts the position of a point *M* in object space which is represented by a voxel location [100]. It should be noted that the term voxel used in this context represents two situations (refer to *Valyus* and *Rock* in Section 2.3b). These are:

- for a monoscopic image sequence – the overlapping region produced by two successive views results in motion parallax (sequential parallax);
- for a stereoscopic image sequence – the overlapping region produced by 'simultaneous' views results in binocular parallax (synchronous parallax).

The general parallax equation in the sensor plane with respect to the datum plane is given by:

$$P_{s(n-1)\leftrightarrow n} = Z\left|\tan(\pm\alpha_{n-1}) - \tan(\pm\alpha_n)\right| \qquad ...(4\text{-}3)$$

In this case β is the perspective angle of the reference view, thus,

$$P_{s1\leftrightarrow n} = Z\left|\tan\beta - \tan(\pm\alpha_n)\right| \qquad ...(4\text{-}4)$$

It should be noted that the reference plane for parallax as indicated in *Equation 4-3* is fixed at the datum plane. After the introduction of the time delay, the reference plane is shifted to a range Z_c and the parallax value for an object point is determined with respect to this convergence plane.

Therefore, by subtracting the parallax value produced at the offset distance $\Delta d_{1\leftrightarrow n}$, from the original parallax the relative parallax can be determined:

$$P_{rs1\leftrightarrow n} = Z\left|\tan\beta - \tan(\pm\alpha_n)\right| - \Delta d_{1\leftrightarrow n} \qquad ...(4\text{-}5)$$

The term 'relative parallax', is defined in the context in this work as the parallax produced with respect to the convergence plane. This can also be expressed as a function of the convergence plane:

$$P_{rs1\leftrightarrow n} = (Z - Z_c)\left|\tan\beta - \tan(\pm\alpha_n)\right| \qquad ...(4\text{-}6)$$

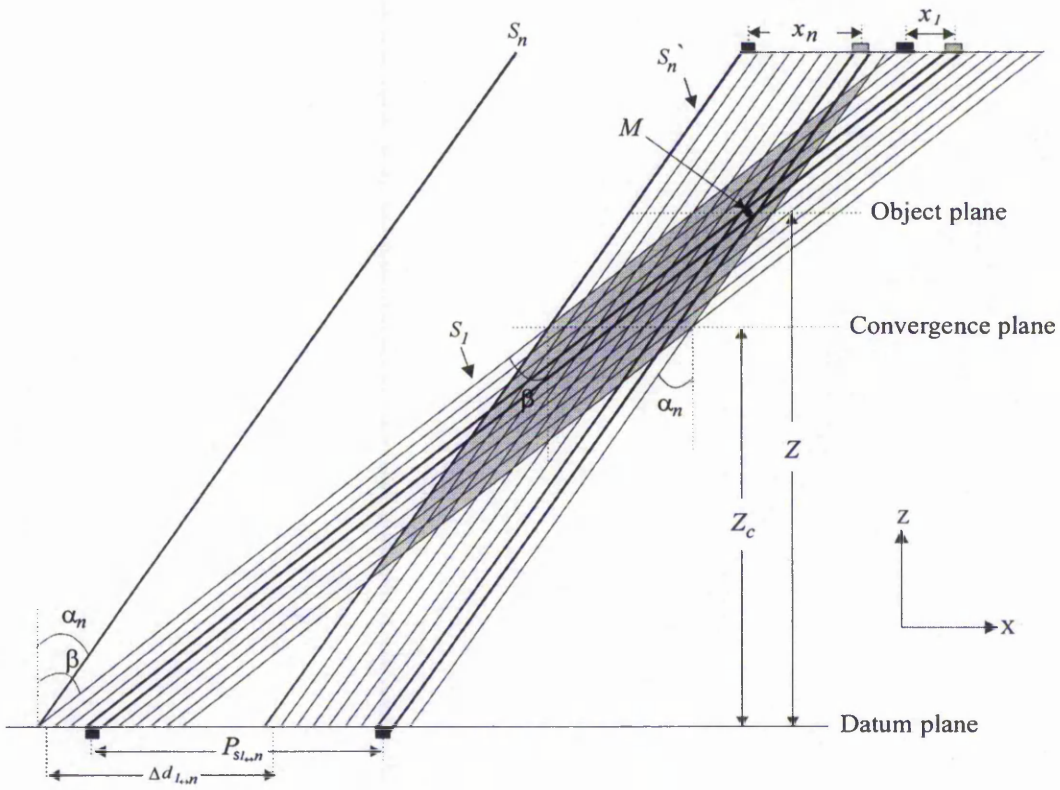

Figure 4-4 *Parallax determination in the line-scan arrangement*

Parallax information can also be obtained by determining the difference between the x-coordinates in two successive images and can be expressed by:

$$P_{rs1\leftrightarrow n} = P_{s1\leftrightarrow n} - \Delta d_{1\leftrightarrow n} = x_n - x_1 \qquad ...(4\text{-}7)$$

where x_1 and x_n are the x-coordinate values for the corresponding points in the reference view and the perspective view n.

4.2.3 The multiple view region and the binocular stereoscopic depth of field

In order to preserve the human observer's fusion of a binocular stereoscopic image sequence requires that the maximum displacement between successive conjugate features on the screen must

not exceed a maximum permissible parallax $P_{d(max)}$ [38, 101, 102]. The magnitude of this displacement on the monitor screen $P_{d(max)}$ is linearly related to the displacement on the sensor plane $P_{s(max)}$ and can be expressed as:

$$P_{s(\max)} = \frac{P_{d(\max)}}{M_{ls}} \qquad ...(4\text{-}8)$$

where M_{ls} is the line-scan magnification factor.

The concept of a maximum permissible parallax $P_{s(max)}$ can be used to estimate the two limiting values of ranges Z_{near} and Z_{far} in order to determine the extent of the binocular stereoscopic depth of field. The multiple view region is therefore truncated by Z_{far} and Z_{near} as illustrated in Figure 4-5.

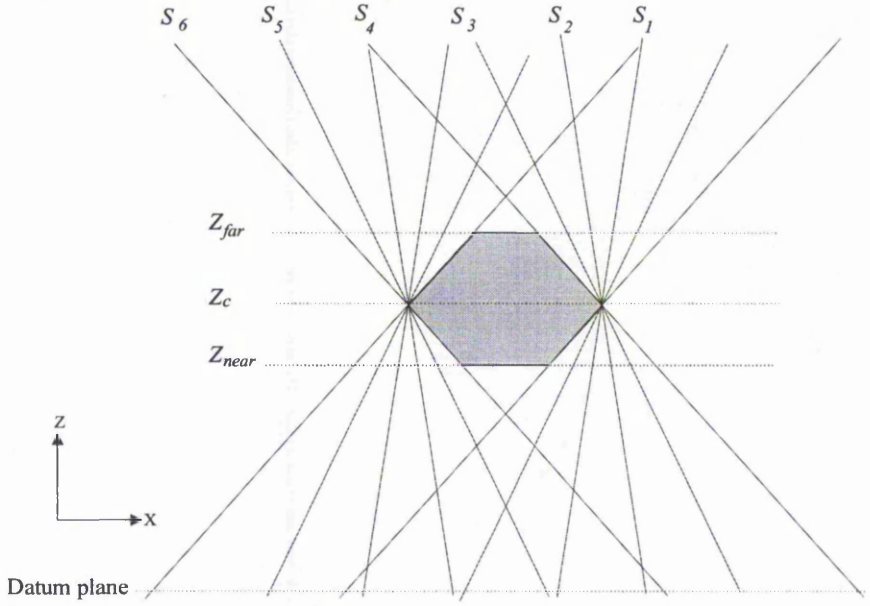

Figure 4-5 *Binocular stereoscopic depth of field truncating the multiple view region*

The relative position of Z_{near} and Z_{far} with respect to the convergence plane Z_c in the multiple view region is given by:

$$Z_{near} = Z_c - \frac{P_{s(\max)}}{|\tan(\pm\alpha_{n-1}) - \tan(\pm\alpha_n)|} \qquad Z_{far} = Z_c + \frac{P_{s(\max)}}{|\tan(\pm\alpha_{n-1}) - \tan(\pm\alpha_n)|}$$

where,

Z_{far} = range to the far limit of the binocular stereoscopic depth of field;

Z_{near} = range to the near limit of the binocular stereoscopic depth of field.

The depth of field for two successive views is expressed by:

$$\Delta Z = \frac{2P_{s(\max)}}{|\tan(\pm\alpha_{n-1}) - \tan(\pm\alpha_n)|} \qquad ...(4\text{-}9)$$

where ΔZ is the binocular stereoscopic depth of field of the multiple view region.

The region of object space bounded by these values represents an area of permissible binocular stereoscopic fusion. The three-dimensional distribution of the 'truncated' multiple view region in object space is depicted in Figure 4-6.

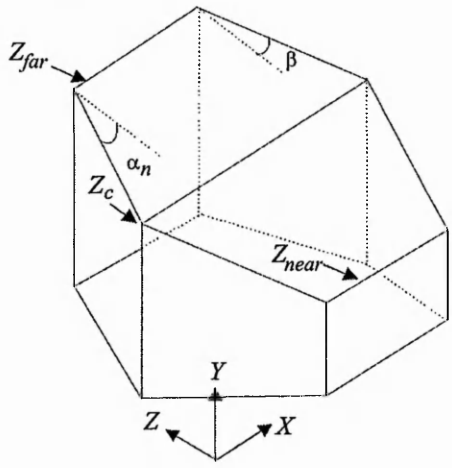

Figure 4-6 *Binocular stereoscopic multiple view region in object space*

4.2.4 Minimum detectable range increment in object space

The minimum detectable increment δZ in the z-axis in object space indicates the potential spatial resolution in the z-axis for a given arrangement. The concept of δZ is important in this discussion as it enables a relationship between corresponding pixels in the display and range in object space to be established. For instance, if the magnitude of the δZ is reduced the depth plane density for a given region will be increased and this in turn would increase the extent of apparent motion in the display of a given image sequence. In the case of a binocular stereoscopic display, the perceived depth in the display increases with depth plane density. The minimum range increment can be obtained by differentiating the formulae for parallax (*Equation 4-3*) in the sensor plane. Thus for both visible light and x-ray arrangements the minimum detectable increment in the range axis is:

$$\delta Z = \frac{\delta P}{\left|\tan(\pm\alpha_{n-1}) - \tan(\pm\alpha_n)\right|} \qquad ...(4\text{-}10)$$

where

δP = minimum detectable parallax in the sensor plane;

δZ = minimum detectable increment in the z-axis in object space.

The quantity δP may be interpreted as the smallest resolvable increment in the parallax in the sensor plane. With reference to *Equation 4-10*, the minimum range increment is independent of object range which implies that this technique produces a constant spatial resolution in the z-axis. Therefore resolution can be increased by increasing the angle inclined by two perspective views (i.e. convergence angle). Figure 4-7a illustrates the sampling pattern for a 3-view arrangement, the convergence plane is set at Z_c and the entire multiple view region is formed from voxels.

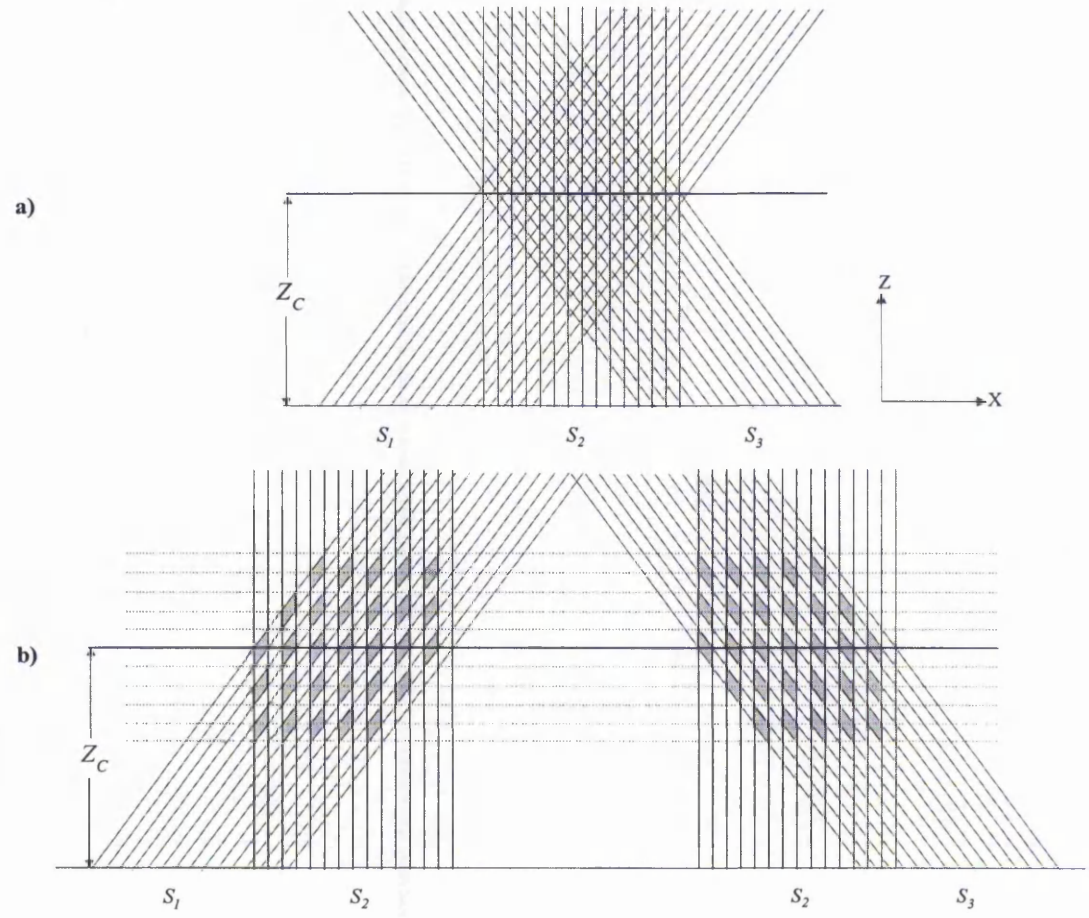

Figure 4-7 *Multiple view region produced by a) a 3-view line-scan system and b) two possible image pairs produced by three successive views (i.e. ignoring the S_1-S_3 view)*

This multiple view region is considered to be split into two successive image pairs, i.e. image pairs S_1-S_2 and S_2-S_3, as illustrated by Figure 4-7b in order to aid the following discussion. The z-axis dimensions of the voxels, in both image pairs, are identical thus indicating the spatial resolution remains unchanged when the perspective view is changed. However, it can now be appreciated that the voxel structures undergo a lateral shift about the convergence plane. This results in the perception of a change in viewing position/motion in the resultant display.

'Zoom' in the z-axis

The production of a number of perspective images enables a zoom in the z-axis to be realized. However, it should be noted that the z-axis zoom discussed here is different from that of the 'conventional stereoscopic' zoom [77]. In that the zoom function is isolated to the z-axis and the x and y axes do not undergo a change in magnification. Two possible combinations of perspective views in object space are illustrated in Figure 4-8. The arrangement is said to be zoomed when the transition of the stereoscopic image pair S_1-S_2 to S_1-S_3 occurs.

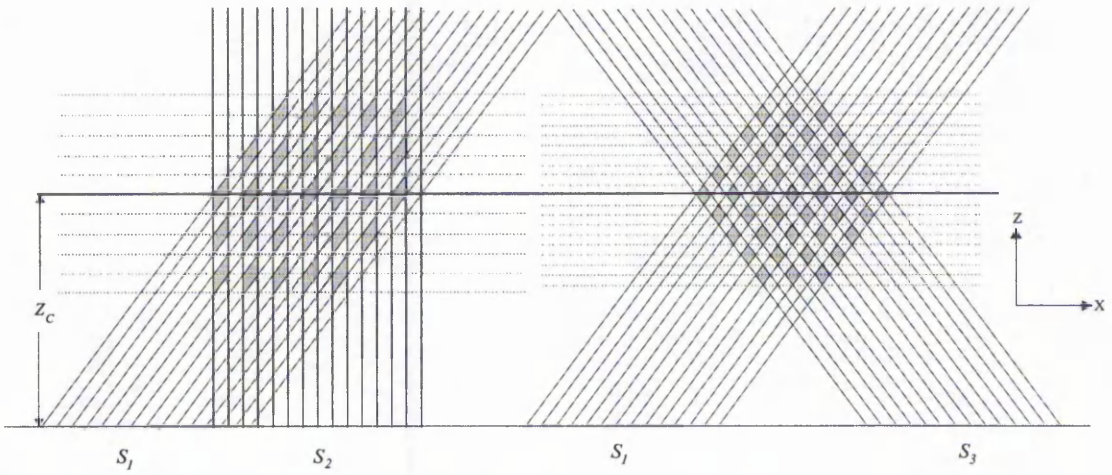

Figure 4-8 *Spatial sampling pattern for the z-axis zoom in the line-scan arrangement*

The zoom function is possible as the parallax is increased when the convergence angle is increased. It can be appreciated from Figure 4-8 that the voxel/depth plane density increases with increasing convergence angle. This consequencely increases the perceived depth in the display [103]. However, the z-axis zoom is limited by the maximum permissible parallax tolerated by binocular stereoscopic fusion for a human observer as determined by *Equation 4-8*.

4.2.5 Motion parallax distribution

As mentioned in Section 2.3, when the resultant images are displayed in a correct sequence, the object image in the display appears to move about a fixation *point*. In the line-scan arrangement the display of the sequential images produce apparent motion about a fixation *plane*. This is a result of the perspective views being produced by relative translation rather than relative rotation. Further, it should be noted that the object movement in the display is *not* the result of the movement introduced during the image acquisition, instead, it is produced by the production of parallax by virtue of the angular distribution of the slits fields of view. Thus, the illusion of rotation is due to the object image undergoing an apparent angular displacement during the production of the perspective images. This is illustrated in the following diagram of Figure 4-9a. The sampling of object space in the z-axis is a function of the angular relationship between the successive perspective views. In this example, the convergence plane is set at range Z_c from the datum plane. The relative change in perspective information can be represented by rearranging the fields of view to be perpendicular to the datum plane as illustrated in Figure 4-9b. These diagrams create an equivalent 'top view' of the object under inspection. The portion of the object under inspection nearer to the datum plane is depicted as being dark grey whilst the light grey portion is further away. The portion of the object that appears in the display is different in the visible light and x-ray cases because the respective sensors are physically on the opposite side of the datum plane. The relative changes in position of these object features as a function of range produces the apparent motion or motion parallax in the resultant display.

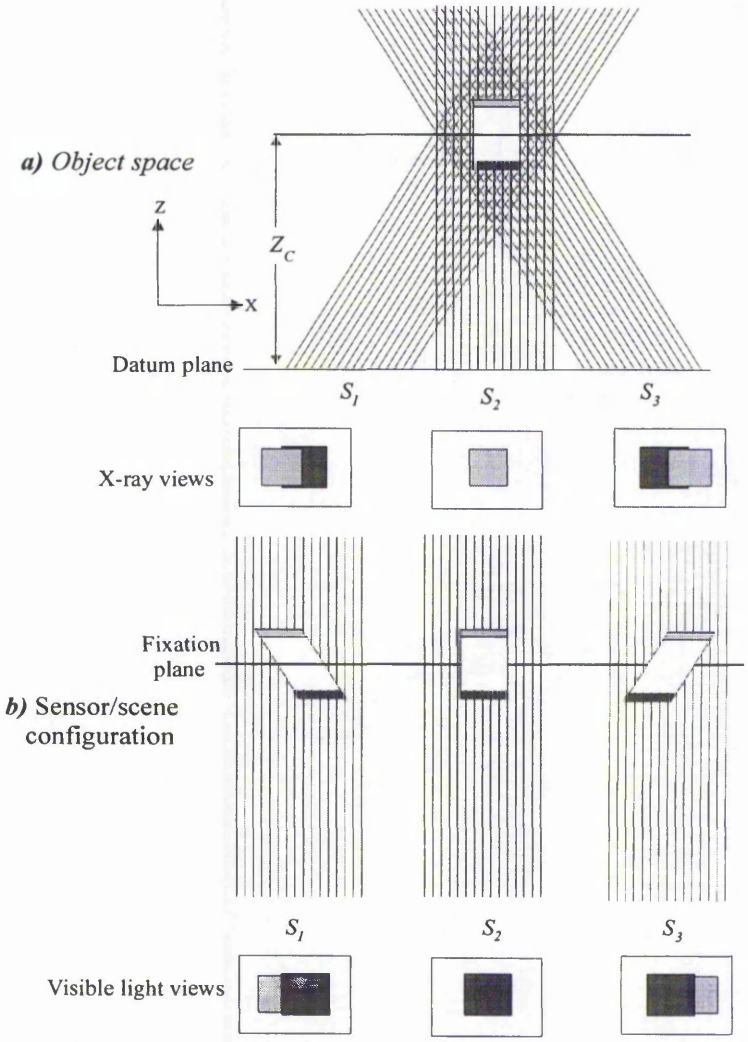

Figure 4-9 *Spatial sampling pattern in a 3-view line-scan technique a) object space and b) sensor/scene configuration*

The fixation plane in the display can be repositioned by re-registering the perspective images with respect to the reference image. This can be achieved by applying a horizontal pixel shift to each of the perspective images. The effect of repositioning the fixation plane in the display changes the convergence plane in object space. With reference to *Equation 4-6*, the convergence plane during the image acquisition is given by:

$$Z_c = Z - \frac{\pm P_s S t}{|\tan\beta - \tan(\pm\alpha_n)|} \qquad ...(4\text{-}11)$$

Thus the position of z-axis is a function of the horizontal pixel shift introduced into the perspective images. The difference between the original convergence plane and the new convergence plane is given by the following equation.

$$Z_{c(diff)} = Z_c' - Z_c = \frac{N_p}{|\tan\beta - \tan(\pm\alpha_n)|}$$

where N_p is the number of pixel columns in the display.

It is noted that the difference between the original and new convergence plane in the z-axis $Z_{c(diff)}$ is linearly related to the number of pixel column shifts. In other words, the minimum detectable depth increment δZ in the line-scan arrangement is independent of object range and produces a linear change in $Z_{c(diff)}$.

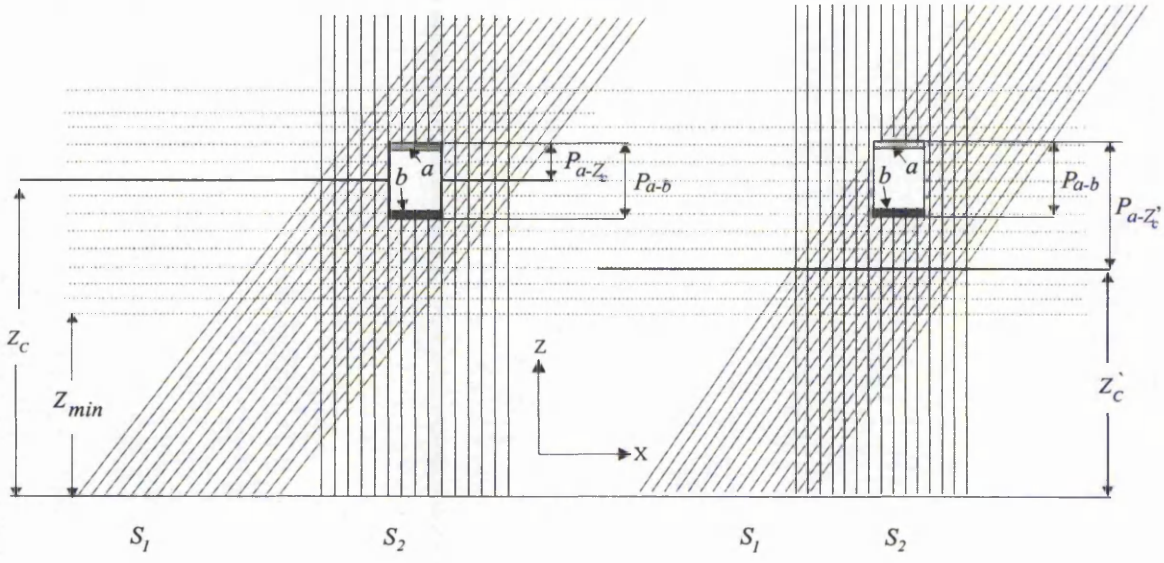

a) *b)*

Figure 4-10 *Sampling pattern of an object under inspection when the fixation plane is changed*

Figure 4-10 illustrates two possible positions of the convergence plane in object space, when the convergence plane in object space is changed (from Figure 4-10a to Figure 4-10b) the relative parallax of an object point (i.e. point *a* with respect to the convergence plane ($P_{a\text{-}Zc}$)) is changed. However, the relative parallax between two object points ($P_{a\text{-}b}$) remains unchanged.

4.3 Lateral shift technique

4.3.1 Registration of the perspective views

Figure 4-11 illustrates the multiple view region formed by the overlapping fields of view for two different sets of base separations, d_{o1} and d_{o2}. The relative positions of the perspective views are denoted by S_1 to S_6. Thus it can be appreciated from Figure 4-11 that the multiple view region (shaded area) is a function of the base separation between two successive views. Thus there is a limit for the *nearest usable range* Z_{min}. This range is a function of the angle θ subtended by the sensor's field of view and the base separation between the two outermost views (e.g. S_1 and S_6 in this example). This minimum usable range can be expressed by:

$$Z_{\min} = \frac{(N-1)d_o}{2\tan\left(\frac{\theta}{2}\right)} \qquad \ldots(4\text{-}12)$$

where θ is the angle subtended by the sensors field of view in the x-axis and N is the number of views under consideration.

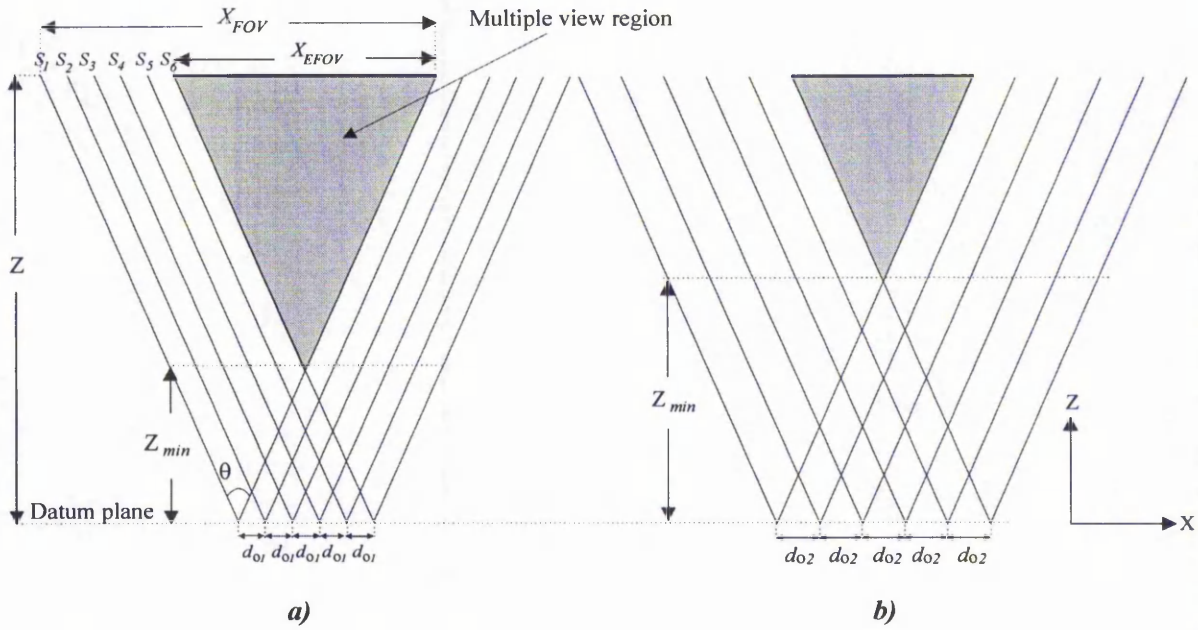

Figure 4-11 *The effect of increasing the base separation on the position of the multiple view region in object space*

The extent of the usable x-axis field of view of an area array sensor is reduced with increasing the number of views utilized (Figure 4-11). Thus the x-axis field of view is said to be reduced because only the overlapping or 'effective' region is utilized in the multiple view arrangement. This reduced field of view is termed the *effective x-axis field of view* X_{EFOV} for a multiple view arrangement and is given by:

$$X_{EFOV} = X_{FOV} - (N-1)d_o \qquad \ldots(4\text{-}13)$$

where,

X_{FOV} = x-axis field of view of an area array sensor;

X_{EFOV} = effective x-axis field of view for an N-view arrangement;

L_{xs} = dimension of the area array sensor in the x-axis, in mm;

d_o = base separation between the centre of perspectives for two successive views in object space.

Thus, for a given object range, the volume, bounded by Z and Z_{min}, in object space reduces with increasing base separation between successive views.

The resultant images can be registered after the image acquisition to effect a fixation plane in the display. The registration of a fixation plane in the display and the registration of the convergence plane in object space are interrelated and dependent upon each other. The registration process is achieved by introducing a set of displacements $\Delta d_{1\leftrightarrow n}$, into the image acquisition process. Figure 4-12 illustrates the geometric properties of two successive views.

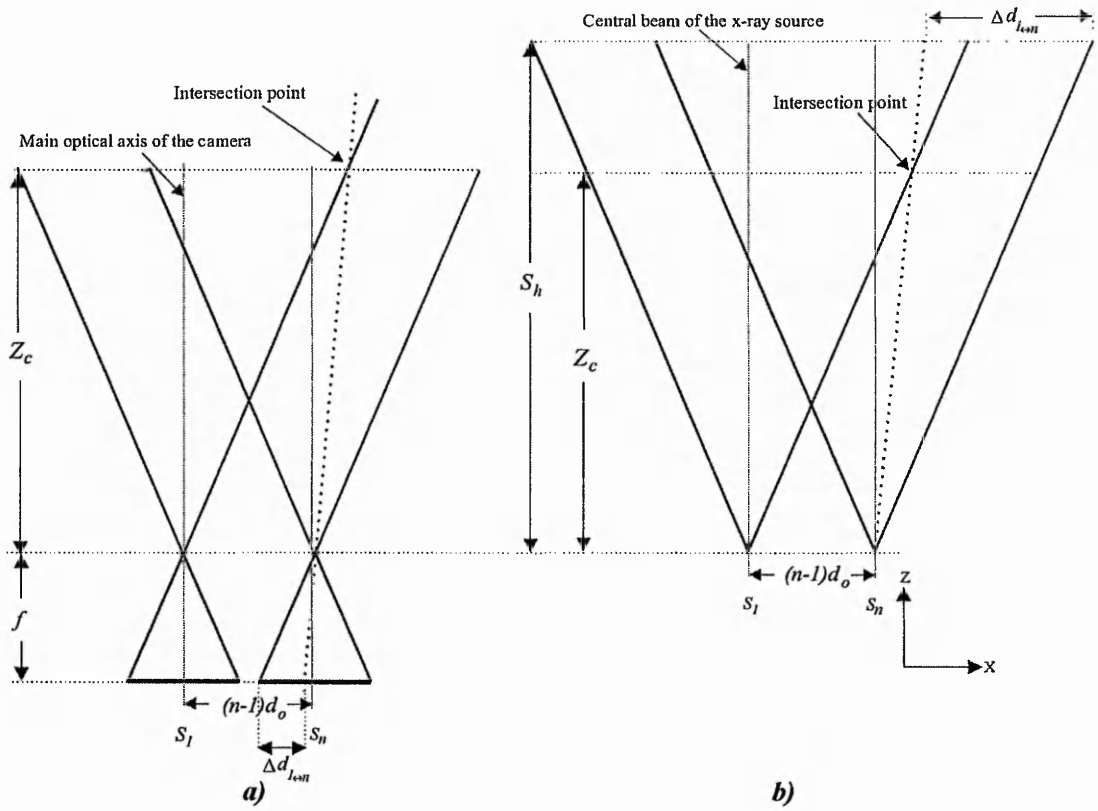

Figure 4-12 *The production of a convergence plane in a) visible light arrangement and b) x-ray arrangement*

When an object point undergoes a relative translation d_o, the corresponding image point also undergoes a displacement on the image sensor. This offset distance $\Delta d_{1\leftrightarrow n}$ in the sensor plane is considered with respect to the reference view S_1 . For example, the offset distance for reference view S_1 is $\Delta d_{1\leftrightarrow 1}$ and it has a zero offset distance value and the perspective view S_2 has an offset distance value of $\Delta d_{1\leftrightarrow 2}$. General equations for the offset distance $\Delta d_{1\leftrightarrow n}$ required to be displaced in the sensor plane for perspective view S_n with respect to the reference view S_1 to effect a convergence plane at range Z_c can be expressed by the following equations:

Visible light: $\Delta d_{1\leftrightarrow n} = \frac{f}{Z_c}(n-1)\,d_o$ ...(4-14)

X-ray: $\Delta d_{1\leftrightarrow n} = \frac{S_h}{Z_c}(n-1)\,d_o$ ...(4-15)

where n is the perspective view number and the base separation is assumed to be equal for each successive pair of views.

In image space, the registration of the perspective views can be achieved by relatively shifting a number of pixel columns in the resultant images with respect to the reference image. This lateral shift of pixel columns in the perspective images effectively registers the perspective views with respect to each other producing a fixation plane in the display.

The number of pixel columns required to be shifted for perspective view n in the display for a given offset distance $\Delta d_{1\leftrightarrow n}$ in the sensor plane can be expressed by:

$$\text{Visible light:} \qquad N_{1\leftrightarrow n\,(pix)} = \frac{f(n-1)\,d_o\,D_{x(pix)}}{Z_c\,L_{xs}} \qquad \ldots(4\text{-}16)$$

$$\text{X-ray:} \qquad N_{1\leftrightarrow n(pix)} = \frac{S_h(n-1)\,d_o\,D_{x(pix)}}{Z_c\,L_{xs}} \qquad \ldots(4\text{-}17)$$

where,

$N_{1\leftrightarrow n(pix)}$ = number of pixel columns to be shifted with respect to the reference view;

D_x = size of the display screen in the x-axis, in mm;

$D_{x(pix)}$ = size of the display screen in the x-axis, in pixels.

Thus, by displacing a number of pixel columns in the resultant image with respect to the reference image S_1, the perspective images can be arranged to converge at a desired range in object space. The registration of perspective images produced by a visible light 6-view arrangement is shown in Figure 4-13. The perspective views, S_1 to S_6, intersect at the convergence plane Z_c and this forms an overlapping region in object space. This region reduces the effective sensor area. The sensor plane is enlarged in the figure in order to show the extent of displacement for views *2* to *6*, $\Delta d_{1\leftrightarrow 2}$ to $\Delta d_{1\leftrightarrow 6}$, required to effect a convergence plane at range Z_c.

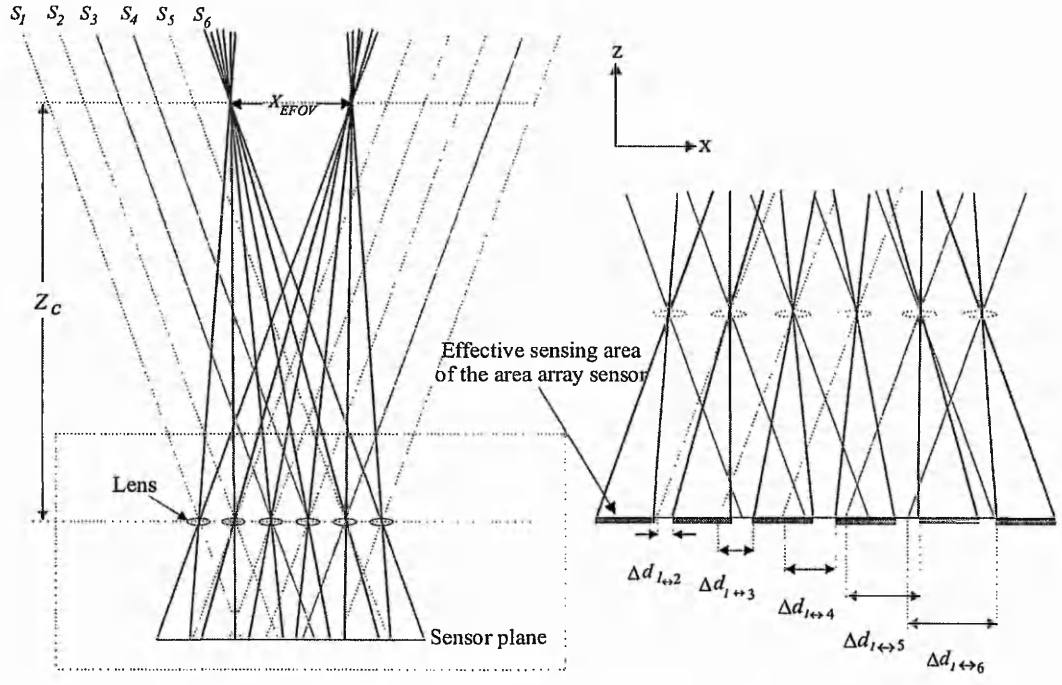

Figure 4-13 *Registration of the perspective images for a visible light arrangement*

The perspective view registration for the x-ray arrangement is shown in Figure 4-14. The sensor plane portion is also enlarged to show the extent of the displacement required to effect a convergence plane.

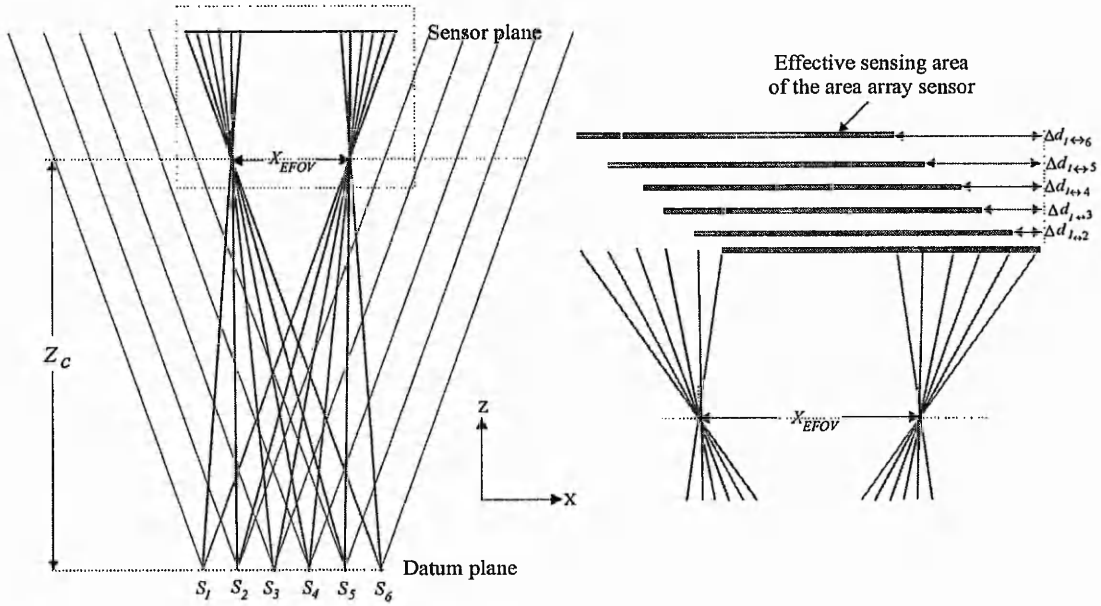

Figure 4-14 *Registration of the perspective images for an x-ray arrangement*

4.3.2 The production of parallax

Figure 4-15 depicts a point M in object space which is is represented by a voxel location. The coordinate difference $(x_n - x_1)$ produced by an object point in two successive views in the sensor plane is dependent upon the base separation. This quantity is termed as *parallax* in the sensor plane P_s.

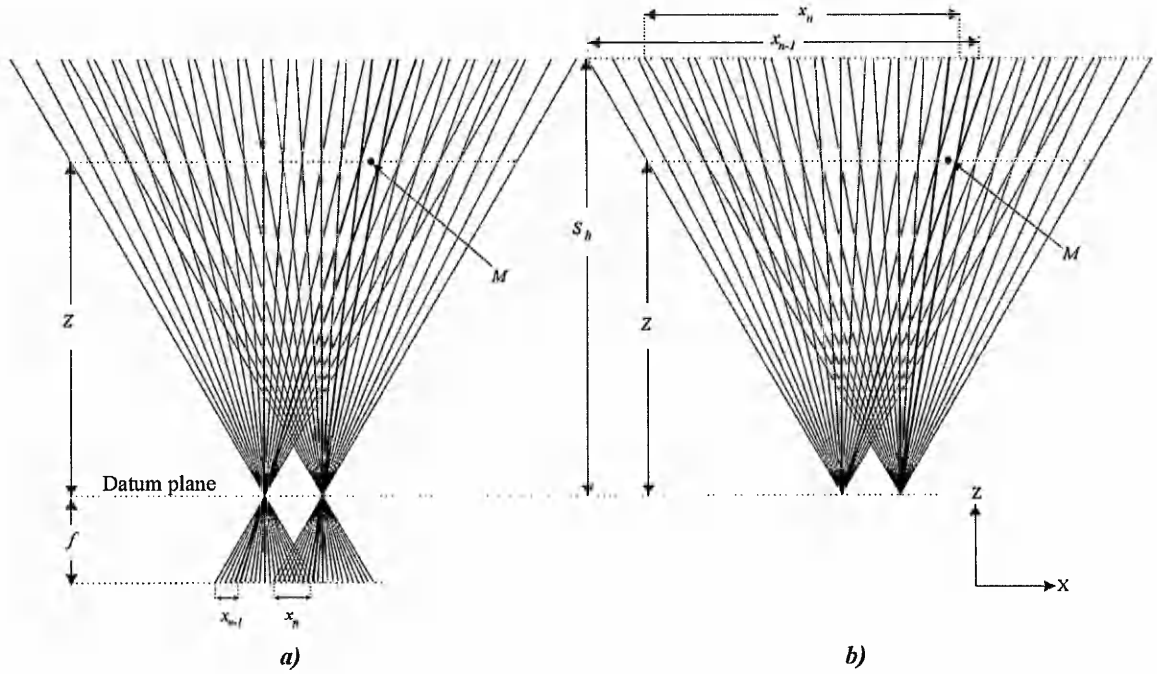

Figure 4-15 *Parallax production for a multiple view lateral shift imaging technique in a) visible light arrangement and b) x-ray arrangement*

With reference to Figure 4-15, the general parallax equations for visible light and x-rays for perspective views $S_{(n-1)}$ and S_n are given by:

Visible light: $P_{s(n-1)\leftrightarrow n} = \frac{f\ d_o}{Z}$ ...(4-18) X-ray : $P_{s(n-1)\leftrightarrow n} = \frac{S_h\ d_o}{Z}$ ...(4-19)

Therefore, the relative parallax value between two object points located at range Z_a and Z_b is given by:

Visible light: $P_{rs(n-1)\leftrightarrow n} = f\ d_o\left(\frac{1}{Z_a}-\frac{1}{Z_b}\right)$ X-ray: $P_{rs(n-1)\leftrightarrow n} = S_h\ d_o\left(\frac{1}{Z_a}-\frac{1}{Z_b}\right)$

After effecting a convergence plane, the parallax value of an object point is no longer referenced to the datum plane. Thus any point in the convergence plane gives rise to zero parallax. The relative parallax between an object point located at range Z with respect to the convergence plane Z_c is expressed in the following equations.

Visible light: $$P_{rs1\leftrightarrow n} = f\,(n-1)\,d_o\left(\frac{1}{Z_c}-\frac{1}{Z}\right) \quad ...(4\text{-}20)$$

X-ray: $$P_{rs1\leftrightarrow n} = S_h\,(n-1)\,d_o\left(\frac{1}{Z_c}-\frac{1}{Z}\right) \quad ...(4\text{-}21)$$

Relative parallax produced by the stereoscopic pair formed by the reference view (i.e. view 1) and view n, with respect to convergence plane Z_c, in the sensor plane $P_{rs1\leftrightarrow n}$ will be magnified by a factor M_{sd} from the sensor plane to the display (*Equation 3-8*):

Visible light: $$P_{rd1\leftrightarrow n} = f\,(n-1)\ d_o\,M_{sd}\left(\frac{1}{Z_c}-\frac{1}{Z}\right) \quad ...(4\text{-}22)$$

X-ray: $$P_{rd1\leftrightarrow n} = S_h\,(n-1)\,d_o\,M_{sd}\left(\frac{1}{Z_c}-\frac{1}{Z}\right) \quad ...(4\text{-}23)$$

This parallax information can also be presented in terms of pixel separations in the display. Therefore:

Visible light: $$P_{rd1\leftrightarrow n(pix)} = f\,(n-1)\,d_o\,\frac{D_{x(pix)}}{L_{xs}}\left(\frac{1}{Z_c}-\frac{1}{Z}\right) \quad ...(4\text{-}24)$$

X-ray: $$P_{rd1\leftrightarrow n(pix)} = S_h\,(n-1)\,d_o\,\frac{D_{x(pix)}}{L_{xs}}\left(\frac{1}{Z_c}-\frac{1}{Z}\right) \quad ...(4\text{-}25)$$

4.3.3 The multiple view region and the binocular stereoscopic depth of field

In order to preserve the observer's binocular stereoscopic fusion of an image sequence on the monitor screen, the maximum displacement between conjugate image features must not exceed the maximum permissible parallax $P_{d(max)}$ given by:

$$P_{s(\max)} = \frac{P_{d(\max)}}{M_{sd}} \qquad \ldots(4\text{-}26)$$

Once the convergence plane is established, the region in object space for comfortable viewing is bounded by Z_{near} and Z_{far}. These limits are referenced to the convergence plane Z_c and may be calculated by consideration of maximum permissible parallax in the sensor plane $P_{s(max)}$. Thus by modifying *Equation 4-20 & 4-21* and replacing the object range with Z_{near} and Z_{far} respectively for the near and far limit:

Far limit:

Visible light: $Z_{far} = \dfrac{Z_c f d_o}{f d_o - Z_c P_{s(\max)}}$ X-ray: $Z_{far} = \dfrac{Z_c S_h d_o}{S_h d_o - Z_c P_{s(\max)}}$

Near limit:

Visible light: $Z_{near} = \dfrac{Z_c f d_o}{Z_c P_{s(\max)} + f d_o}$ X-ray: $Z_{near} = \dfrac{Z_c S_h d_o}{Z_c P_{s(\max)} + S_h d_o}$

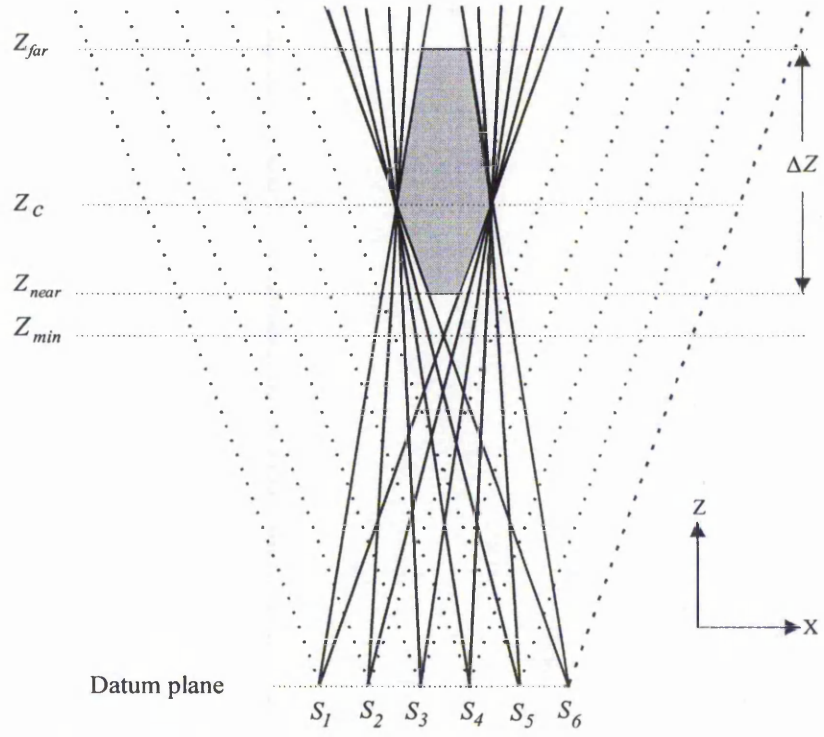

Figure 4-16 *Binocular stereoscopic depth of field truncating the multiple view region*

The asymmetric geometry of the binocular stereoscopic depth of field can be appreciated from the diagram of Figure 4-16. This effect may be described in terms of the minimum detectable depth plane interval in object space. This will be discussed in more detail in Section 4.3.4. Thus the effective depth of field ΔZ is defined by the limits, Z_{far} and Z_{near}, and are common to the visible light and the x-ray arrangement and can be expressed as:

$$\Delta Z = Z_{far} - Z_{near} \qquad \ldots(4\text{-}27)$$

Hence,

$$\text{Visible light: } \Delta Z = \frac{2 Z_c^{\,2} f d_o P_{s(\max)}}{(f d_o)^2 - (Z_c P_{s(\max)})^2} \qquad \text{X-ray: } \Delta Z = \frac{2 Z_c^{\,2} S_h d_o P_{s(\max)}}{(S_h d_o)^2 - (Z_c P_{s(\max)})^2}$$

It should be noted that Z_{near} must be greater that the minimum permissible range for the accumulated base separation $(N\text{-}1)\ d_o$,

$$Z_{near} \geq Z_{\min}$$

Similarly, the position of the convergence plane is limited to a minimum value given by:

$$\text{Visible light: } Z_c \geq \frac{f(N-1)\,d_o}{2f \tan\left(\frac{\theta}{2}\right) - (N\text{-}1)P_{s(\max)}} \qquad \text{X-ray: } Z_c \geq \frac{S_h\,(N\text{-}1)d_o}{2f \tan\left(\frac{\theta}{2}\right) - (N\text{-}1)P_{s(\max)}}$$

A depiction of the multiple view volume in object space is depicted in Figure 4-17.

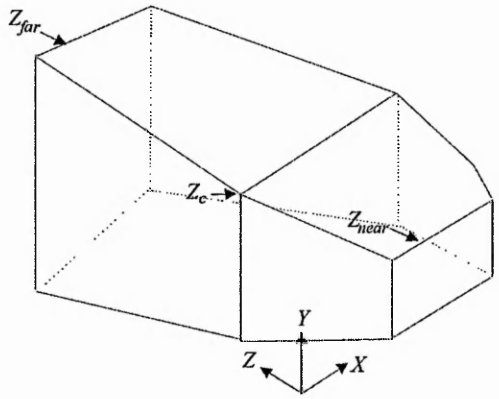

Figure 4-17 *Binocular stereoscopic multiple view region in object space*

Any non-occluded point which lies in this region is present in all the perspective views.

4.3.4 Minimum detectable range increment in object space

The miniumum detectable range increment in object space z-axis can be obtained by differentiating the formulae for parallax in the sensor plane. Thus, differetiating *Equation 4-18 & 4-19* for the visible light and the x-ray cases.

$$\text{Visible light: } \delta Z = \frac{Z^2\ \delta P}{d_o f} \quad \ldots(4\text{-}28) \qquad \text{X-ray: } \delta Z = \frac{Z^2\ \delta P}{d_o\ S_h} \quad \ldots(4\text{-}29)$$

The quantity δP may be interpreted as the smallest resolvable increment in the parallax in the sensor plane. With reference to *Equation 4-28 & 4-29*, the minimum range increment is a function of object range which implies that this technique produces a non-linear spatial resolution in the z-axis. This indicates that the change in the x-axis coordinate between successive views has a non-linear relationship with respect to the range increment in object space. This resolution can be increased by increasing the base separation between successive views. Figure 4-18a illustrates the sampling pattern for a 3-view arrangement, the convergence plane is set at Z_c and the entire multiple view region is formed from voxels. The multiple view region formed by three perspective views is considered to be split into two successive image pairs i.e. image pairs S_1-S_2 and S_2-S_3 as illustrated in Figure 4-18b in order to aid the following discussion.

The z-axis dimensions of the voxels, in both image pairs, are identical indicating that the spatial resolution remains unchanged. However, the orientation of the voxel structures in each of the image pairs are different indicating that the image pair is produced by a 'mirror image' configuration of perspective views.

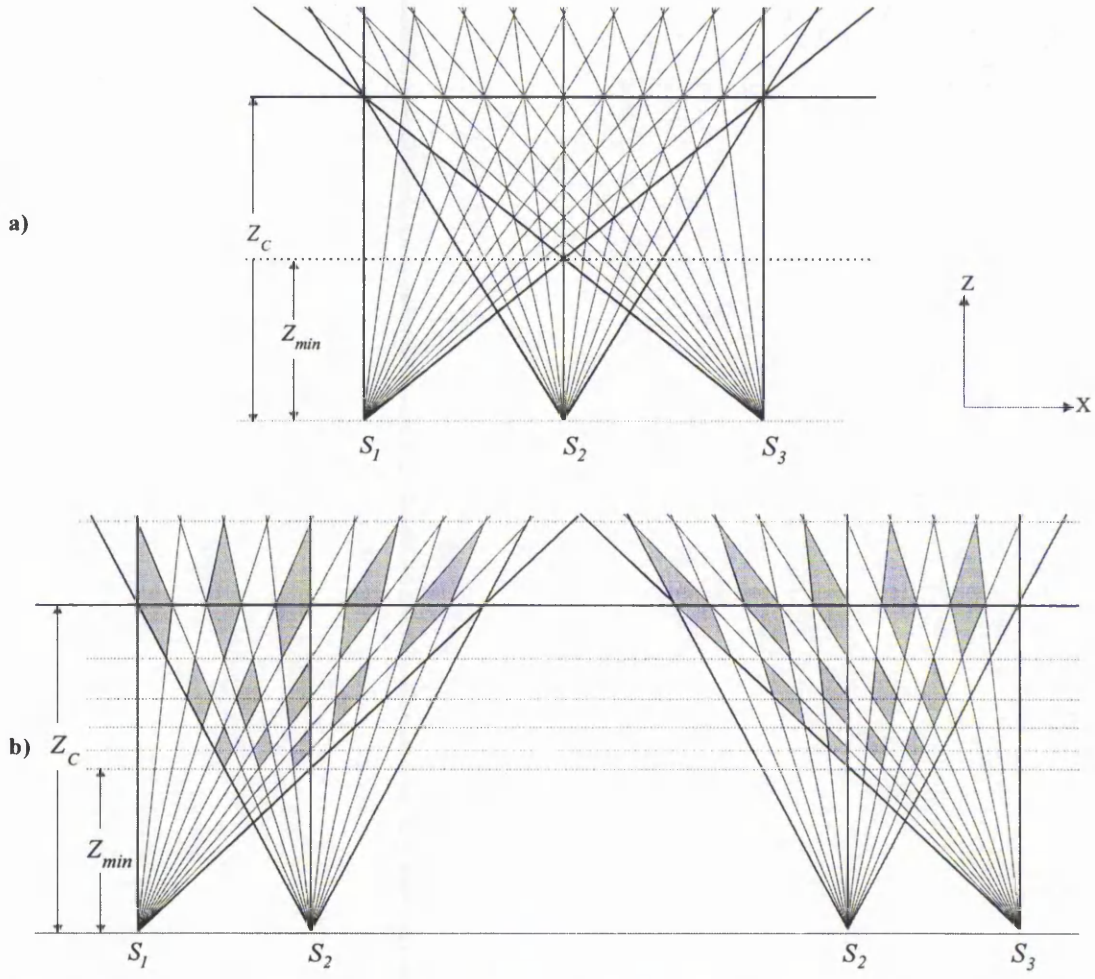

Figure 4-18 *Multiple view region produced by a) a 3-view lateral shift system and b) two possible image pairs produced by the three successive views (i.e. ignoring view S_1- S_3)*

Similar to the line-scan technique, the lateral shift technique also enables a z-axis zoom to be realized by using different combinations of perspective images. Two of the possible combinations are shown in Figure 4-19.

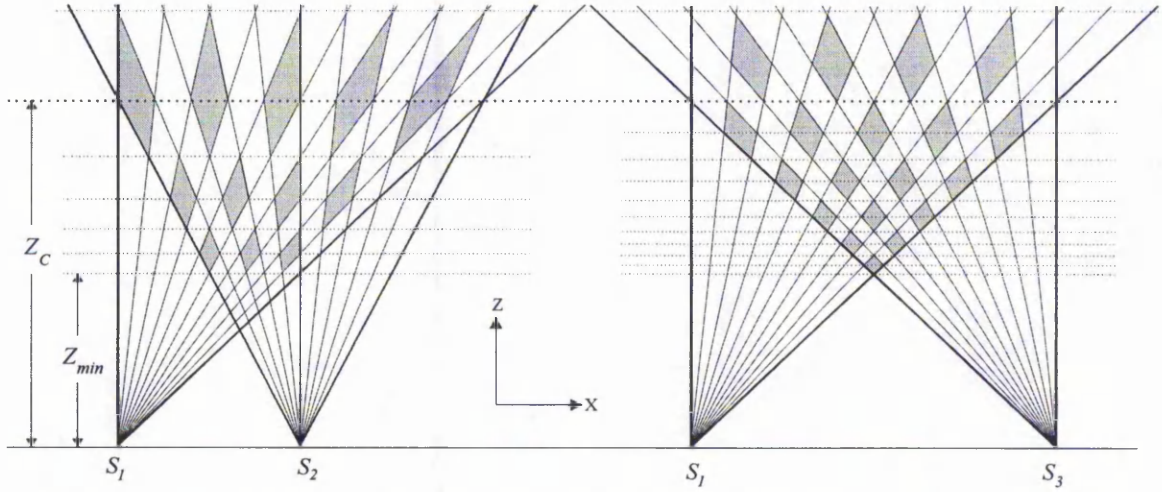

Figure 4-19 *Spatial sampling pattern for the z-axis zoom in the lateral shift arrangement*

The arrangement is said to be zoomed when the transition of the stereoscopic image pair S_1-S_2 to S_1-S_3 occurs. It should be noted that the zoom function is isolated to the z-axis and the x and y axes do not undergo a change in magnification. The zoom function is possible as the parallax is increased when the base separation is increased. It can be appreciated from Figure 4-19 that the voxel/depth plane density increases with increasing base separation. This consequently increases the perceived depth in the display. However, the z-axis zoom is limited by the maximum permissible parallax tolerated by binocular stereoscopic fusion for a human observer as determined by *Equation 4-26*.

4.3.5 Motion parallax distribution

Similar to the line-scan technique the lateral shift technique is produced by relative translation rather than relative rotation. Therefore the resultant object image sequences produce an apparent movement about the fixation plane in the display. Thus the illusion of rotation is due to the object image undergoing an apparent angular displacement during the transition of the perspective images. When perspective images are acquired the object under inspection is sampled as a function of its position in object space. Figure 4-20a illustrates the sampling pattern of an object under inspection for a 3-view lateral shift arrangement. The sampling of object space in the z-axis is a function of the angular relationship between successive perspective views. In this example, the convergence plane is set at a range Z_c with respect to the datum plane.

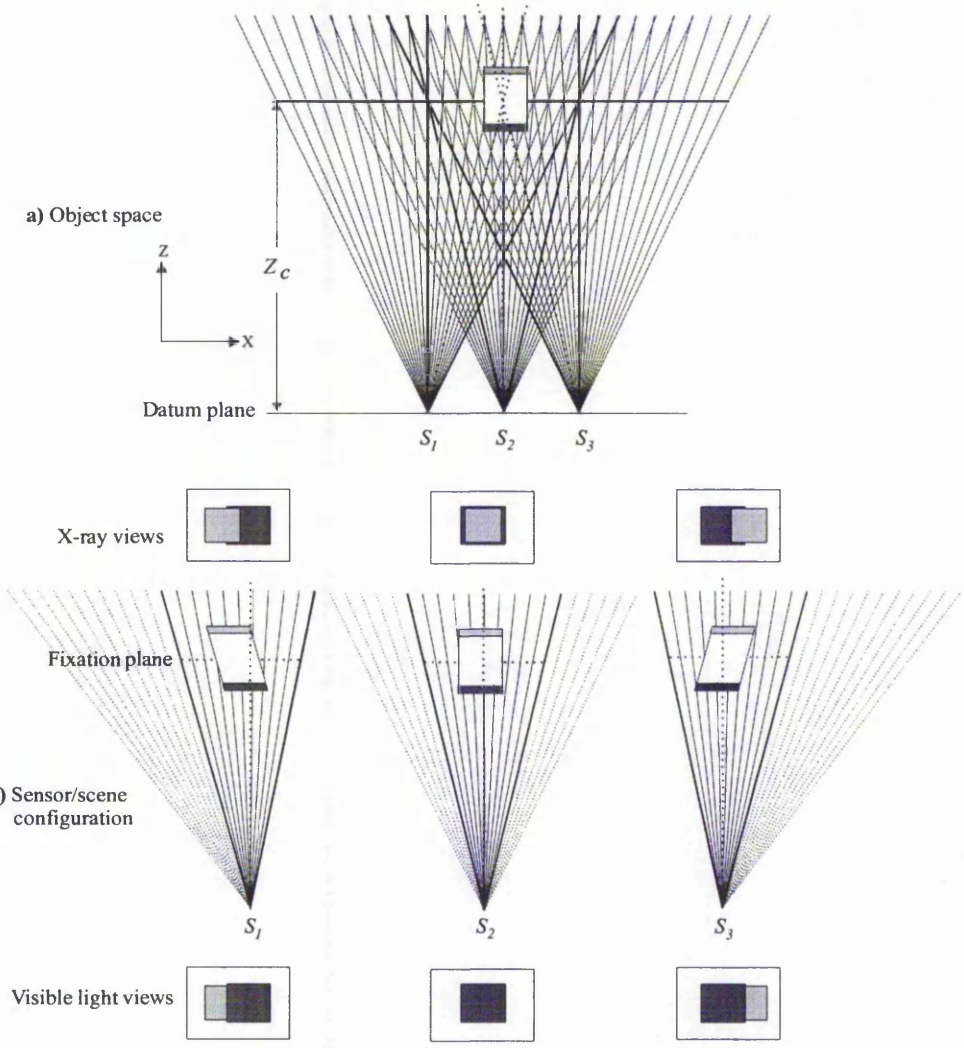

Figure 4-20 *Spatial sampling pattern of a 3-view lateral shift technique a) object space and b) sensor/scene configuration*

Similar to the line-scan technique, the relative change in perspective information can be represented by rearranging the field of view of each perspective view to be perpendicular to the datum plane as shown in Figure 4-20b. These diagrams create an equivalent 'top view' of the object under inspection. The portion of the object under inspection nearer to the datum plane is depicted as being dark grey whilst the light grey portion is further away. The relative changes in position of these object features as a function of range produces the apparent motion or motion parallax in the resultant display. Similar to the line-scan technique, the portion of the object that appears in the display is different in the visible light and x-ray cases as the respective sensors are physically on the opposite sides of the datum plane. Similar to the line-scan technique, the fixation plane in the display can be repositioned by re-registering the perspective images with respect to the reference image. This can be achieved by applying a horizontal pixel column shift to each of the perspective images. The effect of repositioning the fixation plane in the display produces a new

convergence plane in object space. Modifying the equation for parallax in image space, the new convergence planes in object space, are given below:

Visible light: $$Z_c = \frac{f(n-1)\,d_o\,D_{x(pix)}}{N_{1\leftrightarrow n(pix)}\,L_{xs}}$$ X-ray: $$Z_c = \frac{S_h(n-1)\,d_o\,D_{x(pix)}}{N_{1\leftrightarrow n(pix)}\,L_{xs}}$$

Thus the position of z-axis is a function of the horizontal pixel shift introduced into the perspective images. The difference between the original convergence plane and the new convergence plane is given by the following equation.

Visible light: $$Z_{c(diff)} = Z_c' - Z_c = \frac{f(n-1)\,d_o\,D_{x(pix)}}{N_{1\leftrightarrow n(pix)}\,L_{xs}\left(\frac{N_{1\leftrightarrow n(pix)}}{N_p}+1\right)}$$

X-ray: $$Z_{c(diff)} = Z_c' - Z_c = \frac{S_h(n-1)\,d_o\,D_{x(pix)}}{N_{1\leftrightarrow n(pix)}\,L_{xs}\left(\frac{N_{1\leftrightarrow n(pix)}}{N_p}+1\right)}$$

where N_p is the number of pixel columns shifted in the display.

Figure 4-21 illustrates two different positions of the convergence plane in object space.

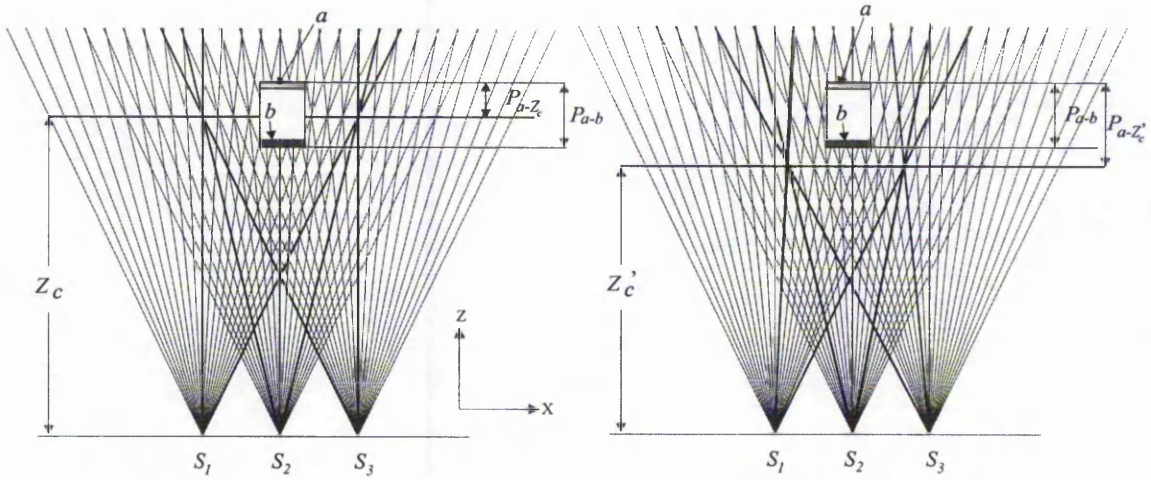

Figure 4-21 *Sampling pattern of an object under inspection when the fixation plane is changed*

Similar to the line-scan technique, the relative parallax of an object point (i.e. point *a* with respect to the convergence plane ($P_{a\text{-}Zc}$)) is changed when the convergence plane is altered. However, the relative parallax between two object points ($P_{a\text{-}b}$) remains unchanged even though the convergence plane is changed.

4.4 Comparison of the multiple view techniques

This section presents the comparison of the two proposed multiple view techniques. This is based on the theoretical appraisal presented in the previous sections. The multiple view line-scan

technique has inherent advantages over the multiple view lateral shift technique in a number of respects.

i) Voxel distribution

The line-scan technique produces a linear voxel structure whereas the lateral shift technique produces a non-linear voxel structure (i.e. increasing with object range). However the linear structure is desirable for the following reasons:

- linear relationship between parallax in image space and a physical separation in object space;
- linear relationship between the fixation plane in the display and the convergence plane in object space.

ii) Field of view of the resultant images

The field of view in the x-axis is dependent upon the registration method adopted in order to effect a convergence plane in object space. The convergence plane in the line-scan technique can be effected by two different methods:

- temporal convergence (during image acquisition); produced by the relative time delay between the start of image acquisition for each line-scan sensor;
- horizontal pixel shift (after image acquisition); produced by the introduction of a horizontal pixel shift to perspective images with respect to a reference image; this method suffers from a reduction in the x-axis field of view as image data is lost in effecting the lateral shift after the images are acquired.

The temporal convergence method is more desirable in effecting a convergence plane as no truncation of the x-axis field of view is required. This is not an option for the lateral shift technique, as only the horizontal pixel shift method can be applied. Therefore, the lateral shift technique produces images with a smaller x-axis field of view in comparison to the line-scan technique.

iii) Multiple view region

For the line-scan technique, the multiple view region in object space is symmetrically distributed about the convergence plane in the z axis. Thus the depth of field of this region is fixed regardless of the object range. The determination of the depth of field of a new multiple view region is not required whenever the convergence plane is repositioned. Whereas for the lateral shift technique, the multiple view region is asymmetrically distributed about the convergence plane. Therefore, changes in the position of the convergence plane can affect the depth of field in the multiple view region. Thus the depth of field in the multiple view region is required to be recalculated whenever the convergence plane is changed.

5 SIMULATED X-RAY IMAGING EXPERIMENTS

5.1 Introduction

This chapter presents the development of the visible light experimental system, for implementing the line-scan multiple view imaging technique and the lateral shift (area array) multiple view imaging technique. The experimental strategy used to evaluate these imaging techniques is presented in terms of: repeatability tests; two-dimensional acquisition experiments and three-dimensional or multiple view imaging experiments. The display of the image data for the human observer is fully discussed in Chapter 7.

5.2 The experimental system

An experimental system has been constructed to enable the evaluation of the proposed multiple view imaging techniques, that is, the line-scan and lateral shift techniques. The experimental system consists of the following components:

- an area array camera;
- a frame grabber;
- a motorized linear translation stage and its controller (for the line-scan technique);
- a manual lateral translation stage (for the lateral shift technique).

Each of these components is discussed in the following text.

a) The area array camera

The CCD area array camera used for this research is manufactured by Pulnix, model TM840 [85] as shown in Figure 5-1.

Figure 5-1 *The CCD area array camera*

The imaging sensor is a 0.5-inch frame-transfer device comprising 699 x 576 photosites producing a 2:1 interlaced video frame rate of 25 Hz. The camera uses a C-mount lens [104] and the fixed focal length lenses used for the experiments are 12.5 mm, 16 mm, 25 mm and 50 mm. The camera is implemented either in an area array/standard mode or a novel line-scan mode. The details of the camera operation in each mode is discussed in Section 5.5.1 and Section 5.6.1 respectively.

b) The frame grabber

A Corona [105] frame grabber manufactured by *Matrox Imaging Electronic Systems Limited* is used in this work; it has 8 MB of on-board video memory. The main function of the frame grabber is to acquire and store an image frame produced by the camera. When the camera is used in a line-scan mode, the frame grabber is not only used to store in real time image frames produced by the area array sensor but also used to store sequential image data produced by the 'selected' photosite columns during the image acquisition process. This is discussed in detail in Section 5.5.1.

c) The motorized linear translation stage

The continuous lateral movement required for the line-scan technique is produced by a motorized linear translation stage as shown in Figure 5-2.

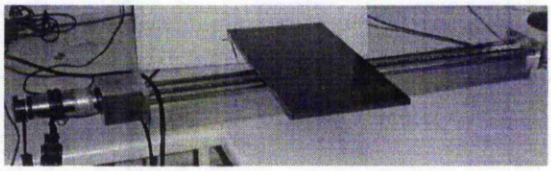

Figure 5-2 *The motorized linear translation stage*

This stage is manufactured by *McLennan Servo Supplies Limited.* The speed of the translation stage is controlled by an off-the-shelf microprocessor unit [106] and it can be adjusted from 2 mm/s to 7 mm/s. The maximum travel of the system is 0.9 m.

d) The manual lateral translation stage

The manual lateral translation stage as illustrated in Figure 5-3 is utilized in the lateral shift arrangement to position the object under inspection with respect to the camera.

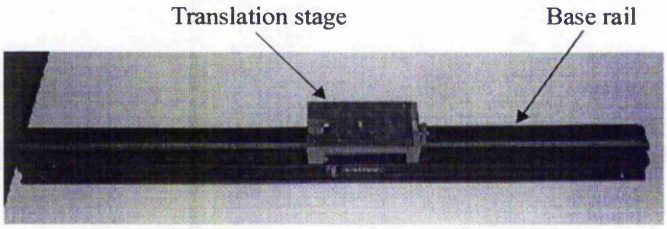

Figure 5-3 *The manual lateral translation stage*

This stage incorporates a calibrated base rail such that the stage can be repositioned to an accuracy of less than 1 mm over a range of 1.5 m.

5.3 Experimental strategy

The experimental work is categorised into three broad areas. These are:

a) Repeatability experiments; aiming to establish the repeatability of the system parameters.

b) Two-dimensional experiments; in order to verify the theoretical analysis relating to the production of individual perspective images.

c) Three-dimensional experiments; in order to verify the theoretical analysis of the geometric interrelationship between perspective images for production of 3-D information in the resultant image display.

a) Repeatability tests

The integrity of the experimental arrangement is evaluated by conducting repeatability tests. The consistency and long-term repeatability, over the course of experiments, is crucial to the integrity of the resultant images. The repeatability tests conducted are:

- noise level (in terms of grey level) of the resultant images;
- consistency of the image components in the x-axis and the y-axis as a function of camera-to-object range;
- consistency of the translation speed of the linear translation stage;
- consistency of the line acquisition time of the experimental system.

b) 2-D experiments

The parameters that affect the production of a two-dimensional image are examined.

Line-scan technique:

- variation in the camera-to-object range;
- variation in the focal length of the camera lens;
- variation in the translation speed of the linear translation stage;
- variation in the line acquisition time of the experimental system.

Lateral shift technique:

- variation in the camera-to-object range;
- variation in the focal length of the camera lens.

c) 3-D experiments

A similar approach is used to evaluate the three-dimensional imaging characteristics. These are:

- the spatial registration of the perspective images in image space; this examines the fixation plane in the display and the convergence plane in object space;
- the parallax production; this examines the system parameters that affect the parallax production, that is, the *convergence angle* in the line-scan arrangement and the *base separation* in the lateral shift arrangement;
- the interrelationship between the parallax produced by successive views;
- voxel distribution; this indirectly examines the z-axis dimension of the voxel structures, spatial resolution, and the depth plane distribution;
- sample set of perspective images produced by the multiple view techniques.

5.4 Establishing the repeatability of the system parameters

A 50 mm black square attached to a transparent plate as illustrated in Figure 5-4a is used as a test object for experiments. This object provides high contrast images. A slotted mounting rack (Figure 5-4b) is used to hold the test object at various ranges with respect to the camera.

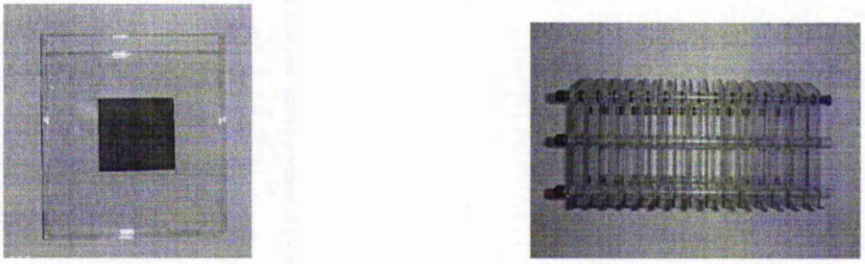

a) *b)*

Figure 5-4 a) *A 50 mm square attached to a transparent plate and b) a slotted mounting rack*

Four parameters are identified and independently tested as discussed in the following text. The full experimental results of the repeatability tests can be found in Appendix A. A description of each experiment together with a summary is presented in the following text.

a) Grey level noise

This experiment evaluates the noise level in terms of grey level intensity of images obtained from the experimental arrangement. Ten sample images were obtained from a test object at different instants in time. The average grey level value of a fixed area, 100 pixels x 100 pixels, in the sample images is examined. The maximum variation of the grey level was ±12 grey levels and considered acceptable for human observation [107].

b) Camera-to-object range

The test object is imaged at four different camera-to-object ranges and the pixel components of the imaged black square in the x and y axes are measured. The same test was repeated ten times to obtain an average value. The repositioning in the x and y axes is within ±3 pixels for the different camera-to-object ranges used.

c) Translation speed

The translation speed in the motion axis (x-axis) is evaluated by passing the test card along the x-axis within the field of view of the camera, while sixteen perspective line-scan images are collected. The x-axis image components of the imaged black square were measured. This experiment is repeated ten times to obtain an average value. The translation speed is consistent for repeatability; the observed error rate in terms of pixel separations is ±2 pixels.

d) Line acquisition time

The line acquisition time is determined by using a timer function in the *Matrox* imaging software library [108]; this produces a time resolution accuracy of 1 μs. Initially, the time taken to execute this timer function is determined. It is found that it has a negligible value, 96 μs, in comparison to the minimum time required for a line acquisition, which is 80 ms. The timer function is implemented via software code between each line acquisition process to obtain the time interval between two successive line acquisitions. The experiment was repeated ten times to obtain an average value. Thus the line acquisition time can be considered to be constant, throughout the image acquisition process.

5.5 Experiments using a line-scan mode of operation

A photograph of the hardware for the experimental arrangement for the line-scan technique is shown in Figure 5-5.

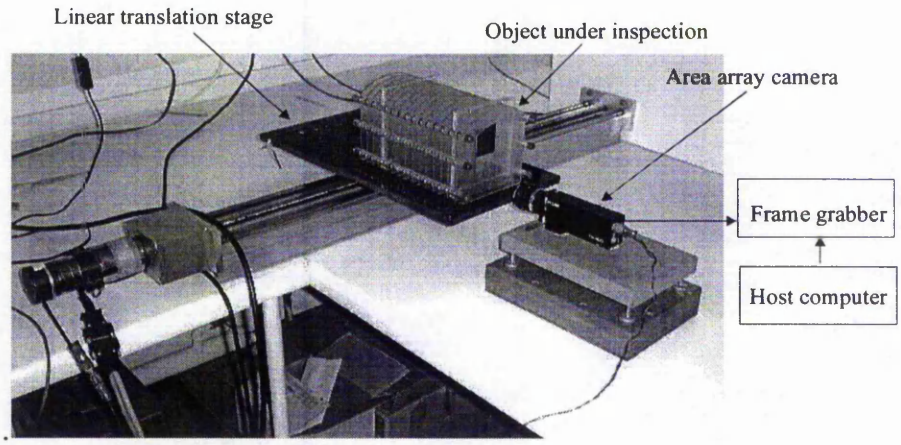

Figure 5-5 *The experimental multiple view arrangement for the line-scan technique*

5.5.1 Image acquisition

The image acquisition using the experimental system for the line-scan technique is discussed with respect to the following areas:

a) utilization of the area array camera in a line-scan mode;
b) perspective view production;
c) time delay implementation;
d) system operation.

a) Utilization of the area array camera in a line-scan mode

Image information produced by a photosite column on an area array imager can be obtained by accessing the pixel data stored in a memory region in the frame grabber. Thus the image data in the region of interest can then be transferred to the image buffer specifically created for the sequential

line-scan storage. This is illustrated in Figure 5-6 where the 'growth' of the image information in the image buffer is a function of the line acquisition time t_1 to t_n.

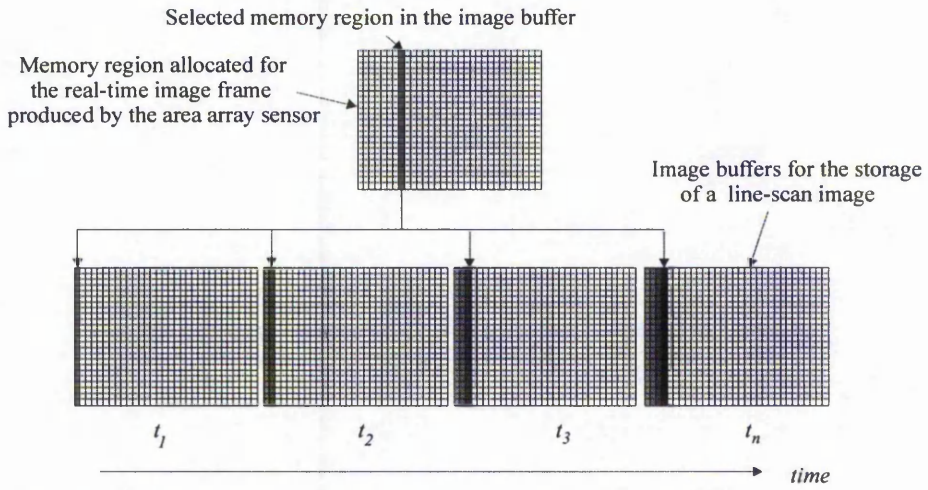

Figure 5-6 *Sequential storage process using image information produced by a single photosite column*

The resultant two-dimensional image is made up from image information obtained from the same photosite column for many successive frames. Thus the maximum line acquisition frequency for the experimental system is 25 Hz. This is because the full video frame produced by the CCD camera has to be stored before the information from a column of photosites can be extracted. In other words, the frame synchronizing pulses determine the line acquisition time when the camera is utilized in a line-scan mode. Seventeen buffers are allocated in the frame grabber's memory for image storage. One buffer is used for real-time image capture whilst the other sixteen buffers are assigned to accumulate perspective images. Figure 5-7a depicts the timing diagram for line acquisition in a camera utilized for line-scan mode.

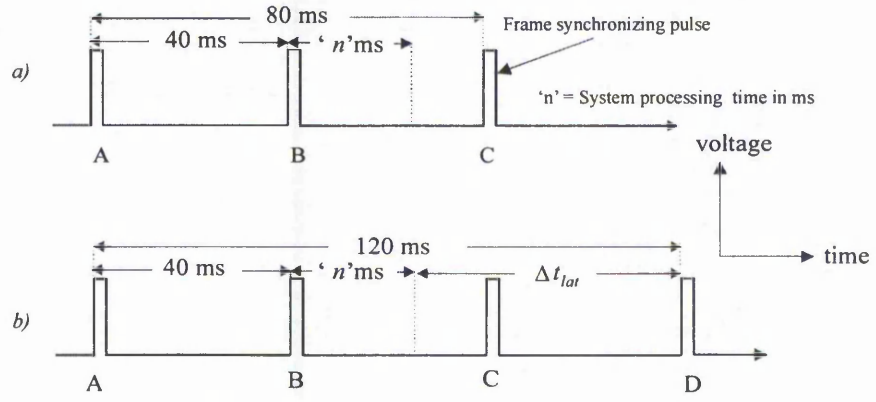

Figure 5-7 *Timing diagram for the line acquisition time a) the minimum time and b) the increase in line acquisition time produced by introducing a time delay*

The line acquisition time as a function of synchronizing pulses, *A* to *C* is depicted in Figure 5-7, where it can be appreciated that the minimum time required to acquire a full frame image is 40 ms.

However, a period of time, 'n' ms is required for system processing. Therefore, the minimum time required to acquire a column of image data is in fact 80 ms. Since the line acquisition time is dependent upon the frame synchronizing pulse, it is an integer multiple of 40 ms. The line acquisition time can be increased by introducing a short time delay Δt_{lat} in between two successive line acquisitions to produce a longer line acquisition time (e.g. 120 ms) as illustrated in Figure 5-7b. This effectively makes the next synchronizing pulse, B in this example, transparent to the frame grabber. Further information regarding the time delays implemented in the experimental system can be found in Appendix B. It should be pointed out that the brightness of the resultant image remains unchanged with increasing line acquisition time as the photon integration period is fixed by the camera's scan rate.

b) Perspective image production

To determine the angular distribution of the slit fields of view in object space requires that a relationship between a selected photosite column and a reference photosite column in the sensor plane be established. Thus the slit field of view perpendicular to the sensor plane is used as a reference for perspective angle determination. This reference field of view corresponds to the central photosite column in the area array sensor assuming the sensor is perfectly aligned to the camera's lens. The central photosite column is used as a reference column in this discussion. With reference to Figure 5-8, the distance d between the reference photosite column and the selected photosite column is a function of the perspective angle α and the focal length f as expressed by:

$$d = f \tan(\pm\alpha)$$

where d is the distance, in mm, between the reference column and the selected column and f is the focal length of the camera lens.

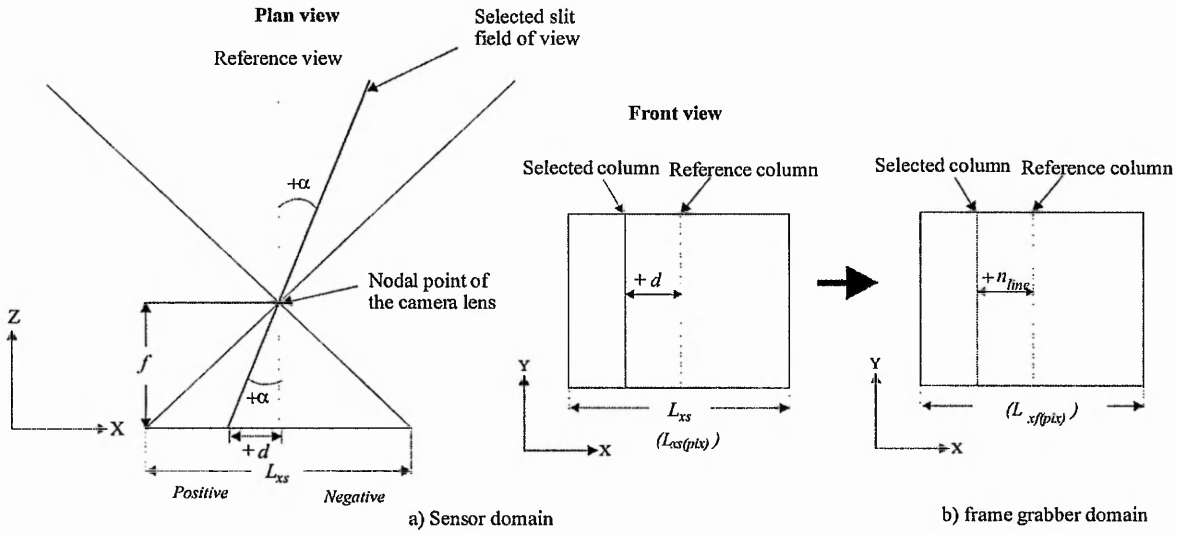

Figure 5-8 *Determination of the perspective angle of a line-scan sensor using an area array camera*

The sign of the perspective angle α can be positive or negative dependent upon the position of the selected column with respect to the reference column. For this research, the left half of the area array sensor corresponds to a positive α and the right half of the sensor corresponds to a negative α. The distance, in mm, from the reference photosite column *d* can also be expressed in terms of the number of photosite columns n_{line} which is the relative displacement with respect to the central photosite column.

$$n_{line} = \frac{d\, L_{xs(pix)}}{L_{xs}} \qquad \ldots(5\text{-}1)$$

where,

L_{xs} = dimension of the area array sensor in the x-axis, in mm;

$L_{xs(pix)}$ = dimension of the area array sensor in the x-axis, in pixels.

The image information produced by the area array sensor is transferred to the frame grabber in a particular video format (e.g. CCIR or RS-170). The image size in terms of pixels is different in each case, for example CCIR–768 pixels x 572 pixels and RS-170 is 640 pixels x 480 pixels. The image information obtained from the photosite column is converted into an analogue video signal and is resampled by the frame grabber according to the particular video standard being used. Assuming $L_{xf(pix)}$ is the number of photosite columns on the frame grabber for a particular video format. The image information is transferred from the area array sensor to the image buffer (frame grabber). Therefore, the number of video columns required to be displaced, with respect to the central video column, in order to produce a perspective angle α is:

$$n_{line} = \frac{d\, L_{xf(pix)}}{L_{xs}} = \frac{f d \tan(\pm\alpha) L_{xf(pix)}}{\mathrm{L_{xs}}} \qquad \ldots(5\text{-}2)$$

Therefore, the perspective view can be achieved by using the appropriate photosite column.

c) Time delay implementation

The time delays introduced into the start of perspective image acquisition with respect to the start of the reference image acquisition can be implemented in the following ways:

- parallel processing implemented with dedicated timers for each of the line-scan sensors;
- using frame synchronizing pulses as a timer for every line-scan sensor in the multiple view arrangement.

The first approach produces an accurate time delay for each of the line-scan sensors; however, this involves complicated programming algorithms where an individual timer has to be allocated for each line-scan sensor. The second approach uses the frame synchronizing pulse (Figure 5-7) as a clock pulse for each of the line-scan sensors in the experimental arrangement. The synchronizing pulse in this experimental system can be referred to as the line acquisition time since this is also derived from the frame synchronizing pulse (it has been shown to be consistent in the repeatability

test). The latter approach of utilizing a synchronizing pulse as a timer is chosen in this work for its simplicity and accuracy. For example, if the line acquisition time is 80 ms, a time delay of n seconds in terms of line acquisition time is expressed by:

$$\Delta l = \frac{\Delta t_{1\leftrightarrow n}}{t} = \frac{n \text{ seconds}}{80 \text{ ms}} \qquad \ldots(5\text{-}3)$$

where $\Delta t_{1\leftrightarrow n}$ is the time delay required to achieve a convergence plane in object space and t is the line acquisition time.

d) System operation

A High-Grade Pentium 200 MHz MMX PC is used as the host computer for the experimental arrangement. This computer provides the following functions:

- transmitting 'start' signals for the linear translation stage's controller to synchronize the image capture process;
- a platform for image storage, processing and display.

Software code, written in the *C++* language with the aid of imaging functions from the *Matrox imaging* software library, are implemented in order to control the operating parameters for both the frame grabber and the linear translation stage's controller. This program allows the user to control the following parameters:

- translation speed;
- line acquisition time;
- number of lines used to form a two-dimensional image;
- time delay required to effect a convergence plane in object space;
- angular distribution of the slit fields of view produced by the selected photosite columns.

The operation flowchart is depicted in Figure 5-9.

An image capture cycle begins with the initialisation of the frame grabber. This entails setting the camera interface parameters, video standard and reference photosite columns. During the initialisation, the memory allocation for image storage is allocated. Following this, live images are displayed on the monitor screen which allows the user to adjust the orientation of the camera and lighting required for optimum image quality. In this system, sixteen photosite columns are allocated as individual line-scan sensors to produce sixteen perspective images. The host computer produces a 'start' command for the linear translation stage controller in order to simultaneously initiate the image acquisition process and the translation stage movement.

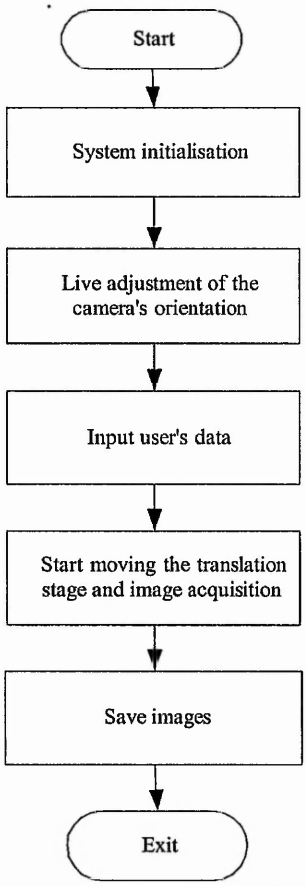

Figure 5-9 *System operation flowchart for image acquisition using the line-scan technique*

As discussed in Section 5.5.1, the image frame produced by the area array camera is stored in a real-time buffer. To acquire three perspective images, the specific memory regions, R_1 to R_3 (i.e. the memory region used to store the information obtained from the selected photosite column), are assigned as the image source to form a line-scan image. This image data is then transferred to the appropriate storage buffers, B_1 to B_3, to form the line-scan images as illustrated in Figure 5-10. The acquisition of image data for each corresponding line in the sequential image buffer occurs in parallel with the line acquisition process. With reference to Figure 5-11, once the image acquisition process for the first photosite column (P_1) is initiated, the photosite columns, P_2 and P_3, are required to wait for a period of time $\Delta t_{1\leftrightarrow n}$ before starting the image acquisition as discussed in Section 4.2.1. This is achieved by introducing time delays, $\Delta t_{1\leftrightarrow 2}$ and $\Delta t_{1\leftrightarrow 3}$, at the start of the image acquisition process for the relevant photosite columns. Thus there are a number of overlapping scanning regions, A to E, during the image acquisition process. For instance, the timing diagram of the image acquisition process for a 3-view arrangement is illustrated in Figure 5-11.

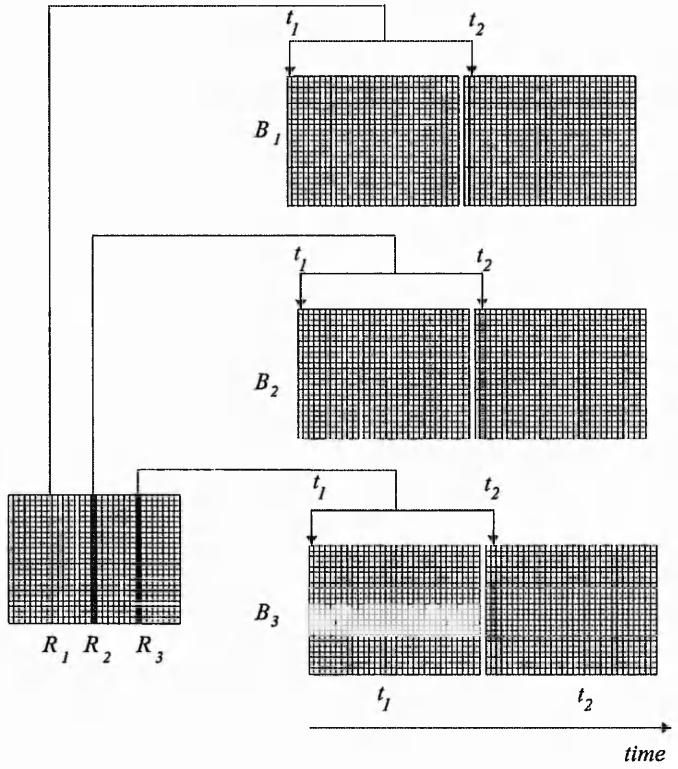

Figure 5-10 *The production of multiple line-scan images using specific memory allocation in order to store image information from a number of predetermined photosite columns*

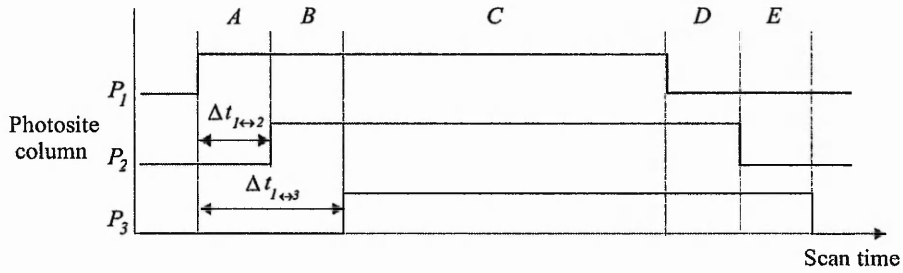

Figure 5-11 *Timing diagram for the production of an overlapping region in object space during the image acquisition process*

The sequential image capture process is repeated until the predetermined number of columns chosen to form a line-scan image is completed. At this point, perspective images are resident in the frame grabber's memory; image information from each column is stored in the correct orientation in order for human observer to interpret the scene under inspection. The resultant images are saved in a *Bitmap* (*BMP*) format for the following reasons:

- to produce a compatible image format for the sequential display system;
- can be read by most image processing application packages for coordinate determination and image processing (e.g. manipulation of contrast or brightness of the image).

5.5.2 Experiments with the two-dimensional arrangement

This section examines the two-dimensional imaging characteristics of the line-scan imaging technique. These are empirically evaluated in terms of system parameters that affect the production of a line-scan image in both x and y axes. These are:

Motion axis (x-axis)	Y-axis
Translation speed	Camera-to-object range
Line acquisition time	Focal length

Table 5-1 *System parameters that affect the production of a line-scan image*

The effect of independently changing the values of each of these parameters is investigated in a series of experiments. Each experiment uses a test object as shown in Figure 5-4a. The test card is placed on the mounting rack as illustrated in Figure 5-12. The horizontal sides of the test card is arranged to be parallel with the direction of motion. The perimeter of the imaged square provides a convenient edge from which the pixel measurements $L_{xi(pix)}$ and $L_{yi(pix}$ can be determined in the resultant images.

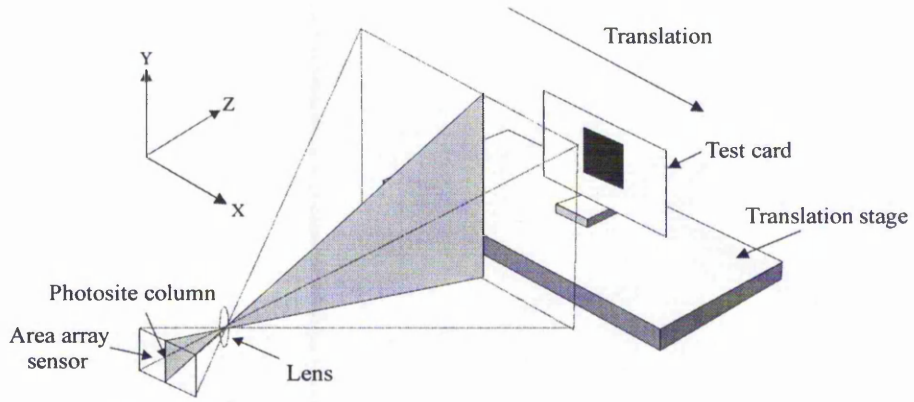

Figure 5-12 *Experimental set-up for the two-dimensional line-scan experiments*

A single perspective image with a resolution of 512 pixels x 480 pixels of the test card (Figure 5-4a) is produced at the end of each experiment.

X-axis evaluation

To evaluate the x-axis imaging characteristics *Equation 3-3* is used. The equation can be represented in terms of pixels when the screen size is measured in pixels. Thus:

$$L_{xi(pix)} = \frac{L_{xo}\, D_{x(pix)}}{S\, t\, N_x} = \frac{L_{xo}}{S\, t} \qquad \ldots(5\text{-}4)$$

where $D_{x(pix)}$ and N_x are the number of pixel columns on the screen and the number of scan lines in object space respectively. In normal circumstances $D_{x(pix)} = N_x$.

a) Translation speed

The range of translation speeds used in this experiment is from 1.5 mm/s to 7 mm/s, with 0.25 mm/s increments. The x and y axis components of the imaged square are plotted against speed in Graph 5-1. Experimental conditions: $f = 25$ mm, $Z = 700$ mm, $t = 120$ ms.

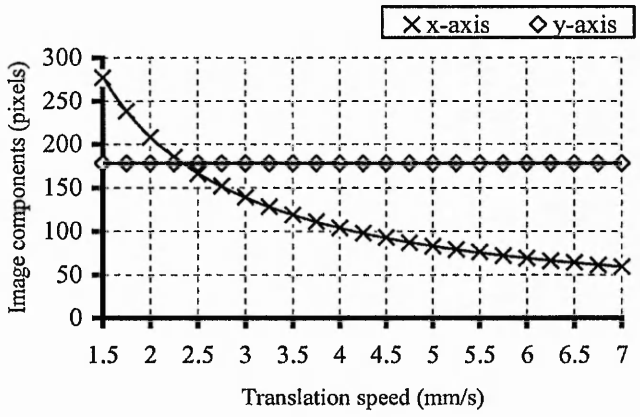

Graph 5-1 *Change in the x-axis image component and the y-axis image component with respect to the translation speed*

b) Line acquisition time

The line acquisition time is tested from 80 ms to 440 ms in 40 ms increments. The components of the imaged square for each image axis are plotted against the line acquisition time in Graph 5-2. Experimental conditions: $f = 25$ mm, $Z = 700$ mm, $S = 1.5$ mm/s.

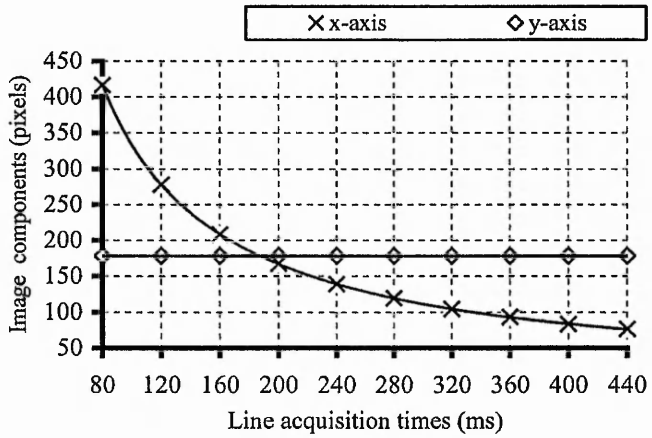

Graph 5-2 *Change in the x-axis image component and the y-axis image component with respect to the line acquisition time*

Discussion of the experimental results for x-axis evaluation

From Graph 5-1 and Graph 5-2, the following characteristics are evident:

- the y-axis image component of the 'square' is constant and independent of speed and line acquisition time;

- the motion axis image component of the 'square' decreases with increasing translation speed and the line acquisition time;
- the rate of change of the motion axis image component decreases as an inverse square function of the translation speed and line acquisition time; this can be explained by differentiating *Equation 3-3* with respect to translation speed and line acquisition time as follows:

$$\frac{dL_{xi(pix)}}{dS} = -\frac{D_{x(pix)}\,L_{xo}}{S^2\,t\,N_x} \quad ...(5\text{-}5) \qquad \frac{dL_{xi(pix)}}{dt} = -\frac{D_{x(pix)}\,L_{xo}}{S\,t^2\,N_x} \quad ...(5\text{-}6)$$

- the crossover point in both graphs (Graph 5-1 & Graph 5-2) indicate the speed and line acquisition time at which a 1:1 aspect ratio image can be produced as indicated by *Equation 3-11*. This only applies to the line-scan technique since the magnification in imaging axes produced by the area array technique are identical.

Samples of the resultant images for a variation of speed and line acquisition time are shown in Figure 5-13. It is observed that the brightness of the resultant images is the same for different line acquisition times. This is due to the photon integration period being independent of the line acquisition time. The speed and line acquisition time determine the amount of time taken to produce a line-scan image. Thus, if either of these parameters is increased, the inspection distance in object space will be increased and consequently results in an increase in the motion axis field of view as expressed by *Equation 3-1*; this leads to the imaged square appearing compressed in the motion axis.

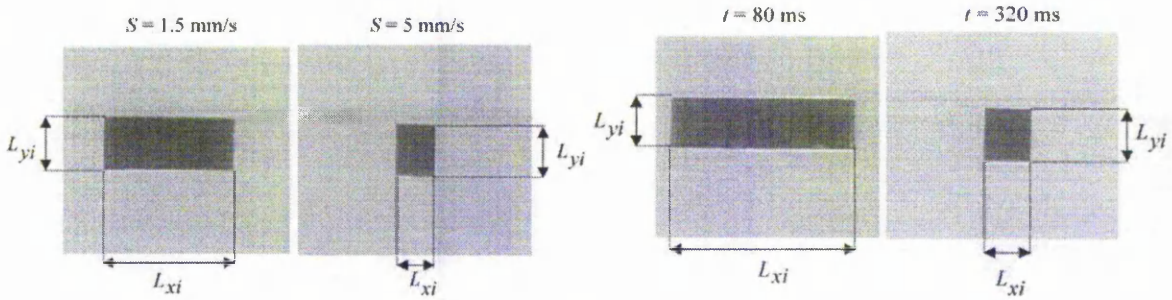

Figure 5-13 *The 'square' in the x and y axes with a) increasing translation speed and b) increasing the line acquisition time*

The reduction of the translation speed or line acquisition time will *'stretch'* the imaged square in the x-axis.

Y-axis evaluation

To evaluate the y-axis imaging characteristics *Equation 3-10* is used.

a) Camera-to-object range

The camera-to-object range is tested at 50 mm increments for ranges between 250 mm to 700 mm and the components of the imaged square for each image axis are plotted against range in Graph 5-3. Experimental conditions: $f = 25$ mm, $S = 3.4$ mm/s, $t = 80$ ms.

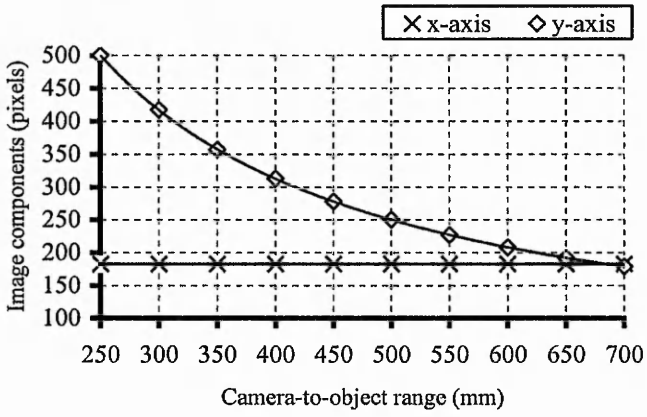

Graph 5-3 *Change in the x-axis image component and the y-axis image component with respect to the camera-to-object range*

b) Focal length

The focal length utilized in this experiment are 12.5 mm, 16 mm, 25 mm and 50 mm. The components of the imaged square for each image axis are plotted against focal length as shown in Graph 5-4. Experimental conditions: $Z = 600$ mm, $S = 3.4$ mm/s, $t = 80$ ms.

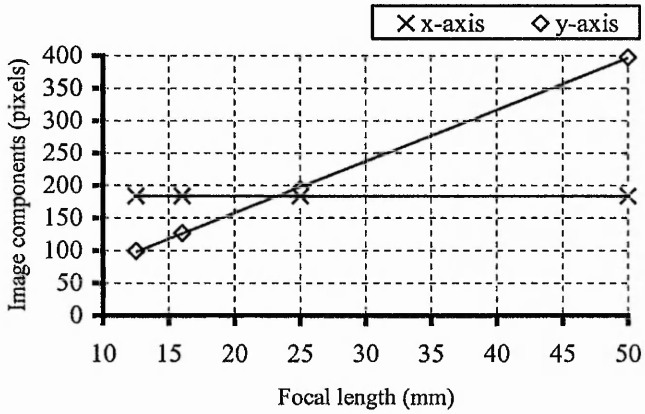

Graph 5-4 *Change in the x-axis image component and the y-axis image component with respect to the focal length*

Discussion of the experimental results for y-axis evaluation

From Graph 5-3 and Graph 5-4, the following characteristics are evident:

- the motion axis image component of the 'square' is constant and independent of range and focal length;
- the y-axis image component decreases with a) increasing camera-to-object range or b) decreasing focal length in each experiment;
- the rate of change of the y-axis image component decreases linearly with the focal length and decreases non-linearly with the camera-to-object range as indicated in *Equation 5-7*:

$$\frac{dL_{yi(pix)}}{dZ} = -\frac{L_{yo}\, f\, D_{y(pix)}}{Z^2\, L_{ys}} \qquad \ldots (5\text{-}7)$$

- the crossover point in both graphs (Graph 5-3 & Graph 5-4) indicate the range or focal length at which a 1:1 aspect ratio image can be produced as indicated by *Equation 3-11;*

Examples of the resultant images for variation of camera-to-object range and focal length are shown in Figure 5-14.

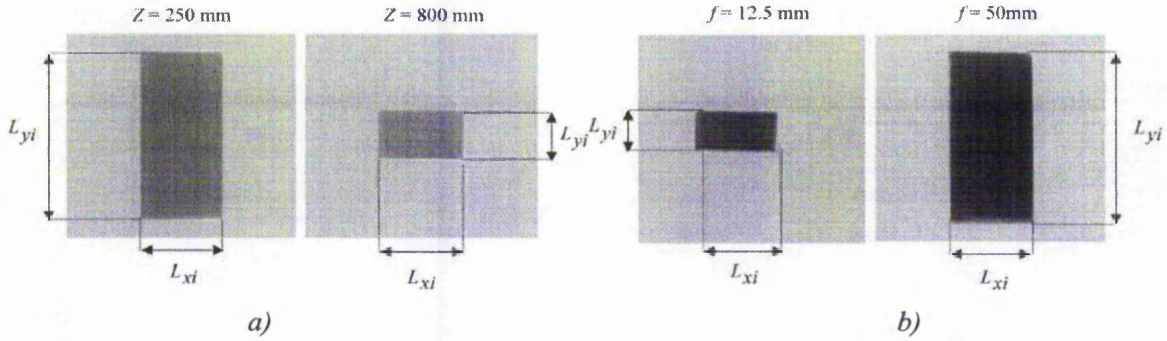

Figure 5-14 The *'square' in the x and y axes with a) increasing camera-to-object range and b) increasing the focal length*

It can be concluded that the potential spatial resolution in the y-axis is governed by the camera-to-object range and the focal length. This resolution increases with a) decrease in the camera-to-object range or b) increases in the focal length.

5.5.3 Experiments with the multiple view line-scan arrangement

To evaluate the three-dimensional imaging characteristics of the multiple view line-scan technique the experimental arrangement as shown in Figure 5-15 is set up. Experiments to evaluate the three-dimensional imaging aspects of the line-scan arrangement are listed in Section 5.3c. Two photosite columns are used as individual sensors to produce line-scan images. The test object is placed normal to the optical axis of the camera lens and its horizontal sides are arranged to be parallel with the direction of motion.

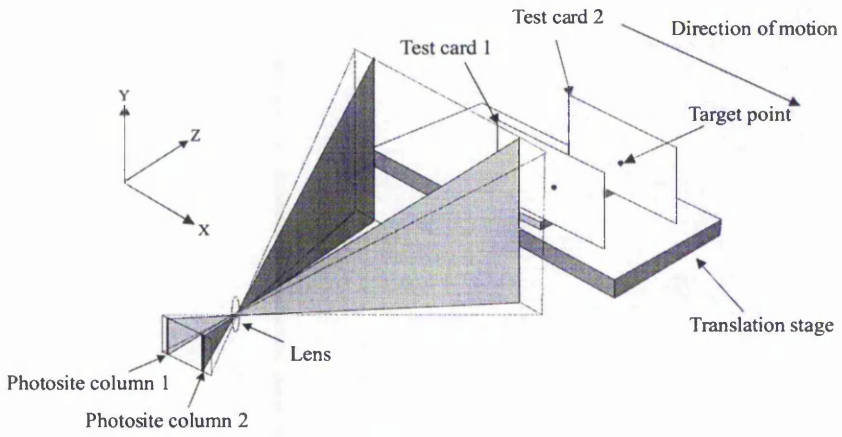

Figure 5-15 *Experimental line-scan arrangement in order to produce an image pair for parallax determination*

a) Spatial registration of perspective images

A single test card is used in this experiment to evaluate the spatial registration of the perspective images with respect to a convergence plane in object space. The convergence plane produces a fixation plane in the display where zero parallax will be observed for an imaged point for successive views. As described in Section 4.2.1, a convergence plane can be effected by introducing a time delay into the image acquisition process. In this experiment, the slit field of view produced by line-scan sensor No.1 is used as a reference view. The convergence angle used in this experiment is 5°. The central photosite column (i.e. photosite column No. 320) is used as a reference column. In order to produce an even distribution of the perspective views an angular distribution of +2.5° and -2.5° is used. The number of photosite columns to be displaced from the central column to effect a convergence angle of 5° is determined from *Equation 5-2.*

$$n_{line} = \frac{f \tan\alpha \; L_{xf(pix)}}{L_{xs}} = \frac{25\text{ mm x }\tan 2.5^\circ\text{ x }640}{6.4\text{ mm}} = 109\text{ lines}$$

Thus, the two photosite columns chosen for this task are 320+(109) = 429 and 320-(109) = 211. This method of determining the convergence angle is adopted, throughout this work, for the line-scan arrangement. The convergence plane in this experiment is fixed at a range of 370 mm from the nodal point by applying *Equation 4-2.*

$$\Delta t_{1\leftrightarrow n} = \frac{Z_c(2\tan\alpha)}{S} = \frac{370\text{ mm x }2(\tan 2.5^\circ)}{5\text{ mm/s}} = 6.4\text{ seconds}$$

Therefore, a time delay of 6.4 seconds is introduced to the start of the image acquisition of line-scan sensor No. 2. As discussed in Section 5.5.1c (page 55) the extent of the time delay introduced in this experimental arrangement is set in terms of the number of line delays before the start of image acquisition of sensor No. 2. Thus the time delay is achieved by delaying

80 lines (6.4 s/80 ms) before sensor No. 2 is used in the image acquisition process. The test card is imaged at a camera-to-object range of 200 mm. Two perspective images, each from one of the line-scan sensors, are obtained at the end of the experiment. The procedure is repeated for camera-to-object ranges of 250 mm to 550 mm in increments of 50 mm. The identical time delay is used for each of these experiments. The difference in the x-coordinate (parallax) produced by a pair of perspective images are plotted against the camera-to-object range in Graph 5-5. Experimental conditions: $f = 25$ mm, $Z_c = 370$ mm, $S = 5$ mm/s, t = 80 ms, $\sigma = 5°$, $\Delta l = 80$.

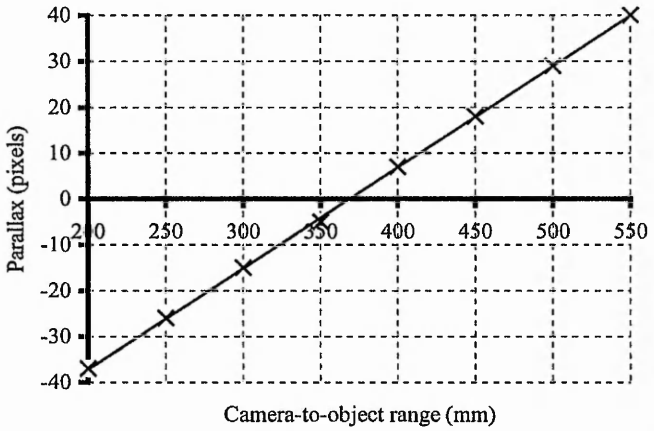

Graph 5-5 *Parallax as a function of increasing camera-to-object range*

Discussion of the experimental results for spatial registration

From Graph 5-5, the following characteristics are evident:

- the parallax value increases linearly with respect to object range as predicted in *Equation 4-3*;
- the crossover point (i.e. the x-coordinate of the imaged point is the same in two resultant images) indicates the position of the convergence plane in object space. This convergence plane in the graph is approximately 370 mm from the nodal point;
- both positive and negative parallax are produced as a function of the test card's position in object space with respect to the convergence plane (i.e. 370 mm from the nodal point). A test card which lies in front of this convergence plane produces a negative parallax value whilst a test card which lies behind the convergence plane produces a positive parallax value as predicted by *Equation 4-6*.

b) Convergence angle

To evaluate the effect of the convergence angle on the production of parallax value *Equation 4-6* is used. The parallax value (x_{bl} - x_{al}) is obtained by determining the difference between the x-coordinate of the corresponding points in each of the successive perspective images. The convergence angle used in these experiments ranges from 1° to 5° in increments of 0.5°. The perspective slit field of view is obtained by applying *Equation 5-2* and the calculated pixel columns

to be chosen for a given convergence angle are tabulated in Table 5-1. The central column, 320, is used as a reference to produce an even distribution of perspective views. The convergence plane in this experiment is fixed at 600 mm from the lens's nodal point at a convergence angle of 1°. This is determined by *Equation 4-2* and the calculated time delay required for the start of the image acquisition process for sensor No. 2 is 5.2 seconds (or 5.2 s/80 ms = 65 lines after sensor No. 1 has started line acquisition).

Convergence angles (degrees)	Photosite column 1	Photosite column 2	Number of photosite column separations
1.0	298	342	44
1.5	288	353	65
2.0	277	364	87
2.5	266	375	109
3.0	255	386	131
3.5	244	397	153
4.0	233	408	175
4.5	222	419	197
5.0	211	430	219

Table 5-2 *Convergence angles with the corresponding separation (in pixels) between the selected photosite columns*

The experiment is repeated with identical time delays for the other convergence angles listed in Table 5-2. Parallax values produced by the two line-scan sensors are plotted against the convergence angle and are depicted in Graph 5-6. Experimental conditions: f = 25 mm, Z_c = 600 mm, S = 2 mm/s, t = 80 ms.

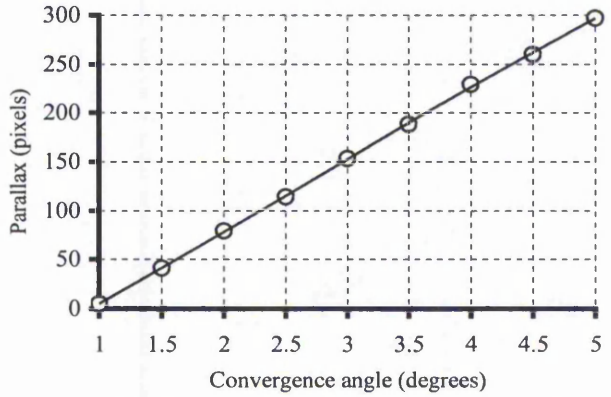

Graph 5-6 *Change in parallax with increasing the convergence angle*

Discussion of the experimental results for convergence angle variation

From Graph 5-6, it can be appreciated that the parallax increases linearly with respect to convergence angle. This is because the identical time delay (i.e. 5.2 seconds) is used for all the experiments having different convergence angles. Thus rearranging *Equation 4-2*, the position of the convergence plane in object space is governed by the time delay and the convergence angle. In this experiment, the time delay is fixed and the convergence angle is increased. When the

convergence angle is increased for a given time delay, the convergence plane is brought closer towards the camera which in turn gives rise to an increasing parallax value for a given point in object space. In fact, the parallax value is not linearly proportional to the convergence angle. Instead, it is a tangential function as expressed in *Equation 4-3*. The linearity observed is in fact a result of the small angles used (< 5°). The rate at which the convergence plane changes its position is dependent upon the convergence angle as depicted in Graph 5-7.

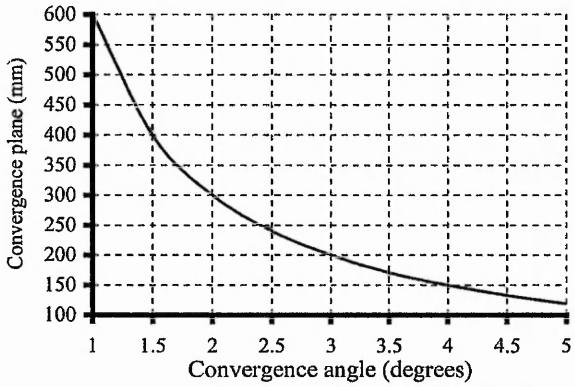

Graph 5-7 *Change in the position of the convergence plane in object space as a function of convergence angle*

c) Relative parallax produced by successive image pairs

The interrelationship of the perspective images produced with different convergence angles, is evaluated in terms of parallax. The same test card arrangement as shown in Figure 5-15 is imaged with different orientations, for the same convergence angle, at a range of 300 mm. This test card arrangement is linearly translated through the field of view of three different pairings of line-scan sensors as shown in Figure 5-16.

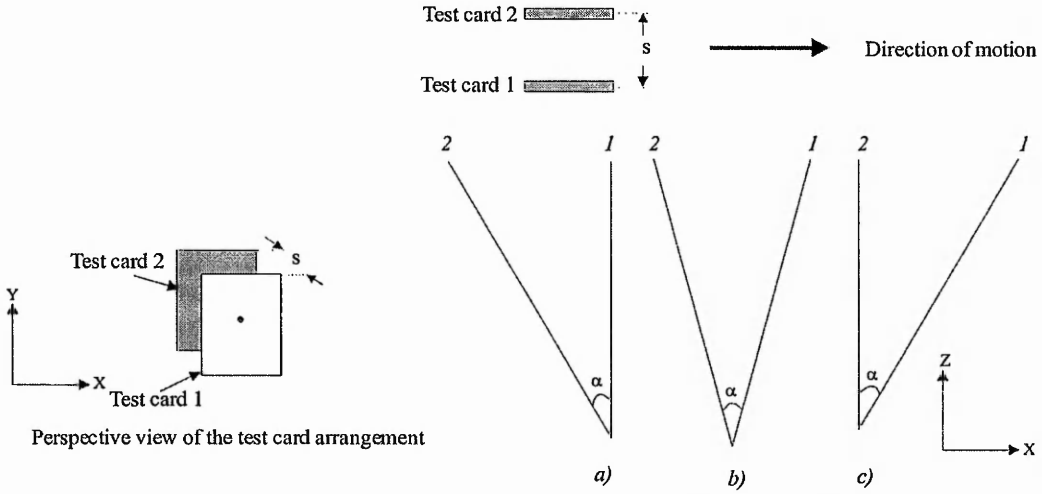

Figure 5-16 *Three sets of 'two successive line-scan sensors' with the same convergence angle*

Point *a* is located at a fixed location in object space and point *b* is moved away from point *a* to produce a range separation in object space. Six perspective images or three successive image pairs (i.e. S_1-S_2, S_3-S_4 and S_5-S_6) are obtained at the end of the experiment. This experiment is repeated for an increasing range separation of 30 mm between the two test cards. Two images with two imaged targets are obtained at the end of each experiment. The difference in the x-coordinate position between imaged targets is measured. The procedure for relative parallax determination is discussed is the following text.

Procedure for relative parallax determination

Figure 5-17 depicts two perspective images, for each range separation of object points, obtained from two different positions with respect to the test card arrangement. The x-coordinate of the imaged points, with respect to the most left pixel column, for each image are determined. For instance, resultant image No. 1 has two imaged points, *a1* and *b1*, and the coordinate positions of these are given by x_{a1} and x_{b1}. Therefore, the coordinate difference is expressed as $(x_{b1} - x_{a1})$ where '1' represents the 'number' of the perspective image.

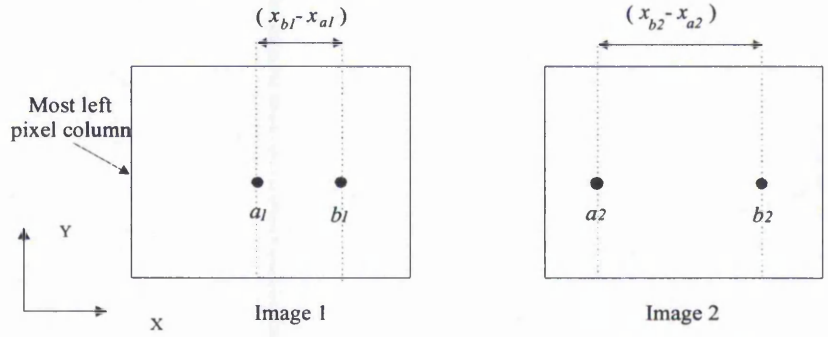

Figure 5-17 *Diagrammatic representation of the two-dimensional images produced by a pair of line-scan sensors for relative parallax determination*

The same procedure is applied to the second perspective image where the coordinate difference is $(x_{b2} - x_{a2})$. The notations for relative parallax determination are summarised in Table 5-3.

Image 1		Image 2	
x-coordinate of point 'a'	x_{a1}	x-coordinate of point 'a'	x_{a2}
x-coordinate of point 'b'	x_{b1}	x-coordinate of point 'b'	x_{b2}
coordinate difference	$(x_{b1} - x_{a1})$	coordinate difference	$(x_{b2} - x_{a2})$

Table 5-3 *Determination of relative parallax value*

Thus the difference between the 'coordinate differences', $(x_{b1} - x_{a1})$ and $(x_{b2} - x_{a2})$, for two perspective images gives rise to a relative parallax value. This may be expressed by:

$$P_{rd} = (x_{b2} - x_{a2}) - (x_{b1} - x_{a1}) \qquad ...(5\text{-}8)$$

The methodology of determining the relative parallax for a given range separation in object space is adopted in the following experiments for both line-scan and lateral shift techniques.

The relative parallax produced by the range separation for object points is plotted against the range separation in Graph 5-8a to Graph 5-8c. Experimental conditions: f = 25 mm, Z_c = 100 mm, S = 2 mm/s, t = 80 ms.

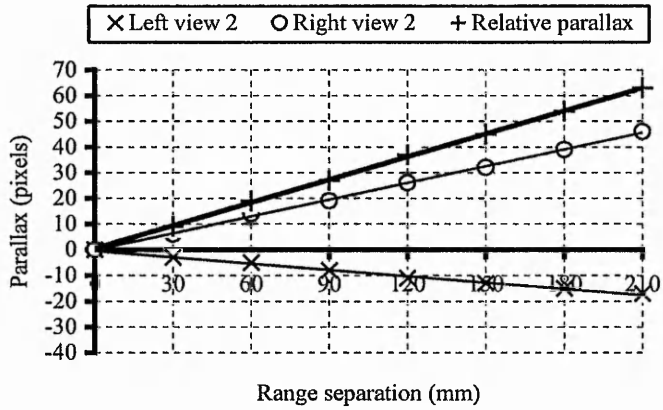

Graph 5-8a *The growth of relative parallax in the first image pair*

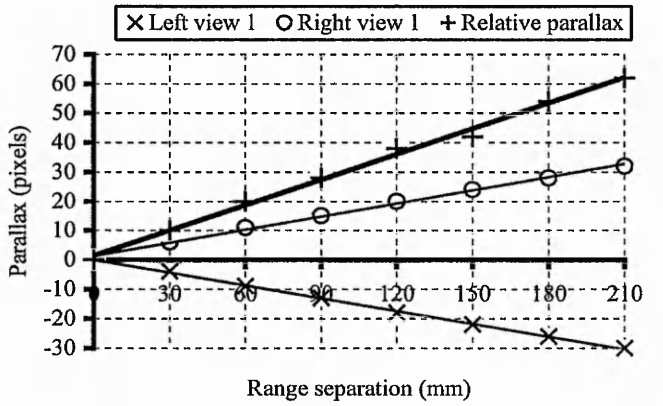

Graph 5-8b *The growth of relative parallax in the second image pair*

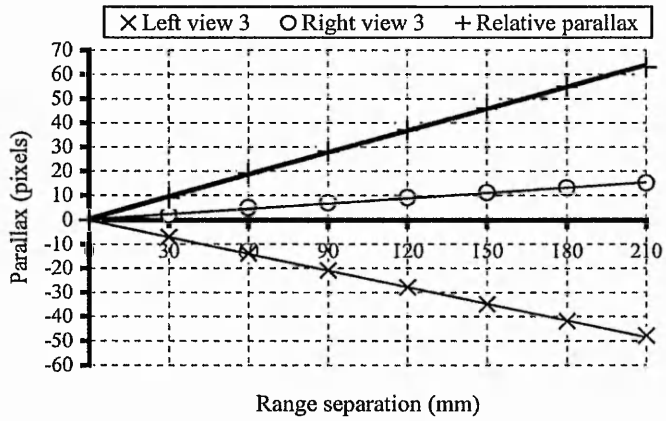

Graph 5-8c *The growth of relative parallax in the third image pair*

Discussion of the experimental results for the production of relative parallax

Graph 5-8a to Graph 5-8c depict the growth of parallax information for three image pairs for a given convergence angle. It is observed that the relative parallax value is produced by the difference in x-coordinate positions between two imaged points. The total parallax produced by three of the image pairs is nominally the same when a small convergence angle is used (< 5° between successive views).

d) Voxel distribution

i) Depth plane distribution

Two test cards, with an increasing range separation in object space from 0 to 210 mm in steps of 30 mm, are imaged at three different convergence angle settings, namely 1°, 3° and 5°, in each experiment. Two line-scan sensors with a convergence angle of 1° are used to produce two perspective images. Point *a* is fixed and point *b* is moved away from point *a* to create a range separation in object space. The relative parallax value (i.e. separation between point *a* and point *b*) is plotted against the range separation as depicted in Graph 5-9. This experiment is repeated for convergence angle of 3° and also 5°. Experimental conditions: $f = 25$ mm, $S = 2$ mm/s, t = 80 ms.

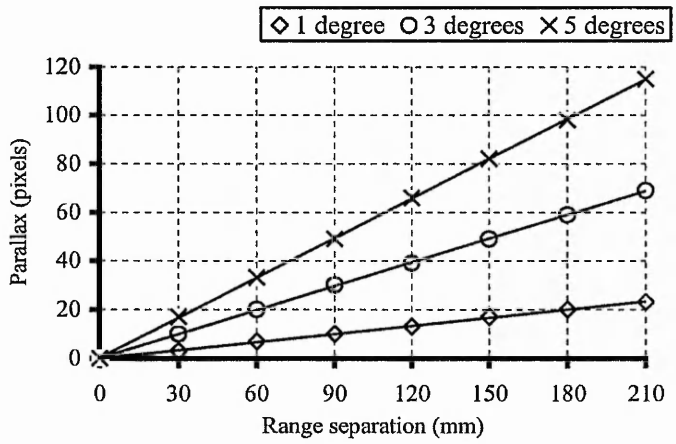

Graph 5-9 *Change in parallax with increasing range separation between two test cards in object space for three different convergence angles*

Discussion of the experimental results for depth plane distribution

From Graph 5-9, the following characteristics are evident:

- the gradient for all convergence angles in Graph 5-9 is constant with increasing range separation. This implies that the depth plane intervals and the dimensions of the voxel structures are constant and independent of the object range as indicated in *Equation 4-10.* This in turn infers that the potential spatial resolution in the z-axis is constant and this is diagrammatically presented in Figure 5-18;

- the increasing rate of change of parallax as a function of convergence angle observed in Graph 5-9 infers a corresponding increase in voxel density, depth plane density and potential resolving capability in the z-axis.

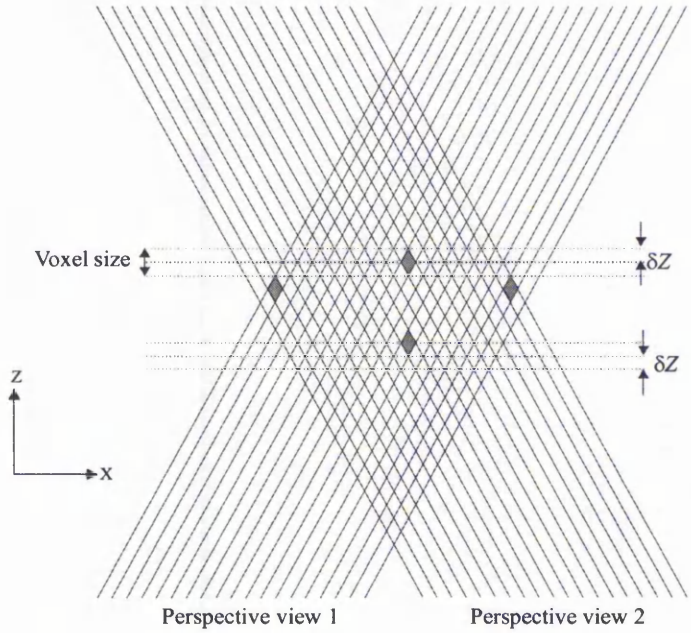

Figure 5-18 *Spatial sampling pattern in object space produced by the line-scan technique*

ii) Depth plane characteristics

A test card with eleven points each with a fixed separation of 5 mm (Figure 5-19) is imaged by two line-scan sensors with a convergence angle of 3° at an object range of 300 mm. Two perspective images, each from the respective sensor, are obtained at the end of the experiment. The separations between two successive targets are measured in each resultant image. The difference, in pixels, for the corresponding separations between both images is plotted in Graph 5-10. The experiment is repeated for a camera-to-object range of 400 mm and also 500 mm. Experimental conditions: $Z_1 = 300$, $Z_2 = 400$ mm, $Z_3 = 500$ mm, $\sigma = 3°$.

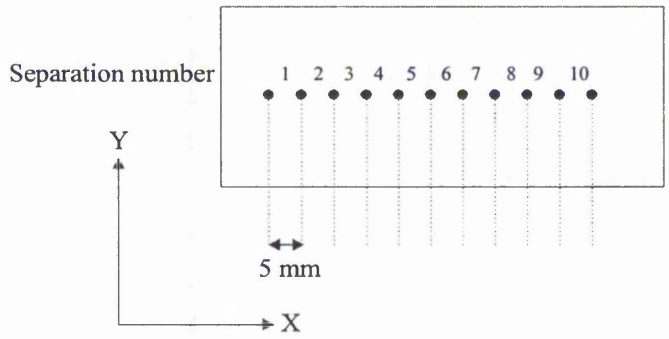

Figure 5-19 *Test card with eleven equidistant circular targets*

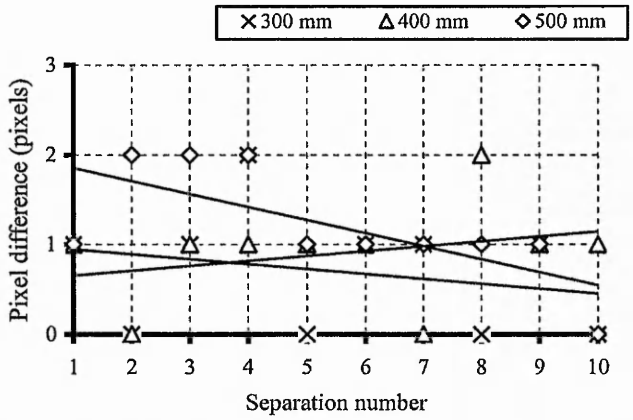

Graph 5-10 *Difference in parallax produced by a series of separations between two object points*

Discussion of the experimental results for the characterization of the depth planes

This experiment investigates the geometric properties (i.e. parallel or curvilinear) of depth planes produced by the line-scan arrangement. If the depth planes are parallel, ideally, the coordinate difference between the two corresponding point separations in the perspective images is the same. From Graph 5-10, it is observed that there are negligible pixels differences (±1 pixel) between two imaged points. A nominally flat line relationship between pixel difference and the corresponding target separation inferring parallel depth planes as predicted by the theoretical analysis (Section 4.2.4). Also this result infers that this technique will not produce vertical parallax (i.e. parallax in the y-axis in the display).

e) Sample perspective images produced by the multiple view line-scan technique

Figure 5-20 illustrates perspective images produced by the line-scan technique. The imaged objects include a camera, a pair of scissors, radio circuit board and a reel of tape (these objects are located, in sequence, from foreground to background in object space). The images are produced using the following experimental conditions:

- depth of field : 0.45 m
- maximum width and the maximum height of the objects : 0.2 m x 0.25 m
- pixel resolution of the image : 640 pixels x 480 pixels
- translation speed : 3 mm/s
- line acquisition time : 80 ms
- angular distributions : 3 ° between successive images

The objects were chosen with aviation security screening applications in mind (i.e. passenger luggage inspection). The electronic items are of particular interest in this application as they can form part of an explosive device.

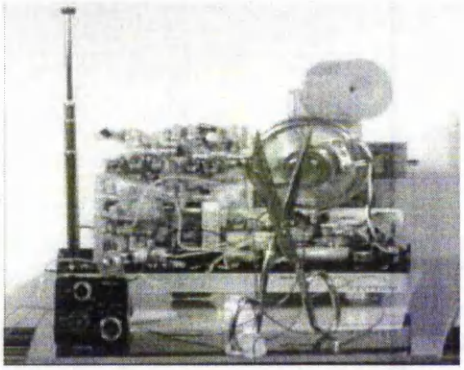

Sample image 1

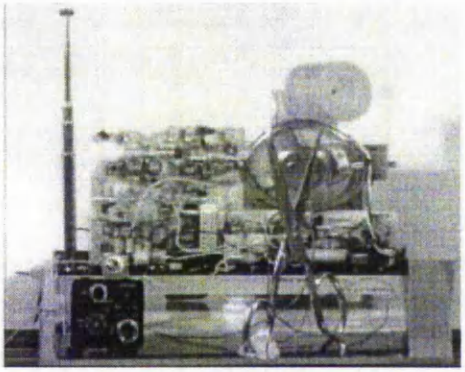

Sample image 2

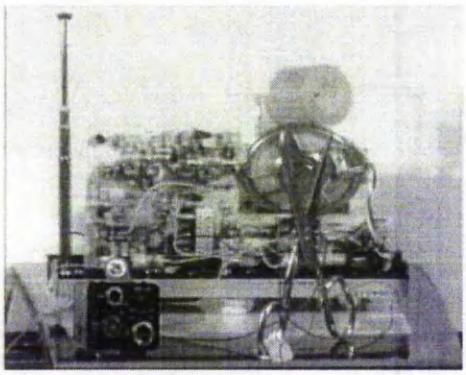

Sample image 3

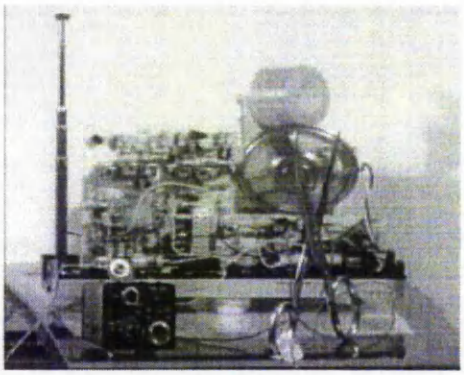

Sample image 4

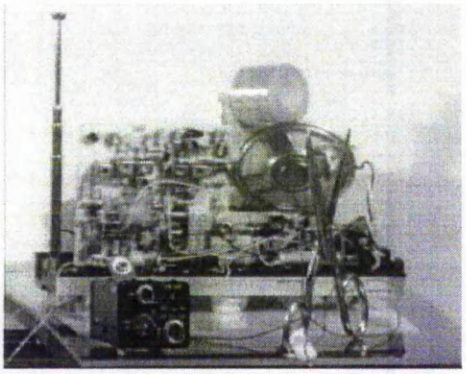

Sample image 5

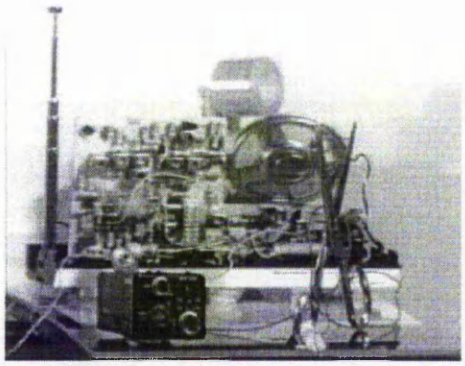

Sample image 6

Figure 5-20 *Sample images produced by the line-scan technique*

The perspective images are arranged as a set of binocular stereoscopic image pairs allowing 'free viewing' to be realized.

5.6 Experiments using an area array mode of operation

The experimental rig for the lateral shift technique is depicted in Figure 5-21.

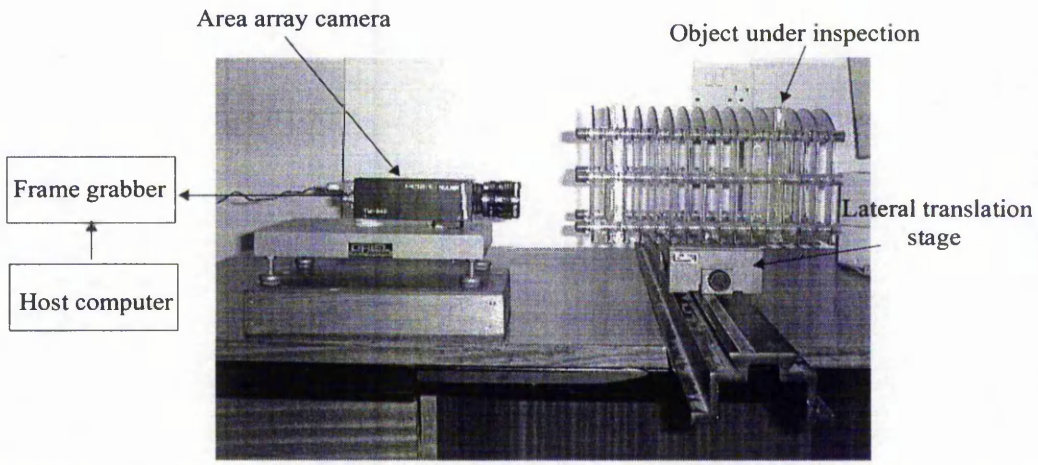

Figure 5-21 *The experimental multiple view arrangement for the lateral shift technique*

5.6.1 Image acquisition

Software code, written in the *C++* language with the aid of imaging functions from the *Matrox* imaging software library, is implemented in order to control the image acquisition process of the lateral shift imaging technique.

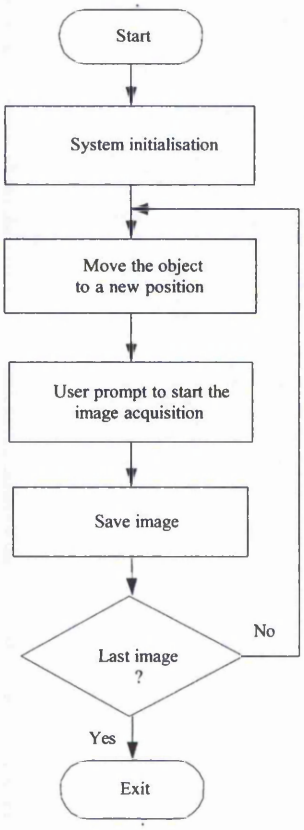

Figure 5-22 *System operation flowchart for image acquisition using the lateral shift technique*

Two-dimensional images or 'snapshots' are acquired using the area array camera. The system is set up such that sixteen snapshots can be acquired one after another at different relative positions with respect to the object under inspection. The imaging position for the object is achieved by the manual location of the translation stage using the measurement information indicated on the base rail. Figure 5-22 depicts the flowchart for the image acquisition process for the lateral shift technique. An image capture cycle begins with the initialisation of the frame grabber. During the initialisation, the buffers or dedicated memory regions for image storage are allocated. Following this, a live image is displayed on the monitor screen which allows the user to adjust the orientation of the camera and the lighting required for optimum image quality. The software is designed to allow sixteen snapshots to be acquired. The resultant images are saved in the *Bitmap* format.

5.6.2 Experiments with the two-dimensional arrangement

This section examines the characteristics of the image produced by the lateral shift technique. To evaluate the imaging characteristics produced by this technique requires the experimental set up as depicted in Figure 5-23. Thus the effects of varying the camera-to-object range and the focal length on the resultant images can be independently identified by measuring the image components in the x and y axes, $L_{xi(pix)}$ and $L_{yi(pix)}$, of the imaged black square.

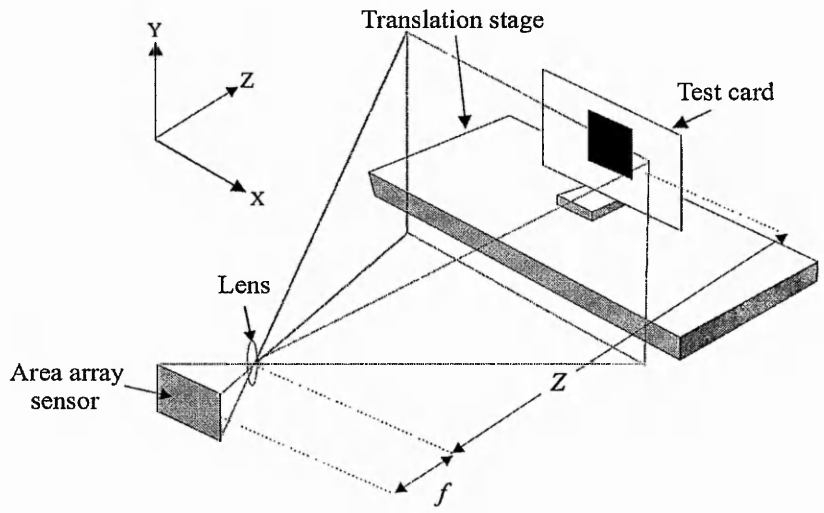

Figure 5-23 *Experimental set-up for the investigation of the 2-D imaging characteristics of the lateral shift technique*

The test card (Figure 5-4a) is placed normal to the optical axis of the camera lens and a number of snapshots are taken at different a) ranges and b) focal lengths in a series of experiments. A single perspective image with a resolution of 640 pixels x 480 pixels, is produced at the end of each experiment.

a) Camera-to-object range

The camera-to-object range is tested at 50 mm increments for ranges between 250 mm to 700 mm and the image components for each axis are plotted against the camera-to-object range in Graph 5-11. Experimental conditions: $f = 25$ mm.

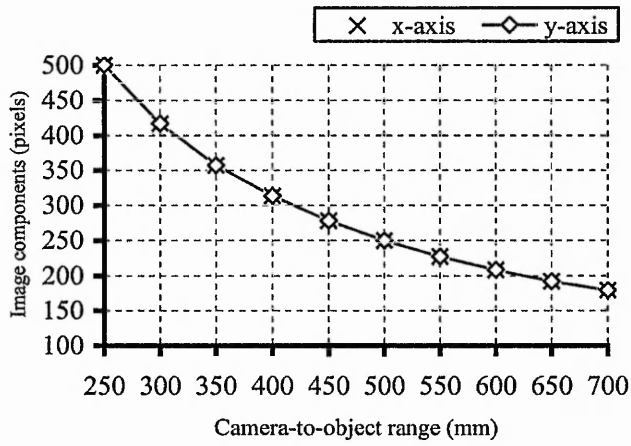

Graph 5-11 *Change in the x-axis image component and the y-axis image component with respect to the camera-to-object range*

b) Focal length

The focal lengths used are 12.5 mm, 16 mm, 25 mm and 50 mm, and the components of the imaged square in each axis are plotted against focal length as shown in Graph 5-12. Experimental conditions: $Z = 700$ mm.

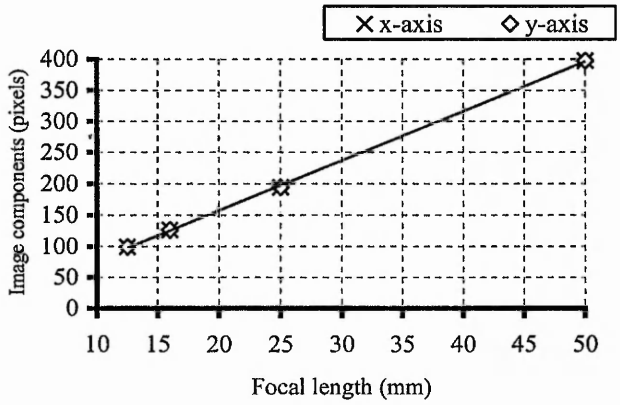

Graph 5-12 *Change in the x-axis image component and the y-axis image component with respect to the focal length*

Discussion of the experimental results for two-dimensional system

The results indicate that the image components in both x and y axes undergo nominally equal magnification from object space to image space for a given camera-to-object range and focal length.

From Graph 5-11 and Graph 5-12, the following characteristics are evident:

- the image components in both x and y axes a) decrease non-linearly with increasing camera-to-object range or b) increases linearly with increasing focal length;
- the resultant image has an aspect ratio of 4:3 due to the physical dimensions of the area array sensor (6.4 mm x 4.8 mm); the dimensions of the image storage buffer are assigned to 640 pixels x 480 pixels to preserve the aspect ratio;
- the image components in the x and y axes exhibit a 1:1 ratio as the magnification in both axes are identical;
- the spatial resolutions in the x and y axes are nominally equal and increase with reducing the camera-to-object range or increasing the focal length.

These findings are as to be expected for a conventional 2-D camera.

5.6.3 Experiments with the multiple view lateral shift arrangement

This section discusses the empirical evaluation of the three-dimensional imaging characteristics of the multiple view lateral shift arrangement.

a) Spatial registration of perspective images

Six perspective images are obtained of a test object for six different base separations. Each base separation increment is 10 mm. The resultant images are illustrated in Figure 5-24a. Experimental conditions: d_o =10 mm, f= 25 mm, Z= 400 mm.

Discussion of the experimental results for spatial registration

The resultant images are obtained from different positions with respect to the camera and thus the object under inspection appeared at different relative positions in the resultant images (Figure 5-24a). Therefore the object under inspection appears laterally shifted as well as exhibiting relative parallax in the resultant images. To produce an effective convergence plane in object space, a relative shift of the perspective images with respect to the reference image, in this case image No. 1, is applied. The desired convergence plane is arranged to be coincident with the test card located 400 mm from the camera. A set of pixel column shifts are introduced to images No. 2 to No. 6 with respect to image No. 1. The number of pixel columns required to be shifted to effect a convergence plane at a range of 400 mm is obtained by applying *Equation 4-16* and stated in Table 5-4.

Perspective image number	1	2	3	4	5	6
Number of pixels column shifts required $N_{1 \leftrightarrow n(pix)}$	0	64	128	192	250	312

Table 5-4 *Number of pixel shifts required to register the perspective images with respect to the reference image*

The relative positions of corresponding image features are illustrated in Figure 5-24b.

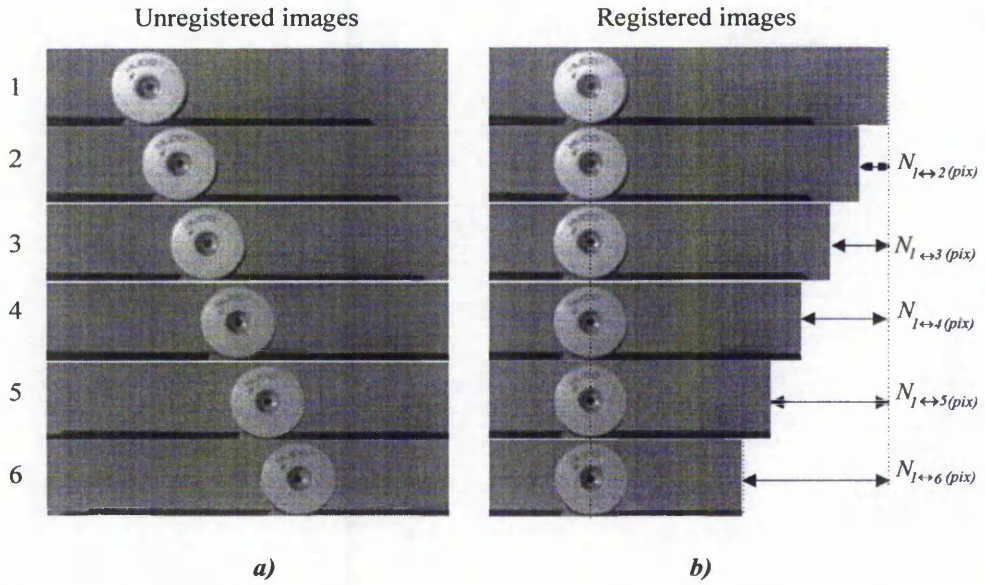

Figure 5-24 *Registration of six perspective images of a circular flat object produced by the lateral shift technique a) unregistered and b) registered*

It is observed that the planar object under inspection located at the convergence plane has a fixed x-coordinate value as indicated in Figure 5-24b.

b) Base separation

This experiment is designed to investigate the effect of base separation on the parallax production between successive views. The parallax value is determined by using two transparent test cards, each with a circular black target at the centre as shown in Figure 5-25. The target provides a convenient datum from which pixel measurements can be determined. Two transparent test cards are arranged as shown in Figure 5-25 to create a range separation in object space which corresponds to a given parallax in the resultant images.

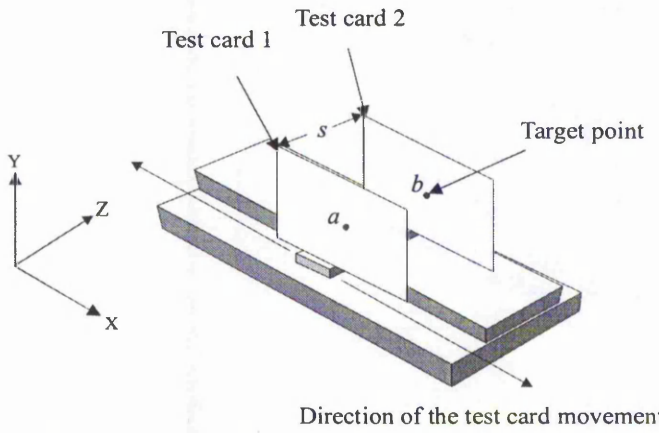

Figure 5-25 *Test card arrangement used to produce a range separation between two object points*

This arrangement is placed nominally parallel with the optical axis of the camera. The test card is located in the rack (Figure 5-4b) and is mounted in the lateral translation stage (Figure 5-3). Thus different base separations between successive views can be set. The test cards with a fixed range separation of 100 mm as shown in Figure 5-25 are imaged; point *a* and *b* are located at 500 mm and 600 mm from the camera respectively.

Twelve snapshots are taken at each position with an increasing base separation increments of 10 mm. The x-coordinates of the imaged points, with respect to the most left pixel column, are plotted against the base separation in Graph 5-13. The difference between the x-coordinate of these two imaged points, *a1* and *b1* (adopting '*a1*' and '*b1*' for imaged point *a* and point *b* respectively; '*1*' represents the number of the resultant image (Figure 5-26)), is also shown in Graph 5-13. For instance, each resultant image has two imaged points, *a1* and *b1*, and the x-coordinate positions of these are given by x_{a1} and x_{b1}. Therefore, the x-coordinate difference between these two imaged points is expressed as $(x_{b1}-x_{a1})$.

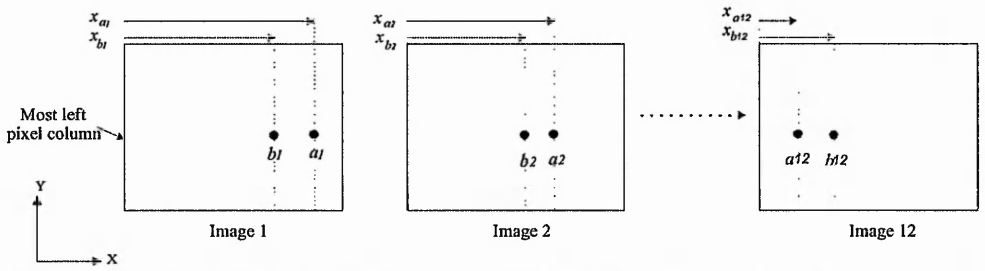

Figure 5-26 *Diagrammatic representation of the resultant two-dimensional images obtained from two test cards in order to produce a relative parallax*

Experimental conditions: d_o =10 mm, f= 25 mm, Z_a = 500 mm, Z_b = 600 mm.

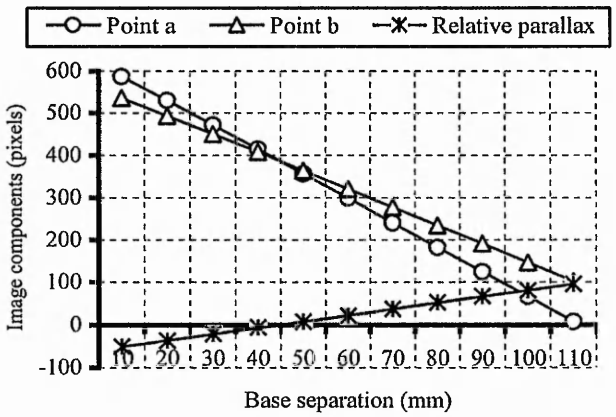

Graph 5-13 *Change in the x-coordinate of the imaged points with respect to the base separation*

Discussion of the experimental results for base separation variation

The results indicate that the change in x-coordinate of each imaged point is a linear function of the base separation. The intersection point of the gradients indicates that the two imaged points are

aligned with the camera optical axis. It should be noted the results presented are for an unregistered set of perspective images. These images may be registered to effect a convergence plane in object space by applying *Equation 4-16.* To observe the coordinate change of the two imaged points, the resultant images are arranged to appear converged at an object range of 600 mm. As there are only two imaged points in each resultant image the perspective images are converged with respect to the coordinate position of imaged point *b*. The pixel coordinates of the two imaged points in the registered set of images are again plotted against the base separation in Graph 5-14.

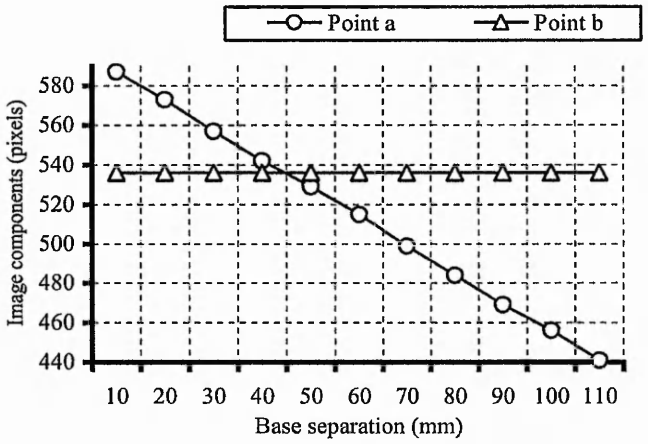

Graph 5-14 *Relative parallax of an object point with respect to the convergence plane*

It can be appreciated that the object point *b* appears at the convergence plane (i.e. no change in the x-coordinate value). Thus the x-coordinate of the point *a* is no longer a reference for the datum plane but the convergence plane in object space, that is, 600 mm from the nodal point. The coordinate difference between point *a* and *b* is the relative parallax of point *a* with respect to the convergence plane. It is observed that the relative parallax value of point *a* with respect to point *b* (convergence plane) remains unchanged in both directions or polarities. It should be noted that the increase in the base separation value is equivalent to a change in perspective views in the multiple view arrangement. Therefore, when these perspective images are displayed in a correct sequence, the image of point *a* will be perceived as moving from the left to the right with respect to the static point *b*.

c) Relative parallax produced by successive image pairs

The test card arrangement as shown in Figure 5-25 is imaged with increasing base separation values in increments of 30 mm at 6 different positions at a range of 300 mm (location of point *a* closest to the camera). The location of point *a* is fixed whilst point *b* is free to move in order to produce a range separation. Six perspective images or three successive image pairs (i.e. S_1-S_2, S_3-S_4 and S_5-S_6) are obtained at the end of the experiment. This experiment is repeated for increasing range separations of 30 mm between the two test cards. The successive image pairs are used to evaluate the growth of relative parallax as a function of range separation. The difference in the

x-coordinates between two imaged points of an image pair is measured. The identical procedure for relative parallax determination discussed on page 68 is applied. The x-coordinate difference between two image points, for all three successive image pairs, are plotted against the range separation in Graph 5-15a to Graph 5-15c. The relative parallax values contributed by these three sets of image pairs are also indicated in the graphs. Experimental conditions: f = 25 mm, d_o = 30 mm, Z_a = 400 mm, Z_b = 400 mm to 610 mm.

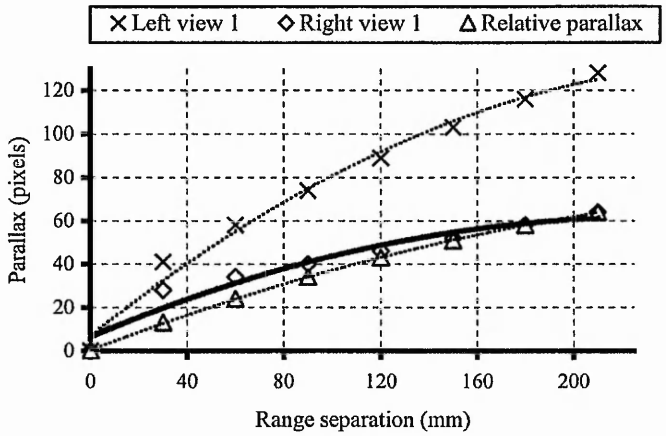

Graph 5-15a *The growth of relative parallax in the first image pair*

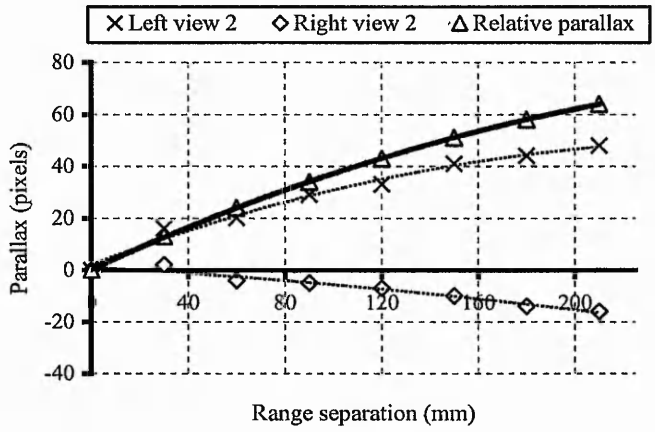

Graph 5-15b *The growth of relative parallax in the second image pair*

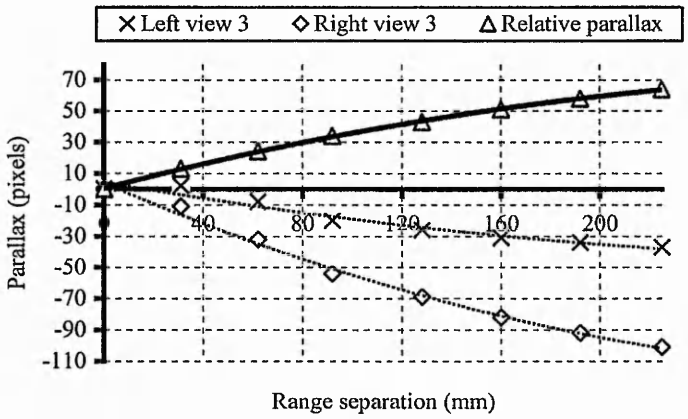

Graph 5-15c *The growth of relative parallax in the third image pair*

Discussion of the experimental results for the production of relative parallax

Graph 5-15a to Graph 5-15c depict the growth of parallax information for three image pairs for a given base separation. It is observed that the relative parallax value is produced by the difference in x-coordinate position between the two imaged targets. It is evident that:

- the difference in x-coordinate between imaged point *a* and point *b* reduces with increasing object range;
- the total parallax produced by all three perspective images is the same and this indicates that for a given range separation, parallax produced by successive views is the same as long as the base separation between successive views is the same (*Equation 4-8*).

d) Voxel distribution

i) Depth plane distribution

Two test cards, with an increasing range separation from 0 to 240 mm in increments of 30 mm, are imaged for three different base separation values; these are 20 mm, 40 mm and 60 mm. Point *a* is fixed in space and point *b* is free to move away from point *a* to produce a range separation. The relative parallax value is obtained by using the method discussed on page 68 where $(x_{b2} - x_{a2}) - (x_{b1} - x_{a1})$ is determined. The relative parallax is plotted against range separation as depicted in Graph 5-16. Experimental conditions: f = 25 mm, d_{o1} = 20 mm, $do2$ = 40 mm, d_{o3} = 60 mm, Z_a = 300 mm, Z_b = 300 mm to 510 mm.

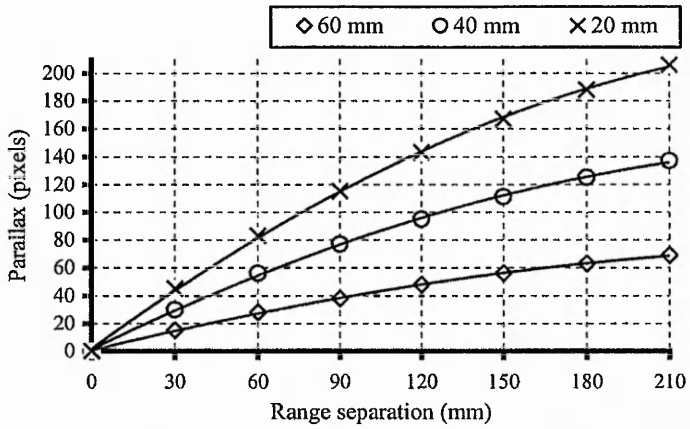

Graph 5-16 *Change in parallax information with increasing range separation between two test cards in object space for three different base separation values*

Discussion of the experimental results for depth plane distribution

From Graph 5-16, the following characteristics are evident:

- the gradient for all base separations in *Graph 5-16* decreases non-linearly with increasing range separation. This implies that the depth plane intervals and dimensions of the voxel structures in the z-axis decrease with increasing object range as predicted by

Equation 4-28. This in turn infers that the potential spatial resolution in the z-axis reduces with object range and this is diagrammatically depicted in Figure 5-27;

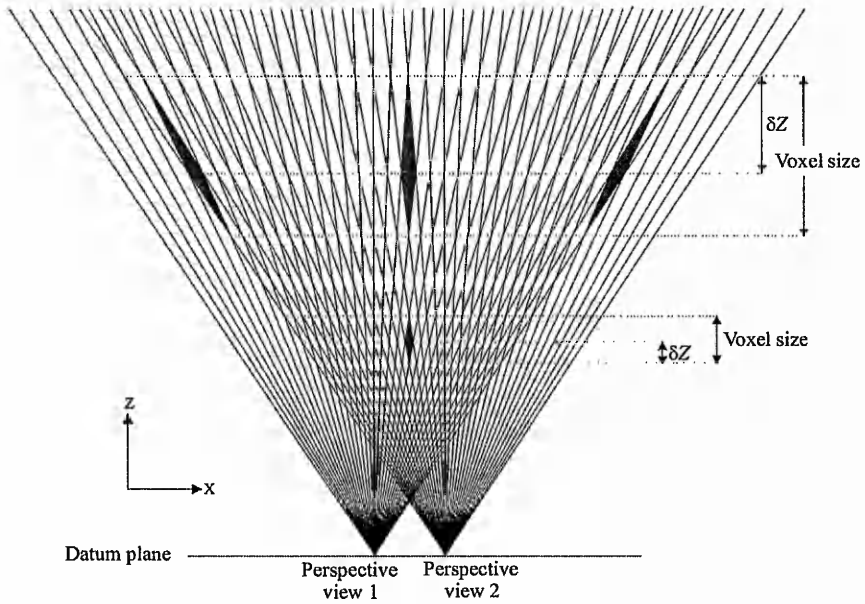

Figure 5-27 *Spatial sampling pattern in object space produced by the lateral shift technique*

- the gradient of the graph decreases when the base separation is increased, that is, the '20 mm experiment' has a lower gradient in comparison to the '60 mm experiment'. Referring to *Equation 4-18*, the magnitude of the base separation determines the magnitude of the gradient. Therefore, the potential spatial resolution in the z-axis can be increased by increasing the extent of base separation between two successive views.

ii) Depth plane characteristics

A test card (Figure 5-19) with eleven circular targets each separated by 5 mm is arranged to be normal with respect to the camera and imaged at a range of 300 mm. Two perspective images are obtained at the end of the experiment. The experiment is repeated for a camera-to-object range of 400 mm and also 500 mm. The separations between imaged targets are measured in each resultant image. The difference, in pixels, for the corresponding point separations between these images are plotted in Graph 5-17. Experimental conditions: $Z_1 = 300$, Z_2, 400 mm, $Z_3 = 500$ mm, $d_o = 30$ mm.

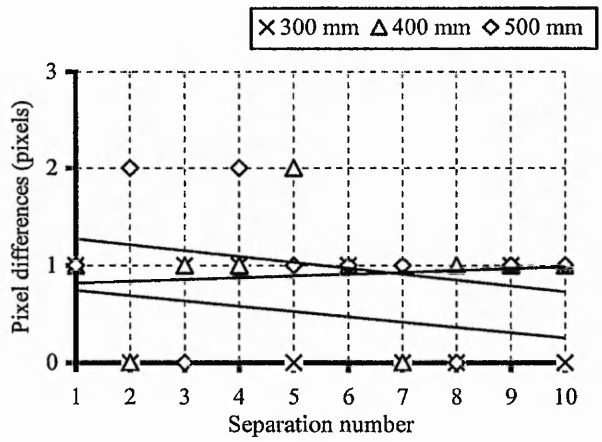

Graph 5-17 *Difference in parallax produced by a series of separations between two imaged points*

Discussion of the experimental results for the characterization of the depth planes

This experiment examines the characteristics (i.e. parallel or curvilinear) of the depth planes produced by the lateral shift arrangement. If the depth planes are parallel, ideally, the coordinate difference between two corresponding point separations in two perspective images is identical. From Graph 5-17, it is observed that there are negligible pixel differences between two imaged points. Thus a nominally flat line relationship between pixel difference and target separation is obtained. This infers parallel depth planes as predicted by the theoretical analysis (Section 4.3.4).

e) Sample perspective images produced by the multiple view lateral shift technique

Figure 5-28 illustrates perspective images produced by the lateral shift technique. The imaged objects include a camera, a pair of scissors, radio circuit board and a reel of tape (these objects are located, in sequence, from foreground to background in object space). These images are produced using the following experimental conditions:

- depth of field : 0.45 m
- maximum width and the maximum height of the object : 0.2 m x 0.25 m
- pixel resolution of the image : 400 pixels x 480 pixels
- base separation : 20 mm

Sample image 1

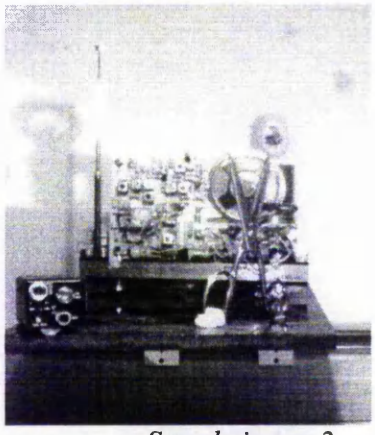

Sample image 2

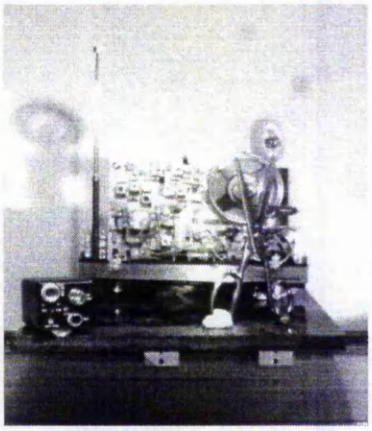

Sample image 3

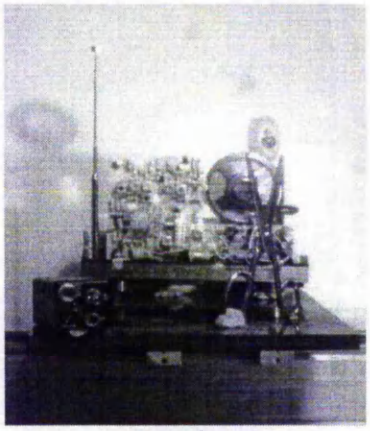

Sample image 4

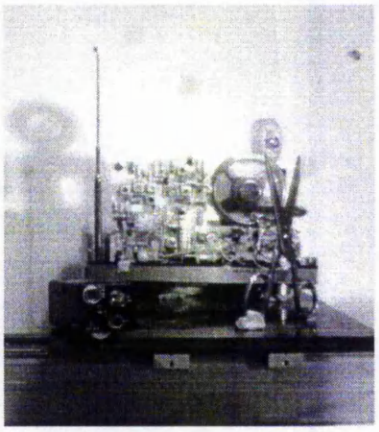

Sample image 5

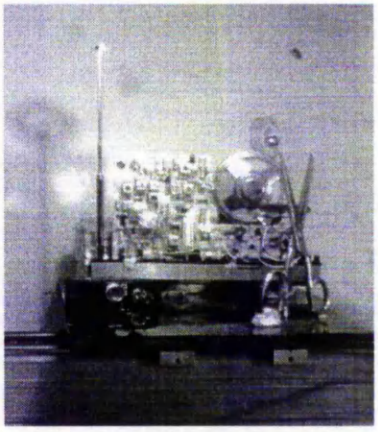

Sample image 6

Figure 5-28 *Sample images produced by the lateral shift technique*

The objects were chosen with aviation security screening applications in mind (i.e. passenger luggage inspection). The electronic items are of particular interest in this application as they can form part of an explosive device. The perspective images are arranged as a set of binocular stereoscopic image pairs allowing 'free viewing' to be realized.

5.7 Interim conclusions

I. Each of the multiple view techniques produce perspective images by utilising a single camera and a single object pass (i.e. lateral translation).

II. Each of the multiple view techniques are proved capable of producing converged images. The lateral shift technique registers the fixation plane after the images have been acquired whilst the line-scan technique enables the registration of the convergence plane/fixation plane during the image acquisition process.

5.7.1 Line-scan technique

Imaging concept

I. Two-dimensional imaging characteristics of the area array sensor, operating in a line-scan mode, are demonstrated to be *equivalent* to those produced by a dedicated line-scan sensor.

II. A visible light camera system operating in a line-scan mode was found to be a powerful tool for modeling the geometric imaging properties of the x-ray line-scan equipment.

2-D imaging characteristics

III. The x-axis field of view is determined by the interaction of the translation speed and the line acquisition time. The y-axis field of view is dependent upon the camera-to-object range and the focal length of the camera lens.

IV. The motion axis (x-axis) magnification is orthographic.

V. The magnification in the x and y axes can be arranged to produce a 1:1 object ratio for a given range.

3-D imaging characteristics

VI. A convergence plane can be effected in a set of perspective images by introducing a time delay into the start of the image acquisition for each line-scan sensor.

VII. The parallax production is dependent upon the convergence angle and the object range.

VIII. Parallax information produced by two successive views with the same convergence angle is identical regardless of orientation when a small angle is used (i.e. <5°).

IX. The dimensions of the voxel structures are nominally constant and independent of the object range therefore the minimum range increment in the z-axis (i.e. depth plane intervals) is also independent of range.

X. The potential spatial resolution in the z-axis can be increased by increasing the convergence angle between successive views.

XI. This technique produces equidistant parallel depth planes in object space.

5.7.2 Lateral shift technique

2-D imaging characteristics

I. The field of view in the x and y axes are dependent upon the focal length of the lens and the camera-to-object range.

3-D imaging characteristics

II. A convergence plane can be effected in a set of perspective images by applying a relative horizontal shift to each perspective image.
III. The parallax production is dependent upon the object range and the base separation between successive views.
IV. Parallax information produced by two successive views with the same base separation is identical.
V. The dimensions of the voxel structures increase with increasing object range which in turn increases the depth plane intervals in the z-axis.
VI. The potential spatial resolution in the z-axis can be increased by increasing the base separation between successive views.
VII. This technique produces parallel depth planes in object space; the separations of adjacent depth planes are a function of Z^2.

6 EXPERIMENTS WITH THE X-RAY SYSTEM

6.1 Introduction

This chapter presents the development of the x-ray experimental system, for implementing the line-scan multiple view imaging technique and the lateral shift (area array) multiple view imaging technique. The experimental strategy adopted in this phase of the work is similar to that used to evaluate the visible light version of these imaging techniques presented in Chapter 5. The empirical analysis comprises of: repeatability tests, two-dimensional acquisition experiments and three-dimensional or multiple view imaging experiments. The display of the image data for the human observer is fully discussed in Chapter 7.

6.2 Preliminary evaluation of the experimental system

The lateral shift technique can be achieved by using a standard cone beam x-ray system as described in Section 2.4.2. However, the line-scan technique requires a line-scan x-ray system that can produce multiple perspective images. To the best of the author's knowledge, such a machine is not available in the industry or any academic institution. Thus in order to evaluate the x-ray line-scan technique, two approaches were considered:

i. modify a two-view binocular stereoscopic x-ray machine that is located on site at *The Nottingham Trent University* [109]. This would require extensive modification to its mechanical and electronic systems in order to produce multiple perspective images.
ii. utilize a standard cone beam x-ray system which incorporates an image intensifier and an area array camera and apply the '*line-scan principle using an area array camera*' as devised in Chapter 3 to simulate a multiple view linear x-ray detector array system.

The first approach is not a practical proposition for the development of an experimental system. In fact it may be more cost effective to build a bespoke machine. However, the second approach utilizes apparatus which may be purchased as a commercial unit. Thus the principle of using an image intensifier to simulate a multiple linear x-ray detector array is presented in the following text and depicted in Figure 6-1.

In order to electronically collect and store the shadowgraph image projected onto the input window of the image intensifier, the output window is optically coupled to an area array sensor. Thus as the object under inspection is translated through the x-ray beam, image information is produced by collecting data from the selected photosite columns on the CCD array. Image positions on the input window of the image intensifier are determined by the corresponding column on the area array sensor. In other words, there is a nominal one-to-one correspondence between a line on the input

window and a column of photosites on the area array sensor. Thus a number of divergent slit 'collimated' x-ray beams can be simulated. Therefore, the multiple view line-scan technique can be evaluated using the image intensifier based x-ray system. This technique in itself represents new research in the field of x-ray imaging and to the author's knowledge has not been reported elsewhere in the literature.

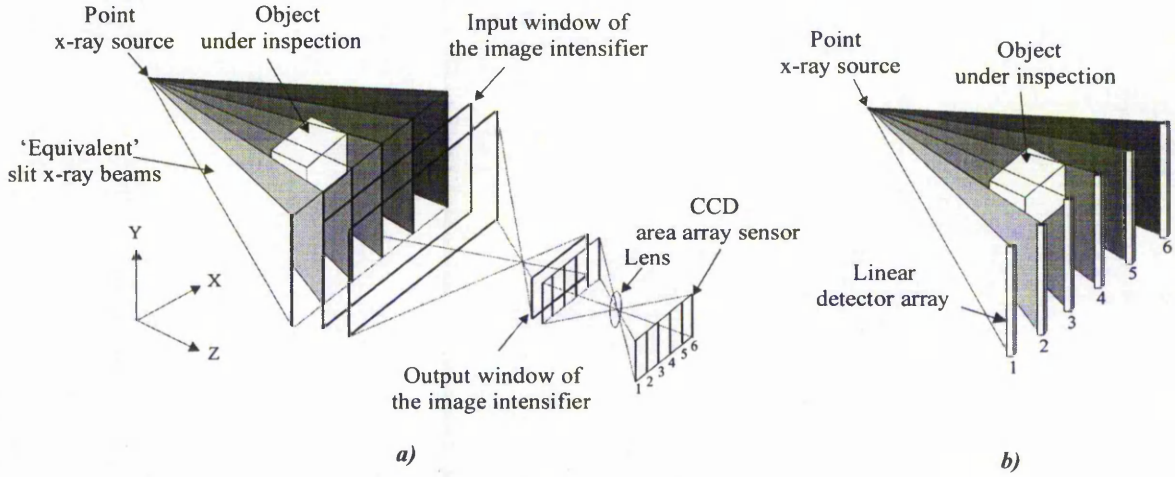

Figure 6-1 *Line-scan principle utilizing a) an image intensifier x-ray system and b) a linear x-ray detector array system*

The cone-beam x-ray system utilizing the '*line-scan principle*' presents a number of operational merits in modelling a multiple view line-scan technique in comparison to building a bespoke linear x-ray detector array system. These include:

a) The angular distribution of the slit 'collimated' x-ray beams can be electronically controlled via a software program. Thus the mechanical reconfiguration of the linear detector arrays is avoided. The software control of this angular distribution greatly increases the versatility of the system for experimental purposes.
b) A live two-dimensional image is available for initial system configuration and set up of the x-ray imaging parameters (e.g. x-ray tube current and voltage).

Having identified the benefits of using an image intensifier to model a linear detector array system, a number of potential limitations were also considered. These include:

a) Difficulties in determining the geometric imaging parameters including:
   - accurate source-to-sensor separation;
   - the accuracy of the electromagnetic focus within the image intensifier;
   - the geometric alignment between the image intensifier and the area array sensor;
   - curvature of the input window of the image intensifier.

b) The size of the input window limits the size of the object that can be inspected using this technique; the maximum object size that can be inspected is limited to 15 cm x 10 cm for the 4-inch diameter image intensifier under consideration. Also, the angular distribution of the 'collimated' x-ray beams is limited by the diameter of this input window. However these considerations did not disrupt the empirical investigation of the scalable concepts encountered in this research programme.

c) When a standard camera (frame rate of 25 Hz) is used, the maximum line acquisition rate is limited to the frame frequency. Thus the speed of the system could be greatly increased by using a high-frame rate camera. However, imaging speed is not an issue in this research programme.

d) The total number of equivalent slit collimated x-ray beams (i.e. corresponding to photosite columns on the area array imager) is limited by the number of photosite columns available (typically 512). However, this is not a limiting factor in this work as a maximum number of sixteen views were used.

Thus it was decided that the image intensifier system is the most suitable choice for the following reasons:

- flexibility in changing the angular distribution of the simulated slit 'collimated' x-ray beams;
- simplicity in implementation;
- no add-on development cost for machine modification is involved.

Therefore, both of the proposed imaging techniques, line-scan and lateral shift, are implemented using the image intensifier x-ray system. The experimental configuration for each technique is discussed in the following sections.

6.3 The experimental system

The experimental system is realized by interfacing the image acquisition hardware utilized in the visible light experimental system with a commercially available microfocus real-time x-ray inspection machine, XTEK VTX 160KV [24] as illustrated in Figure 6-2. The experimental system can be achieved in this way because the output of this x-ray system is the same standard video format as that produced by the camera in the visible light arrangement. Therefore, by feeding the video signal from the x-ray machine to the frame grabber, a 'live' image of the object under inspection can be obtained.

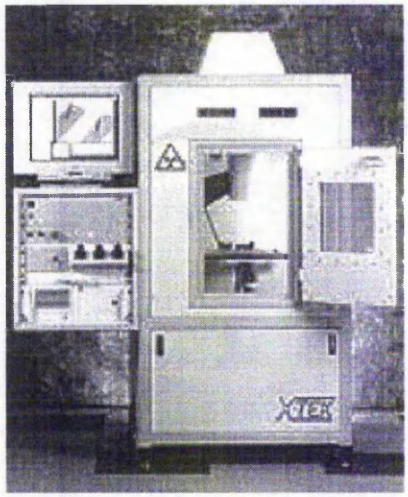

Figure 6-2 *Photograph of the XTEK x-ray real-time inspection machine*

Figure 6-3 depicts the experimental multiple view x-ray arrangement.

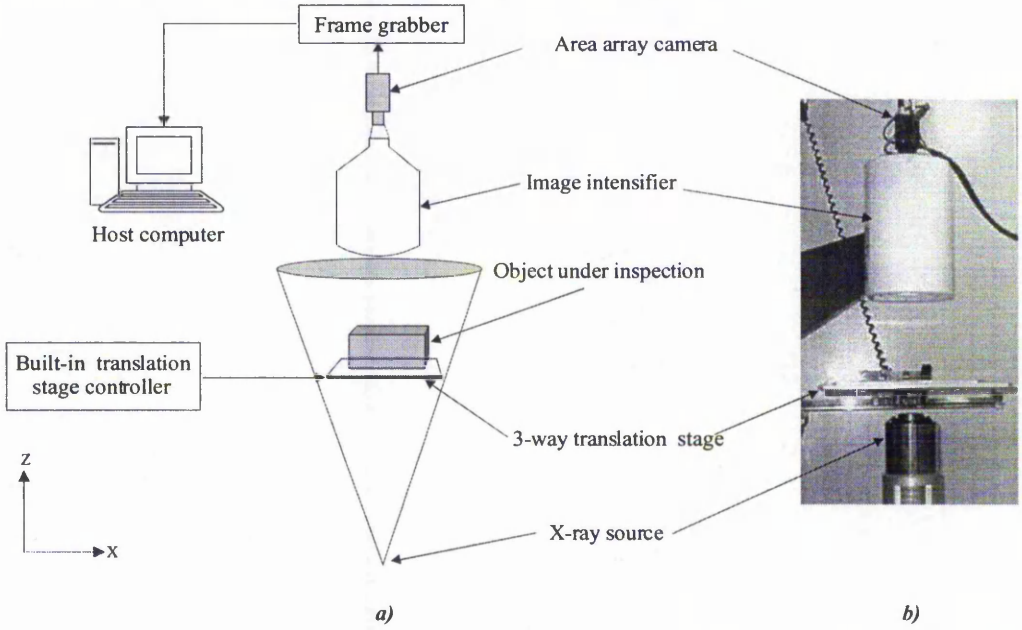

Figure 6-3 *The experimental x-ray configuration a) schematic and b) photograph*

The camera, image intensifier, translation stage and the x-ray source are arranged in a vertical manner such that the shadow of the object under inspection is projected onto the input window of the image intensifier. The output from the image intensifier is optically coupled to an area array camera. The experimental arrangement consists of the following components:

- a micro-focus x-ray source;
- an image intensifier coupled to a CCD area array camera;
- a frame grabber;
- a three-way translation stage.

Each of the components is discussed in the following text.

a) Micro-focus x-ray source

The micro-focus x-ray source is manufactured by *XTEK*. The effective diameter of the focus spot is 2 μm. This enables a high magnification of approximately 1800 times to be achieved.

b) Image intensifier and area array camera

The image intensifier is manufactured by *North American Imaging*, model NA15844JP with an effective aperture of 98 mm [110]. A *Pulnix*, model TM6CN, CCD area array camera [111] is optically coupled to the image intensifier. The area array sensor is a 0.5-inch type, 2:1 interlace, with 752 (H) x 582 (V) picture elements and a frame rate of 25 Hz.

c) Frame grabber

The Corona frame grabber is used for image acquisition for this experimental system. The description of this frame grabber is given in Section 5.2.1b.

d) Three-way translation stage

The linear translation in the experimental arrangement is achieved by utilizing a three-way (x, y and z) translation stage. Therefore, the object position and linear movement required by the line-scan and the lateral shift techniques can be achieved by utilizing this stage.

6.4 Experimental strategy

The lateral shift technique can be achieved by directly using the video signal provided by the XTEK system in order to acquire area array images. However, the line-scan technique requires a modification to the image acquisition method. The experimental strategy used to evaluate the multiple view x-ray techniques is similar to that used for the visible light experimental system presented in Section 5.4. The differences between the visible light and the x-ray experimental strategies are outlined below:

- x-ray source-to-object range replaces the camera-to-object range;
- experiments relating to focal length are not applicable to the x-ray system;
- experiments relating to the translation speed are conducted using the three-way translation stage to produce a linear translation in one axis (x-axis).

The configuration and operation of the two imaging techniques are described independently in the following text.

6.5 Establishing the repeatability of the system parameters

A 26 mm square metal plate as depicted in Figure 6-4 was used as a test object in the experiments. The horizontal sides of this square are arranged to be parallel with the direction of motion. The perimeter of the imaged square provides a convenient edge from which pixel measurements can be

determined; these have all been measured perpendicular to the sides of the imaged square. This metal plate is placed directly on the translation stage for experiments. The full experimental results of the repeatability tests can be found in Appendix C.

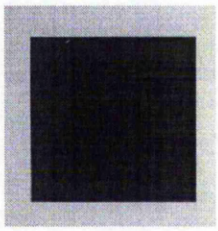

Figure 6-4 *A 26 mm square metal plate used for experiments*

A summary is given following the description of each experiment.

a) Grey level noise

This experiment evaluates the noise level in terms of grey level. The combination of voltage and current setting used for all experiments is 100kV/60μA. This produces high contrast images for the objects under consideration in these experiments. Ten sample images are obtained of the square plate at different instances in time. The average grey level value of a fixed area of 100 pixels x 100 pixels, in the sample images is obtained. A variation of ±20 grey levels was observed. Thus the x-ray image is relatively noisy in terms of grey level fluctuations. However, the visual quality of these images is improved by applying simple image enhancement algorithms.

b) Source-to-object range

The test object is imaged at different source-to-object ranges and the image components in both x and y axes are measured in the resultant images. This test is repeated ten times to obtain an average value. The repositioning in the z-axis for image components in the x and y axes produce a maximum variation of ±2 pixels for the different source-to-object ranges under consideration. This error was found to be acceptable for the experimental analysis conducted in this work.

c) Translation speed

The translation speed is evaluated by passing the square metal plate along the motion axis through the x-ray beam, while sixteen perspective line-scan images are collected. The width (x-axis) of the square metal plate in the resultant images are measured and recorded. This process is repeated ten times to obtain an average value. The observed error rate in terms of pixels is ±2 pixels. Thus the translation speed is found consistent.

b) Line acquisition time

The line acquisition time is determined by using the timer function as described in the visible light system. The timer function is implemented in software code in order to obtain the time interval

between two successive line acquisitions. The process is repeated ten times to obtain an average value. Thus it is concluded that the line acquisition time can be considered constant throughout the image acquisition process.

6.6 Experiments using a line-scan mode of operation

6.6.1 Image acquisition

The image acquisition process for the line-scan technique is discussed in terms of:

a) perspective image production.
b) system operation.

The utilization of the CCD camera in a line-scan mode and the time delay determination are based on the principles (in the visible light system) as described in as in Section 5.5.1.

a) Perspective image production

The perspective angle determination in the experimental arrangement is different to that described in the visible light arrangement. This is due to the complexity in the optical path from the object space to the display as illustrated in Figure 6-5.

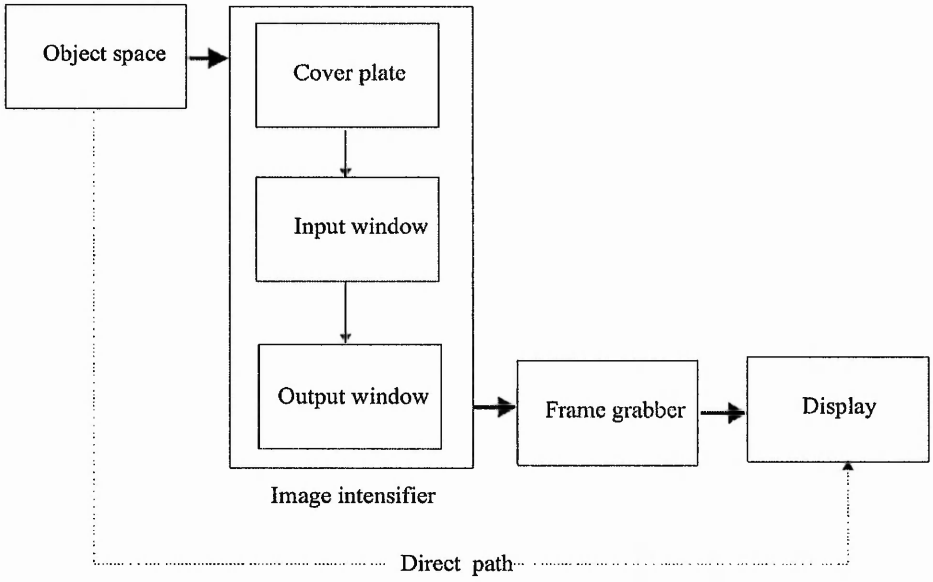

Figure 6-5 *Optical path of the image formation from object space to the display*

In order to determine the angular distribution of the 'collimated' x-ray beams in object space requires that a relationship between a line on the sensor's surface and the reference video column be established. Therefore the image intensifier is considered transparent in the determination of the perspective angle. The slit x-ray beam that is perpendicular to the sensor plane is used as a reference for the angle determination.

This reference view corresponds to the central pixel column on the video display. By considering *Equation 3-7 & 3-8*, magnification from the object space to the display can be determined as follows:

$$M_{od} = \frac{D_x}{L_{xs}}$$

where L_{xs} is the sensor's size in the x-axis.

The image intensifier and area array camera are considered to be perfectly aligned with the x-ray source. With reference to Figure 6-6, the path length of the main/reference x-ray beam (i.e. the beam that is perpendicular to the sensor plane) and the selected slit x-ray beam d_o is governed by the perspective angle α and the source-to-sensor separation S_h.

$$d_o = S_h \tan\alpha$$

The equivalent distance on the monitor screen d_i is obtained by multiplying d_o by the magnification factor M_{od}.

$$d_i = M_{od}\ d_o$$

d_i can also be expressed in terms of a number of photosite columns n_{line} which can be considered as the relative displacement with respect to the central video column.

$$n_{line} = \frac{d_o\ D_{x(pix)}}{L_{xs}} = \frac{S_h \tan(\pm\alpha) D_{x(pix)}}{L_{xs}} \qquad \ldots(6\text{-}1)$$

Where $D_{x(pix)}$ is the total number of video columns in the display.

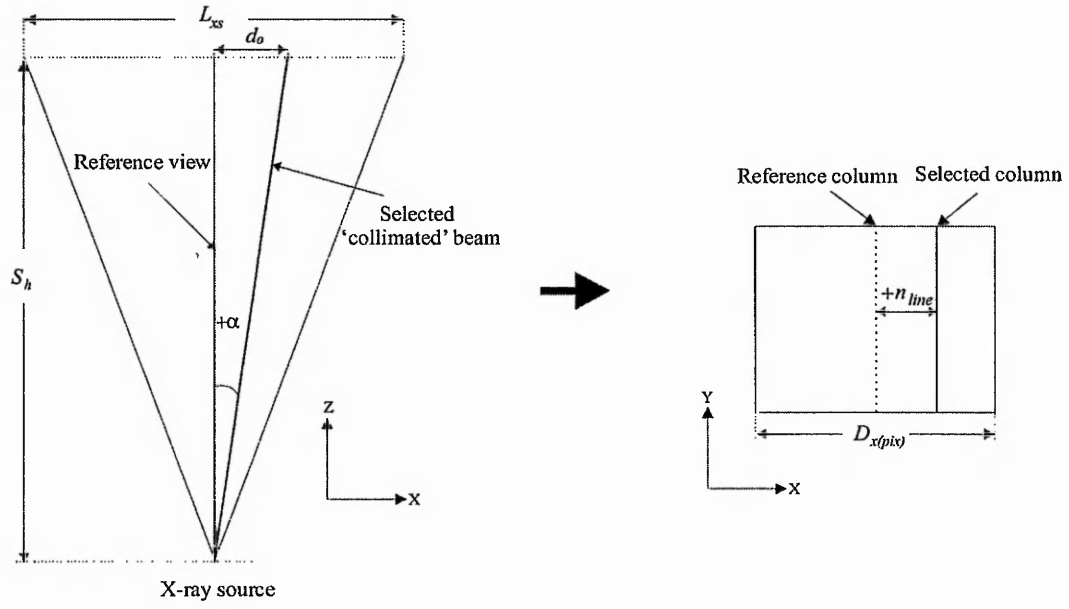

Figure 6-6 *Determination of the perspective angle for a line-scan arrangement using a cone beam x-ray system a) object space and b) image space (display)*

b) Operation of the experimental arrangement

Software code was written to control the operating parameters of the frame grabber. This program allows the operator to control the following parameters:

- line acquisition time;
- the number of lines to be collected to form a two-dimensional image;
- time delay to effect a convergence plane in object space;
- angular distribution of the equivalent slit 'collimated' x-ray beams.

The direction and speed of the linear translation are controlled by a built-in controller in the XTEK x-ray inspection system. A manual control approach was used to start the image acquisition due to the limited access to the machine's software. The system operation flowchart is depicted in Figure 6-7.

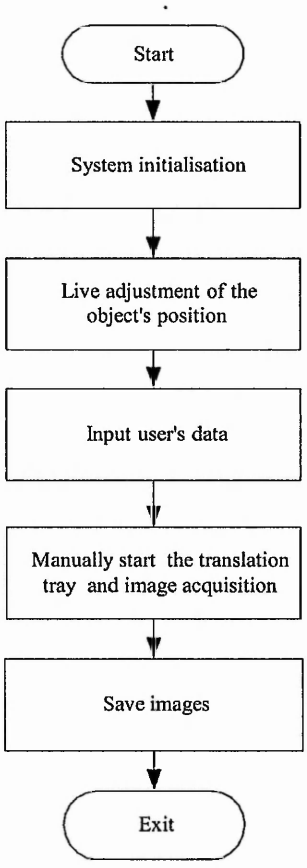

Figure 6-7 *System operation flowchart for the line-scan technique*

An image capture cycle begins with the initialisation of the frame grabber. This entails setting the camera interface parameters, video standard and reference pixel column. During the initialisation, the image buffers for image storage are allocated. Following this, a live image is displayed on the monitor screen which allows the user to adjust the orientation of the object under inspection. In this

program, sixteen video columns are allocated as individual line-scan sensors to produce sixteen perspective images. The movement of the translation stage is manually initiated when the image acquisition process is started. There is no synchronization between the translation stage and the start of the image acquisition process due to the limited software access. Even so, this will not affect the experimental results as the time delays used are referenced to the start of the image acquisition with respect to the reference view. In other words, time delays are referenced to the start time of the image acquisition of the reference view. The synchronization of the image acquisition among the line-scan sensors is achieved by using the frame synchronization pulse. The synchronization pulses are proved to be consistent by the repeatability test for the line acquisition time (see Appendix C). The resultant perspective images are saved in the *Bitmap* format.

6.6.2 Experiments with the two-dimensional arrangement

This section describes the experimentation conducted to determine the imaging characteristics of the two-dimensional experimental arrangement. The geometrical characteristics of the line-scan techniques are empirically evaluated in terms of the fundamental imaging parameters:

- source-to-object range;
- translation speed;
- line acquisition time.

The effect of independently changing the values of each parameter is investigated in a series of experiments. Each experiment uses a test object as depicted in Figure 6-4. The square metal plate is placed on the translation stage which in turn is placed normal to the main axis of the x-ray source. Its horizontal sides are arranged to be parallel to the direction of motion as illustrated in Figure 6-8.

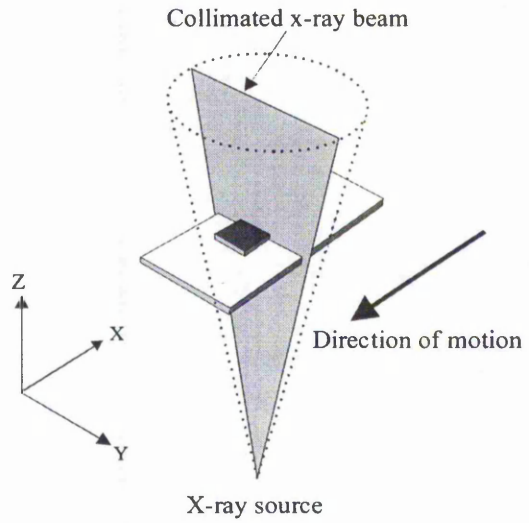

Figure 6-8 *Two-dimensional line-scan experimental configuration*

X-axis evaluation

The x-axis imaging characteristics are evaluated in terms of *Equation 3-3*. A single perspective image of the test object consisting of 512 pixels x 480 pixels (Figure 6-4) is produced at the end of each experiment.

a) Translation speed

The translation speed is tested at 0.1 mm/s increments between 0.3 mm/s to 1.2 mm/s and the components of the imaged square in each axis are plotted against the translation speed in Graph 6-1. Experimental conditions: $Z = 0.3$ m, $t = 80$ ms.

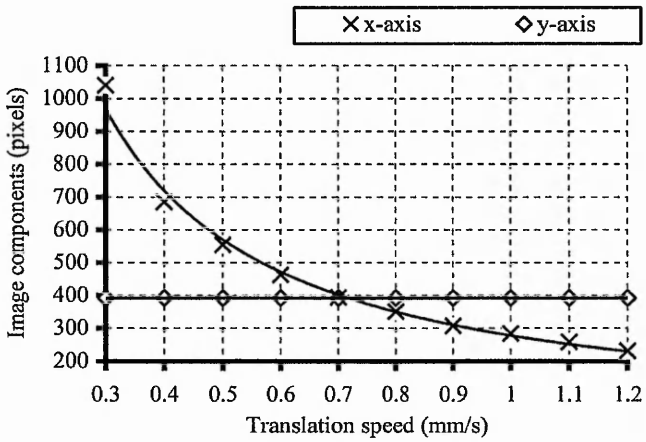

Graph 6-1 *Change in the x-axis image component and the y-axis image component with respect to the translation speed*

b) Line acquisition time

The line acquisition time is tested at 40 ms increments between 80 ms to 440 ms and the components of the imaged square in each axis are plotted against the line acquisition time in Graph 6-2. Experimental conditions: $Z = 0.3$ m, $S = 0.3$ mm/s.

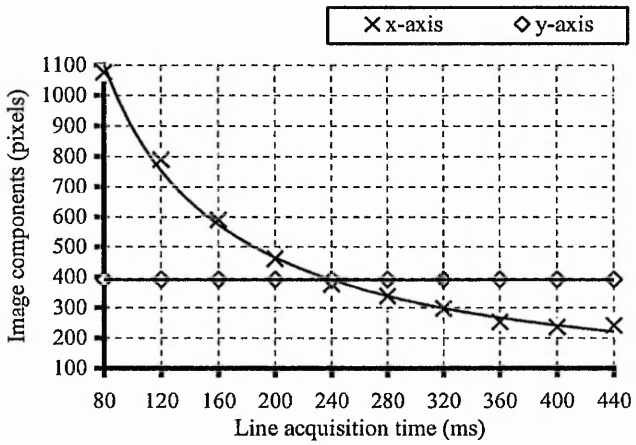

Graph 6-2 *Change in the x-axis image component and the y-axis image component with respect to the line acquisition time*

Discussion of the experimental results for the x-axis evaluation

The results obtained from the two-dimensional x-ray arrangement are in close agreement with the results obtained from the visible light experiments. These are summarised as follows:

- the y-axis image component of the 'square' is constant and independent of speed and line acquisition time;
- the motion axis (x-axis) image component of the 'square' decreases with increasing the translation speed and the line acquisition time;
- the rate of change of the motion axis image component decreases non-linearly with an increase in translation speed and, line acquisition time;
- the crossover point in both graphs indicates the speed and line acquisition time at which a 1:1 aspect ratio image is produced as indicated by *Equation 3-12;*
- the potential spatial resolution in the motion axis is a function of the translation speed and line acquisition time.

Y-axis evaluation

The y-axis imaging characteristics are evaluated in terms of *Equation 3-10*. A single perspective image with a resolution of 512 pixels x 480 pixels of the test object (Figure 6-4) is produced at the end of each experiment.

a) Source-to-object range

The source-to-object range is increased in 15 mm increments for ranges between 300 mm to 450 mm and the components of the imaged square in each axis are plotted against object range as shown in Graph 6-3. Experimental conditions: $S = 0.8$ mm/s, $t = 80$ ms.

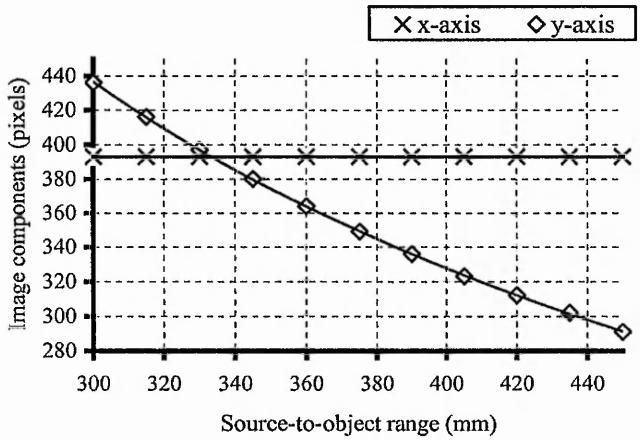

Graph 6-3 *Change in the x-axis image component and the y-axis image component with respect to the source-to-object range*

Discussion of the experimental results for the y-axis evaluation

The results obtained are in close agreement with the results obtained in the visible light experiments. These are summarised as follows:

- the image component of the 'square' in the motion axis is constant and independent of range;
- the y-axis image component is proportional to the reciprocal of the object range (1/Z);
- the potential spatial resolution in the y-axis is proportional to the reciprocal of the object range (1/Z);
- the crossover point in both graphs indicate the range at which a 1:1 aspect ratio image can be produced.

6.6.3 Experiments with the multiple view arrangement

The three-dimensional imaging characteristics of the multiple view line-scan technique are experimentally evaluated. A test tower as depicted in Figure 6-9 is utilized as a supporting structure in order to conduct parallax experiments. The test tower provides a convenient mechanism for introducing an increment between two object points; each step in the test tower is 20 mm apart. Two metal targets are placed at different heights to produce a range separation in object space. This range separation manifests itself in the image pair as a parallax between the two imaged points.

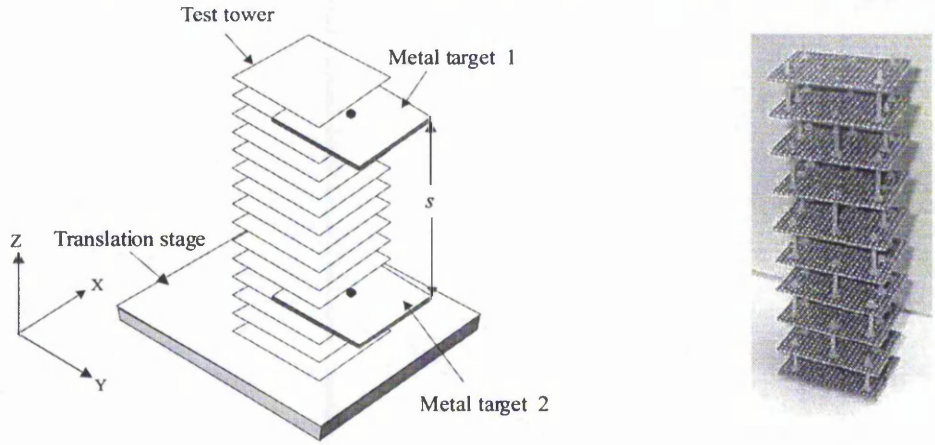

Figure 6-9 *Two metal targets are located in a slotted mounting rack a) schematic and b) photograph*

During the image acquisition process, the test tower is placed on the translation stage and it is arranged to be normal to the x-ray sensor input window.

a) Spatial registration of the perspective images

A single target is used in this experiment to evaluate the spatial registration of the perspective images with respect to a convergence plane in object space. This experiment was devised for the

visible light arrangement as described in Section 5.5.3a. A convergence plane is effected by introducing a time delay into the image acquisition process. In this experiment, a collimated x-ray beam 'No.1' is used to produce the reference view. The convergence angle used in this experiment is 5°. The central photosite column (i.e. photosite column 384) is used as a reference column. In order to produce a symmetrical angular distribution for the perspective views +2.5° and -2.5° is used. The number of photosite columns to be displaced from the central column to effect a convergence angle of 5° is determined by applying *Equation 6-1.*

$$n_{line} = \frac{S_h \tan\alpha \; L_{xf(pix)}}{L_{xs}} = \frac{670\text{ mm x }\tan 2.5^\circ\text{ x }768}{98\text{ mm}} = 460\text{ lines}$$

Thus, the two video columns chosen for this task are 384+(460/2) = 614 and 384-(460/2) = 154. The convergence plane in this experiment is fixed at a range of 370 mm from the point x-ray source. Thus by applying *Equation 4-2.*

$$\Delta t_{1\leftrightarrow n} = \frac{Z_c\,(2\tan\alpha)}{S} = \frac{370\text{ mm x }2\tan 2.5^\circ}{5\text{ mm/s}} = 6.5\text{ seconds}$$

A time delay of 6.5 seconds is introduced into the start of the image acquisition of line-scan sensor 'No.2'. This time delay can be achieved by waiting for (6.5 s/80 ms) = 81 video lines to elapse before sensor 'No. 2' starts its image acquisition process. The test card is imaged at a source-to-object range of 200 mm. Two perspective images are obtained at the end of the experiment. The procedure is repeated for source-to-object ranges of 300 mm to 450 mm in increments of 15 mm. The corresponding parallax values in terms of a pixel separation produced by a pair of perspective images are plotted against the source-to-object range in Graph 6-4. Experimental conditions: Z_c= 370 mm, S = 5 mm/s, t = 80 ms, Δt = 6.5s, σ = 5°, Δl = *81.*

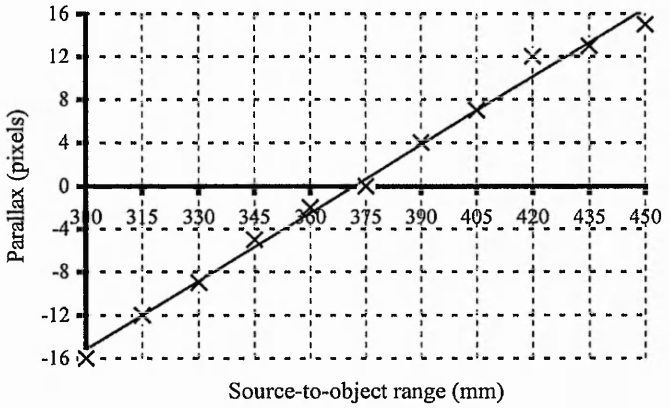

Graph 6-4 *Change in magnitude and sign of parallax with increasing source-to-object range*

Discussion of the experimental results for spatial registration

The results are in close agreement with the results obtained from the visible light experiments. These are summarised as follows:

- the parallax value increases linearly with respect to the object range;
- the 'crossover point' indicates the position of the convergence plane in object space. This is approximately 370 mm for this experiment;
- both positive and negative parallax is produced as a function of the relative position of the test card in object space with respect to the convergence plane.

b) Convergence angle

To evaluate the effect of the convergence angle on the production of parallax *Equation 4-6* is used. This experiment is similar to an experiment conducted for the visible light technique as described in Section 5.5.3b. The convergence angles used in these experiments ranges from 1° to 5° in increments of 0.5°. The perspective angle of the equivalent collimated x-ray beam is obtained by applying *Equation 6-1* and the calculated pixel column positions for a given convergence angle are tabulated in Table 6-1. The central column, 384, is also used as a reference to produce a symmetrical angular distribution of perspective views.

Convergence angles (°)	Photosite column 1	Photosite column 2	Number of photosite column separations
1.0	338	430	92
1.5	315	453	137
2.0	292	476	183
2.5	269	499	230
3.0	246	522	275
3.5	223	545	321
4.0	200	568	367
4.5	177	591	413
5.0	154	641	460

Table 6-1 *Convergence angles with the corresponding separation (in pixels) between two collimated x-ray beams*

Two object points with a range separation of 100 mm are imaged at convergence angles between 0.5° to 5° in steps of 0.5° at source-to-object range of 300 mm. The calculated time delay (using *Equation 4)* required to be introduced into the start of the image acquisition process associated with collimated beam No. 2 is 5.2 seconds or (5.2 s/80 ms) = 65 video lines after the image acquisition associated with collimated beam No.1 has started. The convergence plane is set at 300 mm with a convergence angle of 1°. The experiment was repeated with the identical time delay for the other convergence angles listed in Table 6-1. Parallax values produced by the two collimated x-ray beams are plotted against the convergence angle in Graph 6-5. Experimental conditions: $S = 1$ mm/s, $t = 80$ ms, $Z_c = 300$ mm.

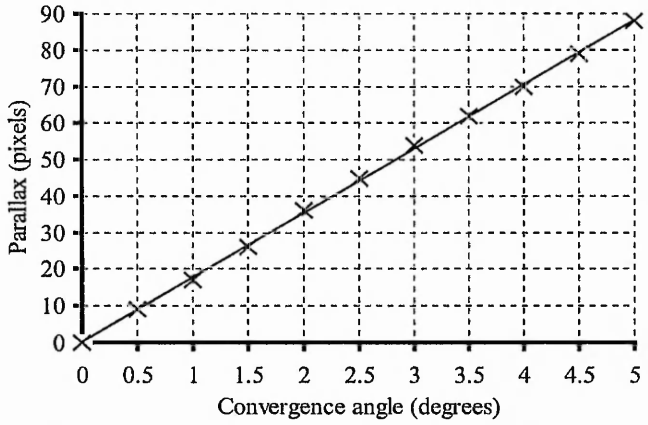

Graph 6-5 *Change in parallax with respect to the convergence angle*

Discussion of the experimental results for the convergence angle variation

The results obtained are in close agreement to those obtained in the visible light experiments. The results indicate that the parallax is a function of the convergence angle. Also that, the parallax value increases with increasing convergence angle. This is because a constant time delay is implemented for the different convergence angles used. Therefore, the convergence plane Z_c is moved towards the x-ray source and results in an incremental change in parallax. In fact, the parallax value is not linearly proportional to the convergence angle. Instead it is a tangential function as expressed in *Equation 4-2*. The linearity observed is the result of utilising a small angle.

c) Relative parallax produced by successive image pairs

This experiment examines the interrelationship between the angular distribution of the fields of view produced by the line-scan sensors. As such it is similar to that conducted for the visible light techniques discussed in Section 5.5.3c. The test tower with two object points, point *a* and point *b*, separated by 20 mm are linearly translated through the slit fields of view as depicted in Figure 6-10.

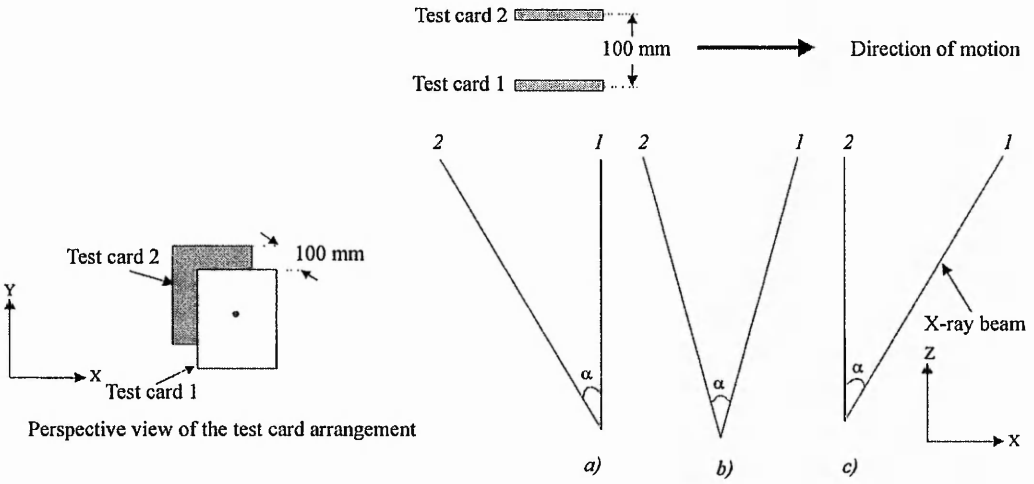

Figure 6-10 *Orientation of the x-ray beams with the same convergence angle*

Point *a* is located at a fixed location in object space and point *b* is moved away from point *a* to produce a range separation in object space. Three successive image pairs (i.e. S_1-S_2, S_3-S_4 and S_5-S_6) are obtained at the end of the experiment. This experiment is repeated for an increasing range separation of 20 mm increments between point *a* and point *b*. The relative parallax produced is plotted against the range separation in Figure 6-10a to Figure 6-10c.

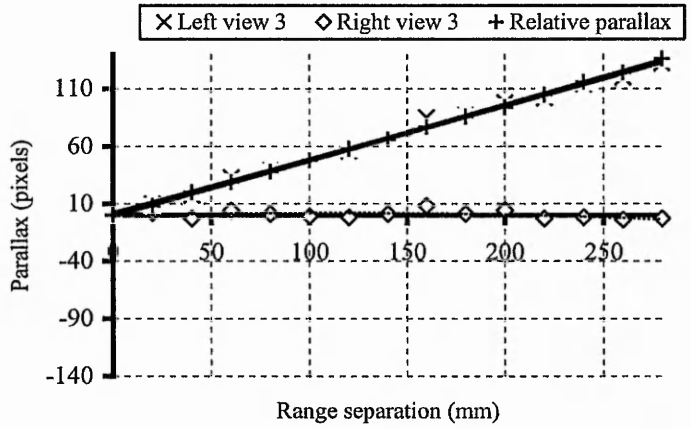

Graph 6-6a *The growth of relative parallax in the first image pair*

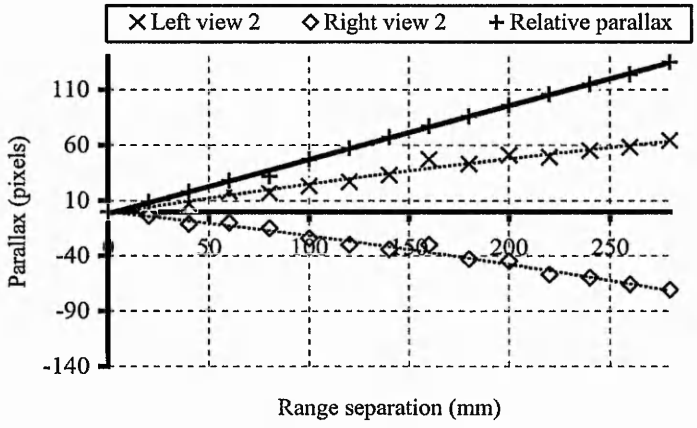

Graph 6-6b *The growth of relative parallax in the second image pair*

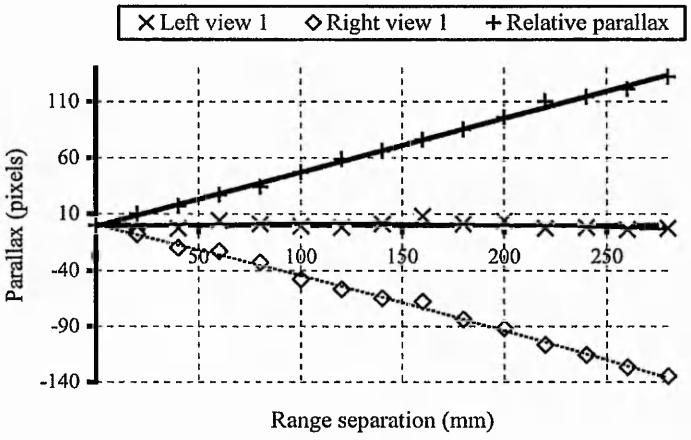

Graph 6-6c *The growth of relative parallax in the third image pair*

Discussion of the experimental results for the production of relative parallax

The results are similar to the visible light experiment described in Section 5.5.3c. Graph 6-6a to Graph 6-6c depict the growth of parallax information for three image pairs for a given convergence angle. It is observed that the relative parallax value is produced by the difference in x-coordinate positions between two imaged points. The total parallax produced by the three image pairs is approximately equal for small convergence angles (< 5°).

d) Voxel distribution

These experiments are similar to those described in Section 5.5.3d for the visible light technique.

i) Depth plane distribution

Two targets, with an increasing range separation from 0 to 180 mm in steps of 20 mm, are imaged at three different convergence angles, namely 1°, 3° and 5°. Point *a* is fixed and point *b* is free to move away from point *a* to create a range separation in object space. The relative parallax values between these points are plotted against the range separation as depicted in Graph 6-7. The experiment is repeated for a convergence angle of 3° and also 5°. Experimental conditions: $S = 2$ mm/s, $t = 80$ ms.

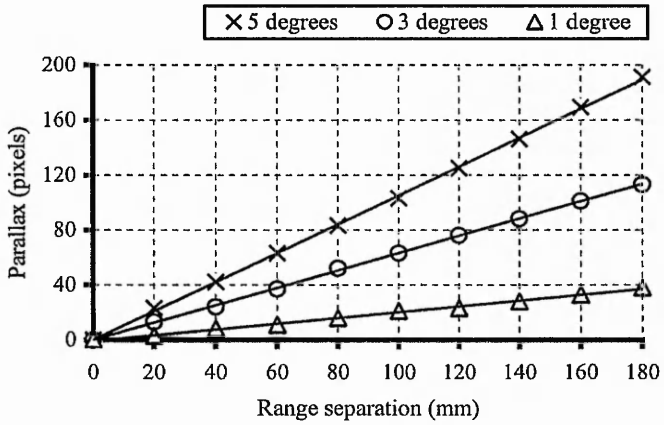

Graph 6-7 *Change in parallax with increasing range separation between two points in object space*

Discussion of the experimental results for depth plane distribution

The results obtained from this experiment are in close agreement with the results obtained from the visible light experiments. These are summarised as follows:

- The depth plane intervals and the dimensions of the voxel structures are nominally constant and independent of the object range. This in turn infers that the potential spatial resolution in the z-axis is constant;

- the increasing rate of change of parallax as a function of convergence angle observed in Graph 6-7 infers a corresponding increase in voxel density, depth plane density and potential resolving capability in the z-axis.

ii) Depth plane characteristics

A test card with eleven equally separated points (10 mm) (Figure 5-19) is imaged by two collimated x-ray beams at a range of 300 mm. Two perspective images are obtained at the end of the experiment. The separations between two consecutive points are measured in each resultant image. The difference, in pixels, for the corresponding separations in each image is plotted in Graph 6-8. The experiment is repeated for a source-to-object range of 400 mm and also 500 mm. Experimental conditions: $Z_1 = 300$ mm, $Z_2 = 400$ mm, $Z_3 = 500$ mm, $\sigma = 3°$.

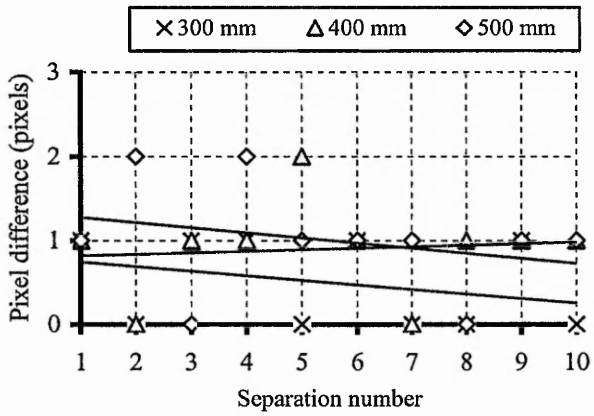

Graph 6-8 *Difference in parallax produced by a series of separations between two object points*

Discussion of the experimental results for the characterization of the depth planes

The results obtained are similar to those obtained from the visible light experiments, that is, a nominally flat line inferring parallel depth planes.

e) Sample perspective images produced by the multiple view lateral shift technique

Figure 6-11 illustrates perspective images produced by the line-scan technique. The imaged objects include a paper clip, a resistor, a fuse, a nut and a printed circuit board (these objects are located, in sequence, from foreground to background in object space). These images are produced using the following experimental conditions:

- depth of field : 150 mm
- maximum width and the maximum height of the object : 50 mm x 100 mm
- pixel resolution of the image : 640 pixels x 480 pixels
- translation speed : 1 mm/s

- line acquisition time : 80 ms
- angular distributions : 1.5 ° between successive image

These objects were chosen with industrial inspection of electromechanical devices in mind.

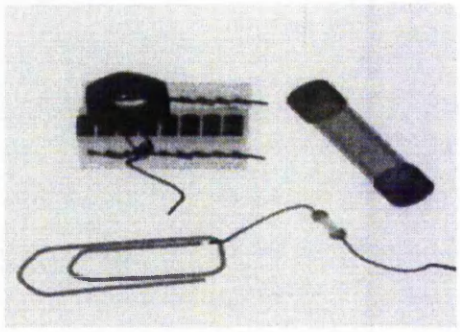

Sample image 1

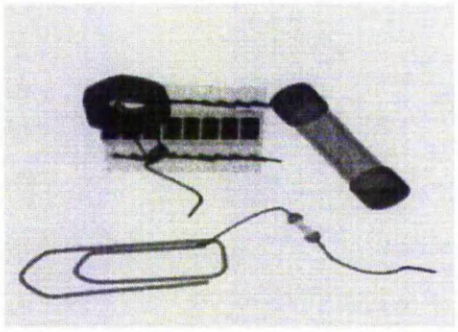

Sample image 2

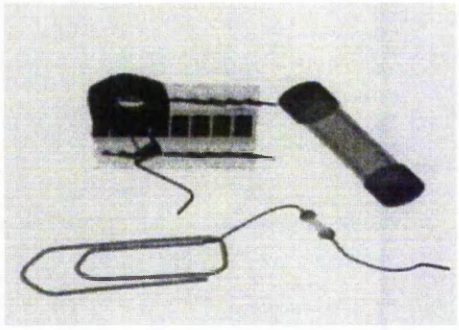

Sample image 3

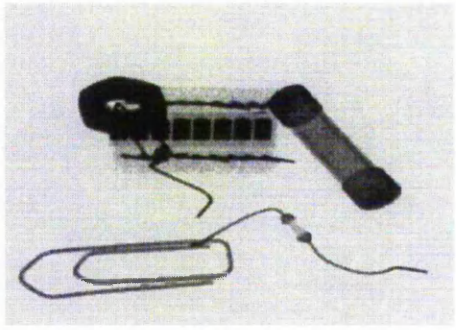

Sample image 4

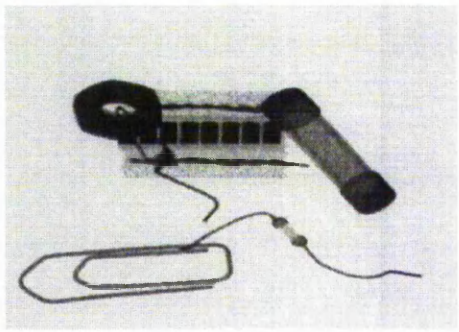

Sample image 5

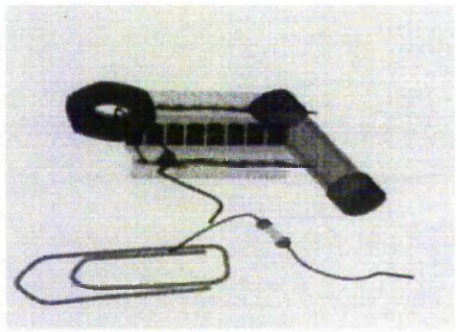

Sample image 6

Figure 6-11 *Sample images produced by the line-scan technique*

The perspective images are arranged as a set of binocular stereoscopic image pairs allowing 'free viewing' to be realized.

6.7 Experiments using an area array mode of operation

6.7.1 Image acquisition

Software code, written in C++, is implemented to control the operating parameters of the multiple view system. Sixteen snapshots are taken one after another at different relative positions. The change in position of the object under inspection is achieved by manually repositioning the 3-way translation stage. The actual position of the stage is indicated by the built-in stage controller in the x-ray machine. The program operation is identical to that discussed in the visible light lateral shift arrangement apart from the repositioning process (a joystick interface is utilized). The position in all three axes, x, y and z, is indicated on the monitor screen of the x-ray machine. Therefore, the flowchart in Figure 5-22 on page 74 may be used to explain the image acquisition process. However, the full explanation of the image acquisition process can be found in Section 5.5.1.

6.7.2 Experiments with the two-dimensional arrangement

This section examines the two-dimensional imaging characteristics produced by the lateral shift technique. The following experimental set up depicted in Figure 6-12 is used for this phase of the work.

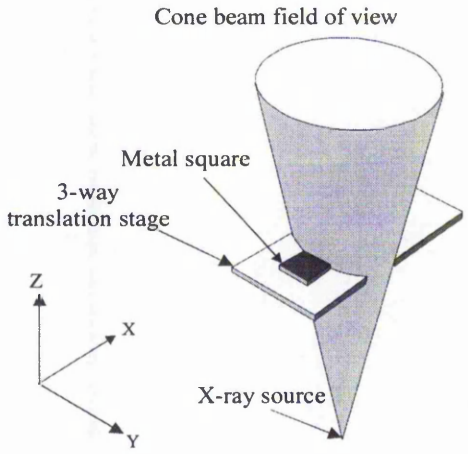

Figure 6-12 *Experimental set-up for a two-dimensional arrangement in order to evaluate the lateral shift x-ray technique*

The effects of varying the source-to-object range on the resultant images can be identified by measuring the image components in the x and y axes, $L_{xi(pix)}$ and $L_{yi(pix)}$, of the imaged square plate. This square metal plate is positioned on the translation stage to be normal to the main axis of the x-ray beam as indicated in Figure 6-12. The results from this work are used to verify the geometrical equivalence between images produced by the visible light and the x-ray imaging techniques.

a) Source-to–object range

The source-to-object range is tested at 15 mm increments for ranges between 300 mm to 450 mm. The components of the imaged square in each axis are plotted against object range as shown in Graph 6-9.

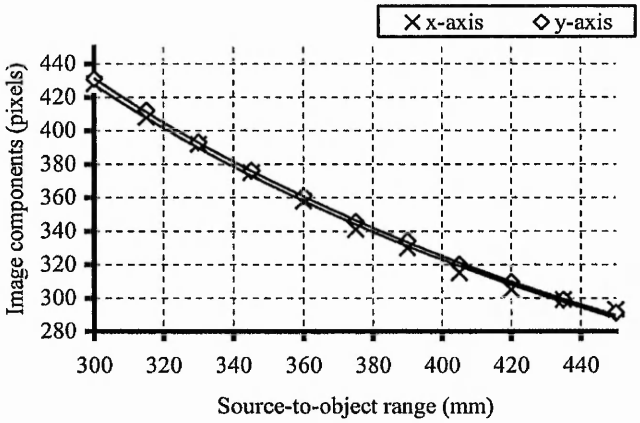

Graph 6-9 *Change in the x-axis image component and the y-axis image component with respect to the source-to-object range*

Discussion of the experimental results for the two-dimensional imaging system

The results obtained from the two-dimensional x-ray experiments are in close agreement with the results obtained from the visible light experiments. These are summarised as follows:

- image components in the x and y axes, in visible light and the x-ray domain, reduce with the camera-to-object range/source-to-object range;
- the rate of change of the image components in both axes decreases non-linearly with respect to the camera-to-object range/source-to-object range;
- spatial resolution in both x and y axes reduce with an increase in the camera-to-object range/source-to-object range in both domains.

The equivalent parameter for the focal length in the x-ray arrangement is the source-to-sensor separation. However this separation is fixed in the x-ray machine and thus no experiments are carried out to examine the effect on the image by varying the source-to-sensor separation. Although no deviation from that which is theoretically predicted is expected.

6.7.3 Experiments with the multiple view arrangement

This section describes the experimentation conducted to evaluate the three-dimensional imaging characteristics of the multiple view x-ray lateral shift technique. The criteria used to evaluate this technique are the same as those used to evaluate the visible light technique described in Section 4.5.3. Therefore, a direct comparison of these techniques is possible.

a) Spatial registration of perspective images

Six perspective images are obtained by incrementally increasing the base separation by 3 mm between each view. The resultant images are illustrated in Figure 6-13a. Experimental conditions: d_o = 3 mm, Z = 400 mm.

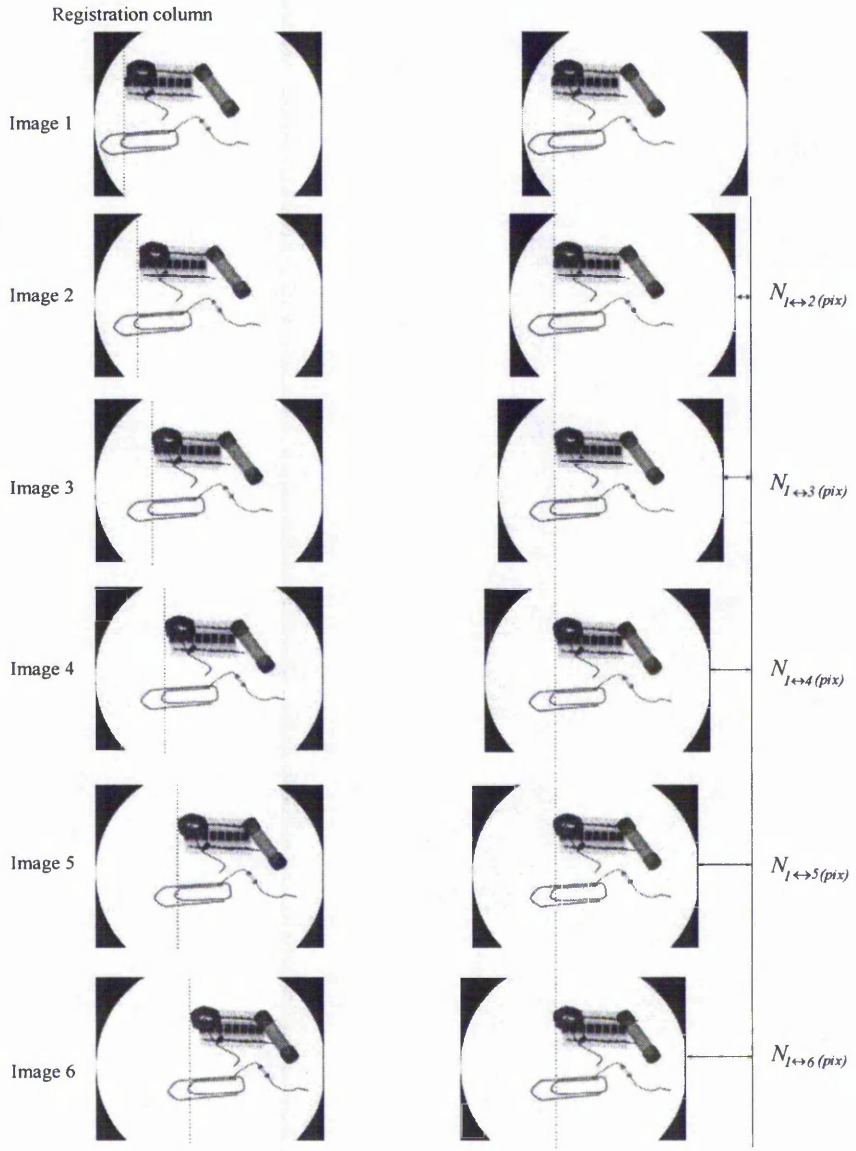

Figure 6-13 *Registration of perspective images produced by the lateral shift technique a) unregistered and b) registered*

Discussion of the experimental results for spatial registration

The resultant images in this experiment are obtained from different lateral positions with respect to the x-ray source. Therefore the object under inspection appears to be shifted in the x-axis as well as exhibiting relative parallax in the resultant images (Figure 6-13a). To produce an effective convergence plane in object space, a relative shift of the perspective images with respect to the reference image, in this case image No. 1, is applied. The desired convergence plane for this

experiment is located 400 mm from the x-ray source. A set of pixel column shifts are introduced to images No. 2 to No. 6 with respect to image No. 1. The number of pixel columns required to be shifted to effect a convergence plane at a range of 400 mm is obtained by applying *Equation 4-17* as indicated in Table 6-2.

Perspective image number	1	2	3	4	5	6
Number of pixels column shifts required $N_{1\leftrightarrow n(pix)}$	0	42	84	126	170	210

Table 6-2 *Number of pixel shifts required to register the perspective images with respect to the reference image*

The resultant images after applying a relative pixel column shift are shown in Figure 6-13b. It is observed that the object under inspection located at the convergence plane (i.e. the nut in the image) in object space now has a fixed x-coordinate value (assuming it has no thickness). Thus this the registration of the perspective images can also be achieved in the x-ray technique. The equivalent visible light experiment is discussed in Section 5.6.3a.

b) Base separation

This experiment examines the effect of the base separation on the parallax production for image pairs. Two metal targets with a range separation of 100 mm are imaged at a fixed source-to-object range of 100 mm; point *a* and *b* are located at 500 mm and also at 600 mm from the x-ray source respectively. Fourteen snapshots are taken at each position with an increasing base separation of 1 mm. The x-coordinates of the imaged points in the resultant images, with respect to the most left pixel column, are plotted against the base separation in Graph 6-10. Experimental conditions: $Z_1 = 100$ mm, $Z_2 = 200$ mm, $Z_3 = 300$ mm.

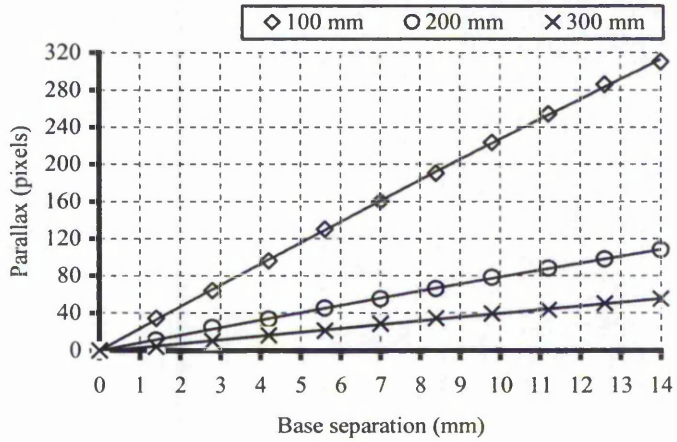

Graph 6-10 *Change in the relative parallax with respect to the base separation for three different source-to-object ranges*

The difference in the x-coordinate (x_{b1}–x_{a1}) of these two imaged points, *a1* and *b1* is also indicated in the same graph. This experiment is repeated for source-to-object ranges of 200 mm and also 300 mm.

Discussion of the experimental results for the base separation variation

From the visible light experiments described in Section 5.6.3.b, the parallax information is proved to increase linearly with respect to the base separation. Thus in this experiment, it can be observed that the parallax value also changes linearly with respect to the object range. A further experiment is carried out to evaluate the effect of base separation in effecting the change of parallax information. Experiments which involve different source-to-object ranges (i.e. 200 mm and 300 mm) are used to effect a change of gradient in Graph 6-10. Thus for a given displacement value, parallax reduces non-linearly with the source-to-object range. This indicates that two object points with a constant range separation between them will exhibit a different parallax values as a function of their overall source-to-object ranges.

c) Relative parallax produced by successive image pairs

The test card arrangement as depicted in Figure 6-9 is imaged with an increasing base separation of 3 mm for six different target separations at a range of 300 mm. Point *a* is fixed whilst point *b* is moved away from point *a* to produce a range separation in object space. Six perspective images or three successive image pairs, S_1-S_2, S_3-S_4 and S_5-S_6, are obtained at the end of the experiments. This is repeated for an increasing range separation of 20 mm. Three successive image pairs from the multiple view arrangement are used to evaluate the relationship of the growth of parallax at increasing source-to-object ranges. The difference in the x-coordinate between two imaged points of each image pair is measured. The difference between x-coordinate values of the two perspective images (i.e. $(x_{b2} - x_{a2}) - (x_{b1} - x_{a1})$) gives rise to the relative parallax produced by an image pair. The coordinate difference between two imaged points, for all three image pairs, are plotted against range separation in Graph 6-11a to Graph 6-11c. The relative parallax values contributed by these three sets of image pairs are also shown in the said graphs. Experimental conditions: $d_o = 1$ mm, $Z_a = 300$, $Z_b = 300$ to 520 mm.

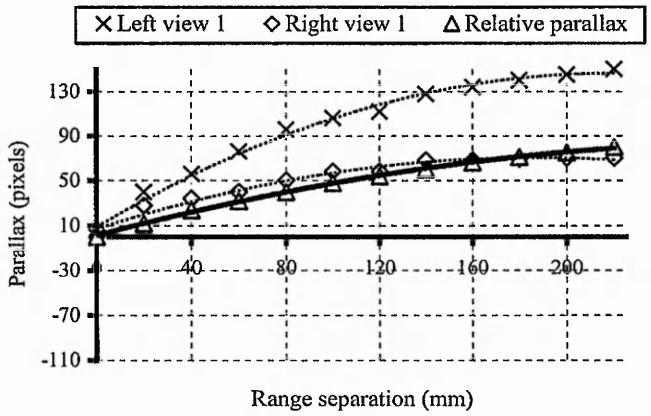

Graph 6-11a *The growth of relative parallax in the first image pair*

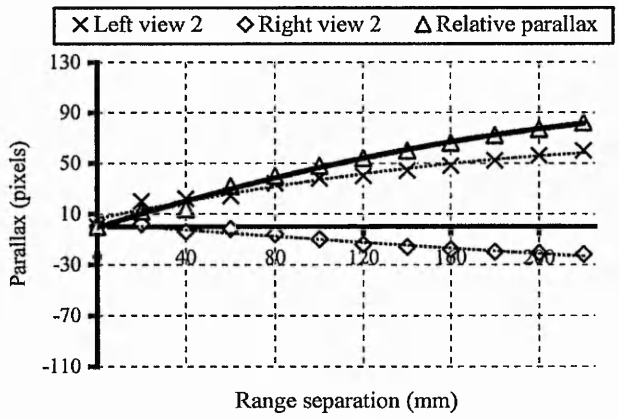

Graph 6-11b *The growth of relative parallax in the second image pair*

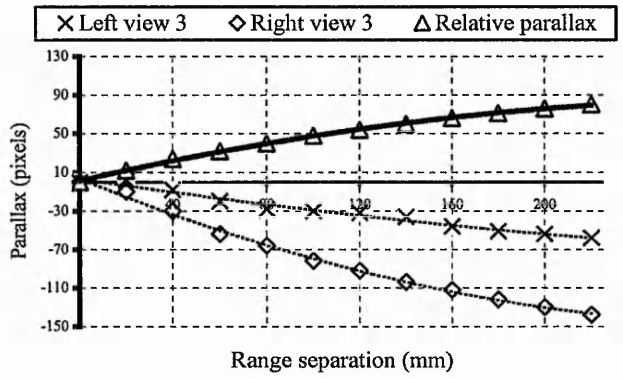

Graph 6-11c *The growth of relative parallax in the third image pair*

Discussion of the experimental results for the production of relative parallax

The results obtained are in close agreement with those obtained in the visible light experiment (Section 5.6.3c), that is, the total relative parallax produced by all three perspective images is approximately the same. This indicates that for a given range separation, parallax produced by successive views is identical if the base separation between successive views is constant (*Equation 4-8*).

d) Voxel distribution

These experiments are similar to those described in Section 5.6.3d for the visible light technique.

i) Depth plane distribution

Two points with an increasing range separation from 0 to 280 mm in increments of 20 mm are imaged for a base a separation of 5 mm. The experiment is repeated with base separation values of 10 mm and 15 mm. The difference in the x-coordinate, in pixels, between the two points in the resultant images are measured and recorded. The relative parallax value is plotted against the range separation as depicted in Graph 6-12. Experimental Conditions: $Z_a = 300$, $Z_b = 300$ mm to 580 mm, $d_{o1} = 5$ mm, $d_{o2} = 10$ mm, $d_{o3} = 15$ mm.

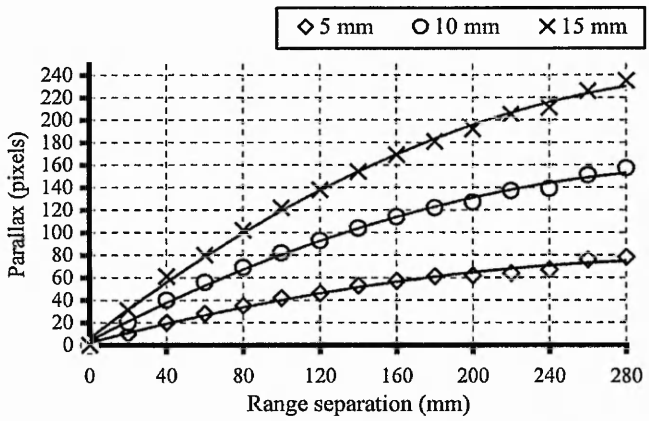

Graph 6-12 *Change in parallax with respect to range separation in object space*

Discussion of the experimental results for depth plane distribution

The results are in close agreement with the results obtained from the visible light experiments. These are summarised as follows:

- the depth plane intervals and dimensions of the voxel structures in the z-axis decrease with increasing object range as predicted by *Equation 4-29*. This in turn infers that the potential spatial resolution in the z-axis reduces with object range;
- the gradient for all three base separations in Graph 6-12 increases when the base separation is increased, that is, the '5 mm experiment' has lower gradient in comparison to the '15 mm experiment'. Therefore, the potential spatial resolution in the z-axis can be increased by increasing the extent of base separation between two successive views.

ii) Depth plane characteristics

A test card with eleven equally separated points (10mm) (Figure 5-19) is imaged by two collimated x-ray beams at range 300 mm. Two perspective images are obtained at the end of the experiment. The separations between two consecutive targets are measured in each resultant image. The difference, in pixels, for the corresponding separations between both images is plotted in Graph 6-13. The experiment is repeated for a camera-to-object range of 400 mm and also 500 mm. Experimental conditions: $Z_1 = 300$ mm, $Z_2 = 400$ mm, $Z_3 = 500$ mm, $\sigma = 3°$.

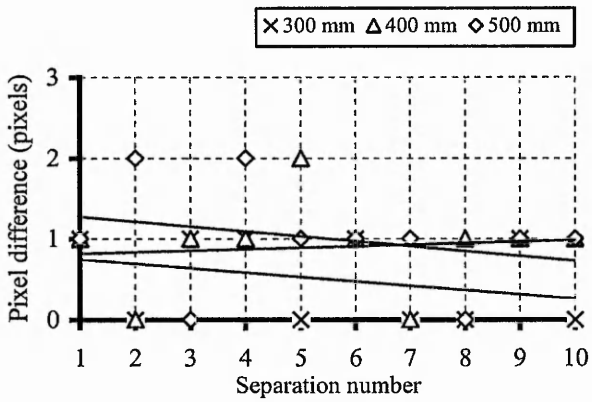

Graph 6-13 *Difference in parallax produced by a series of separations between two object points*

Discussion of the experimental results for the characterization of the depth planes

The results obtained are similar to those obtained from the visible light experiments, that is, a nominally flat line relationship between pixel difference and the corresponding target separation inferring parallel depth planes.

e) Sample perspective images produced by the multiple view lateral shift technique

Figure 6-14 illustrates a set of perspective images produced by the lateral shift technique. The imaged objects were chosen with industrial inspection of electromechanical devices in mind. They include a paper clip, a resistor, a fuse, a nut and a printed circuit board (these objects are located, in sequence, from foreground to background in object space). These images were produced using the following experimental conditions:

- depth of field : 150 mm
- maximum width and the maximum height of the object : 50 mm x 100 mm
- pixel resolution of the image : 640 pixels x 480 pixels
- base separation : 6 mm

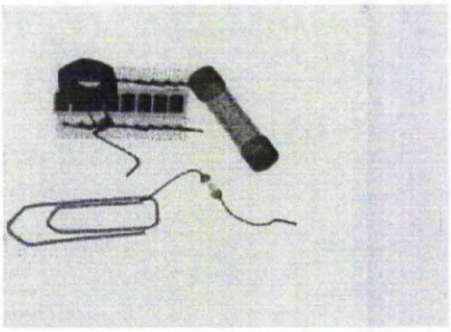

Sample image 1

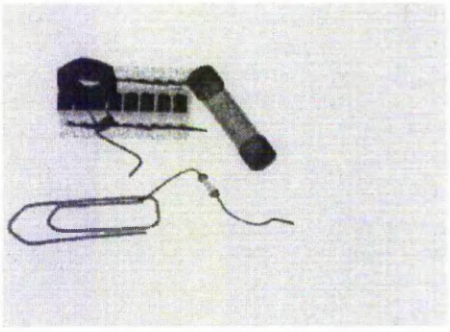

Sample image 2

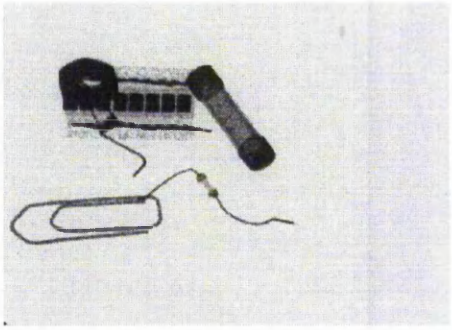

Sample image 3

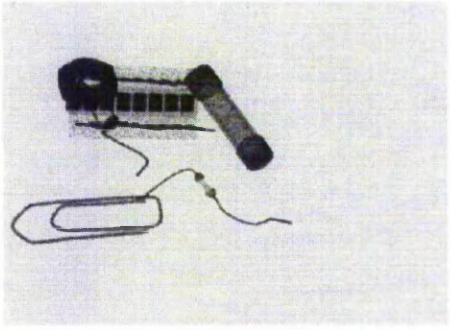

Sample image 4

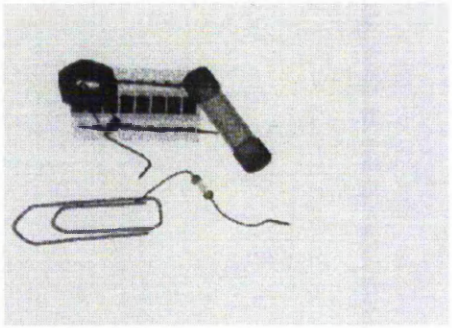

Sample image 5

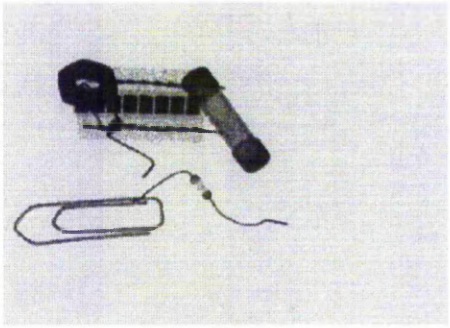

Sample image 6

Figure 6-14 *Sample images produced by the lateral shift technique*

The perspective images are arranged as a set of binocular stereoscopic image pairs allowing 'free viewing' to be realized.

6.8 Interim conclusions

I. Each of the multiple view techniques investigated produce perspective images by utilizing a single x-ray source and a single object pass (i.e. lateral translation)

II. Each of the multiple view techniques are proved capable of producing converged images. The lateral shift technique is required to implement a registration of the fixation plane after the images have been acquired whilst the line-scan technique enables the registration of the fixation plane during the image acquisition process.

6.8.1 Line-scan technique

Imaging concept

I. The concept of using a real-time image intensified x-ray set incorporating an 'area array line-scan' imaging principle has been successfully applied to model a multiple view linear x-ray detector system.
II. The two-dimensional imaging characteristics are demonstrated to be *equivalent* to those produced by a dedicated line-scan sensor.

2-D imaging characteristics

III. The x-axis field of view is determined by the interaction of the translation speed and the line acquisition time. The y-axis field of view is dependent upon the source-to-object range.
IV. The motion axis (x-axis) magnification from object space to image space is orthographic.
V. The magnification in the x and y axes can be arranged to produce a 1:1 object ratio for a given range.

3-D imaging characteristics

VI. A convergence plane can be effected in a set of perspective images by introducing a time delay into the start of the image acquisition for each line-scan sensor.
VII. The parallax production is dependent upon the convergence angle and the object range.
VIII. Parallax information produced by two successive views with the same convergence angle is identical regardless of orientation when a small angle is used (i.e. <5°).
IX. The dimensions of the voxel structures are nominally constant regardless of the object range therefore the minimum range increment in the z-axis (i.e. depth plane intervals) is also nominally independent of range.
X. The potential spatial resolution in the z-axis can be increased by increasing the convergence angle between successive views.
XI. This technique produces equidistant parallel depth planes in object space.

6.8.2 Lateral shift technique

2-D imaging characteristics

I. The field of view in the x and y axes are dependent upon the source-to-object range.

3-D imaging characteristics

II. A convergence plane can be effected in a set of perspective images by applying a relative horizontal shift to each perspective image.
III. The parallax production is dependent upon the object range and the base separation between successive views.
IV. Parallax information produced by two successive views with the same base separation is identical.
V. The dimensions of the voxel structures increase with increasing object range which in turn increases the depth plane intervals in the z-axis.
VI. The potential spatial resolution in the z-axis can be increased by increasing the base separation between successive views.
VII. This technique produces parallel depth planes in object space; the separations of adjacent depth planes are a function of Z^2.

7 IMAGE DISPLAY

7.1 Introduction

This chapter presents the development of the multiple view display system, for image sequences produced by the imaging techniques presented in Chapter 5 and Chapter 6. Initially, the description of the system components is presented. The display of the monoscopic image sequences, stereoscopic image sequences and a stereoscopic zoom function in the z-axis are discussed.

7.2 The image display system

The monoscopic display of the image sequences may be realized by displaying perspective images on a standard video monitor screen. However, in order to display stereoscopic image sequences an off-the-shelf liquid crystal 'shutter mechanism' in conjunction with circularly polarized glasses is utilized. The 'shutter' is placed in front of the monitor as shown in the photograph of Figure 7-1. The set up can be used for monoscopic and stereoscopic display purposes.

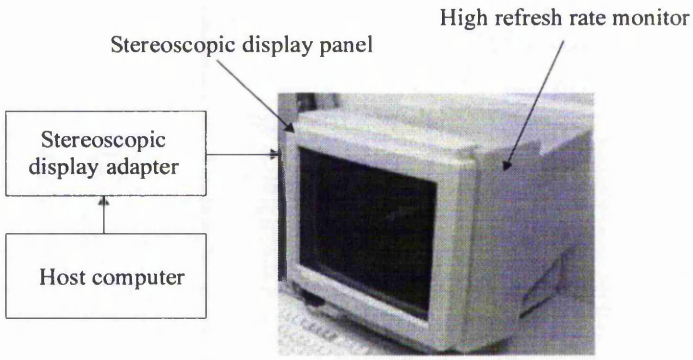

Figure 7-1 *The image display system*

The image display system consists of the following components:

- the *EIZO Flexscan* F56 high refresh rate monitor [112];
- the *NuVision Perceiva 17SX* stereoscopic display panel and circularly polarized glasses [113];
- the *Elsa Gloria-XL* stereoscopic display adapter [114];
- the host computer.

The image display system utilizes the image sequences, visible light and x-ray, produced by the line-scan or lateral shift techniques. An alternative way of presenting the stereoscopic image data is the autostereoscopic [115, 116, 117] technique where a lenticular screen is placed in front of the monitor screen, thus no special spectacles [118, 119] are required by the observer. However, it is not the objective of this research to optimise and characterize binocular stereoscopic display mechanisms.

7.3 Image display modes

The three-dimensional structure of an object can be imparted to the observer by presenting a sequence of perspective images as discussed in Section 2.3. The perspective images can be displayed in the following modes:

a) a sequence of perspective images exhibiting motion parallax.

b) a sequence of binocular stereoscopic images exhibiting motion parallax.

In addition a stereoscopic zoom in the z-axis may be produced. Each of the display modes is discussed in the following section.

7.4 Display of a sequence of perspective images exhibiting motion parallax

The maximum image display rate is dependent upon the computer processing power in this work. However, this frequency can be reduced by introducing a time delay in between the display of successive images as shown in Figure 7-2a.

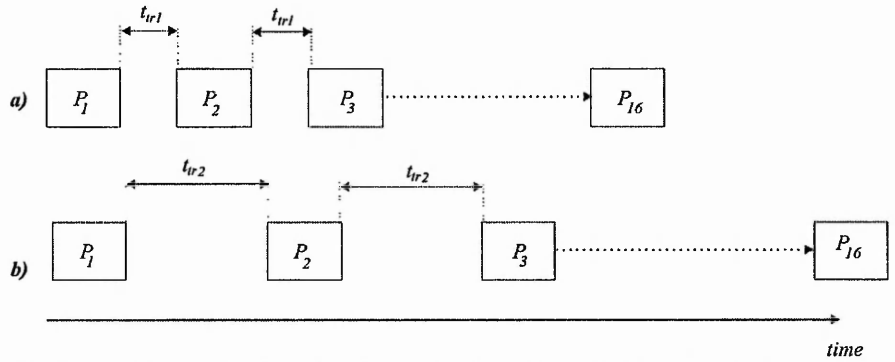

Figure 7-2 *Time delay introduced in between the sequential display of perspective images*

The second perspective image P_2 in the sequence is displayed after the time delay t_{tr} has elapsed; this time delay is introduced between each image transition to reduce the display frequency of the image sequence. Thus increasing the time delay (Figure 7-2b) results in a slower display frequency which in turn produces a slower 'object movement' in the display. It should be noted that to achieve a continuous movement, a minimum display frequency of 16 images/second (refer to Section 2.3) is required.

7.4.1 Control mechanism

Two display mechanisms are devised to control the display of the image sequences. These are:

a) Free-running; the perspective images are displayed cyclically in a continuous loop at a constant rate.

b) Interactive; the user controls the image sequence; via a mouse controlled cursor in the display.

Each of these mechanisms is described in the following text.

a) Free-running

As its name implies, this is a non-interactive display mechanism. The image sequence is displayed cyclically in the display, to create an oscillatory 'object movement'. Thus imparting three-dimensional information to the human observer through motion parallax. The flowchart describing the free-running control mechanism program for a 16-view image sequence is shown in Figure 7-3.

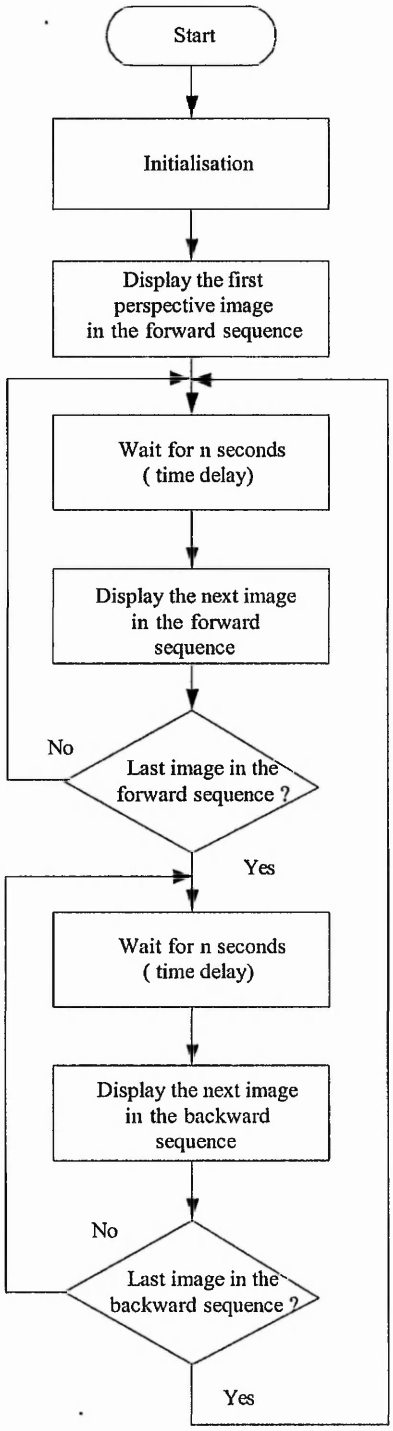

Figure 7-3 *Flowchart for the display of free-running image sequences*

The display of the monoscopic image sequence is initiated by the following memory allocation in the host computer.

- allocation of the memory regions in the computer memory for image storage;
- loading the perspective images into the allocated memory regions.

These are standard procedure and are commonly used in the display of the image sequences in this work. The initialisation continues with the assignment of the image transition rate, i.e. the display frequency selected by the user. It should be noted that this display frequency is defined in terms of the time delay t_{tr} as illustrated in Figure 7-2. After the initialisation, the first image P_1 is produced and after a time delay t_{tr} has elapsed, the second image P_2 in the sequence is subsequently displayed, P_2 -P_{16} etc. Thus this produces a display of a forward sequence of perspective images, i.e. P_1, P_2, ... P_{16}, in the video display monitor. When the last image (P_{16}) in the sequence is reached, the program displays the image sequence in reverse i.e. P_{16}, P_{15}, ... P_1. The overall effect of this is to produce a continuous oscillation of the object under inspection in the display.

b) Interactive control

The interactive display mechanism enables the operator to control the display of the perspective images. The operator can use a sensing device, for example a mouse, joystick or head tracking sensor [120], to control the display of perspective views. In this work, a mouse was chosen. The flowchart of the interactive control mechanism for a 16-view image sequence is illustrated in Figure 7-5. When the operator moves the mouse to the left or right, a number of new perspective images are displayed as a function of the magnitude of the mouse movement.

This initialisation of the display is identical to the free-running mode as discussed earlier. The initialisation continues with the assignment of the sensitivity parameters for the mouse movement. These determine the sensitivity level of the mouse movement, i.e. the number of pixels required to be moved by the operator in order to trigger the transition of perspective images. After the initialisation, a central or the reference image, in this example image 8 (P_8), is displayed on the screen (Figure 7-4).

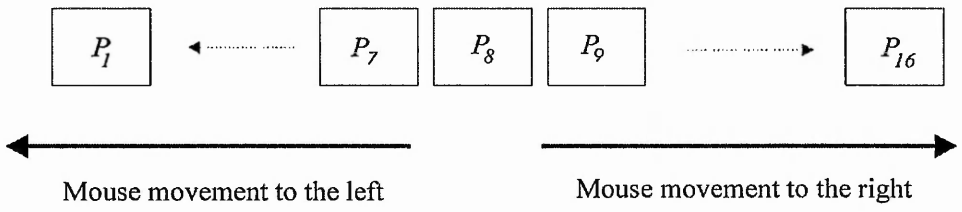

Figure 7-4 *Display of the image sequence using the interactive display mode*

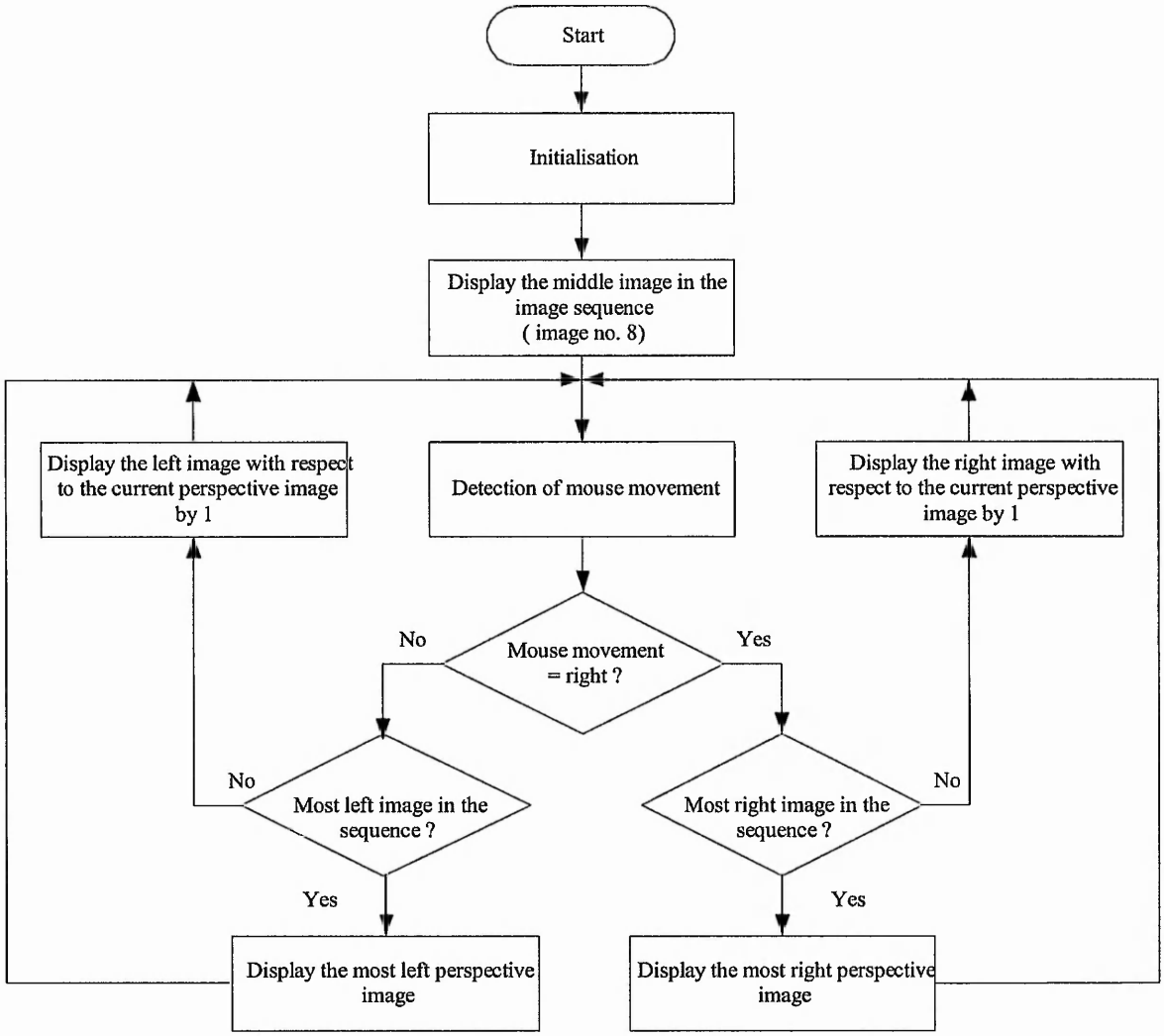

Figure 7-5 *Flowchart for the interactive control of the perspective image sequences*

This program is continually in the 'waiting state' thus no action is taken until the operator moves the mouse. For instance, if the operator moves the mouse to the left, the program will check if the most left perspective image P_1 being displayed; if this is not the case, the program responds by displaying perspective image P_7 in the image sequence. Thus if the most left image is reached, this image remains displayed even if the operator keeps moving the mouse to the left. A similar vice versa situation is implemented for right mouse movement.

7.4.2 Repositioning of the fixation plane

A technique which allows the dynamic repositioning of the fixation plane is devised as an additional image manipulation control. When a sequence of perspective images is presented to the human observer, either in free-running or interactive display modes, the imaged object is perceived to move about a fixation plane in the display. The concept of repositioning the fixation plane is theoretically analysed in Chapter 3 and the implementation of this concept is now discussed. In

order to reposition the fixation plane in the display a horizontal shift of pixel columns, with respect to the reference image, is introduced into the perspective images to produce a new image sequence. This new image sequence is referred to as the derived image sequence in this discussion. The concept is illustrated below in Figure 7-6.

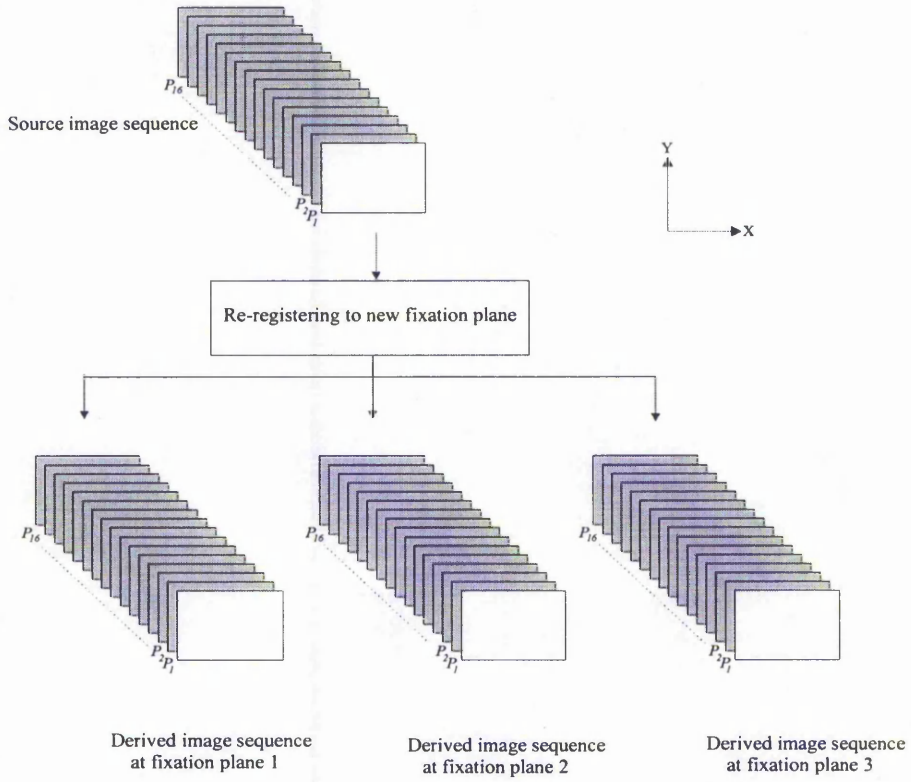

Figure 7-6 *The concept of source image sequence and derived image sequence*

The derived image sequence is produced by re-calculating the number of pixels columns required to be shifted with respect to the reference image (image 1). The pixel column shift process is dynamic and is achieved in the memory before the perspective images are displayed. The control of the fixation plane (i.e. closer or further away from the observer) is assigned to a mouse button.

The simplified flowchart of a free-running sequential display which allows dynamic repositioning by the fixation plane for a 16-view image sequence is depicted in Figure 7-7. The display cycle is similar to the description of the free-running display mechanism discussed in Section 7.4.1. After the initialisation of the system parameters, the forward image sequence is displayed on the monitor screen. After each image is displayed, the program checks for the mouse button usage; and if activated will invoke the corresponding action of re-registering each perspective image in order to effect a new fixation plane. After this process the program will check if the last image P_{16} in the image sequence is being displayed. In this way, the last image in the sequence is monitored enabling the program to initiate the display of the backward image sequence to create a continuous loop.

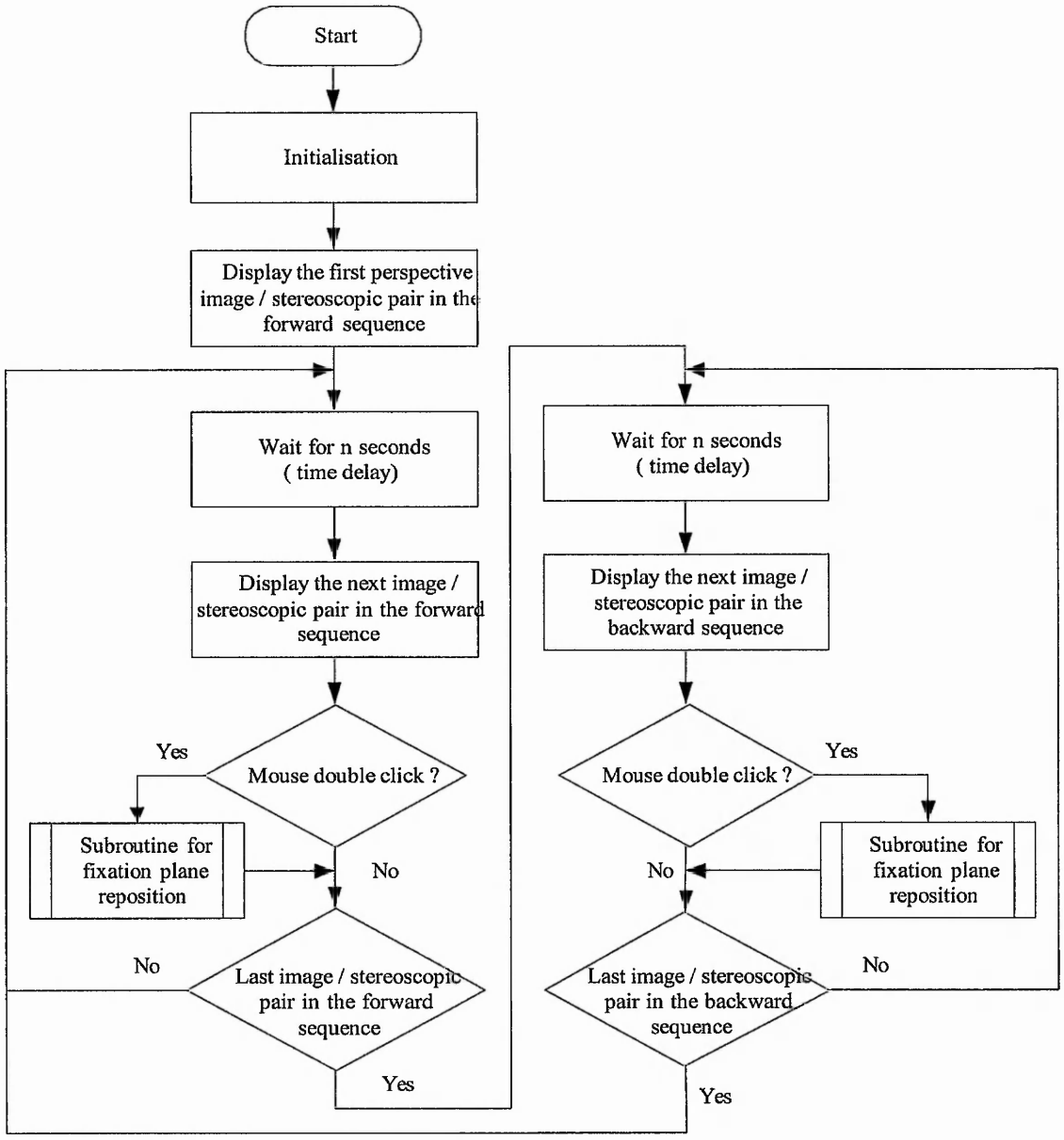

Figure 7-7 *Flowchart for the dynamic repositioning of the fixation plane using a free-running display mechanism*

In the case of the interactive display mode, the fixation plane can also be changed dynamically. The flowchart of this operation is shown in Figure 7-8. The display mechanism is identical to that described in Section 7.4.1a. This program allows the operator to interact with the display and dynamically change the fixation plane.

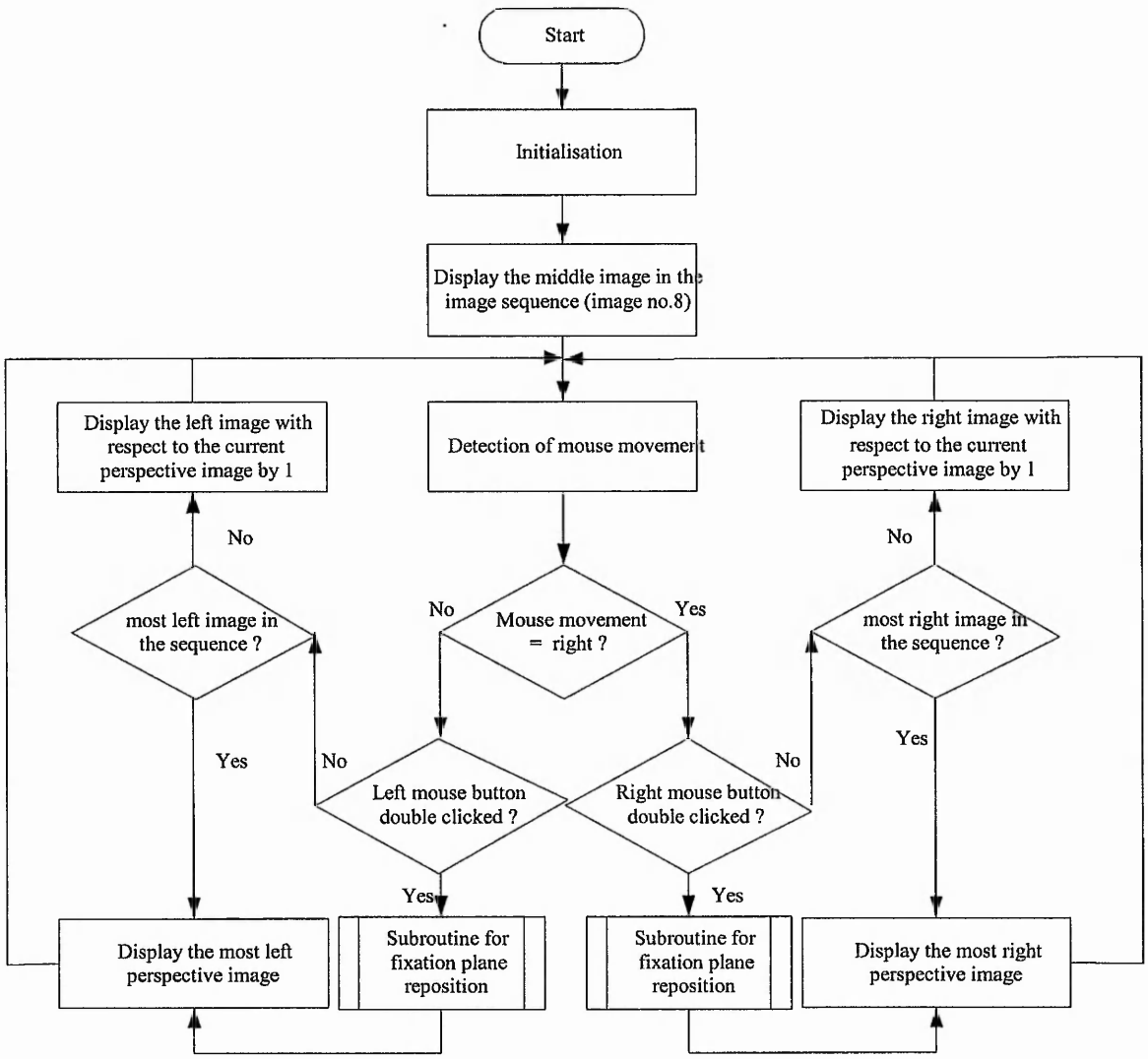

Figure 7-8 *Flowchart for the dynamic repositioning of the fixation plane using an interactive display mechanism*

7.5 Display of a sequence of binocular stereoscopic images exhibiting motion parallax

For the display of a stereoscopic image sequence, an out of phase image sequence is channelled to the respective eyes of the observer. It should be noted that the out of phase image sequence and the in phase image sequence contain identical perspective images. This is illustrated in Figure 7-9.

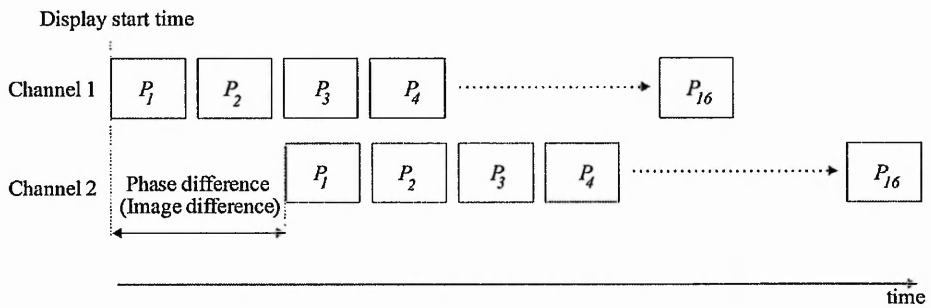

Figure 7-9 *The concept of out of phase image sequences*

For example, P_1 is paired up with P_2 (1 image difference) or P_1 is paired up with P_3 (2 image differences). The phase difference between two image sequences has to be defined prior to the image display. The implementation of a 16-view display of a stereoscopic image sequence with phase shift of '1 image difference' is presented in the following text. The stereoscopic image pairs are defined prior to display of the image sequences and the stereoscopic pair 'n' are displayed on two separate channels, i.e. left channel C_L and right channel C_R, as shown in Table 7-1.

'n'	1	2	3	4	5	6	7	8	9	10	11	12	13	14	15
C_L	1	2	3	4	5	6	7	8	9	10	11	12	13	14	15
C_R	2	3	4	5	6	7	8	9	10	11	12	13	14	15	16

Table 7-1 *Stereoscopic pairs used for display of a stereoscopic image sequence*

Once the phase difference of the stereoscopic image sequence is defined, the first stereoscopic pair, left and right perspective images, are displayed in the respective display channels. The display of the stereoscopic image sequence can also be implemented in the free-running and interactive modes. The flowcharts in Figure 7-3 and Figure 7-5 may be used to explain the display methodology; replacing the 'perspective image' to 'stereoscopic image pair'. Similar to the monoscopic display discussed in Section 7.4, a time delay t_{tr} is required to elapse before the next stereoscopic image pair is displayed. After displaying each stereoscopic pair, the program will check for the last stereoscopic image pair in the image sequence, perspective image 15 and 16 in this example, before it reverses the direction of the display sequence. It should be noted that a reversal in the image sequence does not invert the stereoscopic image. Otherwise, the observer would see a reversal in depth information [121]. Also, depth reversal would destroy the integrity of the visible light image sequence due to a conflict of depth cues.

7.6 Stereoscopic zoom in the z-axis

The stereoscopic display can be realized with off-the-shelf equipment (as discussed in Section 7.2) by channeling appropriate perspective images to each of the observer's eyes. In the multiple view arrangement, a number of perspective images are available. Thus different combinations of the perspective images enables an increase in depth magnification (i.e. zoom in the z-axis) to be effected. Two approaches are utilized to provide a zoom in the z-axis of the display. The sequence of zoomed stereoscopic image pairs are stated in Table 7-2 for each approach.

Stereoscopic pair number 'n'	Left-to-right (perspective image number)		Inside-out (perspective image number)		Parallax magnitude
	Left channel	Right channel	Left channel	Right channel	
1	1	2	8	9	1
2	1	3	8	10	2
3	1	4	7	10	3
4	1	5	7	11	4
5	1	6	6	11	5
6	1	7	6	12	6
7	1	8	5	12	7
8	1	9	5	13	8
9	1	10	4	13	9
10	1	11	4	14	10
11	1	12	3	14	11
12	1	13	3	15	12
13	1	14	2	15	13
14	1	15	2	16	14
15	1	16	1	16	15

Table 7-2 *Various stereoscopic pair combinations for a z-axis zoom*

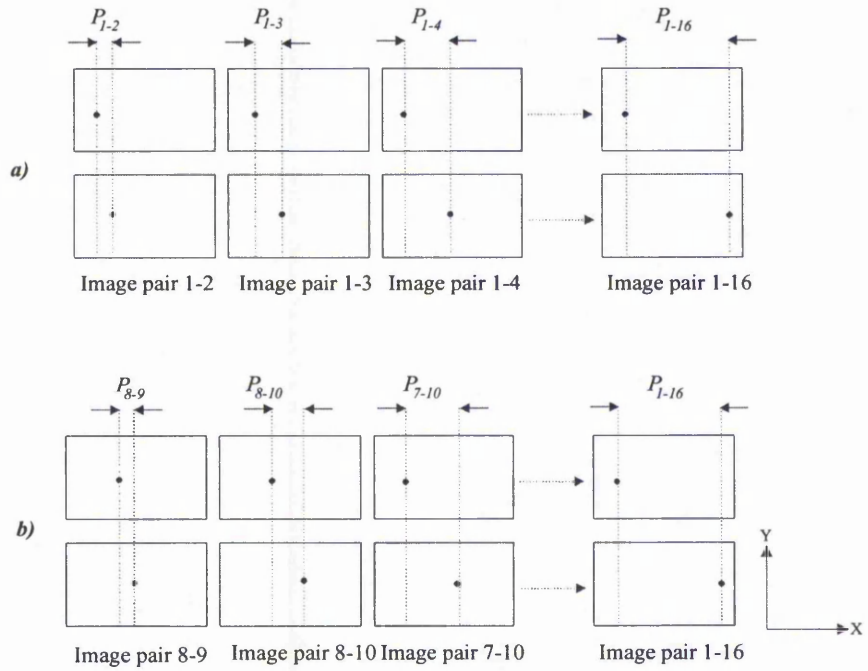

Figure 7-10 *Two different approaches to achieve z-axis zoom a) left-to-right and b) inside-out*

In fact, each approach utilizes the same perspective images to produce an increasing depth effect in the binocular stereoscopic display. However, the dynamic symmetry of the parallax information displayed on the monitor screen is asymmetrical in the 'left-to-right' approach and symmetrical in the 'inside-out' method, as depicted in Figure 7-10. The flowchart of the z-axis zoom program is shown in Figure 7-11. This program enables the display of a static stereoscopic image pair with the capability to dynamically change the magnification in the z-axis on the operator's command. After

the initialisation of the system parameters, the first stereoscopic pair is shown in Table 7-2 is displayed.

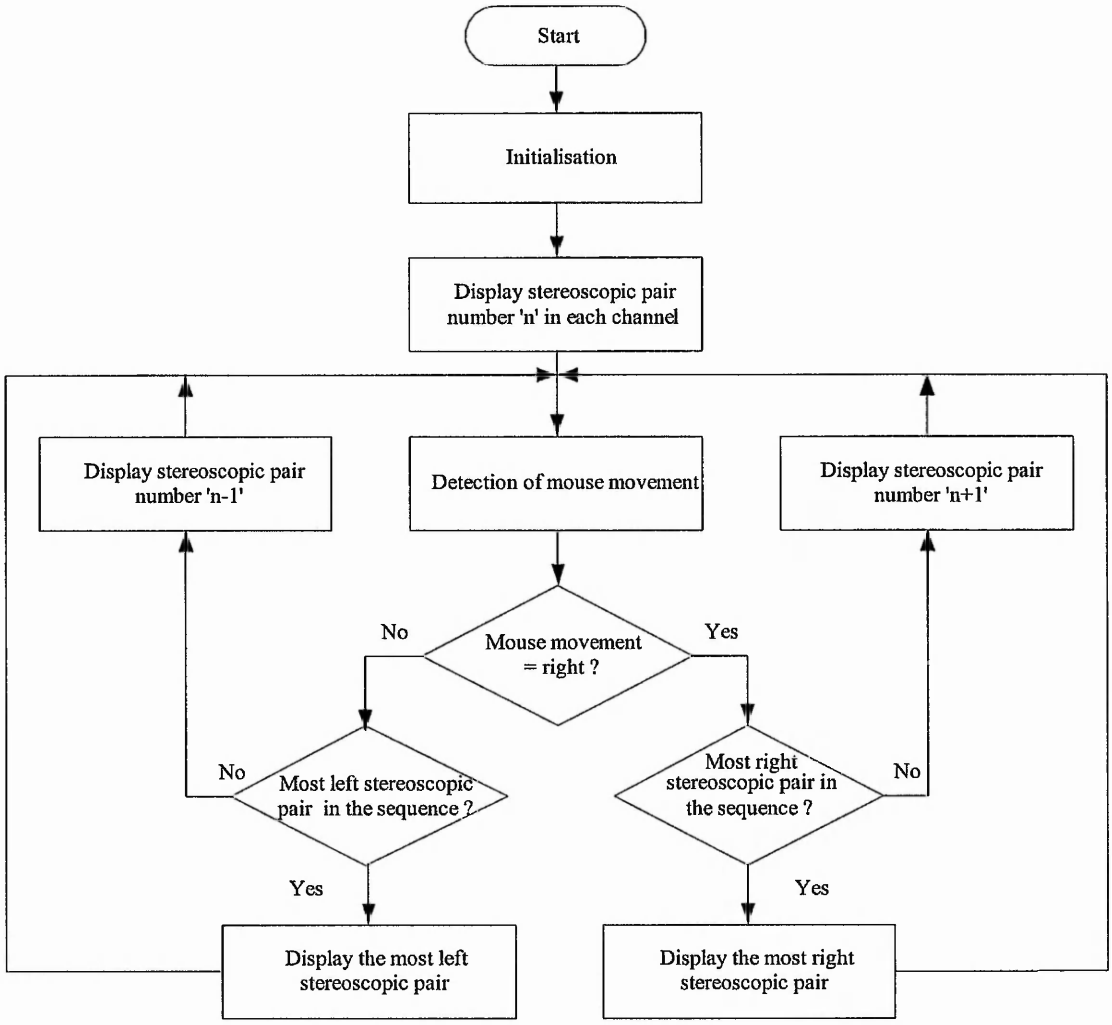

Figure 7-11 *Flowchart for the z-axis zoom*

The z-axis zoom in this program is controlled by a mouse button; left button triggers the 'zoom in' function and the right button triggers the 'zoom out' function. If the operator triggers the 'zoom in' function, the program moves onto the next stereoscopic image pair as listed in Table 7-2 and produces an increased depth magnification in the display. Likewise, if the 'zoom out' function is triggered, the program displays the stereoscopic image pair with a decreased depth magnification.

The source code for the display mechanism is written in Visual C++ and the code can be found in Appendix D.

7.7 Experiments with the display system

Sixteen perspective images (Figure 7-12) produced by the experimental multiple view system are used as a source image sequence in this experiment. The experiment aims to evaluate the change of

the parallax information during the display of the image sequence. The psychological aspects of the image display are beyond the scope of this investigation. Three imaged features are used as a reference for the determination of the 'object movement'. These features are located in front, behind and at the convergence plane in object space. The x-coordinates of these features from perspective image No. 1 to perspective image No. 16, are plotted in Graph 7-1.

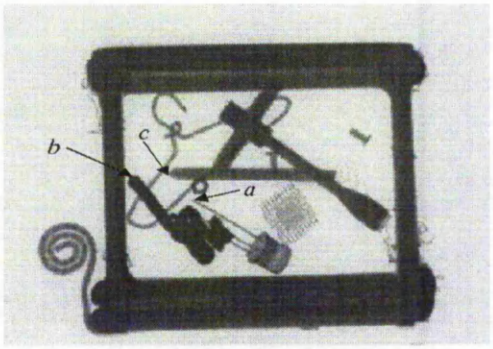

perspective image 1

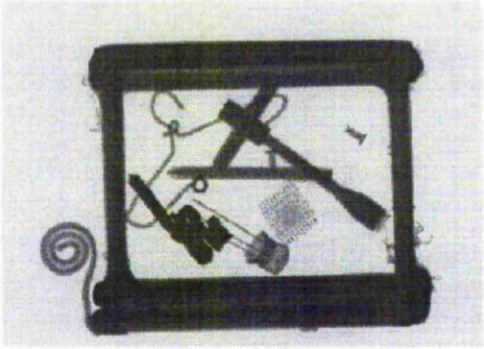

perspective image 2

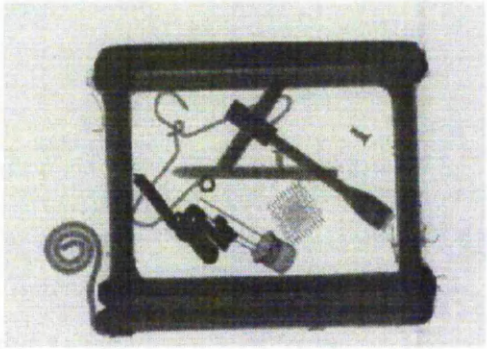

perspective image 3

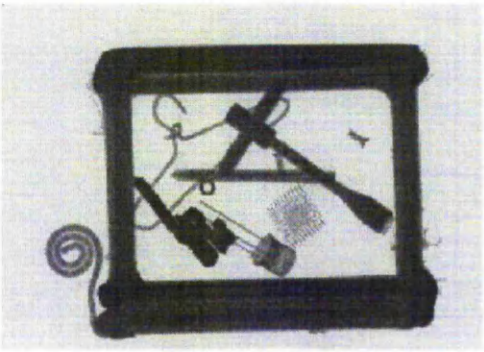

perspective image 4

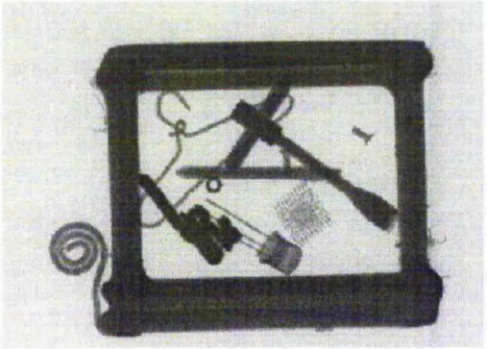

perspective image 5

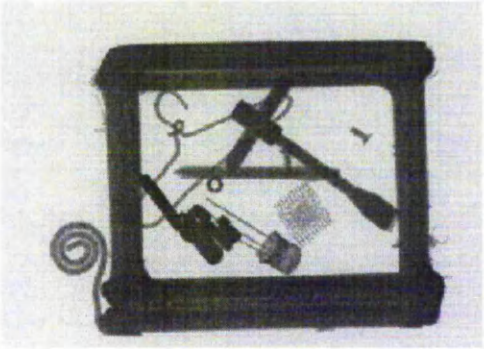

perspective image 6

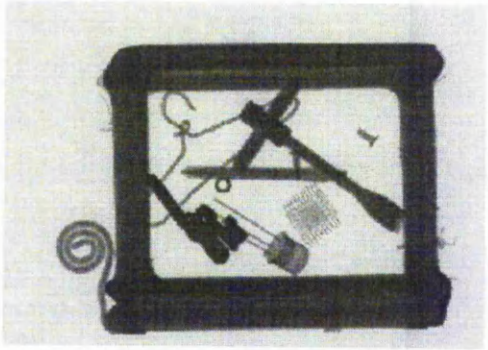

perspective view 7

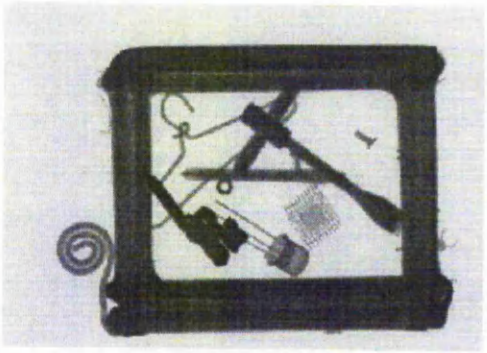

perspective view 8

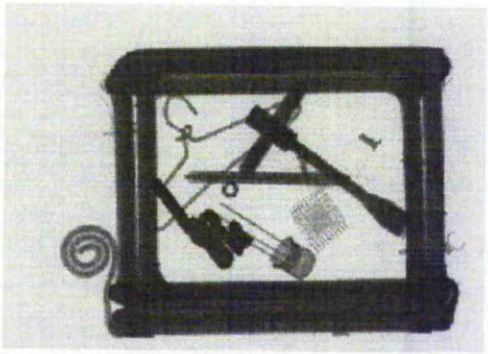

perspective image 9

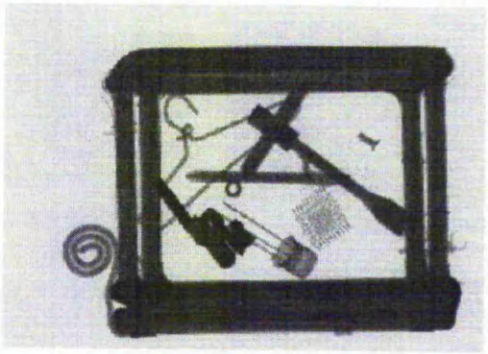

perspective image 10

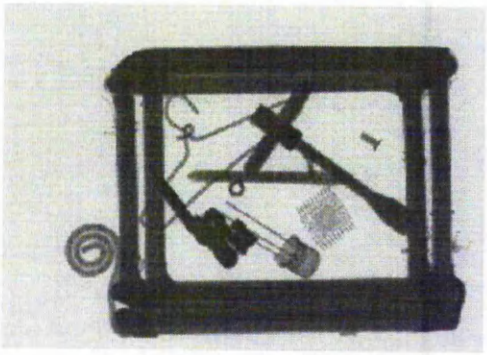

perspective image 11

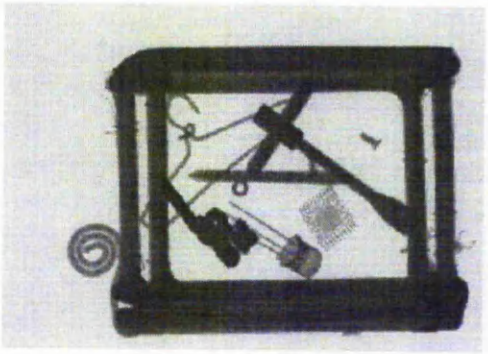

perspective image 12

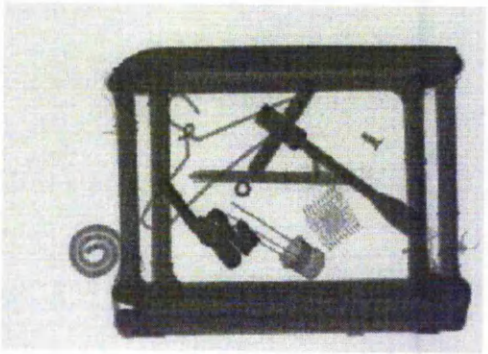

perspective image 13

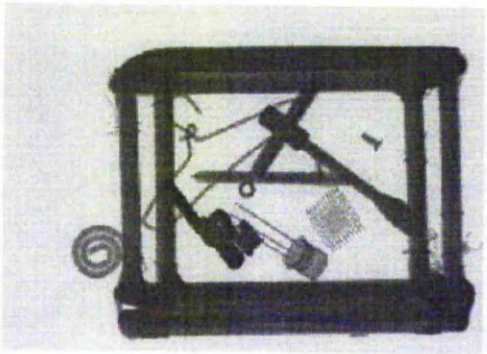

perspective image 14

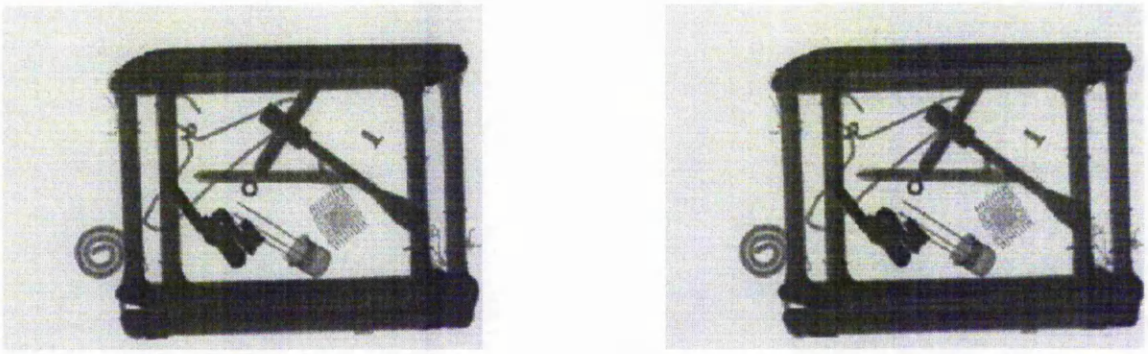

perspective image 15 perspective image 16

Figure 7-12 *Sixteen perspective images produced by the multiple view line-scan system*

A wire frame 'cube' containing a range of objects in order to model a suitcase and its contents. These images are produced, by the line-scan technique, using the following experimental conditions:

- depth of field : 70 mm
- maximum width and the maximum height of the object : 50 mm x 40 mm
- pixel resolution of the image : 640 pixels x 480 pixels
- angular distributions : 1.5 ° between successive image

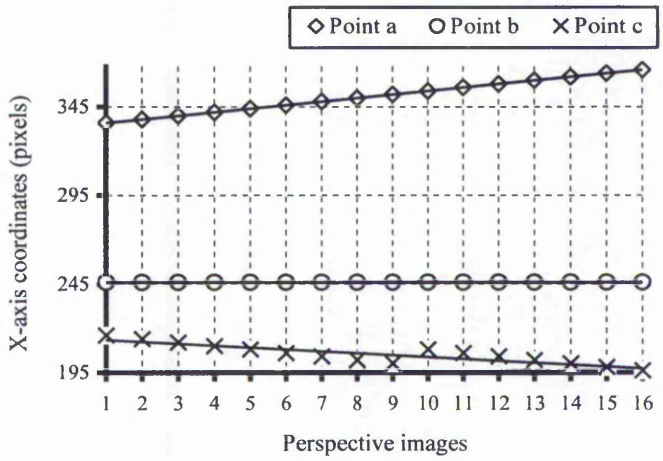

Graph 7-1 *Change in x- coordinate position for three selected imaged points*

Discussion of the results for the image display

From Graph 7-1, the following characteristics are evident:

- the x-coordinate of point *b* is nominally static and this indicates that it is located in the convergence plane in object space;
- the graph for point *a* has a positive gradient and this indicates that this point is located behind the convergence plane;
- the graph for point *c* has a negative gradient and this indicates that this point is located in front of the convergence plane.

The 'imaged point movement' in the display is represented in the diagram of Figure 7-13. It is illustrated that point *a* and point *c* move in the opposite directions (different signs of gradient in Graph 7-1). Whilst point *b* remains static in the display as it is located in the convergence plane in object space which corresponds to the fixation plane in the display.

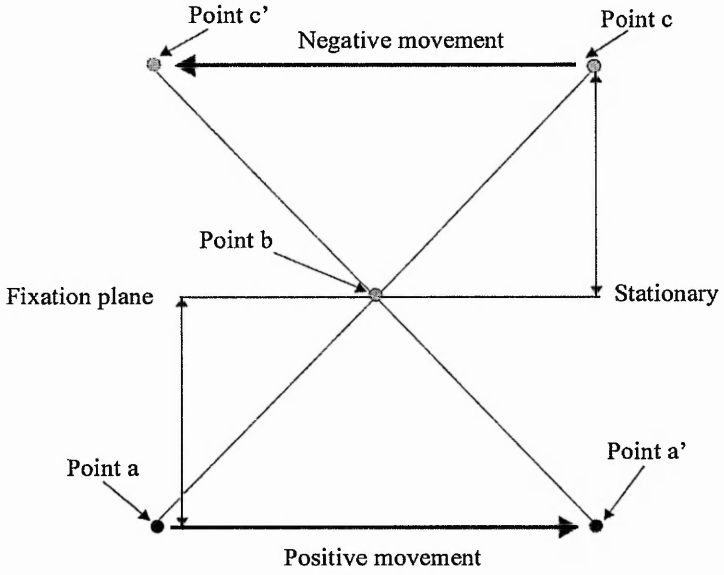

Figure 7-13 *Representation of the movement of the imaged points*

As discussed in Section 7.4.2, the fixation plane in the display can be dynamically changed during the display of an image sequence. Thus the fixation plane is changed to point *a* and again, the x-coordinate of the same selected imaged points are plotted in Graph 7-2.

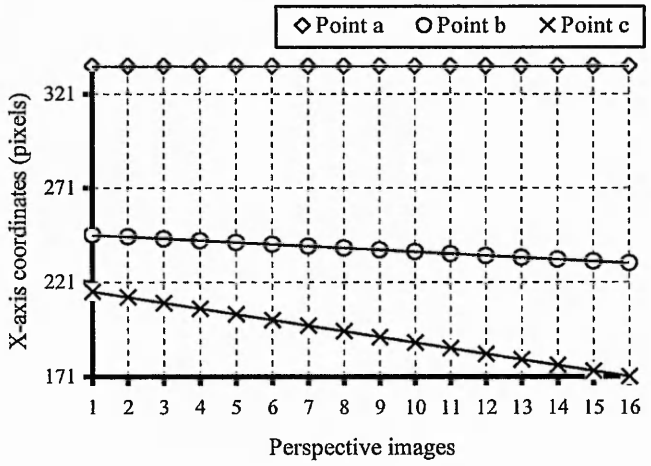

Graph 7-2 *Change in the x-coordinate position for the three selected imaged points after repositioning the fixation plane in the display*

It is observed that point *a* becomes static as it now occurs in the fixation plane. It is evident that:

- the relative movement between the three of the imaged points is the same as that observed in the previous display (i.e. where the fixation plane has not been repositioned);
- the movement of each imaged point with respect to the fixation plane is altered.

This effect can be explained with the aid of Figure 7-14.

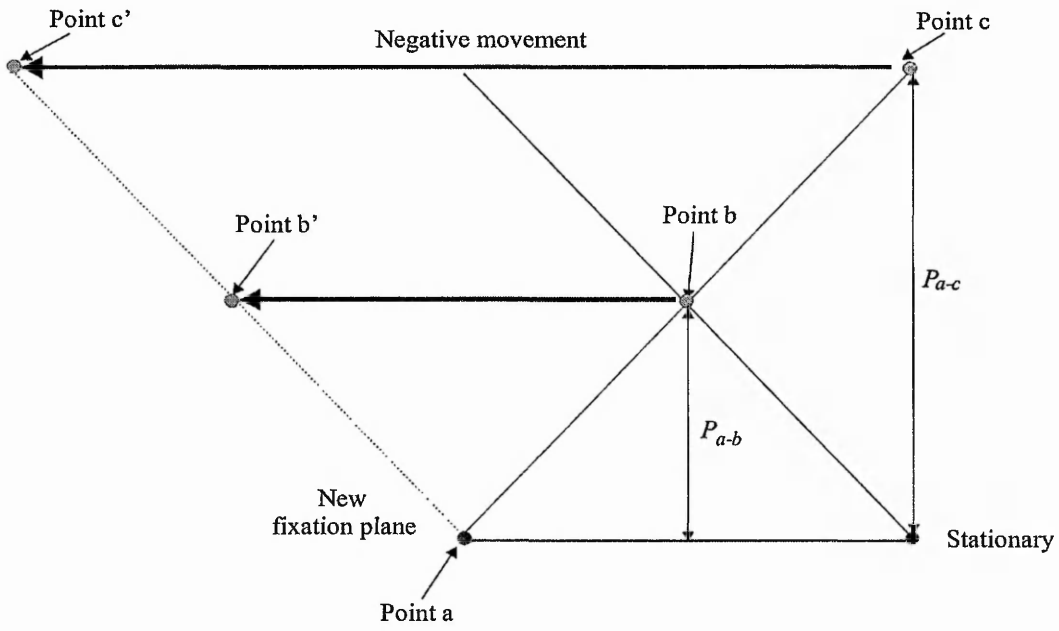

Figure 7-14 *Representation of the movement of the imaged points after repositioning of the fixation plane in the display*

When the fixation plane is repositioned to be coincident with point *a*, the reference plane for the parallax is also changed to this plane. Thus, point *a* becomes static and the relative parallax of point *b* and point *c* (P_{a-b} & P_{a-c}) with respect to the new fixation plane is increased. However, the relative parallax between imaged points remains unchanged as shown in Figure 7-14. This is previously discussed in Section 4.2.5 and Section 4.3.5.

7.8 Interim conclusions

I. Three image display modes are possible:
   - a sequence of perspective images exhibiting motion parallax;
   - the choice of multiple static binocular stereoscopic images;
   - a sequence of binocular stereoscopic images exhibiting motion parallax.

II. Two control mechanisms are possible for the display of image sequences.
   - free-running; the image sequence is displayed cyclically to create an oscillatory 'object movement';
   - interactive; the display of the perspective images can be controlled by the user.

III. Motion parallax in a display can be produced by showing perspective images in a correct sequence.

IV. Preliminary investigations indicate that motion parallax significantly enhances a human observer's understanding of a three-dimensional structure.

V. Zoom in the z-axis is possible by using different combinations of perspective image pairs.

VI. Convergence angles of the order of 1° were found to be satisfactory for the production of motion image sequences.

VII. A video display parallax of up to a maximum of ±5 mm for an observer at a viewing distance of 0.75 m is found to produce stereoscopic images which are comfortable to view.

VIII. The dynamic repositioning of the fixation plane in the display (whilst the observer is viewing the display) is possible.

IX. When the fixation plane is altered in the display:
- relative parallax between two imaged point remains unchanged;
- parallax of an imaged point with respect to the fixation plane is changed.

8 SUMMARY, CONCLUSIONS AND FUTURE WORK

8.1 Introduction

This chapter concludes this research in the following manner:

- summarising the work conducted;
- providing concluding remarks;
- suggesting the possible direction of future work.

8.2 Summary

The problem associated with the interpretation of a radiograph of a complex three-dimensional structure arises as a direct consequence of using transmitted radiation to produce an image. Thus psychological cues to depth associated with 'normal' two-dimensional images such as a photograph are not available in the standard x-ray image. In fact, these cues can be incorrectly interpreted as being present in an x-ray image and may lead to serious ambiguity in the subsequent interpretation of that image. In an attempt to solve this problem previous research has utilized the powerful physiological depth cue of binocular parallax by the production of binocular stereoscopic image pairs. However a static binocular stereoscopic view produces information from a very limited 'arc' about the object. The research presented in this thesis introduces another powerful physiological depth cue of motion parallax into the resultant shadowgraph x-ray images. This is achieved by collecting a number of different views (i.e. from 6 to 16) of the object under inspection and displaying the resultant 'raw' perspective images in a specific sequence on a 'standard' video monitor. This produces the effect of the object appearing to undergo a partial rotation in the display. The resultant image sequences produced by the imaging techniques under consideration in this research utilize motion parallax, binocular parallax or a combination of motion and binocular parallax to enable the three-dimensional structure of an object under inspection to be better understood by a human observer. A number of operational and scientific constraints have been imposed in order to extend the potential applications of the imaging techniques developed.

a) Operational constraints:

The operational constraints have been developed in order to minimize the hardware complexity and also, to maximize the operational simplicity for online visual inspection applications.

i. *Single x-ray source* - A single x-ray source is highly desirable for the development of a multiple view technique for the following reasons:
    - to facilitate the process of alignment/collimation and matching of the x-ray source and x-ray detectors;
    - reducing the overall mechanical/electrical complexity, size, weight and cost of the imaging system.

ii. *No physical rotation* - The imaging technique must incorporate lateral movement of the object under inspection rather than a physical rotation. This is because the internal structure/arrangement of the object under inspection might be disturbed when physical rotation is introduced; thereby destroying the visual integrity of the resultant images. Additionally conveyored systems are commonly used in industrial scenarios.

iii. *Single pass* - The object under inspection is required to pass through the field of view of the x-ray sensor only once. In addition it is highly desirable to obtain many views of the object under inspection in the same time interval as that required for a single view using a given x-ray source/sensor technology.

b) Scientific constraints:

The scientific constraints have been developed in order to minimize effects which may cause visual discomfort to the human observer.

i. *High visual quality* - The perspective images must exhibit high visual quality in terms of equal contrast and brightness in order to minimize intensity flicker and to enhance motion parallax and binocular stereoscopic fusion.

ii. *No geometric distortion* - There must be no geometric distortion of parallax information as this would destroy the visual integrity of the resultant images.

iii. *Smooth 'object motion' in the display* - The parallax produced in the resultant image display must exist in a format which can be directly appreciated by a human observer from a sequence of 'raw' perspective images (i.e. no image reconstruction required). Thus apparent movement in the display must be smooth and comfortable to view.

In order to test the various multiple view imaging techniques proposed would require the development of sophisticated x-ray imaging equipment. However a visible light analogy of transmission x-ray imaging was identified as the theoretical basis for developing a visible light experimental system utilizing a standard charge coupled device area array camera. The camera is used to obtain perspective images during a single linear translation of the object under inspection. The camera in conjunction with an appropriate image capture mechanism is used to obtain multiple perspective images in its standard mode of operation (i.e. area array 'snapshot') or a novel multiple line-scan mode. This latter mode of operation is implemented for the following reasons:

i. The geometric alignment of the individual photosite columns is determined by the construction tolerances of the photosensitive area of the camera's imager. Thus the relative three-dimensional alignment of the sensors is extremely accurate in comparison with dedicated line-scan devices; misalignment in terms of roll, pitch and yaw of each line-scan sensor may be considered non existent as far as this work is concerned.

ii. The angular distribution of the perspective views can be electronically controlled (via software) by the simple expedient of selecting different video lines/photosite columns for the image production process. Thus, *no* mechanical reconfiguration is required.

iii. A live two-dimensional image is available for initial system configuration and set up of the lighting conditions and lens functions.

Further work combined the geometric and temporal design theory developed for the production of motion parallax with that required for the production binocular stereoscopic images. The design is applicable to both the multiple view line-scan technique and the multiple view lateral shift technique. The whole optical path of this design, from object space to the image sensor plane and from the display to the human observer, is examined in order to produce:

- continuity or smoothness of the object movement in the resultant 'monoscopic' display;
- continuity or smoothness of the binocular parallax information in the resultant dynamic stereoscopic display.

This analysis is divided into the following areas:

I. Registration of the perspective views in the z-axis in object space; this determines the position of the multiple view region in object space.

II. The production of parallax; this evaluates parallax as a function of the successive perspective views which form the multiple view region.

III. The multiple view region and the binocular stereoscopic depth of field; this determines the geometric relationship between the multiple view region and the binocular stereoscopic depth of field.

IV. The minimum detectable range increment in object space; this discusses the minimum range increment in the z-axis and the stereoscopic zoom in the z-axis.

V. Motion parallax as a function of the spatial sampling pattern in the z-axis; this evaluates the spatial sampling patterns produced by the overlapping perspective views. Also, the effect of the repositioning of the fixation plane in the display on the sampling pattern in object space is examined.

An experimental visible light system was constructed to enable the empirical evaluation of the proposed multiple view techniques, i.e. line-scan technique and lateral shift technique.

- repeatability tests are used to established the integrity of the experimental systems;
- the effect of independently changing the system parameters in order to control the formation of a two-dimensional image is empirically investigated;
- parallax production is empirically evaluated and the parameters that affect the parallax information are identified;

- the voxel distribution, spatial resolution and depth plane characteristics are empirically evaluated;
- the multiple view line-scan technique and the multiple view lateral shift technique are compared in terms of their two-dimensional and three-dimensional imaging characteristics.

The successful implementation of a visible light system produced sufficient interest by the Home Office Science and Technology Group to provide funding to conduct definitive experiments with shadowgraph images. This was successfully achieved by implementing a real time image intensified x-ray set to replicate the findings of the earlier visible light work. Comparative results were also obtained by conducting the equivalent experiments to validate the visible light analogy of x-ray imaging formulated and adopted in this work.

8.3 Conclusions

There has been no significant deviation experimentally from that which is predicted theoretically in the whole of this research programme. The conclusions drawn from this research are presented in the following text. They are categorised into aspects which are of particular relevance to:

I. Imaging concept.
II. Display method.
III. Comparison of the line-scan technique and the lateral shift technique.

8.3.1 Imaging concept

I. The visible light arrangement is proved geometrically equivalent to an x-ray arrangement by the experimental work conducted in this research.

II. The rotational technique is regarded as unsuitable for on-line visual inspection applications as any unconstrained motion produced by the physical rotation required during the image acquisition process will destroy the visual integrity of the resultant images.

III. Two-dimensional imaging characteristics of the area array sensor, operating in a line-scan mode, are demonstrated to be *equivalent* to those produced by a dedicated line-scan sensor.

IV. A visible light camera system operating in a line-scan mode was found to be excellent tool for simulating multiple view line-scan x-ray systems. Indeed this novel technique represents new research in the field of visible light imaging. Therefore, it is also concluded that this visible light technique may well have applications in its own right.

V. An image intensifier system employing an area array line-scan principle was found to be excellent tool for simulating a multiple linear x-ray detector array system. Indeed this novel

technique represents new research in the field of x-ray imaging. Therefore, it is also concluded that this multiple view technique may well have applications in its own right.

VI. The multiple view imaging techniques developed in this work are scalable. In other words, there are no theoretical limiting factors for the volume of the multiple view region in object space. Therefore, the inspection of either 'very large' (e.g. container lorry) or 'very small' (e.g. integrated circuits) objects would seem possible using the techniques developed. In practice of course there would be limiting factors, although it is envisaged these would concern the implementation the x-ray technology rather than the specific technique developed here.

The line-scan technique

- a convergence plane can be effected in a set of perspective images by introducing a time delay into the start of the image acquisition for each line-scan sensor with respect to a reference sensor;
- the parallax production is dependent upon the convergence angle and the object range;
- no vertical parallax is produced in the display;
- motion parallax is linearly distributed about the fixation plane in the display;
- the dimensions of the voxel structures are nominally constant regardless of the object range therefore the minimum depth increment in the z-axis is also independent of range;
- the potential spatial resolution in the z-axis can be increased by increasing the convergence angle between successive views;
- this technique produces equidistant parallel depth planes.

The lateral shift technique

- a convergence plane can be effected in a set of perspective images by applying a relative horizontal shift to each perspective image with respect to a reference image;
- the parallax production is dependent upon the object range and the base separation between successive views;
- no vertical parallax is produced in the display;
- motion parallax is non-linearly distributed about the fixation plane in the display;
- the dimensions of the voxel structures increase with increasing object range which in turn reduces the potential spatial resolution in the z-axis;
- the potential spatial resolution in the z-axis can be increased by increasing the base separation between successive views;
- this technique produces parallel depth planes in object space; the separation of adjacent depth planes are a function of Z^2.

8.3.2 Display methods

I. Three display techniques can be used to present the image information. These are:
   - a sequence of perspective images exhibiting motion parallax;
   - the choice of multiple static binocular stereoscopic images;
   - a sequence of binocular stereoscopic images exhibiting motion parallax.

II. Two control mechanisms are possible for the display of image sequences.
   - free-running; the image sequence is displayed cyclically to create an oscillatory 'object movement';
   - interactive; the display of the perspective images can be controlled by the user.

III. Preliminary investigations indicate that motion parallax significantly enhances a human observer's understanding of a three-dimensional structure.

IV. The theoretical appraisal did not include a programme to investigate the psychological properties of the display of the resultant image sequences. However, there has been very little indication of any problems associated with the ease and comfort viewing interpretation of the display of monoscopic as well as stereoscopic image sequences. The system has been exhibited to many interested parties (including representatives from the PSDB and DETR) on site at *The Nottingham Trent University*. Many experienced viewers have commented on the instant fusion (for the stereoscopic image sequence) and good visual quality of the images. A sample image sequence can be found in Appendix E.

V. One degree per view is found to be satisfactory for the display of the image sequences for the experimental conditions encountered in this work.

VI. The number of perspective images utilized in this work in order to produce motion parallax ranged from 6 to 16. However it has been noted that whilst generally the apparent smoothness of motion increases with increasing the number of views. The relative visual improvement appears to diminish rapidly for more than 8 views. Thus for the applications under consideration in this work 8 views has been identified as a good compromise between visual effectiveness and system complexity.

VII. A video display parallax of up to a maximum of ±5 mm for an observer at viewing distance of approximately 0.75 m is found to produce stereoscopic images which are comfortable to view.

VIII. Zoom in the z-axis is possible by using different combinations of perspective images.

X. The dynamic repositioning of the fixation plane in the display (i.e. whilst the observer is viewing the display) is possible.

XI. When the fixation plane is altered in the display:
- relative parallax between two imaged point remains unchanged;
- parallax of an imaged point with respect to the fixation plane is changed.

8.3.3 Comparison of the line-scan technique and the lateral shift technique

The line-scan technique has inherent advantages over the lateral shift technique in a number of respects. However, both these imaging techniques exhibit a number of similarities. These are:

- a single x-ray source is required to produce the perspective images;
- a lateral movement of the object under inspection is required;
- motion parallax in the display can be produced by showing perspective images in a correct sequence;
- depth planes are parallel to the x-ray detector;
- no vertical parallax is produced in the display.

This section discusses the dissimilarities of the two techniques and identifies the advantages of the line-scan technique over the lateral shift technique.

Scientific aspects

i) Voxel distribution

The line-scan technique produces a linear voxel structure whereas the lateral shift technique produces a non-linear voxel structure (i.e. increasing with object range). Linear voxel structure has a number of advantages:

- linear relationship between image space parallax and a range separation in object space;
- the fixation plane in the display is linearly related to the convergence plane in object space.

ii) Image quality

A collimated x-ray line-scan technique has the potential to produce higher image quality in terms of image contrast and brightness in comparison to the 'uncollimated' lateral shift x-ray technique.

Design aspects

i) Image acquisition time

The image acquisition time is limited by the sensor technology utilized. Thus assuming the line-scan and lateral shift techniques use identical sensor technology, the time required for the lateral shift arrangement to form a two-dimensional image is N_x times faster than the line-scan

technique; where N_x is the x-axis pixel resolution in a line-scan image. However, the image acquisition time in the lateral shift arrangement is dependent upon the number of views required. Thus the acquisition time for a N-view arrangement requires N times longer than the image acquisition for a single two-dimensional image. Whereas in the line-scan arrangement, the image acquisition time is almost the same (due to the short time delays introduced between the start of image acquisition for each perspective in order to effect a chosen convergence plane) regardless of the number of views required. This is because the image acquisition process for each view takes place in parallel. Thus the total image acquisition time required for the line-scan technique is virtually independent of the number of views in the system arrangement.

ii) Field of view of the resultant images

The field of view in the x-axis is a function of the image registration method utilized in order to effect a convergence plane in object space. The convergence plane in the line-scan technique can be effected by two different methods:

- temporal convergence (during image acquisition); produced by the relative time delay between the start of image acquisition for each line-scan sensor;
- horizontal pixel shift (after image acquisition); produced by the introduction of a horizontal pixel shifts into the perspective images with respect to a reference image; this method suffers from a reduction in the x-axis field of view.

The temporal convergence method is more desirable in effecting a convergence plane as a truncation of the x-axis field of view does not occur. However, for the lateral shift technique, only the horizontal pixel shift method can be applied. Therefore, this technique produces images with a smaller x-axis field of view in comparison to the full view of the area array sensor.

iii) Multiple view region

For the line-scan technique, the multiple view region in object space is symmetrically distributed about the convergence plane in the z axis. Thus the depth of field of this region is fixed regardless of the object range. Whereas for the lateral shift technique, the multiple view region is asymmetrically distributed about the convergence plane. Therefore, changes in the position of the convergence plane affect the depth of field of the multiple view region. Thus the determination of the near and far limits of the binocular stereoscopic depth of field in the multiple view region is required to be recalculated whenever the convergence plane is changed.

iv) Development cost

For a given sensor technology, linear detector arrays are very much cost effective than the area detector technology required for the lateral shift technique. In addition, the radiation dose per inspection can be reduced as a slit collimated x-ray beam is used rather than a cone beam, in turn reducing the extent and cost of radiological shielding necessary.

v) Versatility

Linear x-ray detector arrays are generally far more versatile (i.e. they are available in modular form enabling large fields of view to be realized) in comparison to the area type sensors. Line-scan techniques are inherently slower than area array techniques. However, high resolution planar x-ray detectors (film replacement) are becoming available but readout speeds are slow (typically 3 seconds).

8.4 Future work

This section presents the author's suggestions for possible future work and applications for the multiple view imaging techniques developed.

a) Sensor interlacing

A preliminary investigation in which alternate video lines in each perspective image in the multiple view display were 'switched off' revealed that the human observer is still able to recognise image detail with a high degree of integrity [122]. Interestingly the perceived sharpness exhibited by the dynamic image sequences does not appear to be available in each individual perspective image. This was observed for both the monoscopic and the binocular stereoscopic image sequences. Thus the 'overall' resolving capability of the imaging techniques developed in this research, in terms of visual information, require further investigation. The outcome of this work could have important implications in that the number of x-ray detector elements in each linear x-ray detector array could be reduced by 'interlacing' the detector elements from neighbouring linear arrays. Thus the concept of a 'sensor interlace' could be used to implement the x-ray detector elements made available by the 'redundant' vertical resolution in the display to produce further perspective views of the object under inspection.

b) Blending visible light images and x-ray images

The combination of a visible light image sequence and an x-ray image sequence could be achieved by blending together images produced by a carefully configured visible light camera and x-ray imaging system. The resultant 'hybrid' images would simultaneously contain information from both transmissive and reflected interrogation. It is anticipated that this type of facility may be important for on-line inspection of electronic assemblies, for instance, markings and labels on the

components can be inspected using the visible light inspection mode whilst the internal structure of the electronic component could be examined in the x-ray mode. Also, this concept could be expanded to include dual–energy x-ray techniques for materials discrimination. All the imaging techniques discussed in this thesis could be employed to produce hybrid images.

c) Extraction of three-dimensional coordinate data and 3-D reconstruction

The extension of previous coordinate measurement work to encompass the multiple view imaging technique utilizing folded dual-energy detector arrays is recommended. In relation to this, *Evans* [109] has proved that the parallax production using the linear (standard) detector arrays and the folded detector arrays is identical. Thus, it is expected that the basic form of the measurement algorithms will be very similar for the x and z axes, whilst significantly different for the y-axis due to the folded array configuration. However, the probability of matching corresponding image features automatically would be significantly higher. For instance, an 'outside-in' approach could be used to match the corresponding image features. In other words, the stereoscopic pair which exhibits the highest parallax values is initially used for matching purposes. However, if the image features can not be matched, the 'next' stereoscopic pair is used and so on until the corresponding image features are matched. This approach is useful as the stereoscopic pair with the higher maximum parallax values produces higher range accuracy whilst a stereoscopic pair with lower parallax values is relatively easier to match. Thus a trade off between these functions may be achieved for different parts of the imaged scene. The three-dimensional information extracted could then be used in conjunction with '3-D modelling' software to produce an all-round image model similar to that produced by *Computed Tomography* scanners [123, 124]. Also, an investigation into the capability of the system to determine the volume of selected objects could be assessed. This information could be used in conjunction with dual-energy x-ray techniques [125, 126, 127, 128] to better identify threat material such as plastic explosives

Thus, in conclusion the author recommends that each of the suggested areas of future work be further investigated, since they all represent substantial potential improvements to the techniques already developed.

References

References

1. Michette A. and Pfauntsch S., "X-RAYS: The First Hundred Years", John Wiley & Sons Limited, ISBN 0-471-96502-2, 1996.

2. Evans J. P. O., Robinson M., Godber S. X. and Petty R. S., "The Development of 3-D (Stereoscopic) Imaging Systems for Security Applications", Security Technology, Proceedings. Institute of Electrical and Electronics Engineers 29th Annual 1995 International Carnahan Conference, Sanderstead, Surrey, UK, pp. 505 -511, 1995.

3. Mori K., Hasegawa L., Toriwaki J., Anno H. and Katada K., "Recognition of Bronchus in Three-dimensional X-ray CT Images with Application to Virtualised Brochoscopy System", Pattern Recognition, Proceedings of the 13th International Conference, volume 3, pp. 528-532, 1996.

4. Murray N. C., Lacey R. J. and Mason P. H., "Exploitation of X-ray Technology for the Detection of Contraband-aviation Security Applications, Security and Detection, ECOS 97, European Conference, pp. 13-18, 1997.

5. Neubauer C., "Intelligent X-ray Inspection for Quality Control of Solder Joint", Components, Packing and Manufacturing Technology, Part C, IEEE Transactions, volume 20 1, pp. 111-120, April 1997.

6. Titus J., "X-Ray Systems Reveal Hidden Defects", Test & Measurement, pp. 29 – 36, February 1998.

7. Morton E. J., Luggar R. D., Key M. J., Kundu A., Tavora L. M. N. and Gilboy W. B., "Development of a High Speed X-ray Tomography System for Multiphase Flow Imaging", Nuclear Science, IEEE Transactions, volume 46 3 1, pp. 380 –384, June 1999.

8. Bruning H. and Wolff S., "Automated Explosive Detection Systems based upon CT Technology", Security Technology, Proceedings, 32nd Annual 1998 International Carnahan Conference, pp. 55-58, 1998.

9. Armistead R. A., "Advanced X-ray Systems for Non-destructive Inspection and Contraband Detection", SPIE Conference on Penetrating Radiation Systems and Applications, pp. 98-105, July 1999.

10. McClure D., "Reading between the Component Lines" EP&P, pp. 50-52, March 2000.

11. Okoshi T., "Three Dimensional Imaging Techniques", pp. 49-59, Academic Press, 1976.

12. Russ C., "The Image Processing Hand Book", second edition, p. 152, pp. 411-412, p. 487, ISBN 0-8493-2516-1, 1995.

13. Haber R. N. and Hershenson M., "The Psychology of Visual Perception", second edition, pp. 173-180, Holt Rinehart Wunson, 1980.

14. Sekuler R. and Blake R., "Perception", third edition, McGraw-Hill, ISBN 0-7-056085-4, pp. 241-246, 1994.

15. Sekuler R. and Blake R., "Perception", third edition, McGraw-Hill, ISBN 0-7-056085-4, pp. 219-231, 1994.

16. Tychsen L., "Adler's Physiology of the Eye", fifth edition, Macmillan Press London, pp. 773-853, 1992.

17. Durgin K. H., Proffitt D. R. and Olson T. J., "Baring Depth From Motion With Depth from Binocular Disparity", Journal of Experimental Psychology: Human Perception and Performance, volume x. No.x , pp. 679-699, 1995.

18. Tittle J. S. and Braunstein M. L., "The Interaction of Binocular Disparity and Structure-from-motion in Determining Perceived Relative Depth", Supplement to Investigative Ophthalmology and Visual Science: Associate for Research in Vision Ophthalmology, 30(3), March 1989.

19. Valyus N. A., "Stereoscopy", The Focal Press, p. 67, 1966.

20. Karara H. M., "Manual of Photogrammetry", fourth edition, American Society of Photogrammetry, p. 846, 1980.

21. Moffitt F. H. and Mikhail E. M., "Photogrammetry", third edition, Harper & Row, ISBN 0-700-22517, p. 574, 1980.

22. Burke M. W., "Image Acquisition: Handbook of Machine Vision Engineering", volume 1, Chapman & Hall, ISBN 0-412-47920-6, pp. 505-507, 1996.

23. Evans J. P. O. and Robinson M., "Line-scan Imaging in 3D", British Patent Application 9720864.9, Filed 1st October 1997.

24. X-TEK Systems Limited, 64-66 Akeman Street, Tring, Herts. HP23 6AF, United Kingdom. Website : http://www.xtek.co.uk/systems.htm.

25. Evans J. P. O., Robinson M., Lacey M. and Murray N., "The Development of 3-D X-ray Systems for Airport Security Applications", Proceedings, SPIE Applications of Signal and Image Processing in Explosive Detection Systems, volume 1824, pp. 171-182, ISBN 0-8194-1025-X, 1992.

26. Robinson M., Evans J. P. O., Godber S. X., Lacey R., Murray N. and Mason P., "3D X-ray Image Manipulation", Proceedings, SPIE Substance Identification Technologies: Signal and Image Proceeding for Detection Systems, volume 2093, pp. 483-485, ISBN 0-8194-1366-6, 1993.

27. Robinson M., Evans J. P. O., Godber S. X. and Murray N., "Solid Image Models Derived from Security X-ray Equipment", Publication No 408, IEEE European Conference on Security and Detection, pp. 306-309, ISBN 0-85296-640-7, ISSN 0537-9989, 1995.

28. Godber S. X., Evans J. P. O., Robinson M., Murray N., Mason P. and Lacey R. J., "From Stereoscopic Images to 2.5-D Volume Visualisation", IS&T/SPIE Symposium on Electronic Imaging, SPIE volume 2625, California, January 1996.

29. Evans J. P. O., Robinson M. and Lacey D., "Testing and Evaluation of an Advanced (3-D) X-ray Screening System", Security Technology 1998, Proceedings., 32nd Annual International Carnahan Conference, pp. 50-54, 1998.

30. Evans J. P. O. and Robinson M., "Design of a Stereoscopic X-ray Imaging System using a Single X-ray Source", Journal of Non-Destructive Testing and Evaluation International (JNDT&E), pp. 325-332, volume 35/5, ISSN 0963-8695, April 2000.

31. Robinson M., Evans J. P. O. and Godber S. X., "A 3-D (Stereoscopic) X-ray Imaging Technique based on Linear Array Detectors", Digital Mammography, IEE Colloquium, pp. 11/1 – 11/4, 1996.

32. Evans J. P. O., "Development of a 3-D X-ray System", Ph.D. thesis, The Nottingham Trent University, pp. 165-167, October 1993.

33. Godber S. X., Evans J. P. O. and Robinson M., "From Stereoscopic X-ray Images to 2½-D Volume Visualisation", IS&T/SPIE Symp. Electronic Imaging: Science & Technology, Conf. Visual Data Exploration and Analysis III SPIE, volume 2656, ISBN 0-8194-2030-1, February 1996.

34. Evans J. P. O., Robinson M. and Godber S. X., "3-D X-ray Image Modelling – Latest Developments", Security and Detection, ECOS 97. European Conference, pp. 1-4, 1997.

35. Evans J. P. O., Robinson M. and Godber S. X., "Pseudo-tomographic X-ray Imaging for Use in Aviation Security", IEEE Aerospace and Electronics Systems Magazine, volume 13 7, pp. 25–30, July 1998.

36. Pope J. A., "Medical Physics", HEB, ISBN 0435-68681-x, p. 147, 1987.

37. Burke M. W., "Image Acquisition: Handbook of Machine Vision Engineering", volume 1, Chapman & Hall, ISBN 0-412-47920-6, pp. 861-869, 1996.

38. Davson H., "Davson's Physiology of the Eye", fifth edition, Macmillan Academic and Professional Limited, ISBN 0-33-45860-5, pp. 449-481, 1990.

39. Wicken C. D., Todd S and Seidler K., "Three-dimensional Displays: Perception, Implementations and Applications", Technical Report - Aviation Research Laboratory, ARL-89-11/CSERIAC-89-1, October 1989.

40. Seeman H. E., "Physical and Photographic Principles of Medical Radiography", Wiley, pp. 76-88, 1968.

41. Valyus N. A., "Stereoscopy", The Focal Press, p. 66, 1966.

42. Haber R. N. and Hershenson M., "The Psychology of Visual Perception", second edition, pp. 209-213, Holt Rinehart Wunson, 1980.

43. Ramachandran V. and Anstis S. M., "The Perception of Apparent Motion", June 1986. (This paper can be found in Rock I., "The Perceptual World", ISBN – 0-7167-2068-x, pp. 139-151, W. H. Freeman and Company, 1990.)

44. Anstis S. M. "Apparent Movement". In R. Held, H. W. Leibowitz and H. L. Teuber (eds), Handbook of Sensory Physiology, volume 8, Berlin: Springer-Verlag, pp. 655-673, 1978.

45. Sekuler R. and Blake R., "Perception", third edition, McGraw-Hill, ISBN 0-7-056085-4, p. 506, p. 284. 1994.

46. Sekuler R. and Blake R., "Perception", third edition, McGraw-Hill, ISBN 0-7-056085-4, pp. 283-291, 1994.

47. Gregory R. L., "Eye and Brain - The Psychology of Seeing", fifth edition, Oxford University Press ISBN 0-19-852423-4, pp. 116-119, 1998.

48. Burke M. W., "Image Acquisition: Handbook of Machine Vision Engineering", volume 1, Chapman & Hall, ISBN 0-412-47920-6, pp. 513–520, 1996.

49. Halas J., "Computer Animation", Hasting House, ISBN 0-8038-1178-0, 1974.

50. White T., "The Animator's Workbook", Phaidon Press Limited Littlegate House, ISBN 0-7-148-2439-9, 1986.

51. Marey E. J., "Movement – The Literature of Cinema", Arno Press & New York Times, ISBN 0-405-03900-x, 1971.

52. Foley J. D., Van Dam A., Feiner S. K. and Hughes J. F., "Computer Graphics – Principles and Practice", ISBN- 0-201-84840-6, pp. 1058-1080, 1996.

53. Rourke M., "Principles of Three-dimensional Computer Animation", revised edition, Norton, ISBN 0-393-73024-7, 1998.

54. Bloomer C. M., "Principles of Visual Perception", Van Nostrand Reinhold Company, ISBN 0-442-208825-1, p. 98, 1976.

55. Pope J. A., "Medical Physics", HEB, ISBN 0435-68681-x, pp. 29-44, 1987.

56. Happé L. B., "Basic Motion Picture Technology", Focal Press Limited, ISBN 0-240-50710-x, p. 11, 1971.

57. Bloomer C. M., "Principles of Visual Perception", Van Nostrand Reinhold Company, ISBN 0-442-208825-1, p. 101, 1976.

58. Happé L. B., "Basic Motion Picture Technology", Focal Press Limited, ISBN 0-240-50710-x, p. 17, 1971.

59. Davson H., "Davson's Physiology of the Eye", fifth edition, Macmillan Academic and Professional Limited, ISBN 0-33-45860-5, pp. 363-372, 1990.

60. Inoué S. and Spring K. R., "Video Microscopy - The Fundamentals", second edition, pp. 178-180, 1997.

61. Rock I., "Introduction to Perception", Macmillan Publisher co. line, ISBN: 0-02-402490-2, pp. 114-119, 1975.

62. Foley J. D., Van Dam A., Feiner S. K. and Hughes J. F., "Computer Graphics – Principles and Practice", ISBN- 0-201-84840-6, pp. 616-617, 1996.

63. Roger B. and Graham M., "Motion Parallax as an Independent Cue for Depth Perception", Perception, pp. 125-134, 1979.

64. Landy M. S., "Parallax Model of the Kinetic Depth Effect using Local Computations", Journal of the Optical Society of America, 4(5), pp. 864-877, 1987.

65. Ullman S., "The Interpretation of Visual Motion", MIT Press, Cambridge, Massachusetts and London, England, pp. 133–136, ISBN 0-262-21007-X, 1979.

66. Proffitt D. R., Hecht H., Rock T. and Schubert J., "Stereo Kinetic Effect and its Relation to the Kinetic Depth Effect", Journal of Experimental Psychology: Human Perception and Performance", volume 18, No.1, pp. 3-21, 1992.

67. Wallach H. and O'Connell D. N., "The Kinetic Depth Effect", Journal of Experimental Psychology, 45, 4, pp. 205-217, 1953.

68. Miles W. R., "Movement Interpretation of the Silhouette of a Revolving Fan", Amer. J. Psychology, 43, pp. 392-405, 1931.

69. Metzger W., Tiefenerscheinungen in Optishen Bewegungnsfeldern. Psychol. Forsh., 20, pp. 195-260, 1934.

70. Dember W. N., "The Psychology of Perception", Holt, ISBN 0-03-009990-0, pp.183-185, 1960.

71. Tittle J. S., Perotti V. J. and Norman J. F., "Integration of Binocular Stereopsis and Structure from Motion in the Discrimination of Noisy Surfaces", Journal of Experimental Psychology: Human Perception and Performance, volume 23. No. 4, pp. 1035-1049, August 1997.

72. Tittle J. S., Todd J. T., Perotti V. J. and Norman J. F., "Systematic Distortion of Perceived Three-Dimensional Structure From Motion and Binocular Stereopsis", Journal of Experimental Psychology: Human Perception and Performance, volume 3. No.3, pp. 663-678, 1995.

73. Ho P. K. and Chung R., "Stereo-motion that Complement Stereo and Motion Analyses", Computer Vision and Pattern Recognition, Proceedings 1997 IEEE computer Society Conference, pp. 213-218, 1997.

74. Strintzis M. G. and Malassiotis S., "Object-based Coding of Stereoscopic and 3D Image Sequences, IEEE Signal Processing Magazine, volume 16 3, pp. 14-28, May 1999.

75. Haggren H., " Photogrammetric Machine Vision", Optics and Lasers in Engineering", 10, pp. 265-286, 1989.

76. Wolf P., "Elements of Photogrammetry", second edition, McGraw Hill, ISBN 0-07-071345-6, p. 504, 1983.

77. Evans J. P. O., "Development of a 3D X-ray System", Ph.D. thesis, The Nottingham Trent University, October 1993.

78. Karara H. M., "Manual of Photogrammetry", fourth edition, American Society of Photogrammetry, pp. 848-850, 1980.

79. Petty R. S., "Stereoscopic Line-scan Imaging Using Rotational Motion", Ph.D. thesis, The Nottingham Trent University, 1997.

80. Stereographics, "Developers's Handbook: Background on Creating Images for CrystalEyes® and SimulEyes®", Stereographics Corporation, 1997.

81. Bovik A., "Handbook of Image and Video Processing", Academic Press, ISBN 0-12-119790-5, pp. 238-239, 2000.

82. Boyle W. S. and Smith G. E., "Charge Coupled Semiconductor Devices", Bell System Technical Journal, volume 49, pp. 587-593, 1970.

83. Holst G. C., "CCD Arrays Cameras and Displays", second edition, ISBN 0-964000-4-0, 1998.

84. Vernon D., "Machine Vision: Automated Visual Inspection and Robot Vision", Prentice Hall, ISBN 0-13-543398-3, pp. 20-22, 1991.

85. "Pulnix Imaging Product –TM-8", B/W CCD Cameras", Pulnix America Inc.

86. Zographos A. N., "A Line-scan System for the Inspection and Measurement of Cylindrical Surfaces", Ph.D. thesis, The Nottingham Trent University, 1998.

87. Lecordier R., Martin P., Deshayes M. and Guigueno I., "Image Processor for Automated Visual Inspection", Proceedings of Signal Processing, Theories and Applications, volume 1, pp. 319-322, Grenoble, September 1988.

88. Griffin P. M., Villalobos J. R., Foster III J. W. and Messimer S. L., "Automated Visual Inspection of Bare Printed Circuits Boards", Computer Ind. Engng., volume 18, No.4, pp. 505-509, 1990.

89. Shabushnig J. G., "Inspection of Pharmaceutical Packaging with Linear Array Video Sensors", Proceedings of the Conference on Vision '89, Society of Manufacturing Engineers, 1989.

90. Zographos A., Robinson M., Evans J. P. O. and Smith C. L., "Ballistics Identification using Line-scan Imaging Techniques, Security Technology", Proceedings. The Institute of Electrical and Electronics Engineers 31st Annual 1997 International Carnahan Conference, pp. 82 –87, 1997.

91. Li T., Witty P. and King T., "Machine Vision in the Inspection of Patterned Textile Webs", Industrial Inspection (Digest No: 1997/041), IEE Colloquium, pp. 9/1 -9/5, 1997.

92. Caron, J. and Duvieubourg L., "Defect Detection by Recursive Filters in Packaging Industry", Information, Communications and Signal Processing, ICICS, Proceedings of 1997, International Conference, volume 2, pp. 1189-1193, 1997.

93. Godber S. X., "The Development of Novel Stereoscopic Imaging Sensors", pp. 134-135, Ph.D. thesis, The Nottingham Trent University, 1991.

94. Joo, Y., Park, J., Thomas M., Chung K. S., Brooke M. A., Jokerst N. M. and Wills D. S., "Smart CMOS Focal Plane Arrays: A Si CMOS Detector Array and Sigma-delta Analogy-to-digital Converter Imaging System", Selected Topics in Quantum Electronics, IEEE Journal, volume 5 2, pp. 296 –305, March-April 1999.

95. Kabra R. K., Patel V., Tower J., Lowrance J. L., Mastrocola V. and Misra D., "180 x 180 Element Ultra High Frame Rate Burst Image Sensor", Circuits and Systems, Proceedings of the 40th Midwest Symposium on, Publish volume 2, pp.1423-1425, 1998.

96. Fryer J. G. and Brown D. C., "Lens Distortion for Close-range Photogrammetry", Photogrammetric Engineering and Remote Sensing, volume 52, No. 1, pp.51-58, 1986.

97. Brown D. C., "Decentring Distortion of Lenses", Photogrammetric Engineering", volume 32, No. 3, pp. 444-462, 1966.

98. Thompson E. H., "A Note on Distortion", Photogrammetric Record, volume 9, No. 49, pp. 93-99, 1977.

99. Burke M. W., "Image Acquisition: Handbook of Machine Vision Engineering", volume 1, Chapman & Hall, ISBN 0-412-47920-6, p. 690, 1996.

100. Havalick R. M. and Shapiro L. G., "Glossary of Computer Vision Terms", Pattern Recognition", volume 24, No. 1, pp. 69-93, 1991.

101. Friend D. B. and Jones A., "A Stereoscopic Television System for Reactor Inspection", CEGB Research Division, March 1980.

102. Jones A., "Some Theoretical Aspects of the Design of Stereoscopic Television Systems", CEBG Research Division, March 1980.

103. Hsu J., Pizlo Z., Chelberg D. M., Bbbs C. F. and Delp E. J., "Issues in the Design of Studies to Test the Effectiveness of Stereo Imaging", Systems, Man and Cybernetics, Part A, IEEE Transaction, volume 26 6, pp. 810-819, November 1996.

104. Cosmicar CCTV Lenses, Cosmicar, 1994.

105. "Matrox Corona Installation and Hardware Reference", Matrox Electronic System Limited, Canada, 1998.

106. IF1 & IF2 Stepper Motor Interface, Parker-digiplan Data Book, 1988.

107. Weeks A. R. Jr, "Fundamental of Electronic Image Processing", IEEE PRESS, ISBN 0-7803-3410-8, 1996.

108. "Matrox Imaging Library User Manual", version. 5.03, Matrox Electronic System Limited, Canada, 1998.

109. Evans J. P. O., "Development of a 3D X-ray System", Ph.D. thesis, The Nottingham Trent University, October 1993.

110. "Image Intensifier – Product Data", North American Imaging Inc. America.

111. "Pulnix Imaging Product- Tm-7/TM-6 ½" B/W CCD Cameras", Pulnix America, Inc.

112. "FlexScan F56/F55- User's Manual", EIZO Corporation, Japan.

113. "User Guide- Nuvision 17SX/21SX Stereoscopic Display Kits" and "Installation manual", Nuvision Technologies, Inc, America.

114. "Elsa Gloria – XL Manual", ELSA, Aachen, Germany.

115. Sexton I. and Surman P., "Stereoscopic and Autostereoscopic Display Systems", IEEE Signal Processing Magazine, volume 16 3, pp. 85-99, May 1999.

116. Starks M., "Stereoscopic Imaging Technology", 3DTV Corporation, 1996.

117. Wilson A., "3-D images Using Cylindrical Lenses", Image processing Europe, pp. 9-15, July/August Issue 2000.

118. Park D., Kim K., Lee C., Son J. and Lee Y., "Lenticular Stereoscopic Imaging and Displaying Technique with No Special Glasses", Imaging Processing, Proceeding, International Conference, volume 3, pp. 137-140, 1995.

119. Erza D., "Look, No Glasses – 3D Display System", IEE Review, volume 42 5, pp. 187-189, September 1996.

120. "Tracker 2000 – User Guide", Madentec, Alberta, America.

121. Jarre H. A. and Teschendorf O. E. W., "Roentgen-stereoscopic a Review of its Present Status", Radiology, Volume 21, pp. 130-155, 1933.

122. Bloomer C. M., "Principles of Visual Perception", Van Nostrand Reinhold Company, ISBN 0-442-208825-1, p. 86, 1976.

123. Donaire J. G., Roca J. and Garcia I., "Evaluation of an Interactive Algorithm for Three-dimensional X-ray Cone Beam Reconstruction", Imaging Processing, Proceedings, International Conference, volume 3, pp. 575-578, 1996.

124. Endo M., Nishizawa K., Iwai K., Matsumoto M., Yoshida K., Satoh K., Matsusita M. and Kusakabe M., "Image Characteristics and Effective Dose Estimation of a Cone Beam CT using a Video-Fluoroscopic System", Nuclear Science, IEEE Transactions, volume 64 3 2, pp. 686-690, June 1999.

125. Welch A., Gullberg G. T., Christian P. E., Jia Li and Tsui B. M. W.,"An Investigation of Dual-energy Transmission Measurements for more Accurate Non-uniform Attenuation Compensation in Cardiac Spect", 0-7803-2544-3, IEEE, 1995.

126. Paranjape R., Sluser M. and Runtz K., "Segmentation of Handguns in Dual-energy X-ray Imagery of Passenger Carry-on Baggage", 0-7803-4314-x, IEEE, 1998.

127. Hassler U., Garnero L., and Rizo P., "X-ray Dual-energy Calibration based on Estimated Spectral Properties of the Experimental System", 0018-9499/9, IEEE, 1998.

128. Bentum M. J., Arendsen R. G. J. and Slump C. H., "Design and Realization of High Speed Single Exposure Dual Energy Image Precesing."0-8186-2742-5, IEEE, 1992.

Appendices

A Repeatability tests for the experimental visible light system

a) Grey level noise

Table A-1: Average grey level values for a 100 pixels x 100 pixels region in the resultant image.

Test	Grey level
1	83
2	82
3	86
4	83
5	86
6	86
7	94
8	80
9	85
10	88

Table A-1 *Grey level variation*

b) Camera-to-object range

Table A-2: Image components in the x and y axes with the repeatability test of the camera-to-object range.

Tests	300 mm		400 mm		500 mm		650 mm	
	X	Y	X	Y	X	Y	X	Y
1	410	410	320	320	250	250	210	211
2	412	412	321	322	250	251	210	211
3	412	412	320	321	249	251	211	211
4	409	410	318	320	249	251	212	210
5	410	412	321	322	252	251	212	212
6	410	410	320	320	251	352	212	212
7	409	410	319	319	252	353	209	209
8	412	410	322	320	249	250	210	211
9	412	412	323	322	250	250	209	209
10	409	409	321	322	251	249	209	209

Table A-2 *Consistency of the x-axis image component and the y-axis image component as a function of camera-to-object range*

c) Translation speed

Table A-3: Image components in the x-axis.

Tests	The x-axis component in image space (pixels)
1	316
2	316
3	316
4	317
5	316
6	315
7	315
8	315
9	317
10	316

Table A-3 *Consistency of the translation speed in the motion axis*

d) Line acquisition time

Graph A-1: Accumulated line acquisition time for 80 scan lines.

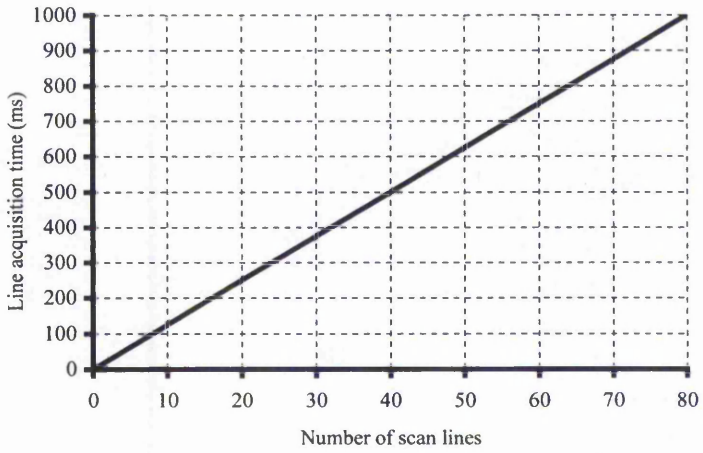

Graph A-1 *Consistency of the line acquisition time in the visible light experimental system*

B Determination of the line acquisition time

Unit delays	Time taken for 500 columns (s)	Distance travelled (m)	Line acquisition time (ms)
0	40	0.06	80
1	40	0.06	80
2	40	0.06	80
3	60	0.09	120
4	60	0.09	120
5	60	0.09	120
6	60	0.09	120
7	60	0.09	120
8	60	0.09	120
9	60	0.09	120
10	60	0.09	120
11	60	0.09	120
12	60	0.09	120
13	60	0.09	120
14	60	0.09	120
15	60	0.09	120
16	80	0.12	160
17	80	0.12	160
18	80	0.12	160
19	80	0.12	160
20	80	0.12	160
21	80	0.12	160
22	80	0.12	160
23	80	0.12	160
24	80	0.12	160
25	80	0.12	160
26	80	0.12	160
27	80	0.12	160
28	80	0.12	160
29	100	0.15	200
30	100	0.15	200
31	100	0.15	200
32	100	0.15	200
33	100	0.15	200
34	100	0.15	200
35	100	0.15	200
36	100	0.15	200
37	100	0.15	200
38	100	0.15	200
39	100	0.15	200
40	100	0.15	200
41	100	0.15	200
42	120	0.18	240
43	120	0.18	240
44	120	0.18	240
45	120	0.18	240
46	120	0.18	240
47	120	0.18	240
48	120	0.18	240
49	120	0.18	240

Unit delays	Time taken for 500 columns (s)	Distance travelled (m)	Line acquisition time (ms)
50	120	0.18	240
51	120	0.18	240
52	120	0.18	240
53	120	0.18	240
54	120	0.18	240
55	140	0.21	280
56	140	0.21	280
57	140	0.21	280
58	140	0.21	280
59	140	0.21	280
60	140	0.21	280
61	140	0.21	280
62	140	0.21	280
63	140	0.21	280
64	140	0.21	280
65	140	0.21	280
66	140	0.21	280
67	140	0.21	280
68	160	0.24	320
69	160	0.24	320
70	160	0.24	320
71	160	0.24	320
72	160	0.24	320
73	160	0.24	320
74	160	0.24	320
75	160	0.24	320
76	160	0.24	320
77	160	0.24	320
78	160	0.24	320
79	160	0.24	320
80	160	0.24	320
81	180	0.27	360
82	180	0.27	360
83	180	0.27	360
84	180	0.27	360
85	180	0.27	360
86	180	0.27	360
87	180	0.27	360
88	180	0.27	360
89	180	0.27	360
90	180	0.27	360
91	180	0.27	360
92	180	0.27	360
93	180	0.27	360
94	200	0.30	400
95	200	0.30	400
96	200	0.30	400
97	200	0.30	400
98	200	0.30	400
99	200	0.30	400
100	200	0.30	400
101	200	0.30	400
102	200	0.30	400
103	200	0.30	400
104	200	0.30	400
105	200	0.30	400
106	200	0.30	400

Unit delays	Time taken for 500 columns (s)	Distance travelled (m)	Line acquisition time (ms)
107	220	0.33	440
108	220	0.33	440
109	220	0.33	440
110	220	0.33	440
111	220	0.33	440
112	220	0.33	440
113	220	0.33	440
114	220	0.33	440
115	220	0.33	440
116	220	0.33	440
117	220	0.33	440
118	220	0.33	440
119	220	0.33	440

C Repeatability tests for the experimental x-ray system

a) Grey level noise

Table C-1: Average grey level values for a 100 pixels x 100 pixels region in the resultant image.

Test	Grey level
1	75
2	78
3	86
4	83
5	86
6	86
7	94
8	74
9	78
10	83

Table C-1 *Grey level variation*

b) Source-to-object range

Table C-2: Image components in the x and y axes with the repeatability test of the source-to-object range.

Tests	300 mm		350 mm		400 mm		450 mm	
	X	Y	X	Y	X	Y	X	Y
1	431	430	371	370	324	324	289	288
2	432	432	370	370	324	324	288	288
3	431	432	370	370	324	325	288	288
4	431	430	371	369	324	325	288	288
5	432	430	370	369	324	324	289	288
6	431	431	370	371	324	323	288	288
7	431	430	369	370	324	324	288	287
8	430	430	370	370	324	324	289	287
9	431	430	370	370	324	324	289	289
10	430	430	371	371	324	324	288	289

Table C-2 *Consistency of the x-axis image component and the y-axis image component as a function of source-to-object range*

c) Translation speed

Table C-3: Image components in the x-axis.

Tests	The x-axis component in image space (pixels)
1	215
2	216
3	216
4	217
5	216
6	215
7	214
8	215
9	217
10	216

Table C-3 *Consistency of the translation speed in the motion axis*

d) Line acquisition time

Graph C-1: Accumulated line acquisition time for 80 scan lines.

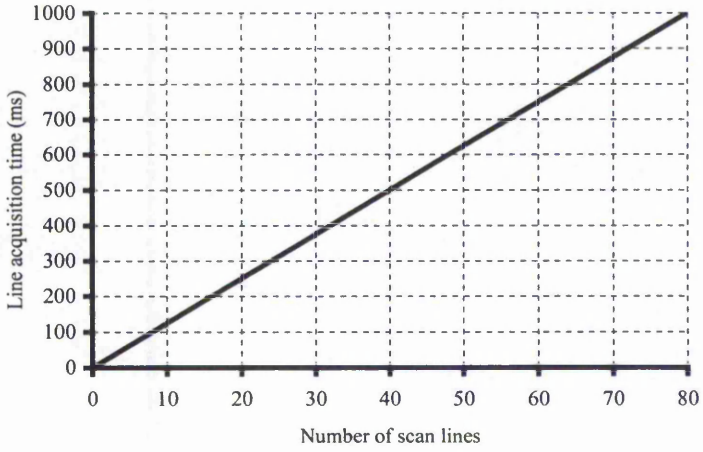

Graph C-1 *Consistency of the line acquisition time of the x-ray arrangement*

D Program listing for the display of image sequences

Main file: Sequential display.cpp

Author : Mr. Hock Woon, Hon

Date : 19 June 1999

Filename : Sequential_Display.cpp

Objectives :

i) To sequentially display perspective images in two control modes,

a) free-running

b) mouse-control.

ii) Dynamic reallocation of the fixation plane

```
#include "stdafx.h"
#include "Texture.h"
#include "TextureDoc.h"
#include "TextureView.h"

#ifdef _DEBUG
#define new DEBUG_NEW
#undef THIS_FILE
static char THIS_FILE[] = __FILE__;
#endif

// Input filenames of the perspective images

char *szFileNames[] = {
                "Perspective_image_1.bmp",  "Perspective_image_2.bmp",
                  "Perspective_image_3.bmp",  "Perspective_image_4.bmp",
                "Perspective_image_5.bmp",  "Perspective_image_6.bmp",
                "Perspective_image_7.bmp",  "Perspective_image_8.bmp",
                "Perspective_image_9.bmp",  "Perspective_image_10.bmp",
                "Perspective_image_11.bmp",  "Perspective_image_12.bmp",
                "Perspective_image_13.bmp",  "Perspective_image_14.bmp",
                "Perspective_image_15.bmp",  "Perspective_image_16.bmp",
                  "Perspective_image_15.bmp",  "Perspective_image_14.bmp",
                "Perspective_image_13.bmp",  "Perspective_image_12.bmp",
                "Perspective_image_11.bmp",  "Perspective_image_10.bmp",
                  "Perspective_image_9.bmp" ,  "Perspective_image_8.bmp" ,
                "Perspective_image_7.bmp" ,  "Perspective_image_6.bmp",
               "Perspective_image_5.bmp" ,  "Perspective_image_4.bmp",
                  "Perspective_image_3.bmp" ,  "Perspective_image_2.bmp" ,
};
// Message Map
```

```
IMPLEMENT_DYNCREATE(CTextureView, CView)
BEGIN_MESSAGE_MAP(CTextureView, CView)
        ON_WM_CREATE()
        ON_WM_DESTROY()
        ON_WM_KEYDOWN()
        ON_WM_SIZE()
        ON_COMMAND(ID_IMAGE_REGISTERS, OnImageRegisters)
        ON_UPDATE_COMMAND_UI(ID_IMAGE_REGISTERS,
      OnUpdateImageRegisters)
        ON_WM_MOUSEMOVE()
        ON_WM_TIMER()
        ON_COMMAND(ID_FILE_MODELANIMATION, OnFileModelanimation)
        ON_COMMAND(ID_FILE_STOPANIMATION, OnFileStopanimation)
        ON_WM_LBUTTONDBLCLK()
        ON_WM_RBUTTONDBLCLK()

END_MESSAGE_MAP()

// Construction / destruction

CTextureView::CTextureView()
{
        xtranslate = 0.00f;
        m_xRotate = 0.0f;
        m_hPalette = 0;
        i=0;
  }

// Window class or styles can be modified in this section
CTextureView::~CTextureView()
{
}

BOOL CTextureView::PreCreateWindow(CREATESTRUCT& cs)
{
        cs.style |= WS_CLIPCHILDREN | WS_CLIPSIBLINGS;
        return CView::PreCreateWindow(cs);
}

// drawing
void CTextureView::OnDraw(CDC* pDC)
{
        CTextureDoc* pDoc = GetDocument();
        ASSERT_VALID(pDoc);

if (m_hPalette)
```

```
        {
          SelectPalette(pDC->m_hDC, m_hPalette, FALSE);
          RealizePalette(pDC->m_hDC);
        }
  wglMakeCurrent(pDC->m_hDC, m_hRC);
        DrawWithOpenGL();
        SwapBuffers(pDC->m_hDC);
  wglMakeCurrent(pDC->m_hDC, NULL);
  }

// Diagnostics
#ifdef _DEBUG
void CTextureView::AssertValid() const
{
        CView::AssertValid();
}

void CTextureView::Dump(CDumpContext& dc) const
{
        CView::Dump(dc);
}

CTextureDoc* CTextureView::GetDocument() // non-debug version is inline
{
        ASSERT(m_pDocument->IsKindOf(RUNTIME_CLASS(CTextureDoc)));
        return (CTextureDoc*)m_pDocument;
}
#endif //_DEBUG
 int CTextureView::OnCreate(LPCREATESTRUCT lpCreateStruct)
{
        if (CView::OnCreate(lpCreateStruct) == -1)
                return -1;

 PIXELFORMATDESCRIPTOR pfd =
  {
    sizeof(PIXELFORMATDESCRIPTOR), // Structure size.
    1,                      // Structure version number.
    PFD_DRAW_TO_WINDOW |        // Property flags.
      PFD_SUPPORT_OPENGL |
    PFD_DOUBLEBUFFER | PFD_STEREO,
    PFD_TYPE_RGBA,
    8,                          // 8-bit color.
    0, 0, 0, 0, 0, 0,           // Not concerned with these.
    0, 0, 0, 0, 0, 0, 0,        // No alpha or accum buffer.
    32,                         // 32-bit depth buffer.
    0, 0,                       // No stencil or aux buffer.
```

```
    PFD_MAIN_PLANE,       // Main layer type.
    0,                    // Reserved.
    0, 0, 0               // Unsupported.
  };

  CClientDC clientDC(this);

  int pixelFormat =
    ChoosePixelFormat(clientDC.m_hDC, &pfd);
  BOOL success =
    SetPixelFormat(clientDC.m_hDC, pixelFormat, &pfd);
  DescribePixelFormat (clientDC.m_hDC, pixelFormat,
    sizeof(pfd), &pfd);
  if (pfd.dwFlags & PFD_NEED_PALETTE)
    SetupLogicalPalette();

  m_hRC = wglCreateContext(clientDC.m_hDC);

  wglMakeCurrent(clientDC.m_hDC, m_hRC);

        glTexParameteri(GL_TEXTURE_2D, GL_TEXTURE_WRAP_S, GL_CLAMP);
        glTexParameteri(GL_TEXTURE_2D, GL_TEXTURE_WRAP_T, GL_CLAMP);
        glTexParameteri(GL_TEXTURE_2D,
          GL_TEXTURE_MAG_FILTER, GL_NEAREST);
        glTexParameteri(GL_TEXTURE_2D,
          GL_TEXTURE_MIN_FILTER, GL_NEAREST);
        glTexEnvi(GL_TEXTURE_ENV, GL_TEXTURE_ENV_MODE, GL_DECAL);
  glEnable(GL_DEPTH);
        glEnable(GL_TEXTURE_2D);
  glClearColor(1.0f, 1.0f, 1.0f, 1.0f);
  wglMakeCurrent(clientDC.m_hDC, NULL);
  m_pDib = new CDib("perspective_image_1.bmp");
  m_pDib1 = new CDib("perspective_image_2.bmp");
        CreateColorTables(m_pDib);
        CreateColorTables(m_pDib1);
        SetupColorTables();
        return 0;
}

// Destroy
void CTextureView::OnDestroy()
{
        CView::OnDestroy();
        advanced.m_advanced=0;
  delete m_pDib;
        delete m_pDib1;
```

```
        wglDeleteContext(m_hRC);
        if (m_hPalette)
          DeleteObject(m_hPalette);
}
void CTextureView::OnKeyDown(UINT nChar, UINT nRepCnt, UINT nFlags)
{

  // Once the 'Left arrow' key is pressed - move the image sequence to the left
   if (nChar == VK_LEFT)
        {
                i--;
    if (i<= 0)
                  i = 0;
         SelectImage(i);
   Invalidate(FALSE);
        }

// Once the 'Right arrow' key is pressed - move the image sequence to the right
        if (nChar == VK_RIGHT)
        {
     i++;
    if (i>= 15)
                  i = 15;
         SelectImage(i);
         Invalidate(FALSE);
        }

// Once the 'Enter' key is pressed - start the sequential image display
if (nChar == VK_RETURN)
        {
                OnImageRegisters() ;
        }


// Once the 'Back space' key pressed - stop the sequential image display
if (nChar == VK_BACK)
        {
                KillTimer(1);
        }
        CView::OnKeyDown(nChar, nRepCnt, nFlags);
}
```

```
// Resize function for display windows
void CTextureView::OnSize(UINT nType, int cx, int cy)
{
        CView::OnSize(nType, cx, cy);
  CClientDC clientDC(this);
  wglMakeCurrent(clientDC.m_hDC, m_hRC);
  glViewport(0, 0, cx, cy);
  glMatrixMode(GL_PROJECTION);
  glLoadIdentity();
  glFrustum(-1.0, 1.0, -1.0, 1.0, 2.0, 10.0);
  glMatrixMode(GL_MODELVIEW);
  glLoadIdentity();
  glTranslatef(0.0f, 0.0f, -3.5f);
  wglMakeCurrent(NULL, NULL);
 }

// Trigger function for image transition
void CTextureView::OnImageRegisters()
{
        SetTimer(1,1,NULL);
        Invalidate(FALSE);
  }

// Update trigger
void CTextureView::OnUpdateImageRegisters(CCmdUI* pCmdUI)
{
 if (m_texture == Resistors) pCmdUI->SetCheck(TRUE);
 else pCmdUI->SetCheck(FALSE);
}
// Draw function (on the screen) and fixation plane reallocation mechanisms
void CTextureView::DrawWithOpenGL()
{
        GLvoid* pTextureBits = (GLvoid*) m_pDib->GetDibBitsPtr();
        GLint width =  m_pDib->GetDibWidth();
        GLint height = m_pDib->GetDibHeight();

  glTexImage2D(GL_TEXTURE_2D, 0, 3, width, height,
         0, GL_COLOR_INDEX, GL_UNSIGNED_BYTE, pTextureBits);

  glClear(GL_COLOR_BUFFER_BIT | GL_DEPTH_BUFFER_BIT);

        glPushMatrix();
          if(i==0)          glTranslatef(8*(-xtranslate),0.0f,0.0f);
          if(i==1 || i==29) glTranslatef(7*(-xtranslate),0.0f,0.0f);
          if(i==2 || i==28) glTranslatef(6*(-xtranslate),0.0f,0.0f);
          if(i==3 || i==27) glTranslatef(5*(-xtranslate),0.0f,0.0f);
```

```
            if(i==4 || i==26)    glTranslatef(4*(-xtranslate),0.0f,0.0f);
            if(i==5 || i==25)    glTranslatef(3*(-xtranslate),0.0f,0.0f);
            if(i==6 || i==24)    glTranslatef(2*(-xtranslate),0.0f,0.0f);
            if(i==7 || i==23)    glTranslatef(1*(-xtranslate),0.0f,0.0f);
            if(i==8 || i==22)    glTranslatef(0*(xtranslate),0.0f,0.0f);
            if(i==9 || i==21)    glTranslatef(1*(xtranslate),0.0f,0.0f);
              if(i==10 || i==20)   glTranslatef(2*(xtranslate),0.0f,0.0f);
            if(i==11 || i==19)   glTranslatef(3*(xtranslate),0.0f,0.0f);
              if(i==12 || i==18)   glTranslatef(4*(xtranslate),0.0f,0.0f);
              if(i==13 || i==17)   glTranslatef(5*(xtranslate),0.0f,0.0f);
              if(i==14 || i==16)   glTranslatef(6*(xtranslate),0.0f,0.0f);
              if(i==15 )           glTranslatef(7*(xtranslate),0.0f,0.0f);
             glRotatef(m_xRotate, x, y, z);
             glBegin(GL_POLYGON);

        glTexCoord2f(0.0f, 1.0f); glVertex3f(-1.2f, 1.2f, 0.0f);
        glTexCoord2f(0.0f, 0.0f); glVertex3f(-1.2f, -1.2f, 0.0f);
        glTexCoord2f(1.0f, 0.0f); glVertex3f(1.2f, -1.2f, 0.0f);
        glTexCoord2f(1.0f, 1.0f); glVertex3f(1.2f, 1.2f, 0.0f);

            glEnd();

         glPopMatrix();
          glFlush();
}

// Perspective image selection
void CTextureView::SelectImage(int u)
{
          delete m_pDib;
          m_pDib = new CDib(szFileNames[u]);
  }

// Logical palette for images
void CTextureView::SetupLogicalPalette()
{
          struct
   {
     WORD Version;
     WORD NumberOfEntries;
     PALETTEENTRY aEntries[256];

   } logicalPalette = { 0x300, 256 };
          BYTE reds[] = {0, 36, 72, 109, 145, 182, 218, 255};
          BYTE greens[] = {0, 36, 72, 109, 145, 182, 218, 255};
          BYTE blues[] = {0, 85, 170, 255};
```

```
    for (int colorNum=0; colorNum<256; ++colorNum)
    {
      logicalPalette.aEntries[colorNum].peRed =
        reds[colorNum & 0x07];
      logicalPalette.aEntries[colorNum].peGreen =
        greens[(colorNum >> 0x03) & 0x07];
      logicalPalette.aEntries[colorNum].peBlue =
        blues[(colorNum >> 0x06) & 0x03];
      logicalPalette.aEntries[colorNum].peFlags = 0;
    }
    m_hPalette = CreatePalette ((LOGPALETTE*)&logicalPalette);
}

void CTextureView::CreateColorTables(CDib* pDib)
{
  LPRGBQUAD pColorTable = pDib->GetDibRGBTablePtr();

  for(UINT i=0; i<256; ++i)
  {
                m_red[i] = (GLfloat) pColorTable[i].rgbRed / 255;
                m_green[i] = (GLfloat) pColorTable[i].rgbGreen / 255;
                m_blue[i] = (GLfloat) pColorTable[i].rgbBlue / 255;
  }
}
void CTextureView::SetupColorTables()
{
  CClientDC clientDC(this);
  wglMakeCurrent(clientDC.m_hDC, m_hRC);
  glPixelMapfv(GL_PIXEL_MAP_I_TO_R, 256, m_red);
        glPixelMapfv(GL_PIXEL_MAP_I_TO_G, 256, m_green);
        glPixelMapfv(GL_PIXEL_MAP_I_TO_B, 256, m_blue);
        glPixelTransferi(GL_MAP_COLOR, TRUE);
  wglMakeCurrent(clientDC.m_hDC, m_hRC);
}

// Mouse-control image transition
void CTextureView::OnMouseMove(UINT nFlags, CPoint point)
{
  y_difference = point.y-m_PrevY;
  x_difference = point.x-m_PrevX;
  m_PrevX = point.x;
  m_PrevY = point.y;

if ( (nFlags & MK_LBUTTON) ==MK_LBUTTON)
{
        if(x_difference>=0)
```

```
            {
                        i++;
    if (i>= 15)
                         i = 15;
             SelectImage(i);
              Invalidate(FALSE);
            }
            else
            {
                        i--;
    if (i<= 0)
                         i = 0;

             SelectImage(i);
              Invalidate(FALSE);
}
 }
            CView::OnMouseMove(nFlags, point);
}

// Timer for image transition rate
void CTextureView::OnTimer(UINT nIDEvent)
{
     i++;
              if(i>=29) i=0;
                        SelectImage(i);
    Invalidate(FALSE);

 CView::OnTimer(nIDEvent);
}

// Control for animation i.e. start and stop
void CTextureView::OnFileModelanimation()
{
   OnImageRegisters() ;
}
void CTextureView::OnFileStopanimation()
{
            KillTimer(1);
}
// Control for fixation plane reallocation
void CTextureView::OnLButtonDblClk(UINT nFlags, CPoint point)
{
             xtranslate += 0.02f;
            CView::OnLButtonDblClk(nFlags, point);
}
```

```
void CTextureView::OnRButtonDblClk(UINT nFlags, CPoint point)
{
        xtranslate -= 0.02f;
        CView::OnRButtonDblClk(nFlags, point);
}
```

Header file : Sequential_display.h

Author : Mr. Hock Woon, Hon
Date : 19 June 1999
Filename : Sequential_Display.h
Objectives : Header file for sequential image display

```
#if !defined(AFX_TEXTUREVIEW_H__C2669D7F_5A3D_11D3_8B0F_D78F0C1CE124__INCLUDED_)
#define AFX_TEXTUREVIEW_H__C2669D7F_5A3D_11D3_8B0F_D78F0C1CE124__INCLUDED_

#if _MSC_VER > 1000
#pragma once
#endif // _MSC_VER > 1000

#include <gl\gl.h>
#include "cdib.h"
#include "super.h"
#include "Info.h"
#include "Advanced.h"
#include "tech.h";
enum {Resistors, Aztec, Gradient};

class CTextureView : public CView
{
protected: // create from serialization only

        CTextureView();
        DECLARE_DYNCREATE(CTextureView)


// Attributes
public:
         CTextureDoc* GetDocument();
        CString strCaption;
        Super super;
   CInfo Info;
        CAdvanced advanced;
   Ctech tec;
        int m_PrevX;
   int m_PrevY;
   int x_difference,y_difference;
   int i;
   float xplane_info,yplane_info,zplane_info;
```

```
protected:

        GLfloat m_xRotate;
          HPALETTE m_hPalette;
        GLfloat m_red[256], m_blue[256], m_green[256];
        CDib* m_pDib;
        CDib* m_pDib1;
        UINT m_texture;
        GLfloat x,y,z;
        GLfloat xtranslate;

char con;
        // Operations
public:

// Overrides
        // ClassWizard generated virtual function overrides
        //{{AFX_VIRTUAL(CTextureView)
        public:
        virtual void OnDraw(CDC* pDC);  // overridden to draw this view
        virtual BOOL PreCreateWindow(CREATESTRUCT& cs);
        protected:
        virtual BOOL OnPreparePrinting(CPrintInfo* pInfo);
        virtual void OnBeginPrinting(CDC* pDC, CPrintInfo* pInfo);
        virtual void OnEndPrinting(CDC* pDC, CPrintInfo* pInfo);
        //}}AFX_VIRTUAL

// Implementation
public:
        virtual ~CTextureView();
#ifdef _DEBUG
        virtual void AssertValid() const;
        virtual void Dump(CDumpContext& dc) const;
#endif

protected:
        void DrawWithOpenGL();
        void SetupLogicalPalette();
  void CreateColorTables(CDib* pDib);
        void SetupColorTables();
        void SelectImage(int);
  void init_general(void);

        // Generated message map functions
protected:
        //{{AFX_MSG(CTextureView)
```

```
        afx_msg int OnCreate(LPCREATESTRUCT lpCreateStruct);
        afx_msg void OnDestroy();
        afx_msg void OnKeyDown(UINT nChar, UINT nRepCnt, UINT nFlags);
        afx_msg void OnSize(UINT nType, int cx, int cy);
        afx_msg void OnImageRegisters();
        afx_msg void OnUpdateImageRegisters(CCmdUI* pCmdUI);
        afx_msg void OnMouseMove(UINT nFlags, CPoint point);
        afx_msg void OnTimer(UINT nIDEvent);
        afx_msg void OnFileModelanimation();
        afx_msg void OnFileStopanimation();
        afx_msg void OnLButtonDblClk(UINT nFlags, CPoint point);
        afx_msg void OnRButtonDblClk(UINT nFlags, CPoint point);
        //}}AFX_MSG
        DECLARE_MESSAGE_MAP()
};

#ifndef _DEBUG  // debug version in TextureView.cpp
inline CTextureDoc* CTextureView::GetDocument()
   { return (CTextureDoc*)m_pDocument; }
#endif
/////////////////////////////////////////////////////////////////////////////

//{{AFX_INSERT_LOCATION}}
// Microsoft Visual C++ will insert additional declarations immediately before the previous line.
#endif // !defined(AFX_TEXTUREVIEW_H__C2669D7F_5A3D_11D3_8B0F_D78F0C1CE124__INCLUDED_)
```

E Sample image sequence produced by the multiple view line-scan technique

The imaged objects include a paper clip, a printed circuit board and a fuse. In addition a 0.303" calibre cartridge case is arranged to resemble a detonator inserted in plastic explosive. The end view of the cartridge case appears as a dark grey disc in the amorphous image of a lump of blue tack. It can be appreciated from the image sequence (1 to 16) that the cartridge case appears to become increasingly tilted with respect to the other objects due to its large relative depth. These images were produced using the following experimental conditions:

- depth of field : 150 mm
- maximum width and the maximum height of the object : 100 mm x 50 mm
- pixel resolution of the image : 640 pixels x 480 pixels
- angular distribution : 0.5 ° between successive image

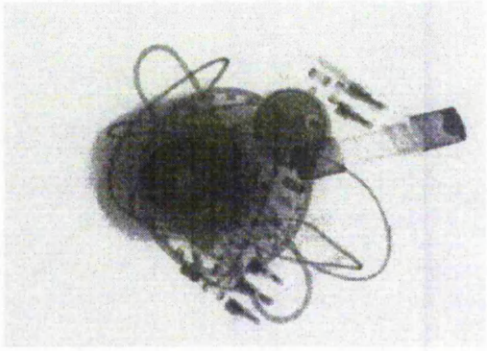

perspective image 1

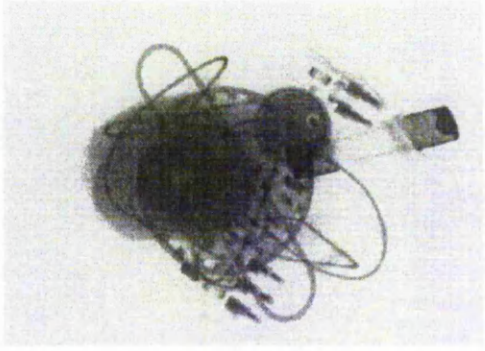

perspective image 2

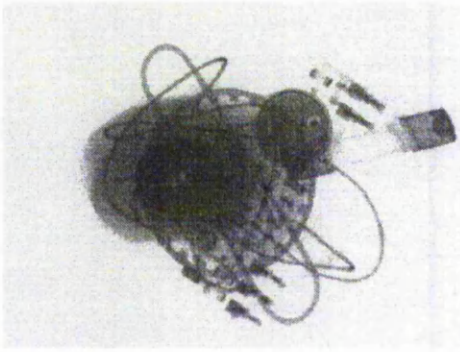

perspective image 3

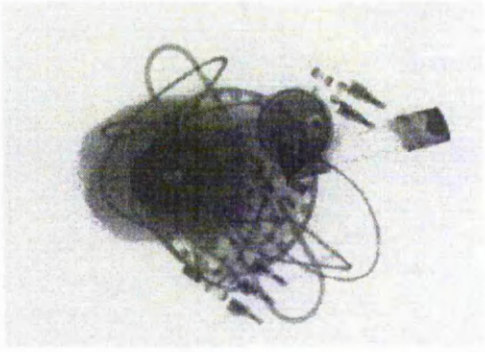

perspective image 4

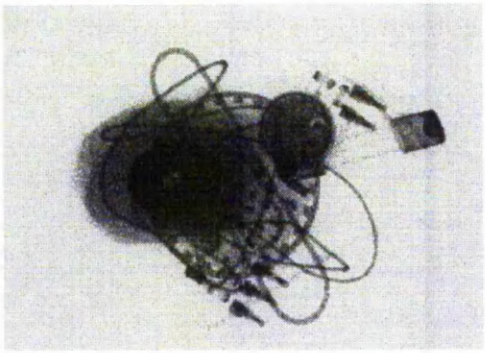

perspective image 5

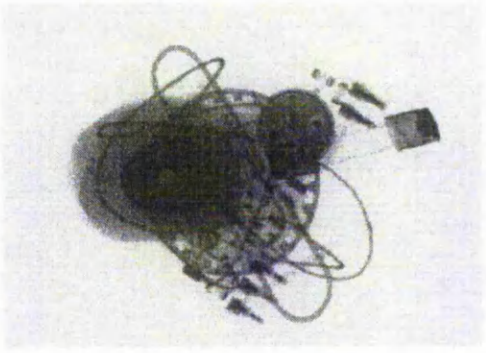

perspective image 6

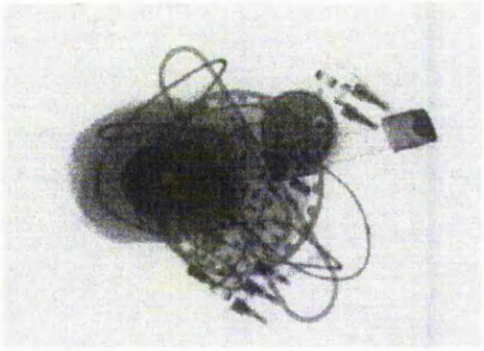

perspective image 7

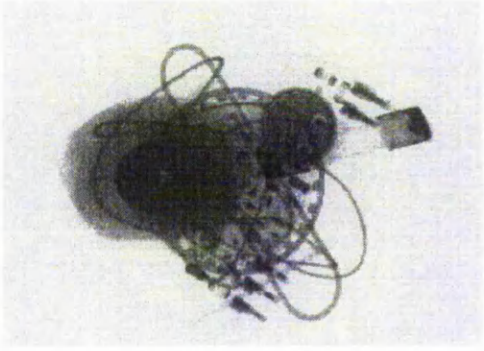

perspective image 8

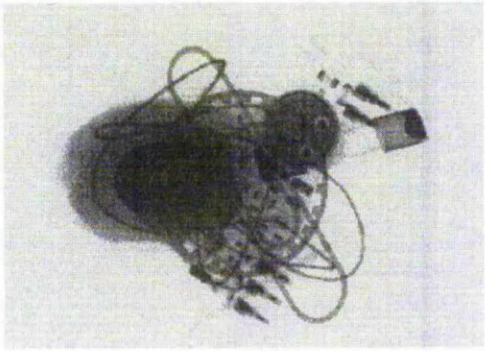

perspective image 9

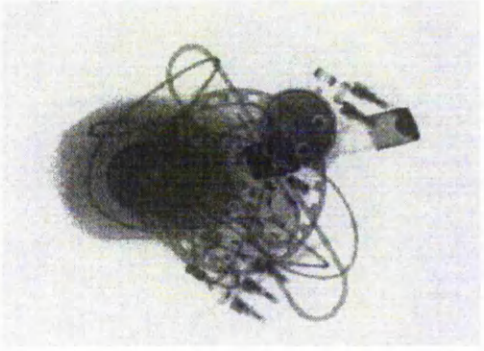

perspective image 10

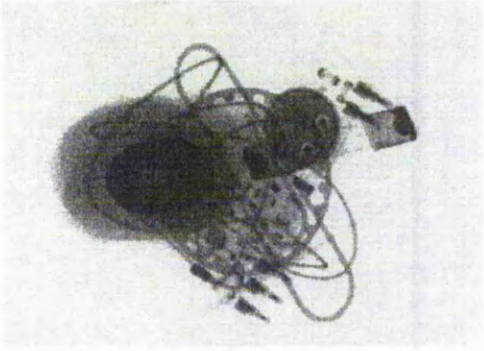

perspective image 11

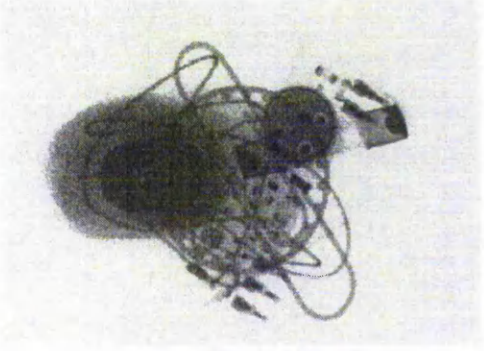

perspective image 12

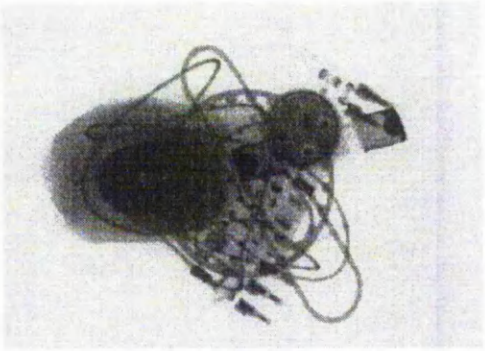

perspective image 13

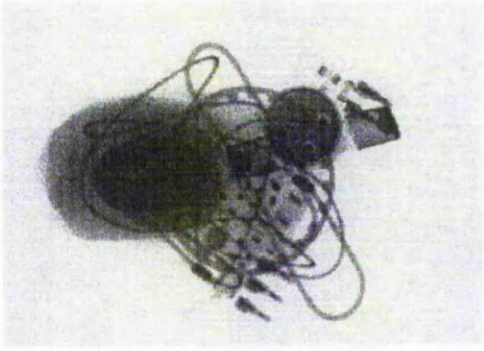

perspective image 14

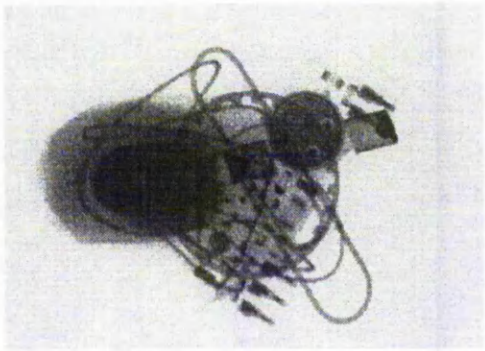

perspective image 15

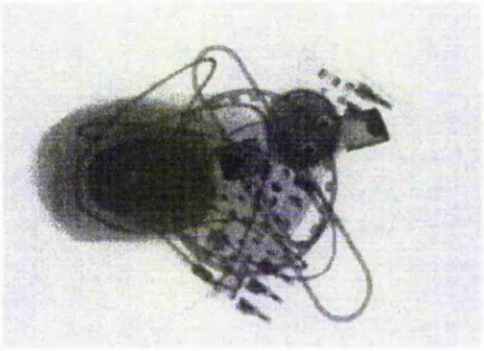

perspective image 16

F Research papers and contracts

1. Hon H.W., Evans J. P. O. and Robinson M., "Multiple View Line-scan Imaging using an Area Array Camera", Proceedings of the IEE, PREP 2000 Second Conference, pp. 309-314, April 2000.

2. Feasibility study conducted for the Police Scientific Development Branch part of the Home Office Science and Technology Group. "The Use of an Area Array Camera in Modelling Multiple View Line-scan X-ray Imaging System". June 1999 (£4,500)

3. Research contract placed by the Police Scientific Development Branch part of the Home Office Science and Technology Group, "Development of a 3D X-ray Moving Stereo Image Acquisition System". November 2000 (£62,500)